Directional Transduction for Guided Wave Structural Health Monitoring

by

Ken I. Salas

A dissertation submitted in partial fulfillment
of the requirements for the degree of
Doctor of Philosophy
(Aerospace Engineering)
in The University of Michigan
2009

Doctoral Committee:

Professor Carlos E. S. Cesnik, Chair
Professor Anthony M. Waas
Associate Professor Bogdan I. Epureanu
Associate Professor Jerome P. Lynch

© Ken I. Salas 2009
All Rights Reserved

For my parents.

ACKNOWLEDGEMENTS

First and foremost I want to thank my parents for their continued support and encouragement in all the activities that I have chosen to pursue in my life. They have always believed in me and have provided me with every imaginable opportunity to succeed in my academic and personal endeavors. This dissertation is a tribute to all their efforts. I will be forever grateful for all their love and support and hope that my lifetime is sufficient to reward them for all they have done for me. I also want to thank my grandparents, uncles, and cousins for their extended love and support.

The career of a graduate student is most definitely shaped by his dissertation advisor. I want to sincerely thank Prof. Carlos Cesnik for his mentorship during the past forty three months. I am particularly grateful for his trust in me, for his flexibility in allowing me to pursue the research directions within the project that best matched my interests and skills, and for always ensuring that I had the best tools needed to succeed in our research. Prof. Cesnik has pushed me (and all his students for that matter) to excel in all areas that an engineer must develop to become successful. In addition to demanding the highest technical quality in our research work, he has spent a great amount of effort teaching us how to best present and document these results in a clear and useful manner. The opportunity to attend multiple leading engineering conferences has also been extremely valuable. I truly believe I have become a much better engineer thanks to my involvement with Prof. Cesnik. I am also very grateful to the rest of my dissertation committee. I want to especially thank Prof. Anthony Waas for giving me the first research opportunity as an undergraduate student and for his guidance and support during my early graduate student career. I learned many important technical and research lesssons from my interactions with Prof. Waas and his research group and I am very grateful for this. I want to thank Prof. Jerome Lynch for his advice and for serving on my dissertation committee. I benefited greatly from my involvement with his research group during field testing, and I want to thank him for his guidance during this time. I want to thank Prof. Bogdan Epureanu for taking the time to read my dissertation and serving on my doctoral committee. Finally, I also wish to thank Prof. Nicolas Triantafyllidis for his kind advice during the early

stages of my graduate education.

My experience as a student at the University of Michigan has been greatly enriched by my interaction with a large number of highly talented people. These individuals helped in shaping my career as a graduate student and I therefore wish to acknowledge them in chronological order. I want to thank Dr. Joseph Rakow (now at Exponent) for his guidance during my first research experience as an undergraduate student. I learned many valuable lessons working in the lab with Joe that have proved very useful during my years as a graduate student. I also wish to thank Dr. Shiladitya Basu (now at Granherne Marine), Prof. Peter Gustafson (now at Western Michigan University), Dr. Wei Ng, and Amit Salvi for their kind mentorship during my time in the Advanced Composites Structures Lab. I also wish to thank Dr. Ajay Raghavan (now at Metis Design Corporation) for his invaluable help in understanding the fundamentals of guided waves and his support during the early stages of my stay at the Active Aeroelasticity and Structures Research Lab (A^2SRL). I have made good friends at A^2SRL and for this I am very grateful. I wish to thank Dr. Satish Kumar Chimakurthi, Kalyan Nadella, Dr. Weihua Su, and Dr. Rafael Palacios (now at Imperial College) for their friendship and support during this time. I also wish to especially thank my colleague in the experimental lab, Devesh Kumar. I want to thank Abhijit Gogulapati for his valuable support during the stressful time of qualifying exams. Finally, I want to thank the undergraduate researchers that worked with me over the past few years: Mr. Danny Lau, Ms. Rachel Lavalley, and Mr. Santosh Kumar.

I would also like to thank the staff at the Lurie Nanofabrication Facility (LNF) at the University of Michigan where several processes needed in the fabrication of the transducers developed in this dissertation were conducted. In particular, I would like to express my gratitude to Mr. Edward Tang, Senior Research Engineer at the LNF, for his mentorship during my time working in the lab. Ed's expertise in a wide range of micro- and nanofabrication processes was extremely valuable in the development of some of the transducers, and his constant willingness to help is very much appreciated. I also want to thank Mr. Leslie George and Dr. Sandrine Martin, also from LNF for their help in the times when I used the lab.

One of the highlights of my years as a graduate student was my participation in field tests of wind turbines with Prof. Lynch's group. I learned a great deal during this trip, and I want to thank Andrew Swartz and Andy Zimmerman (Laboratory for Intelligent Structural Technology at the University of Michigan) for their field testing guidance, help in setting up the tests, and for making the trip very instructive and

enjoyable.

I would like to thank the engineering staff at the Aerospace Engineering technical center: Tom Griffin, Dave McLean, Eric Kirk, and Chris Chartier. From my days as an undergraduate researcher through my years as a Ph.D. student their help in designing and setting up experiments, installing new equipment in the labs, choosing and setting up new computers, and countless other areas has been invaluable. Graduate students in the aero department are lucky to have a very friendly administrative staff. I want to thank Suzanne Smith, Denise Phelps, Cindy Enoch, Michelle Shepherd, Cindy Collins, and Debbie Laird for all their help and support through my years as an undergraduate and graduate student.

Finally, I would like to acknowledge the financial support provided by the Air Force Office of Scientific Research under grants FA9550-06-1-0071 and FA9550-07-1-0522 with Dr. Victor Giurgiutiu as the technical monitor. This work was co-supported by the NASA Constellation University Institutes Project, Grant NCC3-989, Claudia Meyer, Project Manager and by the Exploration Technology Development Program/Advanced Composites Technologies Project, Mark Shuart, Project Manager. The support of these agencies is gratefully acknowledged.

TABLE OF CONTENTS

LIST OF FIGURES

Figure

LIST OF TABLES

Table

LIST OF APPENDICES

Appendix

ABSTRACT

Directional Transduction for Guided Wave Structural Health Monitoring
by
Ken I. Salas

Chair: Carlos E. S. Cesnik

The principal objectives of structural health monitoring (SHM) are the detection, location, and classification of structural defects that may adversely affect the performance of engineering systems. Ultrasonic testing based on guided waves (GW) is one of the most promising solutions for SHM. These waves are capable of inspecting large structural areas, and can be made sensitive to specific defect types by controlling the testing parameters. A key challenge in the development of GW SHM systems is the lack of robust transduction devices for efficient structural interrogation.

This dissertation presents the design, fabrication, and testing of the Composite Long-range Variable-length Emitting Radar (CLoVER) transducer. This device is composed of independent piezocomposite sectors capable of efficiently exciting highly directional GW for structural inspection. The first step in the development of the new device consists of formulating a theoretical model based on 3-D elasticity to characterize its GW excitation properties. In contrast to reduced structural theories, the developed model captures the multi-modal nature of GW at high frequencies (MHz-range). After a thorough numerical verification, the model is used to determine the efficiency of the transducer relative to conventional configurations under similar electric inputs.

The in-house fabrication and characterization procedures for CLoVER transducers are described and applied to more conventional piezocomposite transducer geometries. The free strain performance of these conventional in-house actuators is shown to be similar to that of commercially available piezocomposite ones. An extensive experimental investigation is subsequently presented to assess the CLoVER GW excitation characteristics in isotropic and composite materials. The radiation patterns excited

by these devices are spatially characterized using laser vibrometry, and the results confirm the ability of the devices to induce highly directional GW fields. The performance of the proposed interrogation approach is experimentally assessed using the pulse-echo method with simulated defects, and the ability of CLoVER transducers to detect and localize damage is verified.

The final development presented in this dissertation is the design, fabrication, and characterization of a variable-length piezocomposite transducer. This novel device enables significant modal selectivity (up to 6 dB mode attenuation in the designed prototype), and is able to compensate for environmental effects.

CHAPTER I

Introduction

This chapter presents a brief introduction to the field of guided wave (GW) structural health monitoring (SHM). The fundamental properties of GW are reviewed and its applicability to damage detection is highlighted. The current state of the art in transduction technologies is subsequently presented to motivate the development of the transducers introduced in this dissertation. An outline of the thesis is subsequently presented.

1.1 Structural Health Monitoring

The goal of structural health monitoring (SHM) is to obtain real-time or on-demand information about the condition of engineering structures to identify the presence of damage. In this context, damage is defined as system changes that adversely affect the structure's ability to fulfill its intended objective [1, 2]. This involves interrogating the structure of interest using an on-board network of transducers to determine whether any damage is present and, if so, its location, type and severity. It is envisioned that the information obtained from these systems would be used as input to damage prognosis algorithms which, based on the current condition, would make a prediction about the remaining useful life of the component. There are multiple safety and cost-saving benefits associated with the implementation of this technology in aerospace, mechanical, and civil structures.

The current aerospace structural maintenance approaches are scheduled-based. Therefore, the structure is regularly removed from operation for a given amount of time while technicians employ various NDE tools to determine whether any parts require replacement. A key aspect to note is that the scheduled inspections are not related to the actual state. Therefore, they may occur when the structure is in good condition or when a dangerous amount of damage has already accumulated. This

approach can be greatly improved by employing an online system that can assess the structural condition. For instance, the system could be employed online therefore eliminating the need to take the structure off service. Similarly, the inspection of areas where technician access is difficult could be greatly facilitated. Finally, the maintenance approach could be transitioned to a condition-based approach where, after the SHM system has indicated the presence of damage, a more through inspection is conducted. Similarly, the spacecraft and launch vehicle development and construction industries could significantly benefit from this technology. In particular, a monitoring system able to provide accurate assessments of the condition of various components during assembly, transportation, launch, and operation of space vehicles could significantly reduce the risk associated with such missions. The benefits of SHM technologies are not limited to the aerospace field. Multiple mechanical and civil systems can also benefit from real-time structural information. For instance, wind turbine operators could employ an autonomous SHM system to monitor the condition of the blades and other components with minimal personnel involvement. This would be particularly valuable in offshore wind turbines where technician access is significantly more complicated and expensive. Similarly, the condition of offshore oil platforms and oil pipelines could be inspected with such systems, and repairs scheduled only when they are required.

The majority of the current damage detection methodologies for engineering structures are based on structural dynamics. In general, a network of actuators and sensors are distributed on the structure to record its vibration response to a known excitation input. In order to identify changes in the system, the recorded response is compared to that obtained at a previous stage where the structure was known to be undamaged or "healthy". Using signal processing and system identification algorithms, features related to damage can be extracted from the difference between the two responses. The type and level of excitation characterizes the health monitoring system and determines the amount and type of information that can be recorded. Initial studies were based on identifying shifts in the fundamental vibration modes of the structures that could be associated with the presence of damage. Due to the global nature of the modes, these methodologies showed very low sensitivity to smaller damage (e.g., cracks or delaminations). The detection of these defects is critical as their sudden growth can result in unexpected structural failure.

The detection of smaller defects requires the use of localized interrogation technologies, which can be broadly classified as passive or active. Passive systems employ transducers that are only intended to sense the response of the structure. That is,

there is no active interrogation involved. The most prominent methods in this area are acoustic emission (AE) and strain/load monitoring. In an AE-based SHM system, the distributed sensors are activated at discrete time intervals to "listen" to the response of the structure [3, 4]. The fundamental principle is to use the acoustic energy emitted by the creation or growth of damage to identify its presence and location. As can be intuitively expected, this methodology would require a considerable number of transducers to properly cover the structural surface. Similarly, strain monitoring employs strain gages to ensure that the applied loads do not exceed predetermined critical values. In general, these methods are better suited to support the inspection of areas where damage is expected to occur. As previously noted, passive SHM systems are insufficient for damage detection particularly as they may be ineffective until an undesirable threshold has been reached. Active health monitoring systems offer a better alternative as they rely on on-demand interrogation of structural surfaces. In this case, the transducer network is also capable of exerting some type of excitation on the structure to determine the structural condition. Guided waves (GW) are among the most important methods for active SHM systems and their characteristics are discussed in the following section.

1.2 Guided Wave SHM

GW have received significant attention in SHM research due to several of their features being attractive for this application. GW are stress waves forced to follow a path defined by the boundaries of the substrate in which they travel. In thin plates, they originate from the interaction of dilatational and vertically-polarized shear waves reflected from the top and bottom boundaries of the structure. Cawley *et al.* [5], Guo *et al.* [6], and Dalton *et al.* [7] were among the first to propose the use of GW for the long range inspection of structural components, such as plates and pipes, made of metallic and composite materials. The use of GW enables great flexibility in damage inspection, originating from the wide range of properties of these elastic phenomena. For instance, the active nature of GW, which enables them to be excited at any time, is particularly useful for on-demand inspection. In typical SHM applications, a network of transducers for excitation and sensing of GW is installed on the structure to be inspected. The fundamental hypothesis is that the properties of the inspection pulses (e.g., amplitude, time of arrival, phase, mode composition) will contain information regarding the structural health of the propagating medium. These parameters are typically revealed through advanced signal processing of the

inspection signals. These algorithms must extract certain wave features that are sensitive to the presence of defects or structural damage. It is envisioned that the information collected with these systems will be used as input to damage prognosis algorithms capable of predicting the remaining useful life of the structure.

Among the most important advantages of GW for SHM is their tunable sensitivity to different damage types. By controlling the excitation frequency of the interrogating pulse, the wavelength and through-thickness profile can be controlled. The tunability of the wavelength allows the inspection pulses to be sensitive to different damage types. As will be discussed in subsequent chapters, the reflections from specific defect types can be maximized if the wavelength and a characteristic defect dimension occur in specific ratios. Similarly, by controlling the energy distribution profile different regions through the thickness of the plate can be inspected. This feature can be critical in the inspection of laminated composite materials where specific interfaces need to be monitored for delaminations.

An important property of GW is their multimodal nature. This characteristic indicates that at least two GW modes can propagate in a structure at any frequency-thickness combination. The first of these is a symmetric mode (referred to as fundamental symmetric or S_0) while the second is an antisymmetric mode (referred to as fundamental antisymmetric or A_0), where the symmetry axis is located midpoint through the plate thickness. The properties of these modes are intrinsically different, and they are consequently used for different inspection purposes. The energy of the symmetric mode is predominantly concentrated near the center of the plate, and therefore its main contributions are from the in-plane displacement and stress components. As a result, this is the preferred choice for the inspection of holes in metallic structures and delaminations in composite materials. Furthermore, as its energy is concentrated within the plane of the plate, this mode is not susceptible to attenuation from structural features used in complex structural configurations (e.g., stiffeners). In contrast, the antisymmetric mode (also referred to in the literature as a flexural mode) is dominated by its out-of-plane components. Therefore, it is useful for the detection of surface damage such as surface cracks. At higher frequencies, determined by the material properties and plate geometry, higher GW modes can also propagate in the structure.

Another property of GW that plays a critical role in SHM applications is their dispersive nature. This characteristic results in the phase and group velocity of any GW mode being a function of the excitation frequency. This phenomenon can be easily appreciated from Fig. 1.1, where the wave velocity curves are shown for the

fundamental symmetric and antisymmetric modes in an isotropic plate. In SHM applications, the inspection pulses are necessarily composed of multiple frequency contributions. As a result, points of low dispersion must be selected as this ensures that the excitation pulse will remain compact as it propagates through the medium under inspection. If a mode is excited at a point of high dispersion (indicated by a large slope in the wave velocity curve), the distance between the faster and slower frequency components will increase as the pulse propagates through the structure. The spatial energy spreading results in unnecessary attenuation of the inspection pulses. Furthermore, the physically wider pulse reduces its damage resolution capability, and generally complicates the subsequent signal processing stage.

1.3 Current Transduction Mechanisms for GW SHM

There are multiple options for GW generation for SHM systems. A review of the state-of-the-art in this area was presented by Raghavan and Cesnik [8]. The most common choices rely on piezoelectric materials as the active component of the device. Among these, the simplest option is surface-bonded piezoelectric wafers. These transducers have the advantages of being light, easy to handle, and inexpensive, as shown in Fig. 1.2. However, their implementation in real structures is limited by their brittleness and lack of surface conformability. Furthermore, their wave excitation mechanism is not optimal as it relies on the 1-3 piezoelectric effect. Therefore, the waves are excited through a secondary Poisson effect resulting from the expansion of the piezoelectric element through the thickness direction. To overcome these difficulties, Bent and Hagood [9, 10] developed the Active Fiber Composite (AFC) transducer which used extruded cylindrical piezoceramic fibers. These were encased between interdigitated electrodes and bonded using a structural epoxy. A similar concept, the Macro-Fiber Composite (MFC), was later presented by Wilkie *et al.* [11], but in this case the piezoceramic fibers were diced using computer-controlled dicing saws resulting in a rectangular cross-section. These transducers (collectively referred to as Anisotropic Piezocomposite Transducers or APT) overcome the difficulties associated with piezoceramic wafers, and in addition have higher strain energy density due to the use of the 3-3 piezoelectric effect. In contrast to the aforementioned 1-3 effect, the polarization and primary strain direction are parallel in APTs. A schematic of these devices is shown in Fig. 1.3. Another alternative that has been considered is interdigital polyvinylidene fluoride (PVDF) transducers, where a homogenous piezoelectric substrate is excited through electrode fingers. Monkhouse *et al.* [12, 13] and

Wilcox *et al.* [14] developed this type of transducer in rectangular and wedge-shaped geometries, and showed that modal selectivity (defined as the selective excitation of specific GW modes) could be attained by controlling the width of the electrode fingers. However, the piezoelectric effect is weak in PVDF and it is therefore not well suited for sensing applications. This, combined with its low structural stiffness, makes it an unattractive choice for GW transduction.

Non-piezoelectric alternatives often involve using electromagnetic acoustic transducer (EMAT) arrays, shown in Fig. 1.4. These devices involve a combination of concentric coils that work in conjunction with permanent magnets attached to the structure under inspection to excite GWs. These arrays have the advantage of being able to selectively excite specific wavelengths, but are rather bulky in comparison to piezoelectric alternatives. This approach has been pursued by Wilcox *et al.* [15, 16, 17], who developed an omnidirectional transducer for damage detection using the fundamental symmetric (S_0) mode. Magnetostrictive materials, which undergo mechanical deformations upon application of a magnetic field, have also been explored as mechanisms for GW transduction. For example, Lee *et al.* [18] and Kim *et al.* [19] have used a magnetostrictive patch, combined with a planar solenoid array, to develop transducers for excitation of shear horizontal waves.

An important requirement for GW-based SHM systems is that power and complexity be minimized. A good transducer would focus all the input energy along a given direction on the structure to maximize the reflection levels from possible damage sites. In the case of monolithic wafers, due to their piezoelectric nature, the wave field induced is omnidirectional. Similarly, while APTs are able to generate directional wave fields, they are unable to scan the entire structural surface individually. An option that has been explored in this regard is the use of phased arrays of piezoelectric wafers, where a group of transducers is employed to generate a scanning beam through signal interference. In this approach, each element in the array is excited with a modulated pulse and the response is recorded with all the remaining elements. This procedure is repeated until all independent combinations of actuator and sensor pairs have been used. The result from this scan is later used in a post-processing algorithm that manipulates the phase of the pulses to virtually scan in a specific direction. Wilcox *et al.* [20] used circular and linear arrays for the inspection of large areas of thick plate-like structures. Their study used both piezoelectric discs and shear piezoelectric transducers, and demonstrated that the ratio of the area covered to the array dimension was as large as 3000 to 1. Further efforts along this direction were presented by Fromme *et al.* [21], who developed a ring

array of piezoelectric transducers bonded on plate-like structures using a protective membrane. This concept was also successfully realized experimentally by Giurgiutiu [22, 23], yielding very narrow GW scanning beams that were successful in identifying cracks. However, it was reported that the increased number of transducers needed produced wiring difficulties. Sample phased array architectures are shown in Fig. 1.5. More recently, Kim and Philen [24] extended this approach to consider arrays of APT devices. This interrogation architecture has also been extended to the case of composite laminated plates in the work of Zemmour and Pines [25].

The directionality achieved with phased arrays also has limitations, which are introduced by side lobes that inevitably result from the phased addition algorithm. These lobes are important as they determine the maximum attainable signal to coherent noise ratio, as explained by Wilcox [20]. If the array operates below this ratio, these side lobes may be misinterpreted as structural features or possible damage sites. Furthermore, while this type of array has been successful in obtaining directionality and detecting damage, the fact that this is achieved by the construction and destruction of waves implies that the power is not efficiently deployed.

A different approach, based on MFC rosettes, was presented by Matt and Lanza di Scalea [26]. Their approach was implemented using two rosettes in isotropic and composite plates as well as curved honeycomb sandwich panels. This method is not an active interrogation approach, but it is able to identify the direction of an incident wave which could for example have originated due to the interaction of a separate GW field with a damage site. While GWs generated from traditional monolithic piezoceramic transducers cover all directions, this is achieved in an inefficient manner. On the other hand, transducer arrays achieve directional GW fields but at a high energy cost: directionality is based on construction/destruction of the signal during post-processing. Moreover, as discussed above, the system complexity associated with wiring decreases its reliability. In this dissertation, a novel transducer concept is presented that directs the GWs in an efficient way and keeps the electrical complexity to a minimum.

1.4 The CLoVER Transducer

This dissertation introduces a new transducer concept for efficient damage interrogation and GW excitation in SHM systems. The Composite Long-range Variable-length Emitting Radar (CLoVER) transducer [27, 28, 29, 30], schematically shown in Fig. 1.6, consists of a collection of wedge-shaped APT sectors arranged in a circular

configuration. These transducers are able to efficiently scan a large structural area to identify the presence of defects from a central location, as schematically shown in Fig. 1.7. After exciting each sector with a modulated toneburst signal, a short time delay is introduced to record the reflected waves and allow all reflections from damage and structural features to attenuate. These reflections can be recorded using all sectors in the CLoVER transducer taking advantage of its sensing directionality. Alternatively, a piezoelectric wafer sensor bonded, for instance, at the center of the array could also be used. This procedure is then repeated until an entire 360^0 range has been covered. The experimental results presented in this thesis demonstrate that each CLoVER sector uses the excitation input energy to primarily detect damage when it is located within its azimuthal projection.

A desirable feature for detecting damage using GWs is that the transducer be capable of selectively exciting individual modes. It is well known that different modes are necessary to identify a wide spectrum of damage types [31]. For instance, the S_0 Lamb mode is sensitive to through-the-thickness damage due to its dominant in-plane components, and therefore is well suited for the detection of, for example, full- or part-depth holes. Similarly, the A_0 mode is better suited for surface damage (e.g., surface cracks) due to its dominant out-of-plane component. Furthermore, as higher-order modes are employed for damage characterization, modal selectivity will play a more important role. The interdigitated electrode design used in the first generation of CLoVER transducers, described in Chapter III, uses two independent radial subdivisions that can be used to achieve modal selectivity. This can be accomplished by selecting these dimensions according to the wavelength of the desired modes. Further details about this possibility are explored in Chapter VI. An additional benefit of this feature is the ability of each CLoVER sector to act as an independent actuator and sensor unit in the array, as previously discussed. This would be advantageous in the field implementation of these devices as it decreases the number of separate transducers needed (both actuators and sensors) for data collection. Finally, due to their composite construction, CLoVER transducers have a higher specific strength than piezoceramic wafers, are more resistant to damage due to environmental conditions, and are easily bonded on curved surfaces characteristic of aerospace applications.

1.5 Research Objectives and Dissertation Overview

The principal objective of this dissertation is to advance the state of the art in directional transduction for GW SHM. This is accomplished through the design,

fabrication, and characterization of novel piezoelectric-based transducers for efficient, long-range structural interrogation. The transducer designs are tested in material systems of interest in aerospace, mechanical, and civil structures to demonstrate their improvement over alternative concepts and their damage detection capabilities. This thesis is organized as follows:

Chapter II introduces a theoretical, elasticity-based model for GW excitation by a CLoVER sector. The theory is verified numerically and used to show the directionality and efficiency of the proposed transducer. A model for the response of piezoelectric sensors to the GW field excited by CLoVER transducers is also derived. The transducer fabrication and characterization procedures are reported in Chapter III. The cure and poling parameters are described in detail, and the in-house devices are shown to have free strain performance levels similar to those in commercially available transducers. A comprehensive experimental validation of the theoretical model developed in Chapter II is also presented. The studies are based on piezoelectric sensor response and laser vibrometry, and they verify the accuracy of the theory and the directionality attained with the device. A set of GW experiments in operational wind turbine structures are also reported to show the feasibility of this approach for use in large structures.

Motivated by their increasing use in aerospace structures, Chapter IV reports a numerical and experimental investigation into GW excitation in composite materials. A systematic approach is followed for the anisotropy of the substrate and the transduction mechanisms. Piezoelectric wafers are first considered as a baseline case, followed by the GW excitation properties of CLoVER transducers in various composite plates. The damage interrogation approach proposed with this novel device is experimentally demonstrated in Chapter V where multiple damage detection experiments in isotropic and composite materials are reported. It is shown that the directionality and arrangement of the transducer allows it to correctly identify defects from a central location. Chapter VI reports the development of a variable-length piezocomposite transducer for modal selectivity and environmental compensation. The design procedure intended to optimize the sensitivity to specific GW modes is explained in detail, and a set of experimental tests in isotropic structures are presented to validate the concept. Finally, the results from this thesis are summarized in Chapter VII, where the key contributions to the field of GW SHM are reported and suggestions for future research are presented.

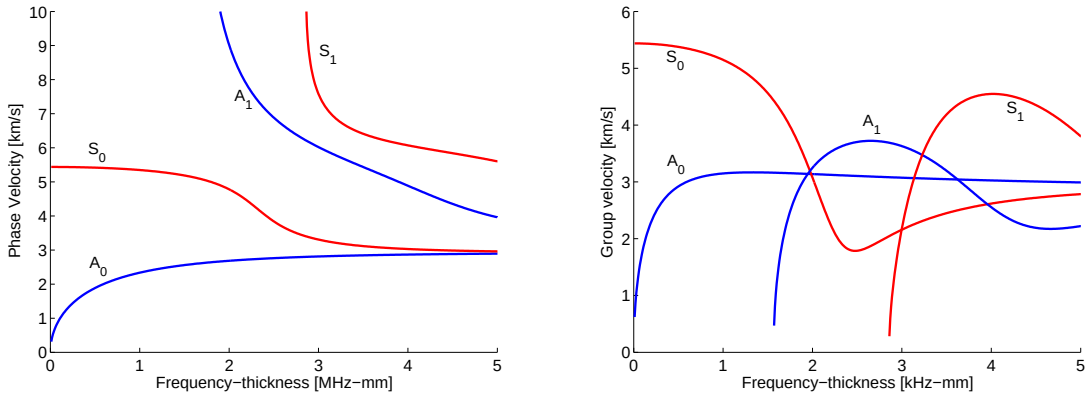

(a) **(b)**

Figure 1.1: Dispersion curves for GW modes in an aluminum plate: (a) phase velocity; (b) group velocity.

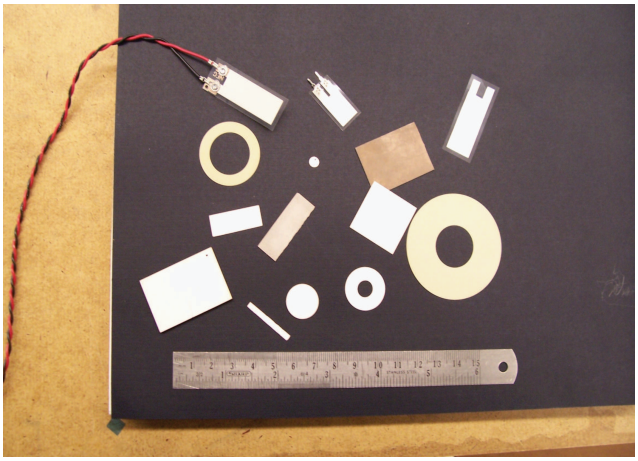

Figure 1.2: Sample piezoelectric wafers used for GW SHM.

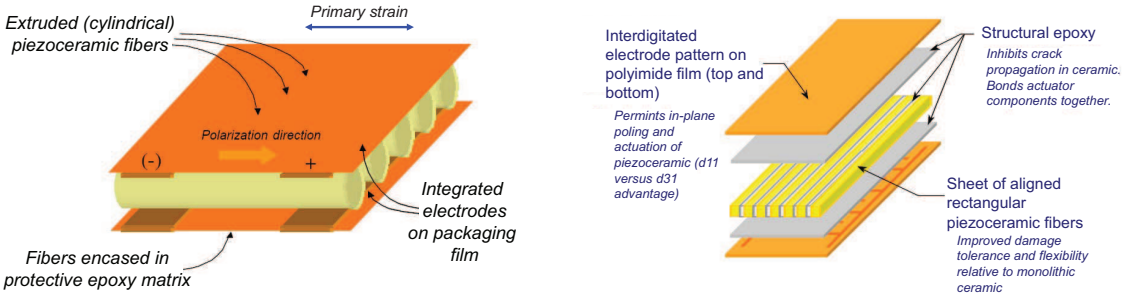

(a): AFC **(b): MFC**

Figure 1.3: The two primary types of APT [32].

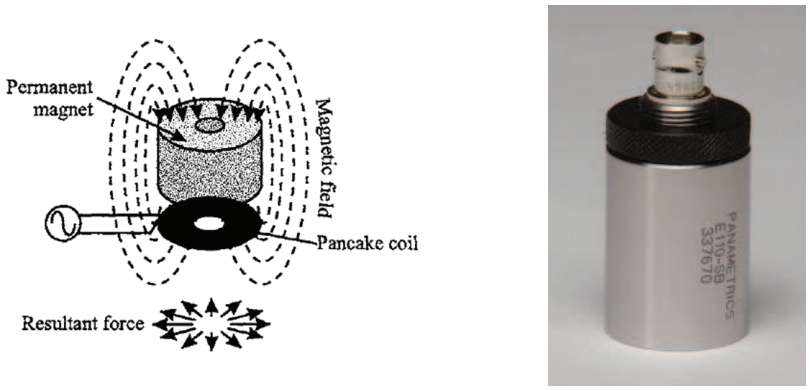

(a) (b)

Figure 1.4: Sample electromagnetic transducer array (EMAT): (a) Operating principle [15]; (b) Actual transducer [33].

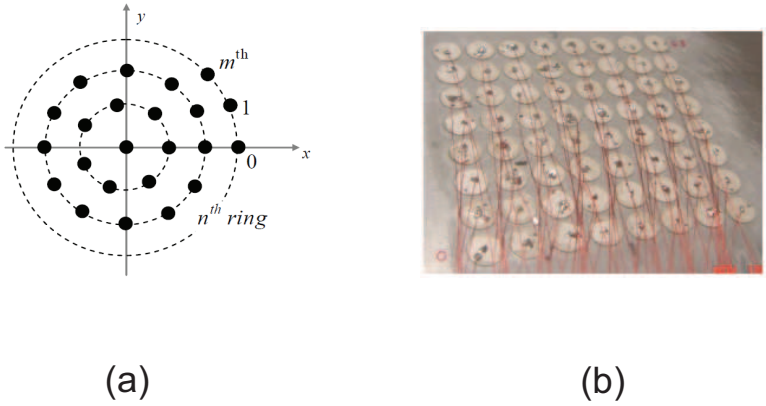

Figure 1.5: Sample piezoelectric wafer phased arrays [22].

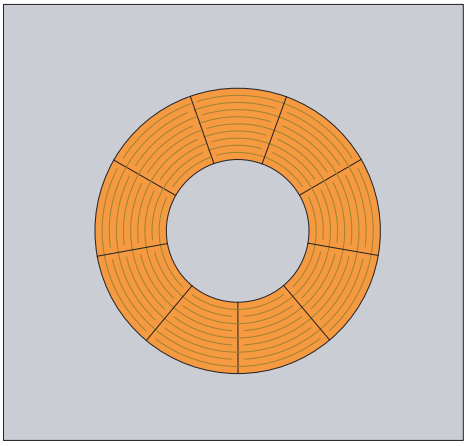

Figure 1.6: Schematic of the CLoVER transducer.

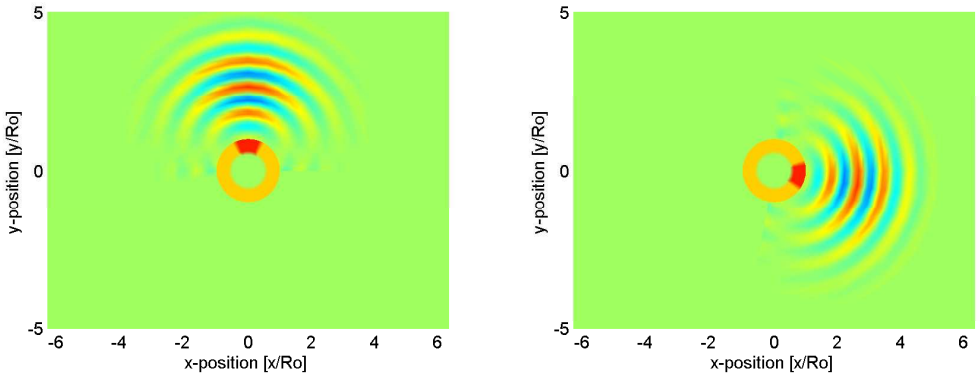

(a) **(b)**

Figure 1.7: Damage interrogation approach used with CLoVER transducers: out-of-plane displacement field for A_0 mode at a frequency-thickness product of 208 kHz-mm.

CHAPTER II

Modeling of Guided Wave Excitation by CLoVER Transducers

This chapter introduces a theoretical model based on three-dimensional elasticity to model the guided wave (GW) excitation properties of CLoVER transducers in isotropic materials. The boundary value problem of linear elasticity is formulated and solved using Fourier transforms and complex calculus. The accuracy of the solution is later verified using a set of three-dimensional finite element simulations. The results of the developed theory are subsequently applied to investigate the effect of the transducer dimensions on the excited wave field, and to characterize the response of various piezoelectric-based sensors to the wave field excited by CLoVER transducers.

2.1 Introduction

After the early development of Lamb wave theory (e.g., the works of Lamb [34] and Gazis [35]), there have been significant efforts in elastodynamics research to develop solutions for the GW field excited by surface-bonded transducers. Various approaches have been taken towards this goal, and some of these are highlighted in this section. Several researchers have analyzed the propagation of GWs in isotropic plates by modeling the actuator as a combination of point sources. For example, Wilcox *et al.* [14] used the Huygens principle to model the acoustic field induced by interdigital polyvinylidene fluoride (PVDF) transducers. In that approach, the electrode fingers were divided into individual elements, each of which was modeled as a point source causing a normal traction on the surface of the substrate. Each of these sources was represented through an excitability function and radiation pattern, both of which depended on wavenumbers found from the Rayleigh-Lamb dispersion relation. The contribution from the actuator was then found by integrating the contributions from

each individual point. The predictions from this analysis were shown to compare well with experimental measurements for rectangular and wedge-shaped transducers. Along a similar direction, although in a more general framework, Achenbach *et al.* [36] expressed the displacements induced by a time-harmonic point load of arbitrary direction, applied either internally or on the surface, as an expansion of symmetric and antisymmetric Lamb modes using Hankel functions as the carrier waves. In their approach, the principle of elastodynamic reciprocity was used to find the expansion coefficients for each mode. This analysis was extended by Huang *et al.* [37] to consider finite-dimensional sources by discretizing the transducer using point loads.

Different studies have used reduced order plate theories in the analysis of wave propagation in an effort to obtain more computationally efficient, but significantly simplified solutions. For instance, Lin and Yuan [38] modeled the excitation of GWs on isotropic substrates using Mindlin plate theory. Their analysis accounted for transverse shear and rotary inertia effects, and considered only axially symmetric motions. The effect of the transducer on the plate was modeled as uniform bending moments around the edges of the actuator. In an effort to correlate their analysis with experimental results, a model for the sensor response under the excited GW field was developed. The experimental measurements, which employed piezoceramic disks, displayed reasonable agreement with the theory until frequency-thickness products of 160 kHz-mm. This was reported to be a result of the shear correction factor needed in the formulation being chosen to match one dispersion curve corresponding to the 3-D elasticity solution. Similarly, Rose and Wang [39] used Mindlin plate theory to derive source solutions that could be combined to represent finite-dimensional transducers. They argued that the range of validity of their solution made it applicable to typical aerospace structures. A higher order plate theory, considering first-order normal strains and second-order transverse shear strains, was developed by Yang and Yuan [40]. In their work, it was argued that this theory produced good agreement with 3-D elasticity solutions until the first cut-off frequencies using a more efficient approach. The main limitation with this type of approaches is that they are limited to low frequency-thickness products and, in most cases, can only model the fundamental antisymmetric mode. As was previously mentioned, one of the main advantages of using GWs is their sensitivity to different damage types, which can be better exploited at higher frequency-thickness products. Furthermore, while damage detection can be typically achieved using the fundamental modes, it may be necessary to use higher modes if the *type* of defect is to be identified. In this case, only 3-D elasticity models will be reliable.

A more accurate model was developed by Giurgiutiu, where the GW field excited by an infinitely wide piezoelectric actuator and an isotropic substrate was modeled using 2-D elasticity [41, 42]. The interaction between both parts was modeled as shear tractions along the transducer edges, and the solution was found using Fourier transforms and the residue theorem from complex calculus. The concept of Lamb wave tuning was demonstrated, and good agreement with experiments was reported. Following this approach, Raghavan and Cesnik developed 3-D elasticity solutions for GW excitation by finite-dimensional transducers in isotropic and composite structures [43, 44, 45]. The analysis used Fourier transforms and complex calculus, and a rigorous Fourier inversion procedure was presented. Several transducer constructions (piezoelectric wafers and piezocomposite transducers) and geometries (rectangular, circular, and ring-shaped) as well as structural configurations (pipes and plates) were considered, and the solution was used to determine optimal actuator and sensor dimensions for use in SHM systems [46].

Multiple approaches to numerically model the propagation of GW have also been proposed. Traditional solution methodologies, such as the finite-difference (FD) and finite element methods (FEM), are not ideally suited for GW analysis due to their high computational cost. An alternative approach was presented in Lee and Staszewski [47] who applied the local interaction simulation approach (LISA) to analyze GW propagation in metallic structures. This methodology was originally developed by Delsanto *et al.* for one-, two-, and three-dimensional structures [48, 49, 50]. Following this approach, the domain was divided into elementary cells that were considered to be discontinuous among each other. Therefore, displacement continuity was enforced at each cell node. The results from this method were favorably correlated with experimental data, and subsequently used in modeling the interaction of GWs with different structural defects [47, 51]. Similarly, the spectral finite element method (SFEM) has been under development by several researchers, such as Apetre *et al.* [52], for SHM applications. The SFEM is based on transforming the dynamic loading and solving the problem in the frequency domain through a FFT algorithm. By using a set of exact shape functions (in the sense that they are solutions to the wave equation as opposed to polynomials) is then used to efficiently interpolate the displacement fields using a smaller number of elements. A comprehensive reference on the development of this method was presented in the book by Gopalakrishnan *et al.* [53].

This chapter presents the development of a 3-D elasticity theory for GW excitation by a wedge-shaped APT in isotropic plate-like structures. The construction of

this theory supports the development of the Composite Long-range Variable-length Emitting Radar (CLoVER) transducer presented in this thesis as an alternative concept for damage interrogation in SHM systems. The theoretical framework is based on the work of Raghavan and Cesnik [43, 44], and the resulting solution is therefore able to capture the multimodal nature of GWs. The boundary value problem of linear elasticity is first formulated in its general form, and later tailored to the case of a CLoVER sector. The solution process is subsequently described in detail and the resulting displacement equations are presented. Results from 3-D FEM simulations are then used to determine the accuracy of the theoretical result as a solution to the elasticity problem considered. Following the verification of the theoretical solution, the result is employed to explore the effect of the transducer dimensions on the GW field excited by a CLoVER sector, and the performance enhancement offered by the geometry of the device. The chapter concludes with a theoretical result for the response of piezoelectric and piezocomposite sensors to the GW field excited by a CLoVER sector.

2.2 Boundary Value Problem Formulation

The GW field excited by a finite-dimensional transducer bonded on the surface of an isotropic substrate is modeled as a boundary value problem of linear elasticity. The dynamics of the actuator and the substrate are assumed to be uncoupled, and their interaction is modeled as surface tractions along the edges of the transducer. There are two implications to this assumption. First, the bonding layer between the actuator and the substrate is assumed to be infinitely thin and not shear deformable, that is, the two parts are assumed to be perfectly bonded. This ensures that strains are transferred only along the actuator edges. This assumption is clearly an idealization, as the bonding layer will have a finite thickness in actual applications. Valuable insight into this aspect was provided by the work of Crawley and de Luis [54], who considered the case of a piezoelectric actuator surface-bonded on a substrate under static conditions. They showed that, for a bonding layer with finite thickness, this assumption becomes accurate if the product of the actuator's modulus and thickness is much larger than that of the substrate on which it is bonded. In fact, it was shown that as this ratio approaches zero, the assumption becomes the exact solution. It was also shown that if this condition was not satisfied, a shear lag solution considering strain transfer along the length of the actuator was necessary. Secondly, so that the dynamics of the actuator can be ignored, its inertia must be a small fraction of

the total inertia of the system in the region where strains are transferred. These assumptions are necessary if tractable semi-analytical solutions are to be obtained. Similar models have been used in the past and good agreement with experiments has been obtained [41, 42, 43, 44].

Based on these assumptions, consider an isotropic substrate of thickness $2b$, with the coordinate system centered midway through its thickness as depicted in Fig. 2.1(a). The substrate is of infinite dimensions along the x- and y-directions, as shown in Fig. 2.1(b), and the transducer is bonded on the surface $z = b$. Using the constitutive law for isotropic materials and linear strain-displacement relations, the equilibrium equations in the absence of body forces may be expressed as:

$$(\lambda + \mu)\nabla\nabla\mathbf{u} + \mu\nabla^2\mathbf{u} = \rho\ddot{\mathbf{u}} \tag{2.1}$$

where λ and μ correspond to the Lamé constants for isotropic materials, and ρ represents the material density. As previously mentioned, the transducer is replaced by surface tractions on the top surface of the substrate, while the bottom surface is traction free. Therefore, the following set of boundary conditions applies:

$$\sigma(x, y, -b) \cdot \mathbf{n_l} = \mathbf{0} \tag{2.2}$$

$$\sigma(x, y, b) \cdot \mathbf{n_u} = \sigma_0 \tag{2.3}$$

where $\mathbf{n_l} = \begin{bmatrix} 0 & 0 & -1 \end{bmatrix}^T$, $\mathbf{n_u} = \begin{bmatrix} 0 & 0 & 1 \end{bmatrix}^T$, and:

$$\sigma_0 = \begin{bmatrix} \sigma^{\circ}_{xz} \\ \sigma^{\circ}_{yz} \\ 0 \end{bmatrix} \tag{2.4}$$

Equation (2.4) reflects the fact that the surface-bonded actuator only induces shear stresses on the substrate. A solution to this problem, for the general case of an arbitrarily-shaped transducer, was presented by Raghavan and Cesnik [43, 55] and their theoretical framework is adopted in this work. The displacement vector, $\mathbf{u}$, is decomposed into its Helmholtz components as:

$$\mathbf{u} = \nabla\varphi + \nabla \times \mathbf{H} \tag{2.5a}$$

$$\nabla \cdot \mathbf{H} = 0 \tag{2.5b}$$

The first term on the right-hand side of Eq. (2.5a) represents the gradient of a scalar potential associated with dilatational deformations, while the second term represents the curl of a vector potential associated with constant volume distortions. This decomposition results in the following four differential equations:

$$\nabla^2\varphi = \frac{\ddot{\varphi}}{c_p^2} \tag{2.6a}$$

$$\nabla^2\mathbf{H} = \frac{\ddot{\mathbf{H}}}{c_s^2} \tag{2.6b}$$

where c_p and c_s correspond to the dilatational and shear wave speeds, respectively, which are defined through:

$$c_p^2 = \frac{\lambda + 2\mu}{\rho} \tag{2.7a}$$

$$c_s^2 = \frac{\mu}{\rho} \tag{2.7b}$$

The solution to these equations, under harmonic excitation, is obtained using two-dimensional Fourier transforms, along with the set of boundary conditions given by Eqs. (2.2) and (2.3). The spatial version of the two-dimensional Fourier transform, $\overline{F}(\xi_x, \xi_y)$, of a generic function, $f(x, y)$, is defined as:

$$\overline{F}(\xi_x, \xi_y) = \int_{-\infty}^{\infty}\int_{-\infty}^{\infty} f(x, y)e^{i(\xi_x x + \xi_y y)}dxdy \tag{2.8}$$

where the terms ξ_x and ξ_y correspond to the wavenumbers along the $x-$ and $y-$ directions, respectively. Applying the 2-D spatial Fourier transform to Eq. (2.6a) results in:

$$-(\xi_x^2 + \xi_y^2)\overline{\varphi} + \frac{\partial^2\overline{\varphi}}{\partial z^2} = -\frac{\omega^2}{c_p^2}\overline{\varphi} \tag{2.9}$$

where the derivatives property of the Fourier transform has been used. It can be seen that the Fourier transform application resulted in a partial differential equation being reduced to an ordinary differential equation in the thickness domain. The solution to this equation can be expressed as:

$$\overline{\varphi} = C_1 \sin \alpha z + C_2 \cos \alpha z \tag{2.10}$$

where the term α is defined as:

$$\alpha \equiv \sqrt{\frac{\omega^2}{c_p^2} - \xi^2} \tag{2.11}$$

and the radial wavenumber ξ is defined through $\xi^2 = \xi_x^2 + \xi_y^2$. A similar procedure is applied to each component of the distortional field, $\mathbf{H}$, which results in the following defintions:

$$\overline{H}_1 = C_3 \sin \beta z + C_4 \cos \beta z \tag{2.12}$$

$$\overline{H}_2 = C_5 \sin \beta z + C_6 \cos \beta z \tag{2.13}$$

$$\overline{H}_3 = C_7 \sin \beta z + C_8 \cos \beta z \tag{2.14}$$

where the term β is defined as:

$$\beta \equiv \sqrt{\frac{\omega^2}{c_s^2} - \xi^2} \tag{2.15}$$

The constants C_1 through C_8 needed to describe the displacement field are found through enforcing the traction boundary conditions given by Eqs. (2.2) and (2.3). This is accomplished by substituting Eq. (2.10) and Eqs. (2.12) through (2.14) in the Fourier-transformed version of Eq. (2.5a) to find the displacement components in the Fourier domain, and combining the result with a linear kinematic relationship of the form given in Eq. (2.16) to obtain the strain components.

$$\epsilon_{ij} = \frac{1}{2}(u_{i,j} + u_{j,i}) \tag{2.16}$$

The strain components are then used in conjunction with a linear elastic constitutive equation to determine the stress components. The boundary conditions given by Eqs. (2.2) and (2.3) are subsequently enforced along with Eq. (2.5b) to form a system of equations from which the necessary constants can be found. This system is of the form:

$$\mathbf{QC} = \mathbf{P} \tag{2.17}$$

where $\mathbf{Q}$ is a matrix dependent on the wavenumbers, material properties, and plate thickness, $\mathbf{C}$ is a vector containing the constants C_1 through C_8, and $\mathbf{P}$ is a vector

composed of the tractions exerted by the surface-bonded transducers. The dispersion equation for Rayleigh-Lamb waves results from seeking a non-trivial solution to this system of equations, i.e., by setting $\det \mathbf{Q} = 0$. A detailed exposition of this procedure can be found in the book by Graff [56]. The resulting displacement field can be separated into symmetric and antisymmetric components. To facilitate the presentation of the theory, only the results corresponding to the antisymmetric mode will be presented from this point on. The derivation of the symmetric component follows an analogous sequence and is reported in Ref. [43]. Note that the complete displacement field is obtained by summing the contribution from both modes. After applying the 2-D inverse Fourier transform, the Cartesian displacement components expressed in Cartesian coordinates are obtained as:

$$\mathbf{u}_A(x,y,t) = \int_{-\infty}^{\infty}\int_{-\infty}^{\infty} \frac{\mathbf{\Gamma}_A(\xi_x,\xi_y)}{D_A(\xi)} \mathbf{\Psi}_A(\xi_x,\xi_y) \cdot \\ \cdot \overline{\mathbf{F}}(\xi_x,\xi_y) e^{-i(\xi_x x + \xi_y y - \omega t)} d\xi_x d\xi_y \tag{2.18}$$

Note that Eq. (2.18) provides the displacement components at the surface $z = b$. All subsequent analytical expressions presented here will be for this surface as well. In Eq. (2.18), $\mathbf{\Gamma}_A$ and $\mathbf{\Psi}_A$ are matrices of coefficients, $\overline{\mathbf{F}}$ is a vector containing the Fourier transform of the surface tractions, and D_A corresponds to the dispersion relation for the antisymmetric mode of Rayleigh-Lamb waves given by:

$$D_A = (\xi^2 - \beta^2)^2 \sin\alpha b \cos\beta b + 4\xi^2 \alpha\beta \cos\alpha b \sin\beta b \tag{2.19}$$

In the following section, the result given by Eq. (2.18) will be expressed in polar coordinates and used to solve for the displacement field produced by a CLoVER sector.

2.3 GW Excitation by a CLoVER Sector

The CLoVER sector geometry is easily described using polar coordinates, and is defined by the transducer's inner and outer radii, R_I and R_O, as well as its left and right angular edges, θ_L and θ_R. Figure 2.2(a) shows a schematic of the transducer's geometry. At this point, Eq. (2.18) must be modified to express the displacement components in polar coordinates. This modification involves the use of the 2-D Fourier transform for polar coordinates which, for a generic function $g(r,\theta)$, is defined as:

$$G(\xi,\phi)=\int_0^{\infty}\int_0^{2\pi} g(r,\theta)e^{i\xi r\cos(\theta-\phi)}rd\theta dr \tag{2.20}$$

where the azimuthal wavenumber ϕ can be found from the Cartesian wavenumbers through $\phi=\tan^{-1}\xi_y/\xi_x$. Similarly, the inverse transform is defined through:

$$g(r,\theta)=\frac{1}{4\pi^2}\int_0^{\infty}\int_0^{2\pi} G(\xi,\phi)e^{-i\xi r\cos(\theta-\phi)}\xi d\phi d\xi \tag{2.21}$$

Using these definitions, along with the transformations $\xi_x=\xi\cos\phi$ and $\xi_y=\xi\sin\phi$, yields the following equation for the Cartesian displacement components expressed in polar coordinates:

$$\mathbf{u}_A(r,\theta,t)=\int_0^{2\pi}\int_0^{\infty}\frac{\mathbf{\Gamma}_A(\xi)}{D_A(\xi)}\mathbf{\Psi}_A(\xi,\phi)\overline{\mathbf{F}}(\xi,\phi)e^{-i\xi r\cos(\theta-\phi)}e^{i\omega t}d\xi d\phi \tag{2.22}$$

The matrix $\mathbf{\Gamma}_A$ is a 3 x 3 diagonal matrix of coefficients whose components are given by:

$$\Gamma_{11}=\Gamma_{22}=\frac{\sin\beta b\xi}{4\pi^2\mu\beta\cos\beta b} \tag{2.23a}$$

$$\Gamma_{33}=\frac{-i\xi^2}{4\pi^2\mu}[2\alpha\beta\cos\alpha b\sin\beta b+(\xi^2-\beta^2)\cos\beta b\sin\alpha b] \tag{2.23b}$$

Similarly, $\mathbf{\Psi}_A$ is a 3 x 2 matrix of coefficients defined through:

$$\mathbf{\Psi}_A=\begin{bmatrix} -\gamma_3^{(1)}-\gamma_4^{(1)}(e^{-2i\phi}+e^{2i\phi}) & \gamma_5^{(1)}(e^{2i\phi}-e^{-2i\phi}) \\ \gamma_1^{(2)}(e^{2i\phi}-e^{-2i\phi}) & -\gamma_4^{(2)}-\gamma_5^{(2)}(e^{-2i\phi}+e^{2i\phi}) \\ \cos\phi & \sin\phi \end{bmatrix} \tag{2.24}$$

where the coefficients $\gamma_i^{(j)}$ (defined in the Appendix) depend on the substrate material properties, frequency, and wavenumbers [57, 58]. Finally, the vector $\overline{\mathbf{F}}$ contains the Fourier transform of the shear tractions produced at the transducer's edges. Only shear stresses along the piezoceramic fiber direction are considered, as shown in Fig. 2.2(b). This choice is supported by the transducer acting on the $3-3$ piezoelectric effect, which makes the strains induced along the fiber's axis significantly larger than those along its normal direction. For a typical piezoelectric material (such as PZT-

5A) poled along the thickness direction, the piezoelectric coupling coefficient normal to the poling direction is approximately 54% smaller than that along the poling direction [59]. This level of actuation is still significant, but the strains induced along this direction are further attenuated due to the high aspect ratio of the fiber and the construction of the APT device. As previously discussed, the APT is a composite transducer with epoxy located in between any two fibers. Thus, the shear lag effect effectively eliminates any strain transmitted normal to the fiber length. As a result, for the case of a CLoVER sector, the boundary conditions given by Eq. (2.3), transformed to polar coordinates, take the form:

$$\sigma_{zr}(r,\theta,b) = \tau_0 f(r,\theta) \tag{2.25}$$

$$\sigma_{zz}(r,\theta,b) = \sigma_{z\theta}(r,\theta,b) = 0 \tag{2.26}$$

where τ_0 represents the amplitude of the traction exerted by the transducer on the substrate, and $f(r,\theta)$ is a function whose purpose is to make the stress non-zero only along the transducer's radial edges, as shown in Fig. 2.2(b). Such an expression is given by [1]:

$$f(r,\theta) = [u(\theta-\theta_L) - u(\theta-\theta_R)][\delta(r-R_I) - \delta(r-R_O)] \tag{2.27}$$

In order to use the formulation presented above, the Fourier transform of Eq. (2.27) must be determined. Before doing so, the function must be decomposed along the x- and y-directions to be compatible with the displacement vector given by Eq. (2.22). This is simply done by defining the x- and y-components as the function multiplied by an appropriate rotation matrix. Then, the necessary Fourier transforms are given by:

$$\begin{aligned}\overline{F_1}(\xi,\phi) = \int_0^{2\pi}\int_0^{\infty} [u(\theta-\theta_L) - u(\theta-\theta_R)]\cdot \\ \cdot[\delta(r-R_I) - \delta(r-R_O)]\cos\theta e^{i\xi r\cos(\theta-\phi)} r\,dr\,d\theta\end{aligned} \tag{2.28}$$

[1]Note that this definition of $f(r,\theta)$ yields correct units for stress as the delta function has units of [1/length] and the unit step function is dimensionless.

$$\overline{F_2}(\xi,\phi) = \int_0^{2\pi}\int_0^{\infty} -[u(\theta-\theta_L)-u(\theta-\theta_R)]\cdot \\ \cdot[\delta(r-R_I)-\delta(r-R_O)]\sin\theta e^{i\xi r\cos(\theta-\phi)} r\,dr\,d\theta \tag{2.29}$$

The integrals given by Eqs. (2.28) and (2.29) cannot be solved analytically. An alternate solution method is applicable since the radial and angular parts of the function are readily separable. For this type of functions, the Hankel transform of the radial part can be combined with a Fourier series representation of the angular part to obtain the desired Fourier transform [60]. In this way, the two-dimensional Fourier transform, $W(\xi,\phi)$, for a generic function $w(r,\theta) = g(\theta)h(r)$ can be expressed as:

$$W(\xi,\phi) = \sum_{k=-\infty}^{\infty} c_k e^{ik\phi}(-i)^k \widetilde{H}_k(\xi) \tag{2.30}$$

where $\widetilde{H}_k$ represents the k^{th} order Hankel transform of $h(r)$, defined through:

$$\widetilde{H}_k(\xi) = 2\pi \int_0^{\infty} h(r) J_k(r\xi) r\,dr \tag{2.31}$$

where J_k represents the Bessel function of the first kind and order k, and c_k are the complex Fourier coefficients of the function $g(\theta)$ defined by:

$$c_k = \frac{1}{2\pi}\int_0^{2\pi} g(\theta) e^{-ik\theta} d\theta \tag{2.32}$$

In the case under consideration, the function $h(r)$ is defined by:

$$h(r) = \delta(r-R_I) - \delta(r-R_O) \tag{2.33}$$

while the two functions $g_1(\theta)$ and $g_2(\theta)$ are given by:

$$g_1(\theta) = [u(\theta-\theta_L)-u(\theta-\theta_R)]\cos\theta \tag{2.34a}$$

$$g_2(\theta) = -[u(\theta-\theta_L)-u(\theta-\theta_R)]\sin\theta \tag{2.34b}$$

Therefore, the necessary Fourier transforms for the shear tractions applied on the

substrate's surface result in:

$$\overline{F_{j1}} = \sum_{k=-\infty}^{\infty} c_k^{(j)} e^{ik\phi}(-i)^k \chi_k, \quad j = 1, 2 \tag{2.35}$$

where:

$$\chi_k = 2\pi[R_O J_k(\xi R_O) - R_I J_k(\xi R_I)] \tag{2.36}$$

The resulting complex Fourier coefficients, obtained by substituting Eqs. (2.34) into Eq. (2.32), can be expressed through:

$$\begin{aligned} c_k^{(1)} = \frac{1}{2\pi(1-k^2)} \big\{ & u(\theta_L) \left[e^{-ik\theta_L}(ik\cos\theta_L - \sin\theta_L) - ik \right] \\ & - u(\theta_R) \left[e^{-ik\theta_R}(ik\cos\theta_R - \sin\theta_R) - ik \right] \big\}, \quad |k| \neq 1 \end{aligned} \tag{2.37}$$

$$c_k^{(1)} = \frac{(2\pi - \theta_L - \sin\theta_L e^{-i\theta_L})u(\theta_L) - (2\pi - \theta_R - \sin\theta_R e^{-i\theta_R})u(\theta_R)}{4\pi}, \quad |k| = 1 \tag{2.38}$$

$$\begin{aligned} c_k^{(2)} = \frac{1}{2\pi(1-k^2)} \big\{ & (\theta_L) \left[e^{-ik\theta_L}(\cos\theta_L + ik\sin\theta_L) - 1 \right] - \\ & u(\theta_R) \left[e^{-ik\theta_R}(\cos\theta_R + ik\sin\theta_R) - 1 \right] \big\}, \quad |k| \neq 1 \end{aligned} \tag{2.39}$$

$$c_k^{(2)} = \frac{u(\theta_L)(-1 + e^{-2i\theta_L} - 4i\pi + 2i\theta_L) - u(\theta_R)(-1 + e^{-2i\theta_R} - 4i\pi + 2i\theta_R)}{8\pi}, \quad |k| = 1 \tag{2.40}$$

Since the CLoVER transducer is primarily meant to interrogate the structure away from the location where it is bonded, the main interest is in characterizing the GW field induced for radial positions such that $r > R_O$, as shown in Fig. 2.3. This set is characterized by both edges of the transducer, inner and outer, sending waves propagating in the positive radial direction (henceforth referred to as outward direction). The form of the solution, i.e., the combination of Eqs. (2.22) and (2.35), suggests that the integral definition of the Bessel function of k^{th} order be used:

$$J_k(\hat{z}) = \frac{1}{2\pi} \int_0^{2\pi} e^{-i\frac{\pi}{2}k} e^{i\hat{z}\cos\phi} e^{ik\phi} d\phi = \frac{1}{2\pi} \int_0^{2\pi} e^{i\frac{\pi}{2}k} e^{-i\hat{z}\cos\phi} e^{-ik\phi} d\phi \tag{2.41}$$

Note that Eq. (2.41) holds because the Bessel function returns a real number for $\hat{z} > 0$. Therefore, taking the complex conjugate of the integrand does not alter the final result as its imaginary part is zero. This equation must be manipulated so that the exponential part of its integrand is similar to that in Eq. (2.22) (taking $\hat{z} = \xi r$). This process is carried out through the following change of variables:

$$\phi = \overline{\phi} - \theta \tag{2.42}$$

This operation results in:

$$J_k(\hat{z}) = \frac{1}{2\pi} \int_{\theta}^{2\pi+\theta} \zeta_k e^{-i\hat{z}\cos(\theta-\overline{\phi})} e^{-ik\overline{\phi}} d\overline{\phi} \tag{2.43}$$

where:

$$\zeta_k \equiv e^{i\frac{\pi}{2}k} e^{ik\theta} \tag{2.44}$$

The right hand side in Eq. (2.43) is almost in the desired form. The only differences between this result and the form of Eq. (2.22) are in the integration limits and the index k in the complex exponential. The difference in the integration limits is of no concern since the integrand of both functions is periodic in ϕ with a period of 2π. The indices in Eq. (2.22) will vary according to the powers of the exponentials given in Eq. (2.24). This can be simply resolved by redefining the resulting index of the complex exponential as $-k$, and incorporating this change in the corresponding multiplying coefficients. As a result, the solution to Eq. (2.22) in the angular wavenumber domain is given by:

$$\mathbf{u}_A(r,\theta,t) = \int_0^{\infty} \sum_{k=-\infty}^{\infty} \left[\frac{2\pi \mathbf{\Gamma}_A(\xi)}{\zeta_k(\theta) D_A(\xi)} \mathbf{\Delta}_A(k,\xi,R_O,R_I,\theta_L,\theta_R) J_k(\xi r) \right] e^{i\omega t} d\xi \tag{2.45}$$

where $\mathbf{\Delta}_A$ is a 3 x 1 column vector of coefficients that represents the source terms and is defined in the Appendix. Note that the effect of the transducer dimensions are included in this term. The Bessel function solution presented in Eq. (2.45) corresponds to a standing wave. In order to obtain a propagating wave, we resort to the following definition of the Hankel function of the first and second kind:

$$H_k^{(1)}(\hat{z}) = J_k(\hat{z}) + iY_k(\hat{z}) \tag{2.46a}$$

$$H_k^{(2)}(\hat{z}) = J_k(\hat{z}) - iY_k(\hat{z}) \tag{2.46b}$$

where Y_k represents the Bessel function of the second kind and order k. Based on the frequency convention we have adopted, the Hankel function of the second kind corresponds to an outward-propagating wave in time. Therefore only this part is retained, which yields:

$$\mathbf{u}_A(r,\theta,t) = \int_{-\infty}^{\infty} \sum_{k=-\infty}^{\infty} \left[\frac{\pi \mathbf{\Gamma}_A(\xi)}{\zeta_k(\theta) D_A(\xi)} \mathbf{\Delta}_A H_k^{(2)}(\xi r) \right] e^{i\omega t} d\xi \tag{2.47}$$

Note that the integration limits in the radial wavenumber domain have changed. This is because retaining the Hankel function of the second kind only is equivalent to replacing the azimuthal wavenumber integration limits from a range of 2π to a range of π; hence, in order to keep the integration domain unchanged, the limits in the radial wavenumber domain must be modified [2]. The resulting integral is solved using the residue theorem from complex calculus. Since Eq. (2.47) is the quotient of two functions of ξ, it follows from the theory of complex calculus that the residue, $\overline{b}$, of this function at a pole ξ_A can be expressed as [61]:

$$\overline{b} = \frac{N_A(\xi_A)}{D'_A(\xi_A)} \tag{2.48}$$

where the $'$ symbol indicates differentiation with respect to ξ, and the pole ξ_A corresponds to values of ξ for which D_A vanishes; these points are the wavenumbers corresponding to the antisymmetric modes of Rayleigh-Lamb waves at a frequency ω. The notation $N(\xi)$ has been used in Eq. (2.48) to illustrate the concept. This result can be combined with the residue theorem to express the solution of the integral in the ξ domain as:

$$\int_{-\infty}^{\infty} \frac{N(\xi)}{D(\xi)} d\xi = 2\pi i \sum_{\xi_A} \frac{N(\xi_A)}{D'(\xi_A)}, \quad \xi_A > 0 \tag{2.49}$$

where the condition that ξ_A be greater than zero indicates that only positive wavenum-

[2] This statement is not fully rigorous as a correction term included in the integral definition of $H_k^{(2)}$ has been neglected. However, it can be shown that the contribution from this term is only significant for very small arguments.

bers are to be included in the integration contour. Therefore, the solution to harmonic excitation may be expressed in final form as:

$$\mathbf{u}_A(r,\theta,t) = \sum_{k=-\infty}^{\infty} \left[\frac{2\pi^2 i \mathbf{\Gamma}_A(\xi_A)}{\zeta_k(\theta) D'_A(\xi_A)} \mathbf{\Delta}_A H_k^{(2)}(\xi_A r) \right] e^{i\omega t} \tag{2.50}$$

Note that since only harmonic excitation is being considered, only one wavenumber needs to be included. The solution given by Eq. (2.50) corresponds to the antisymmetric mode. The symmetric mode is given by a similar equation, which is derived by interchanging all sine and cosine terms whose arguments depend on the substrate half-thickness, b. This is a crucial change since it modifies the dispersion equation D_A, which produces solutions with different wavenumbers.

In typical SHM applications, the structure to be inspected for damage is excited with a stress wave whose shape is determined by a time-dependent modulated signal. This type of signal is generally desired so as to control the frequency bandwidth and avoid dispersion. Hann-modulated signals have been successfully used in the past by several researchers and will be adopted in the present formulation [62]. Such a signal is given by:

$$s(t) = \frac{1}{2} \left[1 - \cos\left(2\frac{\omega_0 t}{n} \right) \right] \sin(\omega_0 t) \tag{2.51}$$

where n is the number of half-cycles and ω_0 represents the center frequency of excitation. In order to account for the time-dependence, the time Fourier transform of Eq. (2.51) must be determined through:

$$S(\omega) = \int_{-\infty}^{\infty} s(t) e^{-i\omega t} dt \tag{2.52}$$

The time-dependent displacements are obtained through the inverse Fourier transform of the product of the transforms of the spatial and temporal parts. Since the excitation signal has several frequency components, a sum over all possible wavenumbers is necessary. Hence, the solution becomes (only antisymmetric mode is presented for simplicity) [57, 58]:

$$\mathbf{u}_A(r,\theta,t) = \frac{1}{2\pi} \int_{-\infty}^{\infty} \sum_{\xi_A} \left[\sum_{k=-\infty}^{\infty} \frac{i\pi^2 \mathbf{\Gamma}_A(\xi_A)}{\zeta_k(\theta) D'_A(\xi_A)} \mathbf{\Delta}_A H_k^{(2)}(\xi_A r) \right] S(\omega) e^{i\omega t} d\omega \tag{2.53}$$

2.3.1 Additional Spatial Regions

While the GW field induced by a CLoVER sector will be used for interrogation away from the transducer, it is still of interest to find a solution for the GW excitation problem in the remaining spatial regions. Therefore, region I is defined as the set of all points such that $r < R_I$, as depicted in Fig. 2.4. The solution for this region is obtained through an analogy to a circular transducer. In that case, the resulting wave pattern for radial positions within the edge of the actuator corresponds to standing waves. This result can be intuitively understood due to the axisymmetry of the source. Therefore, each source term in the Fourier expansion used to obtain the solution for a CLoVER sector will be treated as a standing wave. Once all the terms have been multiplied by the corresponding Fourier coefficient and summed together, the result will correspond to the GW field excited by a CLoVER sector. To emphasize, note that each term in the sum represents a standing wave, but the overall combination yields a propagating wave. Therefore, the expression for the antisymmetric displacement components induced under harmonic excitation at a frequency ω is given by:

$$\mathbf{u}_A = \sum_{k=-\infty}^{\infty} \frac{2i\pi^2 \mathbf{\Gamma}_A(\xi_A)}{\zeta_k(\theta) D'_A(\xi_A)} \mathbf{\Lambda}_A(k, \xi_A) J_k(\xi_A r) e^{i\omega t} \tag{2.54}$$

where $\mathbf{\Lambda}_A$ is a 3 x 1 column vector of coefficients that represent the source terms, presented in the Appendix.

In a manner analogous to region I, region II is defined as the set of all points such that $R_I < r < R_O$. This set of points is characterized by the fact that the each source contribution from the outer edge of the transducer corresponds to a standing wave, while those from the inner edge of the transducer correspond to traveling waves. Thus, the solution for this region is obtained as a combination of the two solutions presented previously. The antisymmetric displacement components under harmonic excitation at a frequency ω are given by:

$$\mathbf{u}_A = \sum_{k=-\infty}^{\infty} \frac{2i\pi^2 \mathbf{\Gamma}_A(\xi_A)}{\zeta_k(\theta) D'_A(\xi_A)} \left[\overline{\mathbf{\Upsilon}}_A(k, \xi_A) J_k(\xi_A r) - \mathbf{\Upsilon}_A(k, \xi_A) H_k^{(2)}(\xi_A r) \right] e^{i\omega t} \tag{2.55}$$

where $\mathbf{\Upsilon}_A$ and $\overline{\mathbf{\Upsilon}}_A$ are vectors of coefficients whose definition is given in the Appendix. Note that $\mathbf{\Upsilon}_A$ is associated with waves originating at the inner radial edge of the transducer, while $\overline{\mathbf{\Upsilon}}_A$ corresponds to waves originating from its outer radial edge.

2.4 Finite Element Verification

Results from the theoretical formulation presented above were compared with three-dimensional FEM simulations conducted in the commercial package ABAQUS [63] to assess its spatial and temporal performance. Taking advantage of the problem's symmetries, only one quarter of an aluminum plate was considered. A summary of the material properties and actuator dimensions considered in the simulations is given in table 2.1.

The mesh consisted of three-dimensional continuum elements, and was primarily composed of eight-node bricks (C3D8). In addition, the geometry of the mesh required the use of six-node tetrahedra (C3D6) for the elements immediately connected to the origin. Similarly, infinite continuum elements (CIN3D8) were used on the outer radial boundary of the model, in an effort to minimize boundary reflections [63]. However, the results showed that these elements were not successful in achieving this, and therefore the radial positions selected for comparison were located far from the radial edge. In all cases, three elements were used through the thickness of the plate. A schematic of the mesh is shown in Fig. 2.5(a), while its relevant dimensions (radius, R, and half-thickness, b) are given in table 2.2. Symmetric (S_0) and antisymmetric (A_0) modes were excited by specifying symmetry or antisymmetry conditions with respect to the $z-$axis, respectively. The symmetric mode was used to validate the out-of-plane displacement, while the antisymmetric mode was used to model the in-plane displacements. This choice was based on the fact that the antisymmetric mode has a higher frequency threshold for the appearance of the SH-mode (shear horizontal mode present only in the in-plane displacements), which is not considered in the theoretical solution and would therefore prevent an accurate verification.

The radial dimension of the elements, Δr_e, was selected so as to have at least 20 nodes per wavelength for the highest frequency of the toneburst excitation. The element azimuthal size, $\Delta\theta_e$, was selected at three degrees providing six nodes along the angular span of the actuator, whose centerline was located at 90 degrees. A summary of the mesh parameters is presented in table 2.2. The shear tractions caused by the actuator were modeled through nodal forces on the nodes corresponding to the actuator edges. Since the theoretical model considers the traction per unit length to be constant along the radial edges of the transducer, the relative force amplitudes must be scaled appropriately. This was achieved by considering point forces of unit magnitude on the outer radial edge and scaling the magnitude on the inner edge accordingly, which results in its amplitude being R_I/R_O. The time-dependent part of this forcing

function was a Hann-modulated toneburst whose properties are also summarized in table 2.2. A schematic showing the details of the shear traction application is given in Fig. 2.5(b). The time step, Δt, was selected so as to satisfy the following criteria: (i) proper sampling of the highest frequency component of the excitation signal, and (ii) sufficient resolution of the time needed for the fastest traveling wave to move across one element in the radial direction [64]. An implicit dynamic analysis was performed with 1404 steps in all cases.

The numerical implementation of the theoretical solution requires that a finite number of terms in the infinite sum given by Eq. (2.53) be selected. This number was chosen based on the normalized error between the angular part of the shear traction function, Eq. (2.34), and its Fourier series representation, Eq. (2.30). This error is defined as:

$$\varepsilon = \frac{\sqrt{\int_0^{2\pi} \mid g_{1,2} - g_{1,2}^F \mid^2 d\theta}}{\sqrt{\int_0^{2\pi} g_{1,2}^2 d\theta}} \tag{2.56}$$

where the superscript F refers to the Fourier series representation of the function. Figure 2.6 shows how this error decreases with increasing number of terms. Based on this result, the sum was truncated at 150 terms as the reduction in error with increasing terms was slower after this point. In addition, the solution was implemented using a larger number of terms and no difference was observed, indicating this selection was sufficient for convergence. For the spatial comparisons, several azimuthal positions were selected at different radial locations sufficiently far from the radial edge to avoid boundary reflections. Figure 2.7(a) shows the set of azimuthal points selected. The radial positions selected were ten times the transducer's outer radius ($\hat{n} = 10$) for the symmetric mode, and five thirds times the outer radius ($\hat{n} = 5/3$) for the antisymmetric mode. Seven azimuthal locations from the transducer's centerline to its opposite direction were selected, which resulted in intervals of 30 degrees. Figure 2.7(b) shows the normalized peak-to-peak comparison between the theory and FE results, while Figs. 2.7(c)-(d) show a similar result for the in-plane displacements. Similarly, Figs. 2.8(a)-(b) show sample time histories for two different azimuthal positions. These figures indicate that the spatial distribution is accurately modeled by the theoretical solution.

A similar comparison was performed for regions I and II, where only the antisymmetric mode was considered due to its shorter wavelength. Figure 2.9(a) shows a schematic of the points selected for comparison. For region I, an azimuthal dis-

tribution similar to the one used in the previous case was employed, but the radial position was changed to one-half the transducer's inner radius. In region II, only six azimuthal points were considered to avoid having a point over the transducer's area, while the radial location selected was the transducer's midpoint along the radial direction. Figure 2.9(b)-(c) show good spatial correlation for the out-of-plane displacement in regions I and II, respectively. Similarly, Fig. 2.9(d) shows that the time history of the analytical displacements also matches very well with FE results.

2.5 Parametric Studies on CLoVER Transducer Dimensions

In this section, the effect of the radial and azimuthal dimension of a CLoVER sector on the induced displacements is explored. This is done by examining the variation of the source term corresponding to the out-of-plane displacements, $\Delta_A^{(3,1)}$. This choice is justified by the observation that the induced displacements have separate contributions from the transducer geometry and the wave propagation parameters of the substrate (referred to as the excitability function). The source term per unit length along the thickness direction corresponding to the out-of-plane component can be expressed as:

$$\Delta_A^{(3,1)} = \overline{\delta}_{1-k}^{(1)} + \overline{\delta}_{-1-k}^{(2)} \tag{2.57}$$

where k represents a summation index and the terms $\overline{\delta}$, for a given index j, are defined as:

$$\overline{\delta}_j^{(1)} = \frac{1}{2}\left(c_j^{(1)} + ic_j^{(2)}\right)(-i)^j \chi_j \tag{2.58}$$

$$\overline{\delta}_j^{(2)} = \frac{1}{2}\left(c_j^{(1)} - ic_j^{(2)}\right)(-i)^j \chi_j \tag{2.59}$$

where c_j correspond to the Fourier coefficients of the azimuthal part of the forcing function defined in Eqs. (2.37) through (2.40). The definition of the terms χ_j has been modified as:

$$\chi_j = 2\pi\left[\frac{R_O}{b}J_j(\overline{\xi}\frac{R_O}{b}) - \frac{R_I}{b}J_j(\overline{\xi}\frac{R_I}{b})\right] \tag{2.60}$$

Observe that the non-dimensional form of the wavenumber used, $\overline{\xi} = \xi b$, generalizes the expression to any substrate thickness. Also note that the source term is given by a sum over the index k which also has contributions from the radiation pattern.

Since the expression to be analyzed is the result of this sum, the two components cannot be separated. Hence, the term considered in the parametric studies is of the form:

$$\sum_{k=-\infty}^{\infty} \frac{1}{\zeta_k(\theta)} \mathbf{\Delta}_A(k, \xi_A) H_k^{(2)}(\xi_A r) \tag{2.61}$$

For all parametric studies, the azimuthal position is fixed along the transducer centerline so that the function $\zeta_k(\theta)$ is equal to one. Similarly, the radial position selected remains fixed at $r = 15R_O$. The effect of the transducer radial dimension is studied first. Due to the geometry of a CLoVER sector, there are two important parameters related to its radial dimension. The first of these is the radial length itself. However, as shown in Fig. 2.10, this parameter is not sufficient to fully characterize the geometry of the transducer as different combinations of inner and outer radii can yield a similar result. It is intuitively expected that this difference in the geometry would manifest itself in the frequency response of the transducer. Consequently, the parameter $\hat{r}$ defined in the manner described below is used [65]:

$$\hat{r} = \frac{R_I}{R_O} \tag{2.62}$$

In the parametric studies conducted a value of $\hat{r}$ is specified, and the position of the transducer radial edges is changed so as to maintain a constant dimension. For each of these, the sum given by Eq. (2.61) is computed over a range of frequencies from 1 kHz to 800 kHz in increments of 0.5 kHz. In order to isolate the effect of the transducer dimension, the results are plotted as a function of the radial length, Δr, normalized by the wavelength which is a function of the frequency. Note that this approach yields results that are valid for both the S_0 and A_0 modes. However, it is important to emphasize that the transducer dimension itself will be different for each mode due to their different wavelengths. The result of this analysis is shown in Fig. 2.11, where a fixed azimuthal span of 15^0, a fixed radial dimension $\Delta r = 75b$, and various values of $\hat{r}$ were used.

There are several important features in the result obtained. First, note that the amplitude of the response decreases as the transducer radial dimension is increased. This effect is partly due to the attenuation induced by the term $H_k^{(2)}(\xi r)$. As the frequency is increased, the increasing wavenumber results in a larger number of wavelengths between the transducer outer radius and the measurement point (which remains constant). Since the amplitude of the propagating wave decays with

the number of wavelengths, a smaller amplitude is observed as the ratio $\frac{\Delta r}{\lambda}$ increases. Furthermore, for the azimuthal dimension considered, the decay in amplitude is only dependent on the attenuation as all the local minima (with the exception of $\hat{r} = 0.95$) are coincident. A more important observation, however, is that for low values of the ratio $\hat{r}$ the response amplitude does not display any zeros. Instead, a series of local extrema is observed where the minima occur when the radial dimension coincides with integer multiples of the wavelength and the maxima correspond to points where this dimension is a factor between 0.35 and 0.5 integer multiples of the wavelength. As the ratio is increased, the local minima progressively approach zero while the local maxima remain essentially unchanged. Note that the location of these points is similar to the case of a rectangular transducer. Since for low values of $\hat{r}$ the transducer response does not display any zeros, modal selectivity cannot be attained. This feature is typically obtained by selecting the transducer dimension so as to operate at a frequency node for a specific mode. When testing below the threshold of the higher Lamb modes (where only the S_0 and A_0 mode exist), this results in the displacement components being composed of only the opposite mode. This observation provides important insight into the nature of modal selectivity attained with finite dimensional transducers. As the value of $\hat{r}$ increases, the geometry of the CLoVER sector approaches that of a rectangle. This geometric configuration is in turn symmetric with respect to an axis normal to the fiber direction. This indicates that modal selectivity is directly related to the symmetry of the transducer relative to the wave propagation direction. For low values of $\hat{r}$, the CLoVER transducer sector is not symmetric with respect to such an axis and modal selectivity cannot be obtained. Therefore, for applications where modal selectivity is needed, larger values of $\hat{r}$ should be selected. The specific value will depend on the level of modal selectivity needed. For example, if one of the modes needs to be largely attenuated, then $\hat{r}$ should be in the order of 0.9. Conversely, for applications where a transducer with high gain over a large frequency range is desired, low values of $\hat{r}$ should be used [65].

The effect of the azimuthal dimension is shown in Figs. 2.12 and 2.13 for a similar range of values of $\hat{r}$. Note that as the span is increased, the location of the local extrema remain essentially unchanged. It can also be observed that the amplitudes of the local minima decrease significantly, especially for larger values of $\hat{r}$. In addition, the amplitude of the local maxima does not decay in the same manner for larger azimuthal spans. This effect, however, does not appear to follow a consistent pattern and the identification of its source is further complicated by the presence of the attenuation term in Eq. (2.61). Nevertheless, as the location of the local extrema

is not significantly altered, this effect is not critical. From these results, it can be concluded that the azimuthal span of the transducer has a secondary effect on the frequency response for the range of values of interest for use in CLoVER transducers ($\Delta\theta < 90^0$). This parameter may therefore be selected based on a different criterion as, for example, the directionality desired.

A potential evolution of the CLoVER transducer that takes advantage of the directionality of the induced GW field and the ability to interrogate a complete 360^0 range is shown in Fig. 2.14. This device would be composed of a piezoceramic ring with the fibers diced in a manner such that the active sectors have a rectangular shape. This device would incorporate the modal selectivity attainable with this transducer geometry which is often critical in SHM applications.

2.6 Performance Improvement Offered by CLoVER Sector Geometry

As explained in the previous section, the displacement field is proportional to the traction amplitude per unit length, τ_0, exerted along the radial edges of the APT. This leads to the intuitive conclusion that actuators with longer edges exert a larger "net traction". In the case of a CLoVER sector geometry, the limiting case is a ring configuration where the length of the radial edge is maximized for fixed inner and outer radii. In this section, we seek to relate the traction per unit length to an electric input metric to explore the increase in performance that can be obtained by the CLoVER sector geometry. To do this, the piezoelectric strain induced by the APT must be considered. Several approaches have been proposed to model the interaction between a structural substrate with a surface-bonded piezoelectric actuator under static conditions. This type of analysis generally employs an assumed strain field for the substrate, while the actuator is typically modeled as having a constant through-the-thickness strain. Crawley and de Luis [54] considered this type of problem using a linear strain distribution for the substrate, which was modeled as an Euler-Bernoulli beam. Their analysis, however, consisted of two surface bonded piezoelectric actuators which resulted in a symmetric system. Chaudry and Rogers [66] conducted a similar study using a linear strain distribution for the actuator and substrate under the assumption of perfect bonding. They provided an expression for the curvature induced on the substrate by a single surface-bonded actuator, from which the force per unit length could be determined using the substrate's cross-sectional properties. In order to obtain a functional relationship between the traction

per unit length and the input voltage, this result will be employed here. It must be emphasized that this is an approximation as the mechanics of the substrate in this work are not those of Euler-Bernoulli beams. It should also be noted, however, that when considering the fundamental antisymmetric mode, a linear strain distribution might provide a good approximation as it captures the essential antisymmetry through the thickness of the substrate. Then, for a rectangular cross-section, the traction per unit length induced along the edges of the actuator can be expressed as:

$$\tau_0 = \frac{4E_B bT(1+T)\psi}{6T + 4T^2 + 4 + \psi T^2 + 1}\epsilon_P \tag{2.63}$$

where T is defined by:

$$T = \frac{2b}{\overline{t}_a} \tag{2.64}$$

and ψ represents the stiffness-thickness ratio given by:

$$\psi = \frac{2E_B b}{E_a \overline{t}_a} \tag{2.65}$$

Finally, the piezoelectric strain can be expressed through:

$$\epsilon_P = d_{33}\frac{V}{d_{IDE}} \tag{2.66}$$

where d_{IDE} represents the center-to-center distance between any two fingers in the APT interdigitated electrode. Note that Eq. (2.66) implies that a uniform electric field through the radial length of the actuator is assumed. In actual APT devices this is not the case since the electric field lines originate and end at the interdigitate electrode fingers. Since the field lines must be normal to the surfaces where they originate and end, there exists a small region close to the electrode fingers where the lines are not oriented along the fiber direction. Nevertheless, it has been shown that this is a reasonable simplification if the distance between any two electrode fingers, d_{IDE}, is sufficiently large. For instance, the work of Nguyen and Kornmann [67] concluded that a minimum electrode spacing of 1.1 mm would be required to obtain a homogenous electric field along the length of the fiber for AFCs. If the APT is modeled as a capacitor with capacitance C, then a suitable metric for the electric input is the electric current drawn. For a harmonic input voltage of amplitude V at a frequency ω, the magnitude of the electric current, I, is given by:

$$I = \omega C V \tag{2.67}$$

At this point, it is necessary to determine the dependence of the APT capacitance on the transducer's radial and azimuthal dimensions. The capacitance of this type of transducer is typically analyzed using the repetitive nature of the interdigitated electrode pattern. In this way, only the electric field in a representative unit cell, defined as the region between any two electrode fingers, is considered. A comprehensive study on this electric field was conducted by Lloyd [68] using conformal mapping techniques. In that work, it was shown that the capacitance of each unit cell was primarily determined by the piezoceramic thickness, electrode finger width, and electrode finger spacing, while it scaled linearly with electrode finger length. Thus, the capacitance of a unit cell can be expressed as:

$$C_{uc} = p(\hat{k}, \epsilon_0, d_{IDE}, \overline{t}_a) L_{IDE} \tag{2.68}$$

where $\hat{k}$ represents the dielectric constant of the material, ϵ_0 represents the permittivity constant, d_{IDE} represents the center-to-center distance between electrode fingers, and $\overline{t}_a$ represents the thickness of the transducer. In the case of a wedge-shaped APT, the electrode finger length is determined by its radial position, r_{IDE}, and the transducer's azimuthal span, $\Delta\theta$, so that:

$$C_{uc} = p(\hat{k}, \epsilon_0, d_{IDE}, \overline{t}_a) r_{IDE} \Delta\theta \tag{2.69}$$

A closed form expression for the function p cannot be readily obtained. However, the work of Lloyd [68] showed that this function is non-linearly dependent on the electrode finger and unit cell geometry, and that it increases exponentially as the center-to-center distance between the electrode fingers approaches zero. It is also important to note that any contribution from the capacitance of the epoxy has been neglected. This is a logical choice since its dielectric constant [69] ($\hat{k} \sim 6$) is much smaller than that for a typical piezoelectric ceramic [59] ($\hat{k} \sim 1700$, PZT-5A). The capacitance of the overall device may be obtained by considering it as a composition of capacitors connected in parallel. Then, the capacitance of each unit cell may be simply added together which results in:

$$C = p(\hat{k}, \epsilon_0, d_{IDE}, \overline{t}_a) \Delta\theta \frac{R_O + R_I}{2} \Delta r \tag{2.70}$$

The results given by Eqs. (2.63), (2.66) and (2.70) combined with the definition of Eq. (2.67), indicate that the current drawn by the actuator will be linearly proportional to the product of the traction per unit length, τ_0, and the APT capacitance. This result further indicates that the actuator with largest angular span

will draw the largest current in order to maintain a constant τ_0. Even though the ring-configuration draws the largest current according to the conclusion above, there are several shortcomings with its performance. For example, the GW field excited has the same amplitude in every direction and therefore no focusing is possible. The wedge-shape APT offers an improvement over these shortcomings, especially if the same current input as in the case of the ring is utilized. Due to its geometry, this configuration is able to concentrate a significant portion of the excitation along the intended scan direction. Similarly, due to its shorter azimuthal span, the larger current input yields a larger magnitude for τ_0, and hence an increased displacement amplitude everywhere. This effect can be quantified using the relationships provided by Eqs. (2.67) and (2.70). Equating the currents drawn by the ring-shaped APT and a CLoVER sector yields:

$$\omega p \Delta\theta \frac{R_O + R_I}{2} \Delta r V^{CLoVER} = \omega p 2\pi \frac{R_O + R_I}{2} \Delta r V^{ring} \tag{2.71}$$

from which, according to Eqs. (2.63) and (2.66), it follows that [65]:

$$\frac{\tau_0^{CLoVER}}{\tau_0^{ring}} = \frac{2\pi}{\Delta\theta} \tag{2.72}$$

A sample result from this analysis is presented in Fig. 2.15. The figures illustrate the peak-to-peak amplitude of the out-of-plane displacement component for the S_0 (Fig. 2.15(a)) and A_0 (Fig. 2.15(b)) modes at a frequency-thickness product of 150 kHz-mm and 500 kHz-mm respectively. The result is represented through polar plots where the radial distance from the origin corresponds to the peak-to-peak amplitude at each azimuthal position. The transducer centerline is oriented along the 90^0 direction in the figure. The results for each azimuthal span considered were normalized by those corresponding to a ring geometry to illustrate the performance gain offered by the CLoVER geometry. For the particular combination of parameters shown, the out-of-plane displacement for a CLoVER sector with an azimuthal span of 15^0 can be made more than six times larger than that corresponding to a ring for the S_0 mode, while in the case of the A_0 mode they are increased by a factor of approximately eight. The results presented in Fig. 2.15 must be carefully interpreted, however, as they do not imply that using a CLoVER transducer will result in the displacement amplitudes being automatically increased. Instead, the implication is that as the array is divided into individual sectors, the electric current needed to obtain a given displacement amplitude using a ring geometry can be more efficiently used. In addition to their increased amplitude, the induced displacements will also be focused along a

desired direction as shown by the directionality of the main lobe. The result given by Eq. (2.72) may also be used to quantify the improvement obtained by reducing the CLoVER azimuthal span from a given reference value.

2.7 Sensor Response

In GW-based testing, a stress wave is excited by the piezoelectric actuator through the structural element whose condition is to be inspected. This wave typically experiences changes in its amplitude, frequency content, and group speed due to its interaction with any defects it encounters (e.g., cracks, corrosion, delaminations). Furthermore, these interactions produce additional waves that, generally, scatter in every direction. This process leads to the use of two primary methods of testing: the pitch-catch and pulse-echo methods. The pitch-catch method is based on identifying damage based on the changes that defects introduce into the wave by locating a sensor a certain distance away from the actuator and recording the received wave. In contrast, the pulse-echo method uses the reflections scattered from defects to identify and locate damage. This typically involves using a transducer that acts both as actuator and sensor. In either method, information about the damage is obtained from strains sensed by the piezoelectric transducer and the corresponding voltage signal generated through the piezoelectric effect. This voltage signal is then used to determine information about damage presence, location, and severity using adequate signal processing techniques. Therefore, it is necessary to relate the strains sensed by the transducer to the induced voltage. This will allow us to identify excitation frequencies and transducer dimensions that maximize the sensor response. Raghavan and Cesnik [43] proposed a model to do this by modeling the sensor as a capacitor. Using the assumption that the sensor is under plane stress conditions, the following expression was presented:

$$V_s = \frac{\hat{k}\epsilon_0 E_s \overline{t}_s g}{(1-\nu_s)C_s} \int_{A_s} \epsilon_{ii} dA \tag{2.73}$$

where E_s represents the Young's modulus of the sensor, $\overline{t}_s$ represents the thickness of the sensor, and g represents the the sensor material piezoelectric constant. The specific value to be used depends on the relative directions of the applied electric field and the induced strain. Similarly, the capacitance of the sensor, C_s, will depend on whether it is a uniform piezo material or an APT. Finally, A_s represents the sensor's surface area. An implication of this model is that the sensor is assumed to be infinitely

compliant, so that it does not disturb the GW field produced by the actuator. The strains necessary to obtain the sensor response can be obtained from the displacement components defined previously by means of a linear strain-displacement relation. In polar coordinates, this is expressed as:

$$\epsilon_{rr} = \frac{\partial u_r}{\partial r} \tag{2.74}$$

$$\epsilon_{\theta\theta} = \frac{u_r}{r} + \frac{1}{r}\frac{\partial u_\theta}{\partial \theta} \tag{2.75}$$

where u_r and u_θ are the radial and azimuthal displacement components, respectively. These components can be expressed in terms of the Cartesian components obtained previously through the transformation:

$$\left\{ \begin{array}{c} u_r \\ u_\theta \end{array} \right\} = \left[\begin{array}{cc} \cos\theta & \sin\theta \\ -\sin\theta & \cos\theta \end{array} \right] \left\{ \begin{array}{c} u_1 \\ u_2 \end{array} \right\} \tag{2.76}$$

Since the Cartesian components were previously obtained in terms of polar coordinates, it follows from Eq. (2.76) that:

$$\frac{\partial u_r}{\partial r} = \frac{\partial u_1}{\partial r}\cos\theta + \frac{\partial u_2}{\partial r}\sin\theta \tag{2.77}$$

and

$$\frac{\partial u_\theta}{\partial \theta} = \cos\theta\left(\frac{\partial u_2}{\partial \theta} - u_1\right) - \sin\theta\left(\frac{\partial u_1}{\partial \theta} + u2\right) \tag{2.78}$$

Similarly, the strain-displacement relation in Cartesian coordinates is given by:

$$\epsilon_{xx} = \frac{\partial u_1}{\partial x} \tag{2.79}$$

$$\epsilon_{yy} = \frac{\partial u_2}{\partial y} \tag{2.80}$$

Since the displacement components were found in terms of polar coordinates, the coordinate transformation $r = \sqrt{x^2 + y^2}$, $\theta = \tan^{-1}(y/x)$ is used along with the chain rule of derivatives to obtain:

$$\epsilon_{xx} = \frac{\partial u_1}{\partial r}\cos\theta - \frac{\partial u_1}{\partial \theta}\frac{\sin\theta}{r} \tag{2.81}$$

$$\epsilon_{yy} = \frac{\partial u_2}{\partial r}\sin\theta + \frac{\partial u_2}{\partial \theta}\frac{\cos\theta}{r} \tag{2.82}$$

Finally, the r and θ derivatives of the displacement components, for the antisymmetric mode, may be expressed in vector form as:

$$\frac{\partial \mathbf{u}_A}{\partial r} = \sum_{k=-\infty}^{\infty}\left[\frac{i\pi^2\xi_A\mathbf{\Gamma}_A(\xi_A)}{\zeta_k(\theta)D'_A(\xi_A)}\mathbf{\Delta}_A\left\{H^{(2)}_{k-1}(\xi_A r) - H^{(2)}_{k+1}(\xi_A r)\right\}\right] \tag{2.83}$$

and:

$$\frac{\partial \mathbf{u}_A}{\partial \theta} = \sum_{k=-\infty}^{\infty}\left[\frac{-2k\pi^2\mathbf{\Gamma}_A(\xi_A)}{\zeta_k(\theta)D'_A(\xi_A)}\mathbf{\Delta}_A H^{(2)}_k(\xi_A r)\right] \tag{2.84}$$

2.7.1 Rectangular Piezo Sensor

The sensor response of a homogeneous rectangular piezoelectric sensor is of practical interest in SHM applications. Consider a rectangular sensor of width w, and aspect ratio A^*, so that, $h = A^* w$ and $A_s = A^* w^2$, as shown in Fig. 2.16(a). The sensor is centered at the point $x = x_s$, $y = y_s$ and is under the GW field excited by a CLoVER sector of radial span Δr and angular span $\Delta\theta$ centered at the point $r_a = 0.5(R_I + R_O)$, $\theta_a = 90°$. In contrast to the case of an APT sensor, the piezo material has isotropic piezoelectric properties in the plane normal to the poling direction, and therefore senses all in-plane extensional strains. In addition, this enables the piezo to be modeled as a parallel plate capacitor filled with a dielectric material. In this way, its capacitance may be expressed through:

$$C_s = \frac{\hat{k}\epsilon_0 A_s}{\overline{t}_s} \tag{2.85}$$

Consequently, its sensor response is given by [43]:

$$V_s = \frac{E_s \overline{t}_s g_{13}}{A_s(1-\nu_s)} \int_{y_s - A^*\frac{w}{2}}^{y_s + A^*\frac{w}{2}} \int_{x_s-\frac{w}{2}}^{x_s+\frac{w}{2}} (\epsilon_{xx} + \epsilon_{yy}) dx dy \tag{2.86}$$

where ϵ_{xx} and ϵ_{yy} are defined by Eqs. (2.81) and (2.82), respectively.

Note that Eq. (2.86) holds for harmonic forcing at a frequency ω. For the general case of a time-dependent excitation, such as the toneburst signal considered before, the integrand is multiplied by the time Fourier transform of this signal and integrated over an infinite frequency range (which in reality is limited to the frequency bandwidth

of the excitation toneburst), as outlined in section 2.3. However, in order to identify optimal excitation frequencies and sensor dimensions a harmonic analysis is sufficient. Once these have been identified, they can be used as center frequencies of time-dependent excitations.

The variation in three parameters is examined. First, we explore the excitation frequencies to determine values at which the sensor response would be maximum, as well as to identify values that should be avoided due to negligible sensing response. Second, two sensor dimensions are explored. The width of the sensor was considered, which resulted in the definition of the non-dimensional parameter w* as $w/\Delta r$. The effect of the sensor's aspect ratio was also studied. The results from this analysis are shown in Figs. 2.17 and 2.18. In the study of the aspect ratio, the value of w* was kept fixed at 1. The two modes show different qualitative behavior over the range of frequencies studied with the A_0 mode showing two main frequencies at which high response is obtained, as opposed to the S_0 case which shows primarily one up to 500 kHz. Note that both dimensions are critical in the response of the rectangular piezoelectric sensor, with smaller sizes resulting in better performance. This observation is consistent with the findings reported in Ref. [43]. In addition to the decrease in amplitude observed for larger sensors, it can also be seen that the number of nodes increases significantly.

2.7.2 Rectangular APT Sensor

The response of a rectangular APT sensor under the GW field excited by a CLoVER sector is now derived. This analysis is based on the assumption that only extensional strains along the piezoelectric fiber direction are sensed. This is a reasonable simplification since the induced shear strains are small compared to the extensional ones. Furthermore, as discussed in section 2.3, the piezoelectric performance of the transducer along the normal direction to the fiber is very weak. Therefore, for the rectangular configuration, only ϵ_{rr} is needed. The rectangular sensor is modeled by using a wedge-shaped geometry whose radial origin coincides with that of the CLoVER actuator. Therefore, while its effective geometry is that of a rectangle, its dimensions will be expressed in terms of radial and azimuthal components. This further assumes that the fibers in the rectangular device are always oriented along the radial direction. Consider a rectangular APT sensor centered at the point $r = r_s$, $\theta = \theta_s$, with radial dimension Δr_s, angular span $\Delta\theta_s$, and surface area $A_s = r_s \Delta r_s \Delta\theta_s$, as shown in Fig. 2.16(b). The sensor is subjected to the GW field excited by a CLoVER sector with radial dimension Δr and angular span $\Delta\theta$ centered at the point $r_a = 0.5(R_I + R_O)$,

$\theta_a = 90°$. In order to use the sensor response equation presented earlier (Eq. 2.73), an expression for the APT capacitance is needed. For this type of transducer, the capacitance is typically analyzed using the repetitive nature of the interdigitated electrode pattern as previously discussed.

Using Eq. 2.70, the voltage induced in the APT sensor due to the induced strains is given by:

$$V_s = \frac{\hat{k}\epsilon_0 E_s \overline{t}_s g_{33}}{(1-\nu_s)pA_s} \int_{\theta_s-\frac{\Delta\theta_s}{2}}^{\theta_s+\frac{\Delta\theta_s}{2}} \int_{r_s-\frac{\Delta r_s}{2}}^{r_s+\frac{\Delta r_s}{2}} \epsilon_{rr} r dr d\theta \tag{2.87}$$

Note that in the case of an APT, g_{33} is used. In addition, for a given APT device, the function p is a constant. Using the definition in Eq. (2.87), the voltage is given by:

$$V_s = \frac{k\epsilon_0 E_s \overline{t}_s g_{33}}{(1-\nu_s)pA_s} \int_{\theta_s-\frac{\Delta\theta_s}{2}}^{\theta_s+\frac{\Delta\theta_s}{2}} \int_{r_s-\frac{\Delta r_s}{2}}^{r_s+\frac{\Delta r_s}{2}} \left[\frac{\partial u_1}{\partial r}\cos\theta + \frac{\partial u_2}{\partial r}\sin\theta\right] r dr d\theta \tag{2.88}$$

This analysis is performed in two separate steps; the ratio of the radial dimension was first explored by defining the non-dimensional parameter r* as the ratio $\Delta r_s/\Delta r$ and obtaining the sensor response, given by Eq. (2.88), over a wide frequency range for both symmetric and antisymmetric modes. The result from this analysis is shown in Fig. 2.19. The location of the sensor was set to $r_s = 15R_O$ and $\theta_s = 90^o$; this azimuthal position was selected since it coincides with the transducer's centerline which is the intended scanning direction. The actuator dimensions were similar to the ones presented in table 2.1. In these and subsequent sensor response plots, the results presented are normalized by the maximum value in each set. Similar qualitative differences between the two modes are observed in this case, with the antisymmetric mode showing the lower response at a higher frequency than in the previous case.

The effect of varying the ratio of azimuthal spans was also examined, which resulted in the definition of the parameter θ^* as $\Delta\theta_s/\Delta\theta$. The results from this analysis, for r* fixed at 1, are shown in Fig. 2.20. As it can be seen, this characteristic does not affect the trend observed in frequency (Fig. 2.19), but instead causes a decrease in amplitude. Notice that this effect is significant only if the actuator is made much smaller than the sensor or vice-versa. These trends are logical since it is expected that changing the sensor dimension in the wave propagation direction will have the most

significant effect. As in the previous case, it is evident that smaller sensors produce better results.

2.8 Concluding Remarks

The development of a three-dimensional elasticity-based theory for guided wave (GW) excitation by a wedge-shaped anisotropic piezocomposite sector was presented in this chapter. The construction of the theory supports the development of the Composite Long-rage Variable-length Emitting Radar (CLoVER) transducer. The theoretical analysis considered uncoupled dynamics for the actuator and substrate, and their interaction was modeled as surface tractions along the actuator's edges in the fiber direction. Under these assumptions, a boundary value problem of linear elasticity was formulated and simplified through the use of two-dimensional Fourier transforms. The solution of the problem was facilitated by separating the spatial domain in three spatial regions based on physical wave propagation considerations. Subsequently, a general solution methodology based on a Fourier series representation of the transducer tractions was presented to find a semi-analytical solution for the displacement field. Results from three-dimensional finite element simulations demonstrated the accuracy of the theoretical result as a solution to the elasticity problem. The theoretical result was subsequently used to conduct parametric studies to reveal the effect of the radial and azimuthal dimensions of a CLoVER sector on the induced GW field. The particular application sought was modal selectivity, where the amplitude of specific GW modes can be controlled by appropriate selection of the transducer dimensions. It was shown that the radial length of the transducer is the critical parameter to be considered in the design. In particular, the results showed that the ratio of the transducer inner to outer radius determined whether modal selectivity was attainable using CLoVER sectors. For ratios smaller than 0.5, the amplitude of the excited GW modes does not reach nullity for any transducer radial dimension indicating that modal selectivity cannot be attained. For ratios larger than 0.5, it was numerically shown that the transducer dimension should be equal to integer multiples of the half-wavelength of a mode to maximize its transmission. Similarly, the transducer dimension must be equal to integer multiples of a mode's wavelength to minimize (or nullify) its transmission. It was found that the azimuthal dimension does not significantly affect the modal selectivity characteristics of CLoVER transducers as long as it lower than ninety degrees. The theoretical model was also employed to demonstrate that due to the geometry of a CLoVER

sector, the induced displacements can be increased by significant factors relative to a similarly sized ring configuration for equal electric current inputs. Finally, a theoretical model for the response of piezoelectric sensors under the GW field excited by CLoVER transducers was presented, and used to verify previously reported trends that smaller transducer dimensions produce larger response amplitudes.

Parameter	Value
E [GPa]	70
ν	0.33
ρ [kg/m^3]	2700
R_O [m]	0.015
R_I [m]	0.005
$\Delta\theta$ [deg]	30

Table 2.1: Substrate material properties and actuator dimensions used in FE simulations and theoretical results.

Parameter	Value (S_0)	Value (A_0)
R [m]	0.54	0.13
Δr_e [m]	0.0025	0.0005
$\Delta\theta_e$ [deg]	3	3
Δt [s]	10^{-7}	10^{-7}
b [m]	0.002	0.002
f_0 [kHz]	100	100
n	7	7
No. of Elements	38700	47336
No. of Nodes	52464	63444

Table 2.2: Mesh and analysis parameters used in FE simulations.

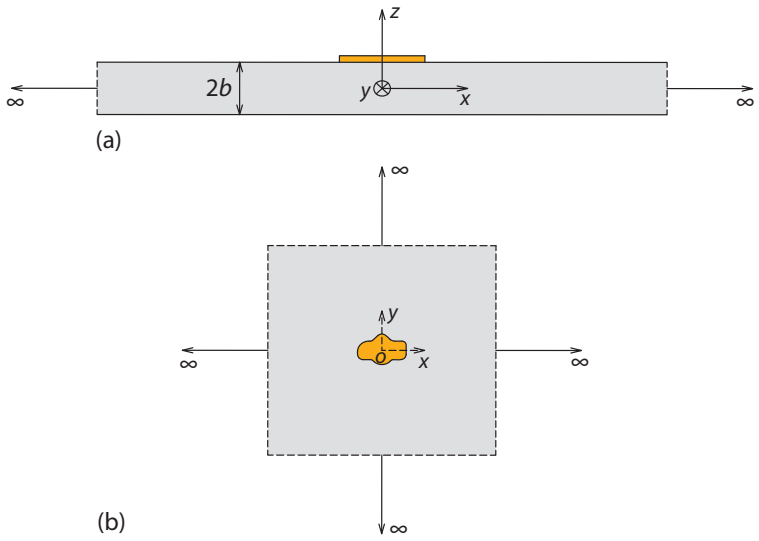

Figure 2.1: Transducer bonded on surface of infinite plate (a) Cross-sectional view (b) Top view.

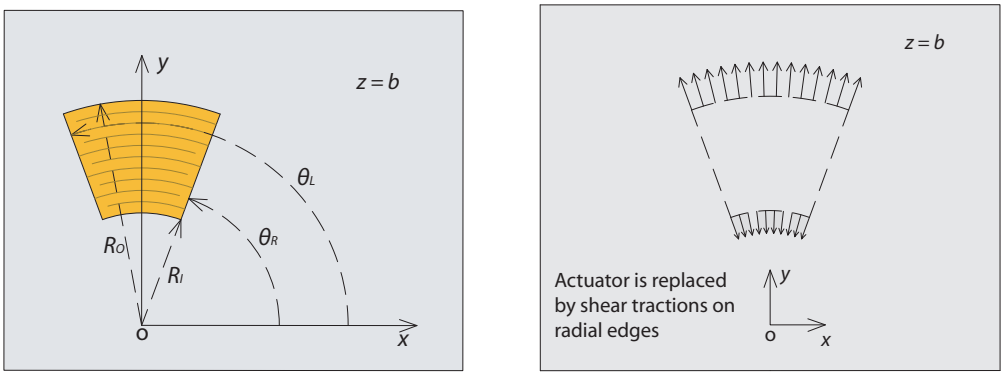

(a) **(b)**

Figure 2.2: **(a)** Geometry of a CLoVER sector; **(b)** Transducer replaced by shear tractions along radial edges.

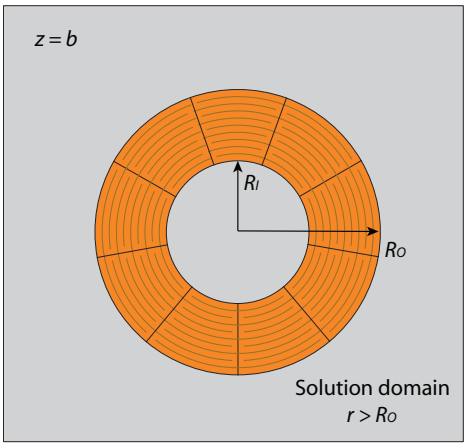

Figure 2.3: Schematic illustrating the solution domain.

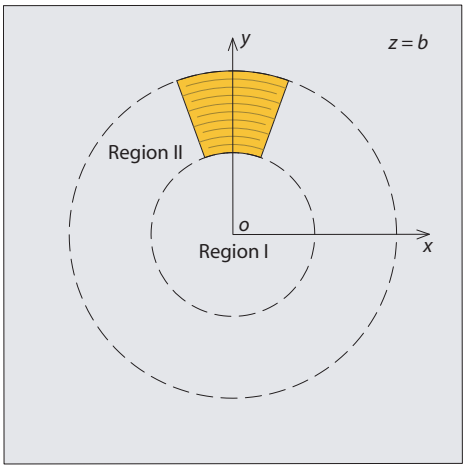

Figure 2.4: Additional solution regions for CLoVER GW excitation.

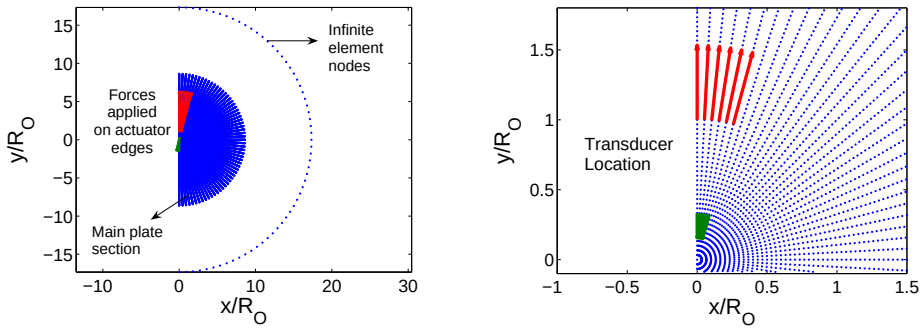

(a) **(b)**

Figure 2.5: FE mesh: **(a)** Complete overview; **(b)** Detail on shear traction application points.

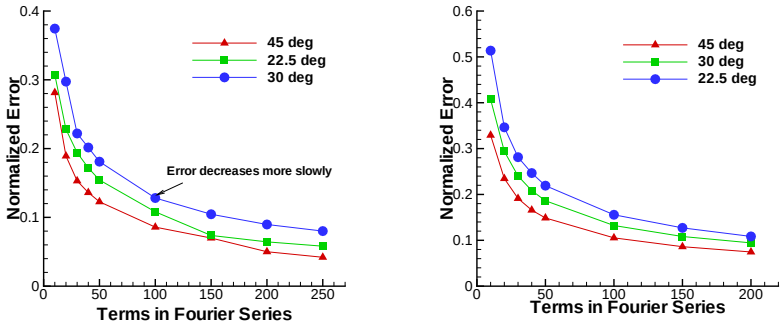

(a) (b)

Figure 2.6: Normalized error between angular part of shear traction function and its Fourier series representation for: **(a)** x_1-component; **(b)** x_2-component.

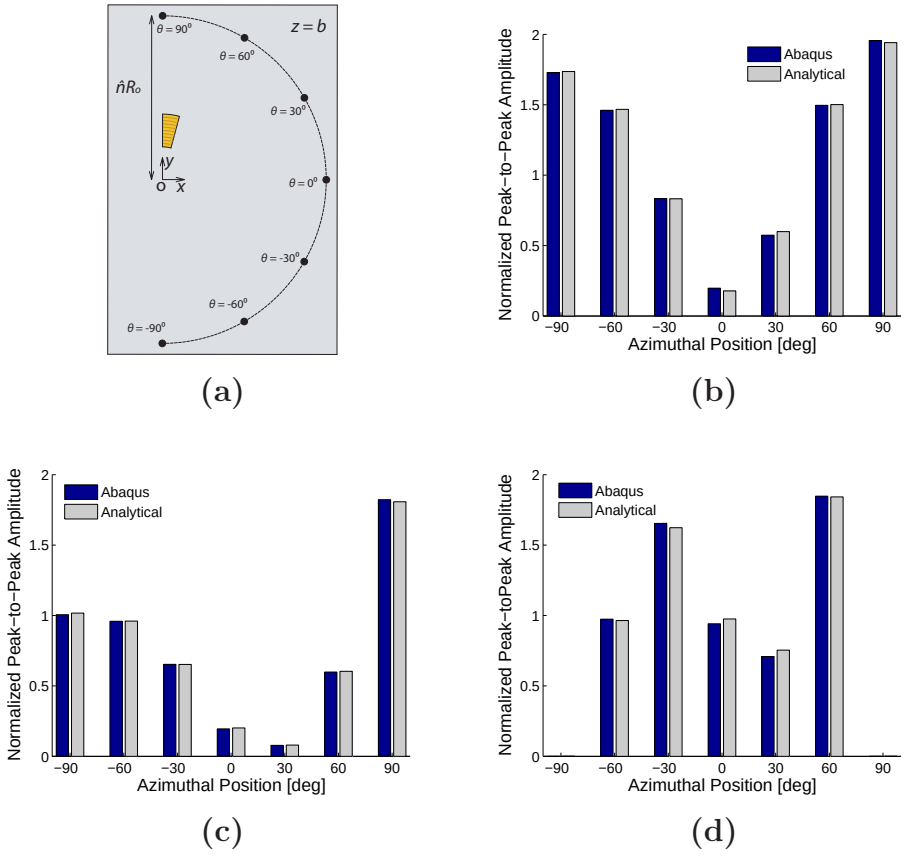

(a) (b)

(c) (d)

Figure 2.7: Comparison between FE and theoretical results **(a)** Points selected for comparison **(b)** Amplitude comparison for symmetric u_3 **(c)** Amplitude comparison for antisymmetric u_2 **(d)** Amplitude comparison for antisymmetric u_1.

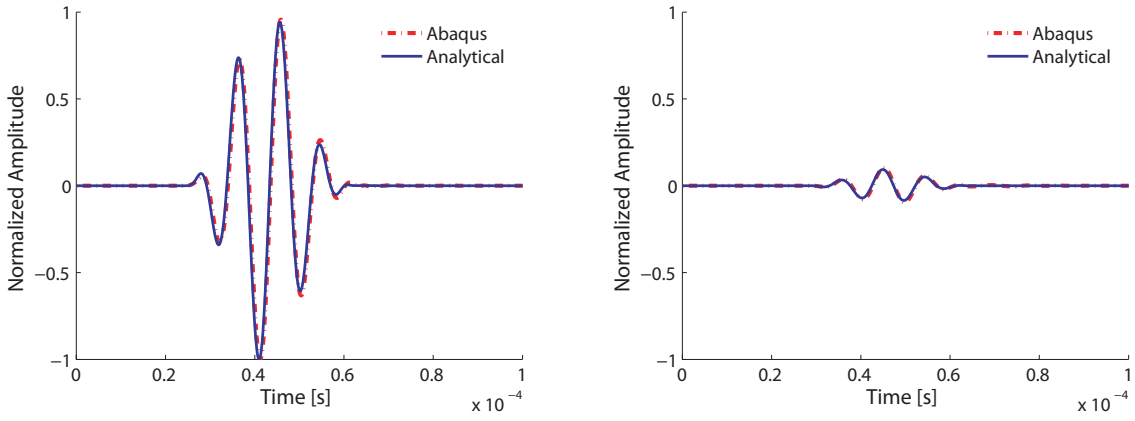

(a) **(b)**

Figure 2.8: Sample time history for out-of-plane displacement at $r = 10R_O$ (with baseline $R_O = 15$ mm and $\theta =$ **(a)** 90° and **(b)** 0°.

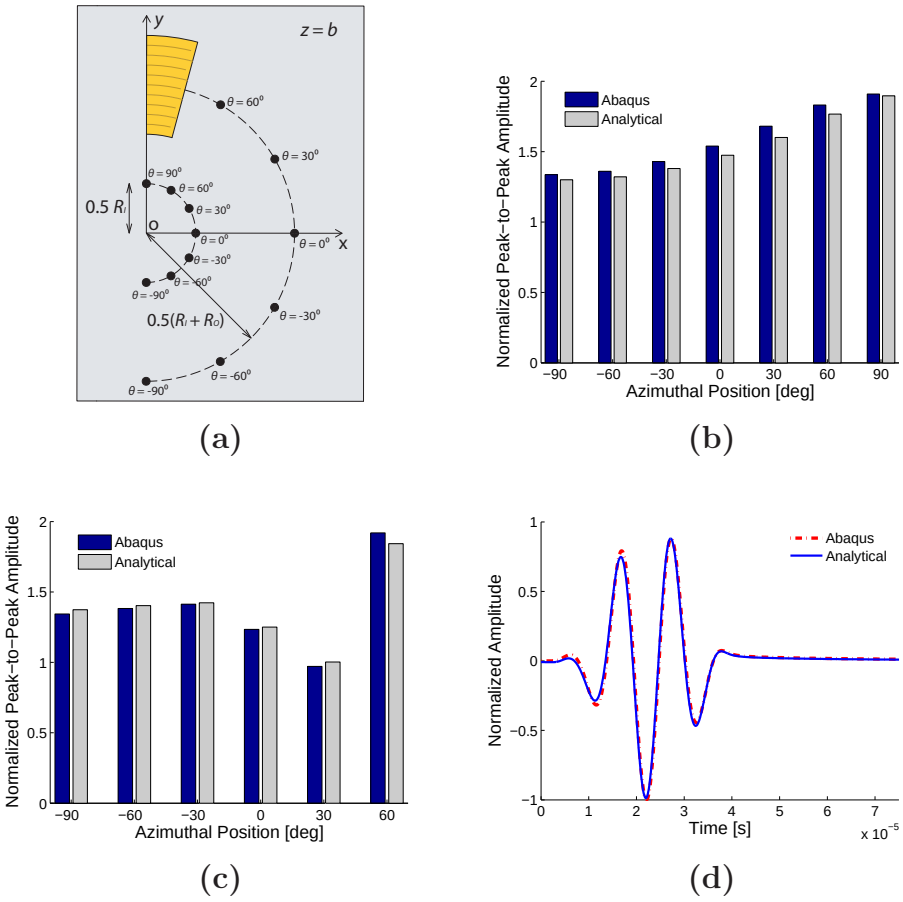

Figure 2.9: Comparison between FE and analytical results in regions I and II. **(a)** Points selected for comparison; **(b)** Amplitude comparison for antisymmetric u_3 in region I; **(c)** Amplitude comparison for antisymmetric u_3 in region II; **(d)** Sample time history for out-of-plane displacement at the origin.

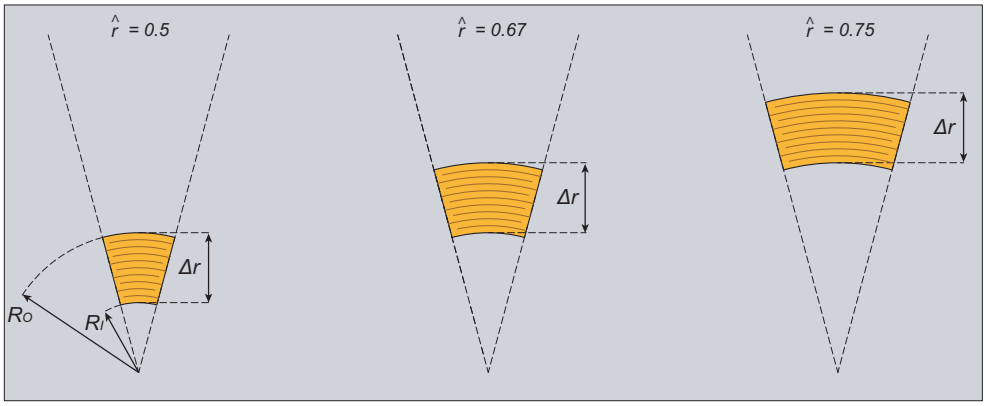

Figure 2.10: Schematic illustrating that different combinations of inner and outer radii can yield similar radial dimensions in a CLoVER sector

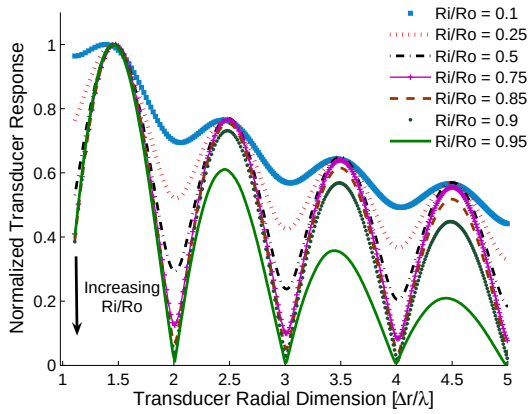

Figure 2.11: Effect of radial dimension on CLoVER sector frequency response for $\Delta r/b = 75$ and $\Delta\theta = 15^0$.

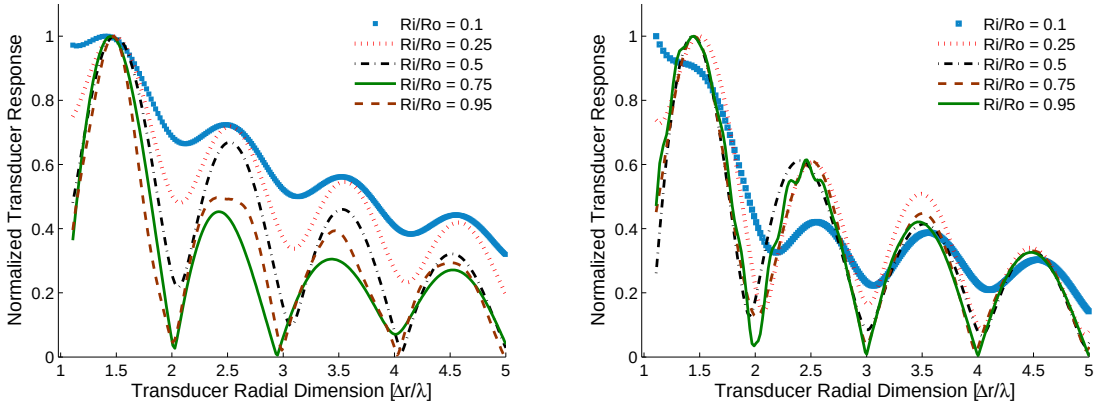

(a) **(b)**

Figure 2.12: Effect of radial dimension on CLoVER sector frequency response for $\Delta r/b = 75$ and $\Delta\theta$ of (a) 45^0; (b) 90^0.

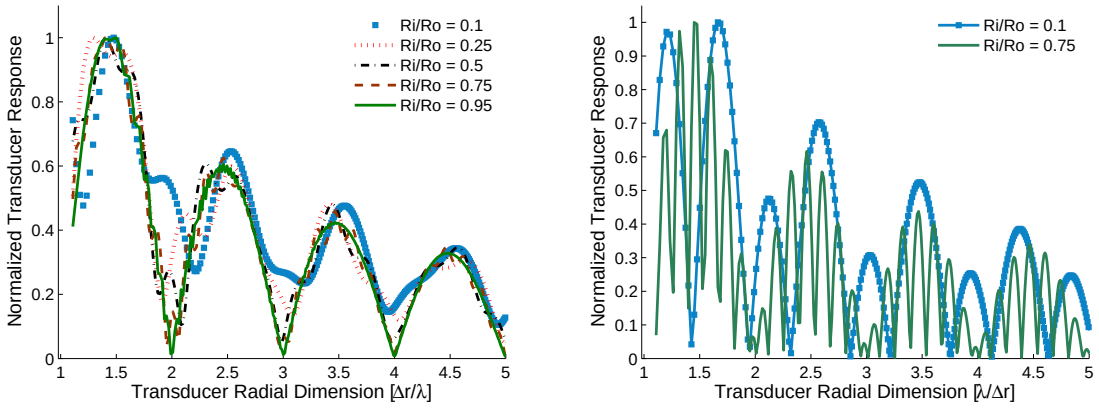

(a) **(b)**

Figure 2.13: Effect of radial dimension on CLoVER sector frequency response for $\Delta r/b = 75$ and $\Delta\theta$ of (a) 270^0; (b) 360^0 (ring).

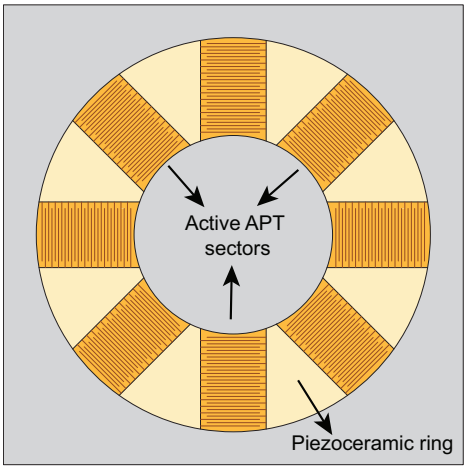

Figure 2.14: Possible evolution of the CLoVER transducer.

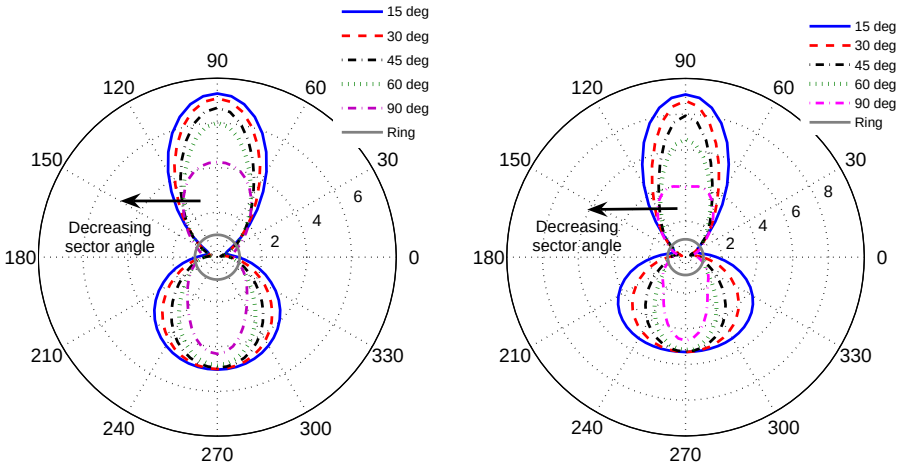

(a) **(b)**

Figure 2.15: Improvement in peak-to-peak amplitude of out-of-plane displacement offered by the CLoVER geometry over a ring configuration for: (a) S_0 mode at 500 kHz-mm, and (b) A_0 mode at 150 kHz-mm.

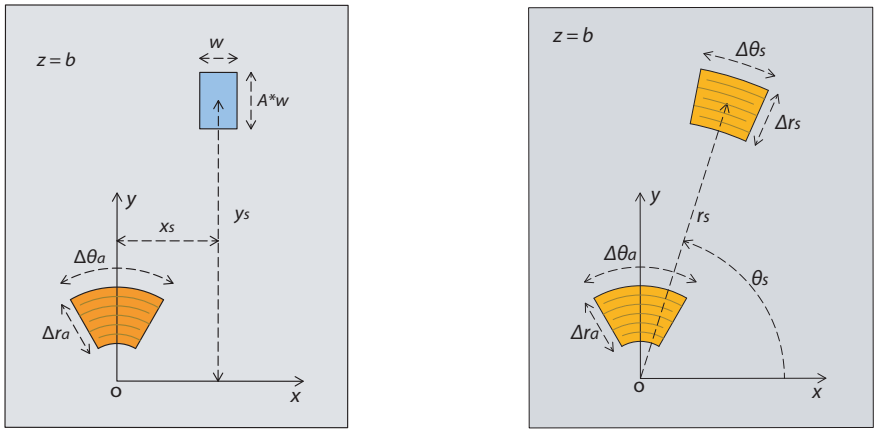

(a) Rectangular piezo sensor **(b) Rectangular APT sensor**

Figure 2.16: Sensor geometry and location used in analysis.

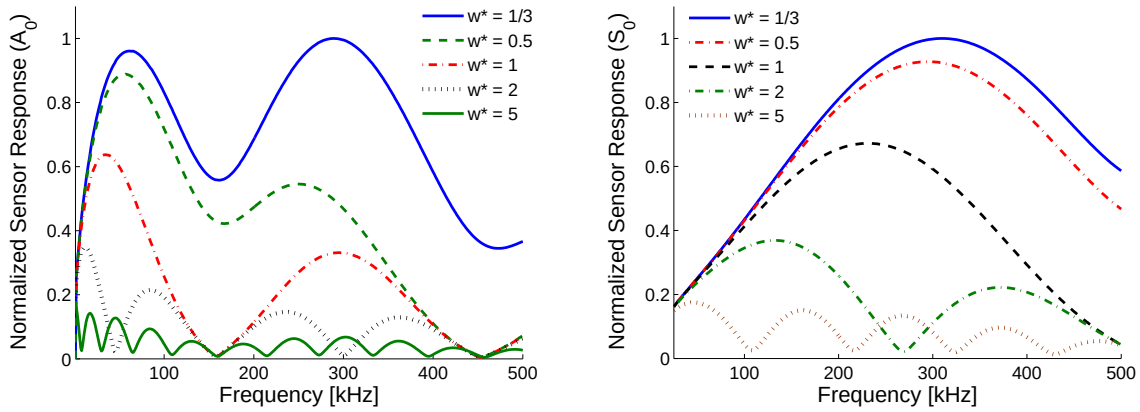

(a) A_0 mode **(b) S_0 mode**

Figure 2.17: Effect of sensor width on piezo sensor response. The baseline case was $\Delta r = 0.005$ m.

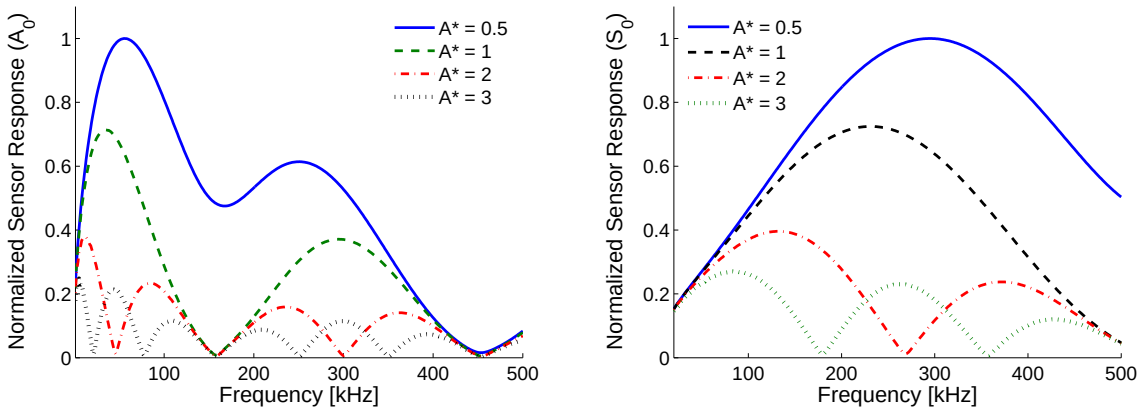

(a) A_0 mode **(b) S_0 mode**

Figure 2.18: Effect of sensor aspect ratio (A^*) on piezo sensor response. The baseline case was $\Delta r = 0.005$ m.

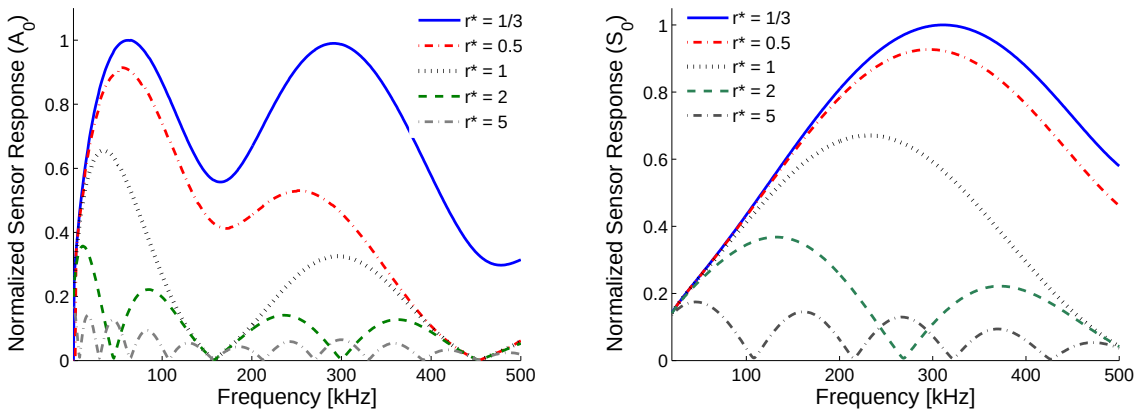

(a) A_0 mode **(b) S_0 mode**

Figure 2.19: Effect of radial dimension on rectangular APT sensor response. The baseline case was $\Delta r = 0.005$ m.

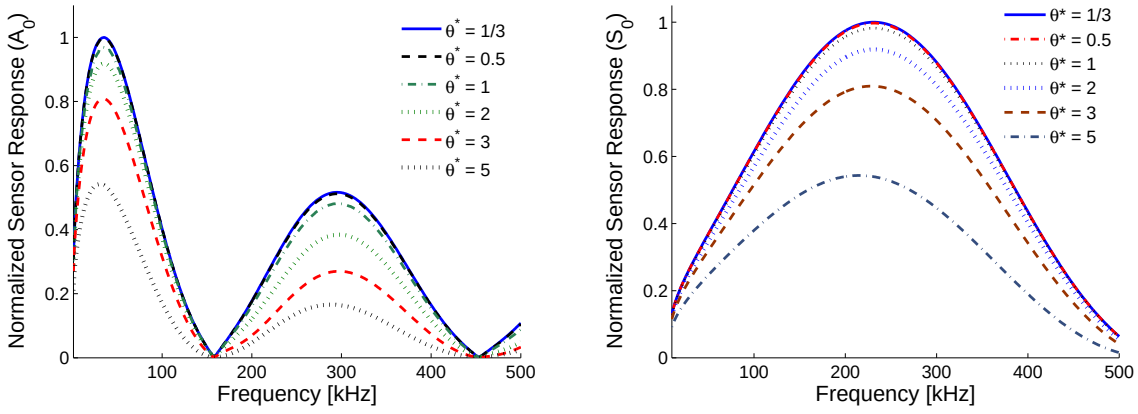

(a) A_0 mode **(b) S_0 mode**

Figure 2.20: Effect of azimuthal dimension on rectangular APT sensor response. The baseline case was $\Delta r = 0.005$ m, r* = 1.

CHAPTER III

CLoVER Transducer Fabrication and Testing in Pristine Isotropic Structures

This chapter describes the procedure used to fabricate prototype CLoVER transducers and their use in experimental tests in pristine isotropic structures. The design of the electrode pattern and choice of piezoceramic material are discussed first, followed by a summary of the assembly, curing, and poling processes. The resulting transducers are then subjected to a set of characterization studies where their free-strain performance is compared to that of commercially available piezocomposite transducers. A series of experimental tests using CLoVER transducers in isotropic structures is then described. In particular, sensor-based and laser-based measurements are reported to validate the theoretical model introduced in Chapter II in the frequency, time, and space domains. Finally, a set of experimental tests and results are presented for GW excitation by in-house developed rectangular transducers in wind turbine walls that show the ability of piezocomposite transducers to interrogate large operational structures.

3.1 Transducer Fabrication

As indicated in Chapter I, the CLoVER transducer is composed of a collection of anisotropic piezocomposite sectors arranged in a ring configuration. By virtue of the directionality of each sector, every direction in a host structure can be interrogated by activating each element in the transducer in a sequential manner. A typical piezocomposite transducer is composed of three main elements: a diced piezoceramic material, an electrode pattern to supply the electric field necessary to induce the piezoelectric effect in the ceramic, and a structural epoxy to hold the transducer together. The independence of each sector in a CLoVER transducer is provided by the interdigitated

electrode pattern which, by being appropriately designed, allows different areas of a single piezoceramic ring to be used.

A sample interdigitated electrode pattern unit cell design used in the prototype CLoVER transducers is shown in Fig. 3.1, while the electrode pattern for the entire transducer is shown in Fig. 3.2. The original layout was designed in a CAD application and then transferred onto a copper-clad kapton film (Pyralux LF7062R) using photolithography . This material has a layer of rolled-annealed copper on the kapton film, which has a thickness of 25 μm (there is, in addition, an adhesive layer with a thickness of 13 μm) and a copper density of 153 g/m^2. Each electrode finger was designed with a width of 0.1 mm, while the separation distance between any two was set at 0.5 mm. These values are similar to those used in NASA-standard MFCs [32, 70]. As previously mentioned, the overall design consists of two independent radial subdivisions that allow to electrically vary the length of the active fibers in a given sector, or to use each element as an independent actuator and sensor. The electrode pattern design was transferred onto the copper-clad kapton film through a photolithography process conducted at the Lurie Nanofabrication Facility at the University of Michigan. This procedure required the use of a transparency mask (PageWorks[1]) which contained the electrode pattern designed in the CAD application. The first step in the procedure consisted of spinning a thin layer of SPR-220 3.0 photoresist onto the copper surface of the kapton film (spun at 1600 RPM for 30 seconds). After curing of the photoresist, the copper-clad film was aligned with the transparency mask and exposed to a ultraviolet (UV) light source using an MA6 mask aligner for six seconds. The exposure to UV light chemically activates the photoresist and prevents it from being dissolved when placed in a developing solution in the parts protected by the mask containing the design. Once the photoresist has been developed, only the parts of the film where the electrode pattern is placed remain covered. The final steps consists of placing the copper-clad film in a sodium persulfate etching solution which dissolves the copper (except for the regions covered with photoresist) and cleansing the resulting pattern with acetone and isopropyl alcohol.

PZT-5A was selected as the active piezoceramic material in the prototype CLoVER transducers. This material was obtained in ring shaped units with a thickness of 0.2 mm (EBL Products [2]), and these wafers were subsequently diced into fibers using a computer-controlled dicing saw (American Dicing [3]). The dicing angle was selected

[1]PageWorks, 501 Cambridge St, Cambridge, MA 02141, (617) 374-6000

[2]EBL Products Inc., 91 Prestige Park Circle, East Hartford, CT 06108, (860) 290-3737.

[3]American Dicing, 344 East Brighton Avenue, Syracuse, NY 13210, (315) 428-1200.

so that the fiber width at the inner radius position was equal to the prismatic fiber width used in conventional MFC transducers (0.36 mm). These fibers remain in position by being attached to an adhesive carrier film. The electrode patterns and the piezoceramic fibers were assembled together using an epoxy adhesive system (Hysol Loctite E-120HP). As the carrier film where the fibers are attached must be removed, two cures are necessary. The first cure, referred to as partial cure, is needed to remove the film while keeping the relative orientation of the fibers. The final cure is needed to completely cure the epoxy and finalize the device. This sequence of steps is similar to the one presented by Wilkie *et al.* [11]. However, in that work, the transducers were cured in a vacuum hot press, and therefore some details of the procedure were modified in this work to adjust it to an autoclave cure. All assembly procedures were done similar to those presented in the standard manufacturing procedure [11]. For the autoclave cure, the curing parameters presented by Wilkie *et al.* [11] were used as a starting point. These indicate that the transducers must be partially cured at a temperature of 46^0 C (115^0 F) for five minutes at a pressure of 480 kPa (70 psi), while the final cure must be performed at 121^0 C (250^0 F) for a minimum of two hours at a similar pressure. These temperatures have been shown to yield satisfactory cure levels using cure kinetics models [71]. Prior to both cures, a vacuum dwell (-28 in Hg) of at least 15 minutes is necessary. Moreover, this vacuum must be maintained throughout the cure cycles. During initial tests, it was found that the recommended 480 kPa curing pressure did not yield a satisfactory compaction level in the final transducer. As a result, the pressure was increased to 690 kPa (100 psi) during both partial and final cures. During the final procedure, the pressure during partial cure was reduced to 550 kPa (80 psi) as it was found that, due to the increased pressure, pieces of the blue carrier film were permanently attached to the piezoceramic fibers. In order to facilitate the removal of air bubbles, an additional dwelling time of 15 minutes was added during the final cure (after reaching the maximum pressure but prior to the increasing the temperature). There was no modification to the temperatures during partial and final cure. The actual cure cycles used (both temperature and pressure) are shown in Fig. 3.3.

The final step in the fabrication process is the poling of the device. During this step, the piezoelectric domains in the piezoceramic material are aligned resulting in a net polarization. In the case of APTs, the polarization direction coincides with the fiber longitudinal direction. The standard procedure specifies that the device must be poled at an electric field of 3 kV/mm (1.5 kV with an interdigitated electrode spacing

of 0.5 mm assuming a uniform electric field[4]) for five minutes at room temperature. However, during initial tests it was found that the high voltage resulting from this electric field requirement sometimes resulted in failure of the transducer during poling, and did not yield satisfactory strain performance. The failure of the device observed during poling was associated with electric arcing induced by microscopic air bubbles remaining in the cured transducers. The strong dielectric breakdown of the air resulted in the surrounding areas in the transducer being burned and rendered useless. Consequently, a more benign poling environment was sought to reduce the possibility of electric failure. In general, the net polarization in a piezoelectric device is dependent on the poling field, poling time, and poling temperature. The primary requirement to achieve a net polarization is that the poling field be larger than the coercive field for the specific device (in principle, the longer the poling time the larger the net polarization will be as long as the electric field is larger than the coercive field of the device). Preliminary experimental tests indicated that for the transducers developed in this work, this field was in the order of 2 kV/mm at room temperature. This value is expected to decrease with increasing temperature until approximately 90^0 C as indicated by Bent [10]. Therefore, in order to increase the strain performance of the transducers while reducing the possibility of electrical failure, the poling time and temperature were increased, while the poling voltage was decreased. Prior to deciding the poling time, several sample APTs were constructed following the procedure specified above, and poled for different times. These were later characterized following the procedure presented in section 3.2 to determine how the increasing time altered the strain performance of the devices. These results, summarized in table 3.5, show that increasing the poling time significantly enhances the performance of the transducers. The values reported in the table correspond to average values for tests conducted for nine transducers (three for each poling time), while the uncertainty corresponds to three times the standard deviation. The error reported for the coupling coefficient, d_{33}, was calculated using the appropriate error propagation equations.

As mentioned earlier, increasing the poling temperature decreases the coercive field, which would allow the transducers to be poled for a shorter time and lower field while still maintaining acceptable performance. As a result, the transducers were poled at an electric field of 2.4 kV/mm for 30 minutes at an average temperature of 87^0 C using an industrial oven. During this procedure, the voltage was increased

[4]The poling parameters will be expressed in electric field form from this point on. This convention assumes a uniform electric field distribution between any two interdigitated electrode fingers, which corresponds to the maximum possible magnitude of the field along the poling direction.

in steps of 20 V, with a holding time of 5 seconds between steps. The holding time was increased to 20 seconds when a 100 V increment was reached [28]. An Agilent 33220A arbitrary waveform generator was used in conjunction with a Trek PZD 2200 high voltage amplifier (with a fixed gain of 200) to supply the necessary voltage. The transducer fabrication stages are summarized in Fig. 3.4.

3.2 Transducer Characterization

A set of characterization studies were conducted on several transducers fabricated in-house to verify the quality of the curing and poling procedures described in section 3.1. Strain gages were bonded on several transducers along the fiber direction to measure the axial strain. The CLoVER transducers were instrumented with EA-06-125AD-120 strain gages from Measurements Group, which covered approximately nine electrode fingers. In this case, the centerline of the strain gage was aligned with the centerline of the transducer. As the unidirectional strain gage is insensitive to transverse strains, there is some unavoidable error in the readings due to the curved geometry of the fiber disposition. Consequently, the strain recorded for the CLoVER transducers is expected to be an underestimate of the actual value. In order to obtain a better correlation with NASA-standard piezocomposite transducers, several rectangular specimens were fabricated following the procedure described in section 3.1. The electrode patterns for these devices were obtained from researchers at NASA Langley. The in-house rectangular transducers were instrumented with EA-06-250AD-350 strain gages, which covered approximately 18 electrode fingers. The gages were bonded using M-Bond AE-150 bonding agent from Measurements Group which was cured for two hours in an oven at 65^0 C according to the manufacturer's instructions. The transducers obtained from NASA were instrumented with CEA-13-250WQ-350 strain gages which are able to simultaneously measure strains along two perpendicular directions [72]. The voltage input was provided using the same waveform generator described in section 3.1 and a Krohn-Hite Model 7500 wide band amplifier. Various voltage inputs were used throughout the tests, while the frequency was maintained constant at 0.1 Hz to simulate quasi-static conditions. Furthermore, during testing, the transducers hung under their own weight to obtain their free response. The strain gage signal was conditioned and amplified using a Vishay 2311 signal conditioning amplifier and recorded using a digital oscilloscope. The experimental setup is shown in Fig. 3.5(a) while the strain gage-CLoVER arrangement can be seen in Fig. 3.5(b).

The results from these studies are shown in Fig. 3.6 where the peak-to-peak axial strain is plotted as a function of the input voltage (note that the electric field in kV/mm can be obtained by multiplying the scale in the horizontal axis by a factor of two). The experimental points show the average of 32 measurements, while the vertical error bars represent three times the standard deviation. The horizontal error bars represent the standard deviation in the peak-to-peak voltage signal supplied to the electrodes. Clearly, the manufacturing and poling procedures implemented in section 3.1 yield actuators with performance levels comparable to those obtained using the standard NASA manufacturing procedure. As it was previously mentioned, it is likely that the lower results seen for the CLoVER transducer are due to the unavoidable misalignment between the electrode and gage patterns. Nevertheless, for the peak-to-peak voltage of interest in SHM applications (up to 400 V), these differences are acceptable [65]. Having determined the performance of the CLoVER transducers, the next section discusses their experimental implementation in experimental studies that validate the theoretical formulation for GW excitation in isotropic structures introduced in Chapter II.

3.3 Experimental Studies on GW Excitation by a CLoVER sector

3.3.1 Sensor-based Experiments

In this section, piezoelectric sensors are employed to verify the accuracy of the theoretical solution in the frequency domain. This method is restricted to single-point measurements, but it is able to provide information on the performance of the transducer over a wide frequency range. This is a critical component of the solution as it enables a transducer designer to determine the transducer size that would induce maximum displacements at a given frequency. This is a key aspect in the transducer design as the excitation frequency is directly related to the damage type to be detected.

3.3.1.1 Experimental Setup

In order to verify the GW excitation model presented in Chapter II, a 3.2 mm-thick square aluminum 5005 plate was used in a series of experimental tests. The plate thickness was selected so that the effect of the actuator's dynamics on the substrate system could be neglected. Past studies have shown successful results employing a

similar arrangement [43]. The plate had a side length of 0.7 m. In an effort to excite pure symmetric and antisymmetric modes over a wide frequency range, one CLoVER transducer was bonded on each surface of the plate at its geometric center. The sectors used had a radial dimension $\Delta r = 1.0$ cm ($R_O = 2.5$ cm, $R_I = 1.5$ cm) and an azimuthal span $\Delta\theta = 45°$. The symmetric mode was obtained by exciting both actuators in phase, while the antisymmetric mode resulted from exciting them out of phase. The induced wave field was recorded using a square piezoceramic sensor with a side length of 11.6 mm and a thickness of 0.3 mm. The sensor was located along the transducer's centerline at a radial distance of 76.3 mm. This position was selected based on the plate's dimension, so that boundary reflections were avoided thereby satisfying the infinite plate assumption. The actuators and the sensor were bonded by applying a thin layer of Epotek 301 bonding agent and allowing it to cure for 24 hours. The actuator and sensor arrangement used is illustrated in Fig. 3.7(a). Each actuator was excited with a 3.5-cycle Hann-modulated toneburst signal using an arbitrary waveform generator (Agilent 33220A). A digital oscilloscope (Agilent Infinuum 54831DSO) was used to monitor and acquire the voltage signal from the sensor, which was averaged over 64 samples at a sampling rate of 10 million samples per second. The overall set up is illustrated in Fig. 3.7(b).

3.3.1.2 Results and Discussion

The sensor frequency response was measured experimentally and simulated using the theoretical model in Chapter II. A sample of these results is shown in Fig. 3.8, which shows the time history predicted by the model is in good agreement with the data recorded from the piezoelectric sensor. The material properties used for the aluminum alloy in the computations are summarized in table 3.5. The figure illustrates the results for the A_0 mode at 65 kHz. It can be noted that the amplitude and time of arrival of each peak are very well captured by the model, as the error in the time of arrival is less than 2% while the largest amplitude difference (which occurs for the final secondary peak) is less than 8% of the peak-to-peak amplitude of the pulse.

Several time histories, similar to that presented in Fig. 3.8, were recorded over a range of frequencies for both the symmetric and antisymmetric modes. These results are summarized in Fig. 3.9 where each data set has been normalized by its maximum value. The experimental data points represent average values, while the error bars represent three times the peak-to-peak standard deviation. This uncertainty was found by taking 64 averages at each frequency. It can be seen that there is good

agreement between the theoretical prediction and the experimental data, especially for the antisymmetric mode where the differences between the two results are within the error bars of the experimental measurements for most of the points. It can also be appreciated that there is good correlation between both results for the symmetric mode until a frequency of approximately 275 kHz. Beyond this frequency, the EMI generated by the CLoVER sector is very strong and its interaction with the excitation pulse is very significant. Consequently, the peak-to-peak amplitude of the response recorded had to be manually measured according to the expected time of arrival of the pulse, calculated based on its group velocity at each frequency. The EMI results from the rapidly changing electric currents flowing through the interdigitated electrode fingers of the transducer. An important area for further development is the shielding of the transducer and sensor to this type of interference.

3.3.2 Laser Vibrometer Experiments

In this section, the non-contact technique of laser vibrometry is used to investigate the GW field induced by a CLoVER sector. This method is an important complement to the sensor-based experiments presented in the previous section as it is able to provide information on the spatial variations of the GW field. The section begins with a brief overview of the operating principles of the scanning laser vibrometer and a description of the experimental setup used. A comprehensive set of results are subsequently presented to verify the spatial and temporal accuracy of the theoretical solution.

3.3.2.1 Setup and Laser Vibrometer Operation

The key instrument used in these studies was a Polytec PSV-400 scanning laser vibrometer. This system is composed of the PSV-I-400 scanning head, the OFV-5000 controller, the PSV-E-401 junction box, and a data management system. The light source used in the PSV-400 is a helium neon laser that provides a linear polarized beam [73]. The vibrometer system is able to measure the out-of-plane velocities by measuring the difference in path lengths between a reference beam and an object beam that is backscattered from the surface under inspection. The PSV-I-400 scanning head houses a high sensitivity vibrometer sensor, a high precision scan unit, and a color video camera used to manipulate the laser and scan points in the PSV software. The OFV-5000 controller is able to decode the interference signal of the object and reference beams, while the PSV-E-401 junction box provides an interface for the

scanning head, controller, and data management system as well as several input channels for triggering and signal generator output. Finally, the data management system houses the PSV software used to operate the laser vibrometer.

The scanning head was supported using a tripod and maintained at a distance of 915 mm from the scanning surface for most of the experimental tests conducted. This distance was selected to operate at a laser visibility maximum [73]. An important consideration when taking laser vibrometer measurements is that the scanning angles be small enough so that contributions from the in-plane components remain negligible. The horizontal and vertical scanning angles are defined in Fig. 3.10(a). Furthermore, large scanning angles ($\sim 10^{\circ}$) are expected to reduce the signal-to-noise ratio. The work of Leong *et al.* [74] provided important insight into this issue. They showed that the vertical scan angle should be kept below four degrees in order to maintain a consistent signal to noise ratio, while the amplitudes of the displacements measured were mostly insensitive to variations in the horizontal scan angle. Consequently, the plate under inspection was arranged so that the vertical scan angle did not exceed the four-degree limit.

The overall experimental setup used in these tests is shown in Fig. 3.10(b) while a block diagram illustrating the interaction among the different components is shown in Fig. 3.11. The process begins by generating an excitation pulse which is amplified through a Trek PZD2000 amplifier (with a fixed gain of 200). At the same time, the PSV system is triggered and laser parameters from the PSV-I-400 scanning head start being recorded. The phase difference produced in the incident laser beam by the surface motion is relayed to the controller, via the junction box, where it is decoded into a velocity signal. This result is later relayed through the junction box to the the data management system where it is visualized via the PSV software. The sampling frequency used in this case was 5.12 MHz.

The test specimen consisted of the same isotropic plate and CLoVER transducer arrangement described in section 3.3.1. The surface to be scanned was lightly sanded using 120 grade sand paper to enhance its backscattering behavior. As the laser vibrometer is primarily sensitive to the out-of-plane velocities, the center frequency of the excitation pulse used was maintained at 65 kHz. It was shown earlier through sensor-response experiments that the A_0 mode is maximized near this frequency. This mode was selected as it is well known that it has a predominantly out-of-plane component. The input voltage used in this set of tests was higher than in the sensor tests to obtain a high signal-to-noise ratio in the laser vibrometer, and varied from 200 to 800 V_{p-p}.

3.3.2.2 Results and Discussion

The first set of tests consisted of evaluating the time history performance of the solution. Three points were selected at a fixed distance of $3.4R_O$ from the outer radial edge of the transducer and various azimuthal locations, as shown in Fig. 3.12(a). The time of arrival is close for both solutions (within 5 %) as shown in Figs. 3.12(b)-(d). The shape of the toneburst signal is also well captured although there are some differences in the relative amplitude of both the main and secondary peaks. The largest of these differences occurs for the time history recorded at 72° and corresponds to approximately 30 % of the peak-to-peak amplitude of the excitation pulse. As previously mentioned, the excitation voltage used in these experiments was significantly larger than that used in the sensor-based experiments, partially to obtain a good signal to noise ratio. A larger voltage input generates larger strains in the transducer, and it is possible that this results in a more pronounced contribution from the transducer dynamics which have been neglected in the theoretical solution. Alternatively, the discrepancy could be explained by the larger amplitudes being caused by ringing of the piezocomposite transducer. This phenomenon is associated with the rapidly changing electric fields exciting a resonant oscillation of the piezoelectric device. It should be noted that there are additional reasons for selecting a higher excitation voltage in this set of experiments. First, in this case only one transducer is being used in contrast to the two used in the previous experiments. This was done because in preliminary testing it was found that due to the sensitivity of the laser beam, minor misalignments in the placement of the transducers ($\sim$ 2 mm) significantly affected the shape of the propagating pulse. It is likely that the sensor is not as sensitive to these differences as it is primarily excited by the weaker (in the A_0 case) in-plane displacements. In addition, the piezoceramic fibers used in the CLoVER transducer are relatively thin. Finally, the antisymmetric mode is being excited using shear tractions in the plane of the substrate. It has been previously reported [20] that, due to this mode's strong out-of-plane component, transducers that apply surface tractions normal to the surface are preferred for A_0 excitation when employing a single device.

The second set of tests consisted of evaluating the decay in the propagating pulse amplitude with radial distance. It is important to accurately capture this parameter in the theoretical solution as it is key in determining the inspection distance that can be achieved with the transducer. In this case, several radial positions oriented along the centerline of a CLoVER sector were selected and the laser was used to measure the time history. The peak-to-peak amplitude obtained from these measurements were then compared to similar results obtained using the theoretical model. This result is

shown in Fig. 3.13, where the results have been normalized by the mean peak-to-peak amplitude in each data set. As in previous cases, the error bars represent three times the standard deviation. This uncertainty was found by repeating each measurement three times, collecting 64 averages in each test. The figure shows that the experimental and theoretical results are in excellent agreement, with the differences bewteen them staying within the experimental uncertainty for all the measurement points. Note that neither the theoretical model nor the numerical simulations have accounted for material damping, and therefore the amplitude attenuation observed in the results in Fig. 3.13 is due to geometric attenuation only. The good agreement between both results suggests that accounting for material damping is not necessary when working with linearly elastic isotropic materials.

Another important consideration is the azimuthal distribution of the induced GW field. This parameter measures the directionality achieved by a CLoVER sector. As in the radial decay study, the peak-to-peak displacement amplitude was measured at several azimuthal and radial locations as shown in Fig. 3.14(a). In this case, a complete 360° range was scanned using a grid consisting of 60 azimuthal points. In addition, three radial locations were chosen to investigate the evolution of the azimuthal distribution with radial distance. The measurements were repeated three different times with each set consisting of 64 averages. The displacement field was calculated theoretically for the same radial locations using a finer grid of azimuthal points. These results are compared in several polar plots shown in Figs. 3.14(b)-(d). In these figures, the transducer centerline coincides with the 90° direction, and the peak-to-peak amplitude is represented by the radial distance from the origin for each azimuthal location. The uncertainty for each point is represented by two finer lines surrounding the experimental points which correspond to three times the standard deviation.

The results show that the azimuthal distribution is captured well by the model. The regions where the largest disagreements are observed correspond to normal directions from the transducer centerline where the GW field is smallest. This decreases the signal-to-noise ratio in the laser vibrometer resulting in larger standard deviations. Some differences are also observed for the wave field induced in the opposite direction, i.e., towards the 270° direction, especially for larger radial distances. The largest error in this case is in the order of 23 % and it occurs for the farthest radial position tested, at an azimuthal location of approximately 300°. It is likely that this disagreement is partly due to the presence of additional CLoVER sectors which are not accounted for in the theoretical solution. These additional transducers introduce

concentrated masses which act as very small GW scatterers. As the radial position is increased, a larger portion of the wave field interacts with the additional sectors, which may explain the increasing difference with larger distance. It can also be appreciated from the figures that as the radial position is increased the main displacement lobe becomes wider, which is consistent with the expectation that in the far field the wavefront would tend to a uniform circular front [56].

The final set of tests consisted of a full-field scan to visually compare the temporal and spatial evolution of the GW field induced by a CLoVER sector. The scanning grid used in this case consisted of 25 radial points distributed over a seven centimeter range, providing approximately three wavelengths with seven points per wavelength. A complete 360° range was covered for each radial position using an azimuthal grid consisting of 40 points, for a total of 1000 scan points. The starting radial position for the measurements was selected at one centimeter from the radial edge of the CLoVER sector to avoid scanning over pieces of kapton film that remain attached to house the electrode bus of the transducer. Similarly, the radial positions scanned excluded points near the origin as a piezoelectric sensor was bonded in this area. These results are summarized in Figs. 3.15 through 3.17, which show very good correlation between the theoretical model and the experiment. The directionality of the transducer is clearly visible, as the induced displacements remain primarily within the azimuthal span of the CLoVER sector. The results presented in the previous sections have shown the accuracy of the three-dimensional elasticity solution in describing the GW field induced by a CLoVER sector in isotropic structures [29, 58].

3.4 GW Excitation in Wind Turbine Structures Using Piezocomposite Transducers

The increasing prominence of wind energy in recent years has emphasized the need to develop SHM technologies that would provide real-time information on the structural condition of wind turbine structures. Such a system would be composed of a network of transducers distributed around the structure that would inform the user of any adverse changes in its condition. There are multiple approaches under consideration that differ in sensing methodology, data transmission, and damage monitoring algorithms. The study reported in this chapter focuses on GW based methods and the ability of piezo-fiber transducers to excite these stress waves in wind turbine structures.

In recent years several approaches have been tested to monitor the condition of

wind turbine structures. Most of these experiments have concentrated on health monitoring of the blades as these are most susceptible to fatigue damage due to the cyclic loading to which they are subjected. In addition, many of the experiments reported in the literature have been conducted on scaled blades in laboratory settings. A review of the different damage detection methodologies suitable to wind turbine inspection was reported by Ciang *et al.* [75]. Goshal *et al.* [76] employed multiple vibration-based damage monitoring algorithms based on piezoelectric patches as the transduction mechanism. In general, it was found that all methods tested, including GW approaches, were able to provide an indication of a change in the structural properties of the blade. This change was provided by the addition of a concentrated mass on one side of the blade specimen. Rumsey and Paquette [77] reported an extensive experimental investigation into health monitoring alternatives for wind turbine blades. A nine-meter wind blade designed by Sandia National Labs (model TX-100) subjected to fatigue loading was used as a test sample. It was found that acoustic emission was the most successful approach, although this was in part due to the proximity of the sensors to the region where damage originated (approximately within a 20-cm radius circle). It was reported that the modal-based algorithms based on accelerometers as well as the impedance measurements based on NASA MFC transducers were unable to identify the presence and evolution of the defect. Similarly, in Pitchford *et al.* [78] a 0.4-m long section of a wind turbine blade designed at Sandia (CX-100) was used as a test sample using the impedance method. It was shown that this technique was able to detect these defects in a range of 10-30 cm from the sensor using a frequency range between 10 and 60 kHz. From the brief literature review presented, it can be noted that most experimental investigations have been restricted to sample specimens in laboratory settings, with no work on operational structures having been reported. Most studies using GW with piezocomposite transducers have also concentrated on laboratory settings using thin ($\sim$ 1-10 mm) metallic and composite plate-like structures, where their ability to excite and sense ultrasonic waves has been demonstrated. However, the capability of these transducers to excite and sense ultrasonic waves in thicker structures, such as wind turbine walls with a thickness in the order of 50 mm, has not been verified. This chapter describes a series of experiments conducted on the walls of an active Vestas V80 wind turbine in an effort to verify the feasibility of using the GW approach to monitor the condition of these structures. It is expected that this inspection method could be sensitive to the corrosion and filtration damage expected for these components [75], especially in off-shore wind turbines which are typically subjected to harsher operational environments.

3.4.1 Experimental Description

The wind turbine structure tested was a Vestas V80 with a power rating of 2.0 MW. The wind turbine has a tubular steel tower with a height of 80 m [79]. These structures were located in Braunschweig in northern Germany. The inside of the wind turbine wall is divided in several stations each with a platform that allows user access. Each of these platforms can in turn be accessed via a lift or a ladder inside the structure. The details of the wind turbine structure can be seen in Figs. 3.18 and 3.19. The GW propagation tests were conducted at the first such station, located at a height of approximately 6 m above the ground, as seen in Fig. 3.18. Based on technical specifications of the wind turbine procured from researchers at the Institute for Structural Analysis at the University of Hanover [80], the diameter of the wind turbine wall was found to be in the order of 3.3 m at the station tested. In the actual tests, the diameter is likely to be smaller due to the thickness of the wind turbine wall, which was estimated at 5 cm. Hence, the actual diameter of the wall is assumed to be 3.2 m which yields a circumference of $\sim$10 m at the station tested.

The wind turbine wall was instrumented with three rectangular piezo-fiber transducers. One of these was used as a source of GW while the other two were used as sensors. The device used as actuator had an active width of 58 mm and an active length of 48 mm with the piezoelectric fibers oriented along the 48-mm direction (along the circumference of the wind turbine tower). Both sensors had a width of 38 mm with one having an active length of 49 mm and the second one an active length of 46 mm. All the piezocomposite transducers had a thickness of 0.3 mm [81]. The piezoelectric fibers have a width of 0.3 mm and are constructed of PZT-5A. These devices were fabricated in-house following the fabrication procedure reported in section 3.1.

The distance between the edge of the actuator and the first sensor was 0.19 m while the second actuator was placed 0.37 m from the edge of the actuator. The transducer arrangement used is shown in Fig. 3.20. As seen in the figure, the second sensor was placed behind a weld-line of the wind turbine wall, with an aim to explore whether the incident GW pulse would display any mode conversion due to its interaction with this feature. The actuator was excited with a 3.5 Hann-modulated toneburst with a peak-to-peak voltage of 300 V. This amplitude is similar to that employed in laboratory settings [8, 9]. The signal was generated through an arbitrary waveform generator (Agilent 33220A) and amplified using a Krohn-Hite 7500 wide band amplifier. The data acquisition was performed using a NI PCI 6036E system, with a maximum sampling frequency of 200 kHz, connected to a laptop computer running a LabView

virtual instrument. The excitation frequency was varied from 2 kHz to 40 kHz in intervals of 2 kHz. These frequency limits were selected based on the maximum sampling rate available from the acquisition system. Figure 3.21 shows a photograph of the experimental setup used.

3.4.2 Time Domain Results

Figure 3.23 shows a sample response signal recorded with one of the piezocomposite sensors. This signal has been processed to remove its DC component. The Lamb wave inspection pulse can be discerned from the response, but it is also clear that multiple frequency components with larger energy contents are collected. This is expected as the transducer is also sensitive to vibrations of the wind turbine wall due to its operational loads. This is an important observation as it demonstrates that the piezocomposite transducers, in addition to their ability to excite and sense GW, can potentially be used to also obtain global information on the structure (e.g., natural frequencies) which can be used in conjunction with damage detection algorithms based on such structural properties (e.g., Zimmermann *et al.* [82] and Lu *et al.* [83]). An FFT analysis on this signal is shown in Figs. 3.24 and 3.25 where the lower frequency components as well as the Lamb wave pulse are identified. The FFT computation used a total of 5000 points. A similar analysis was performed for all sensor signals collected and it was found that three fundamental frequencies, namely 80 Hz, 160 Hz, and 240 Hz, were consistently recorded. In order to facilitate the GW propagation analysis, all signals were passed through a fourth-order band-pass Butterworth filter whose limits were defined as 0.7 and 1.3 times the center frequency of excitation. The signal shown in Fig. 3.22 is shown in Fig. 3.23 after being passed through the filter. The GW pulses are clearly visible in the processed signals.

The analysis performed on the GW signals recorded was aimed at producing wave velocity curves, GW amplitude, and maximum propagation distance on the wind turbine wall all as a function of excitation frequency. This analysis requires that individual Lamb wave modes be used, and it was found that, in general, only one mode propagated in the wall at most frequencies. Therefore, the wave and amplitude analysis was carried out using the Hilbert amplitude of the time-domain signals and identifying the main peak in the response as well as its time of arrival. The Hilbert transform computes an equivalent complex conjugate of a time-domain signal, so that its absolute value provides an amplitude envelope for the original signal. Based on the known distance between the actuator and the sensors, the wave velocities can be calculated. Similarly, the GW amplitude is obtained by recording the amplitude of

this spectrum at that particular time. Figure 3.26 shows the wave velocity distribution collected with both sensors for the main wave packet observed in the signals. The values reported correspond to the average of two separate measurements while the error bars correspond to the standard deviation in these measurements.

Note that the propagating mode is dispersive as different frequency components are seen to propagate at different speeds. Based on this characteristic it can be concluded that an antisymmetric-like mode is excited in the wind turbine wall at these lower frequencies. It is also important to note that due to the small radius of curvature and thickness of the wind turbine wall, the propagating modes can be considered as Lamb waves. Furthermore, observe that the speed calculated by both sensors is not similar. These results were calculated using the distances described earlier which assume that the GW pulse originates at the edge of the actuator which is closest to the sensor, and that the sensor starts collecting the response as soon as the pulse reaches its closest edge to the actuator. Different distance criteria were tried, e.g. assuming the waves were recorded at the center point of the sensor instead of its edge, but these were not sufficient to reconcile the difference between both readings. A possible explanation may found by considering that the smaller distance from the first sensor to the actuator may be providing an estimate of the phase velocity, while the second sensor placed further behind is providing an estimate of the group velocity. It is well known that the wave speed is close to the phase velocity during the first two or three spatial wavelengths away from the source, while it approaches the group velocity for longer distances. Furthermore, the phase velocity is usually lower than the group velocity which is consistent with the observation in the result. For the subsequent propagation distance measurements, the velocities calculated with sensor 2 will be employed as they are expected to be representative of the group velocity. Figure 3.27 shows the amplitude of the propagating GW pulse as a function of frequency. Note that the response for sensor 1 is very flat after 6 kHz while that of sensor 2 shows a small peak at 26 kHz. From these results it can be concluded that frequencies larger than 10 kHz should be preferably employed as their amplitude is consistently larger than for lower frequencies. It cannot in general be concluded that higher frequencies will yield monotonically increasing amplitudes as considerable drops in the response are observed for sensor 2 after 30 kHz.

An important objective of the experiments was to determine the ability of GW pulses to propagate significant distances over the surface of the wind turbine wall. In order to calculate this distance, the Hilbert transform of the entire signal was used as previously described. A peak finding algorithm was employed to rank all the peaks

in the signal envelope with amplitudes larger than 10% of the incident GW pulse recorded by each sensor. The time of arrival of the latest peak was recorded and used with the wave velocity obtained from sensor 2 at each frequency to determine the distance traveled by the pulse. The result from this analysis is shown in Figs. 3.28 and 3.29. Figure 3.28 shows the nominal propagation distance in meters. This result demonstrates the ability of the GW to propagate a significant distance on the surface of the structure and the ability of the piezo-fiber transducers to excite these waves in thicker structures using electric inputs similar to those in laboratory settings [81].

Two important observations can be made. First, the smaller propagation distances observed at lower frequencies are likely a result of the smaller wave speed and the maximum time recorded. It is likely that if measurements were taken for a longer time, longer distances would be observed. Secondly, no specific conclusions about the path of the peak can be made. Some of these may correspond to reflections from structural features (such as ladder and lift attachments to the walls), while others may correspond to parts of the incident pulse that have traveled around the circumference of the wind turbine wall. The result shown in Fig. 3.29 gives an indication of this as it plots the propagation distance normalized by the circumference of the wind turbine at the station tested (denoted as C). Note that, as mentioned earlier, a circumference of approximately 10 m was estimated. Similarly, Fig. 3.30 shows the normalized propagation distance assuming larger amplitude thresholds for the last propagating packet. The result shown in Figs. 3.28 through 3.30 can be partly expected as the construction of the piezocomposite transducer used concentrates most of the GW energy along the circumference of the wind turbine wall. Furthermore, the geometry of the structure makes it a suitable waveguide as it is a closed (continuous) structure where there are no losses associated with structural edges.

3.5 Concluding Remarks

This chapter described the design and fabrication procedures for the prototype CLoVER transducers developed in this thesis. The modifications to the NASA-standard manufacturing guidelines to allow the transducers to be constructed in an autoclave were outlined, and a new set of poling parameters selected to reduce the failure rate during poling was reported. The in-house manufacturing procedure was experimentally shown to yield devices whose free-strain performance is comparable to NASA-standard devices within the voltage range of interest. The prototype devices were then used in an isotropic plate structures in a set of experimental tests that

validated the theoretical formulation for guided wave (GW) excitation introduced in this thesis. The results showed excellent agreement between the experimental and theoretical results over a wide range of frequencies, and in the time and space domains. Furthermore, the high directionality of the guided wave field induced by the directional sectors was demonstrated using laser vibrometry. This directionality will be exploited in subsequent chapters were these devices will be used to detect simulated defects in isotropic and composite structures. This chapter also presented the results of experimental tests conducted on the walls of an operational Vestas V80 wind turbine located in northern Germany. It was shown that rectangular piezocomposite devices are capable of exciting and sensing ultrasonic waves with electric inputs similar to those used in laboratory settings. Furthermore, the sensors are also able to record the vibration of the structure due to its operational loads which shows their potential to be used along with separate health monitoring systems relying on global structural properties. An important conclusion from this study is that the GW excited by piezocomposite transducers are able to travel long distances around the circumference of a wind turbine wall thereby verifying the potential of this approach as a candidate for online structural health monitoring of wind turbine and other aerospace, civil, and mechanical structures.

Transducer Index	Poling Field [kV/mm]	Poling Time [min]	V_{p-p} [V]	$\mu\epsilon_{p-p}$	d_{33} [$*10^{-10}$ m/V]
1	2.22	15	252.4 ± 1.1	52.6 ± 1.5	1.04 ± 0.03
2	2.22	30	251.9 ± 0.2	60.3 ± 0.9	1.20 ± 0.02
3	2.22	60	252.0 ± 0.4	111.9 ± 1.6	2.22 ± 0.03

Table 3.1: Summary of transducer performance under different poling times.

Property	Value
E [GPa]	68.9
ν	0.33
ρ [kg/m^3]	2700

Table 3.2: Aluminum substrate material properties.

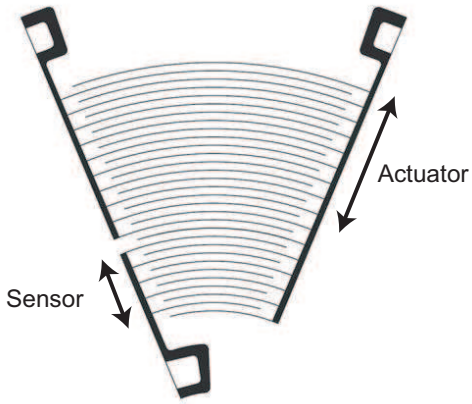

Figure 3.1: Sample interdigitated electrode pattern used in CLoVER transducer sector prototype.

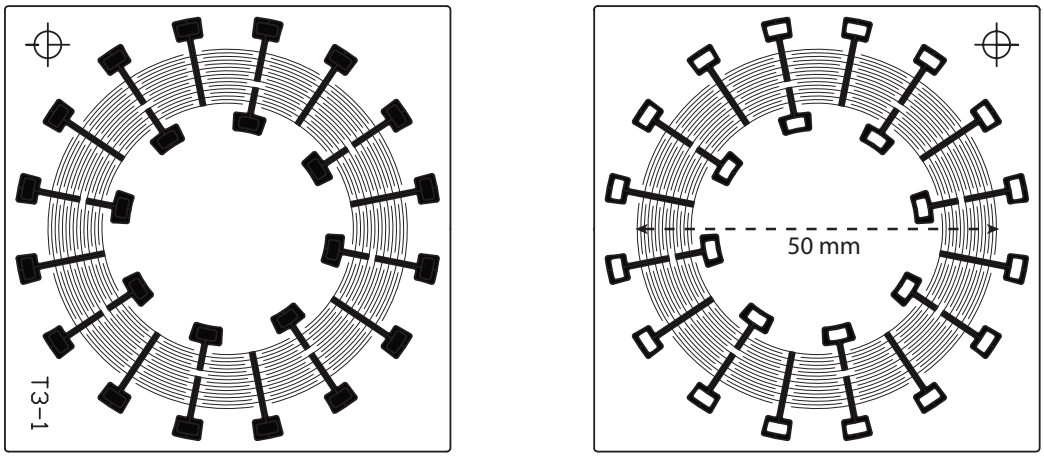

Figure 3.2: Sample interdigitated electrode pattern used in CLoVER transducer prototype.

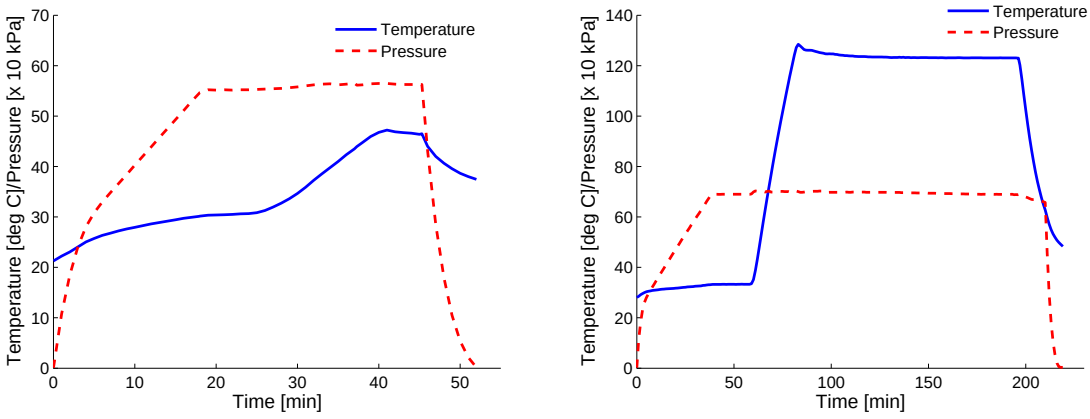

Figure 3.3: (a) CLoVER Partial Cure Cycle; (b) CLoVER Final Cure Cycle.

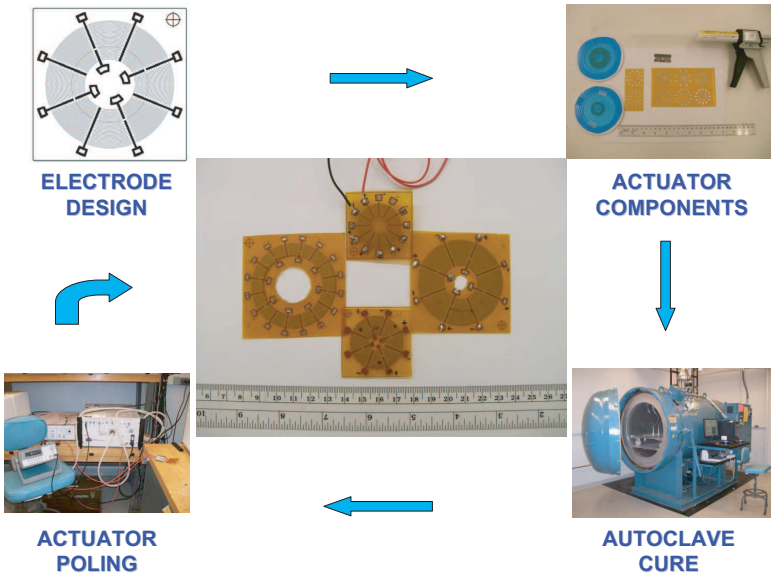

Figure 3.4: CLoVER transducer development stages.

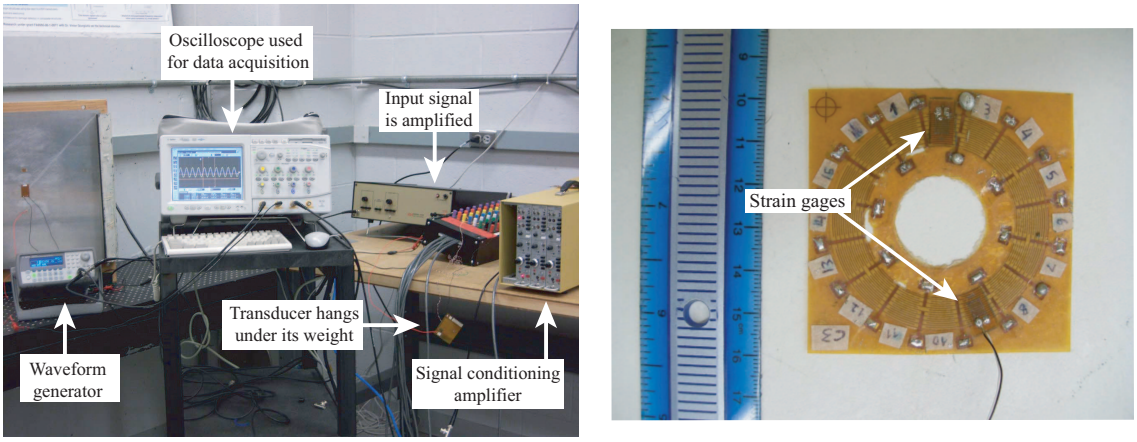

Figure 3.5: (a) Experimental setup for transducer characterization; (b) Detail of CLoVER transducer instrumented with strain gages.

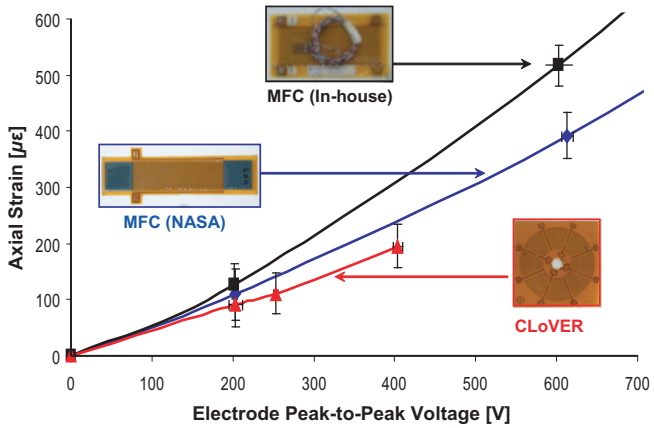

Figure 3.6: Performance comparison among different piezocomposite transducers.

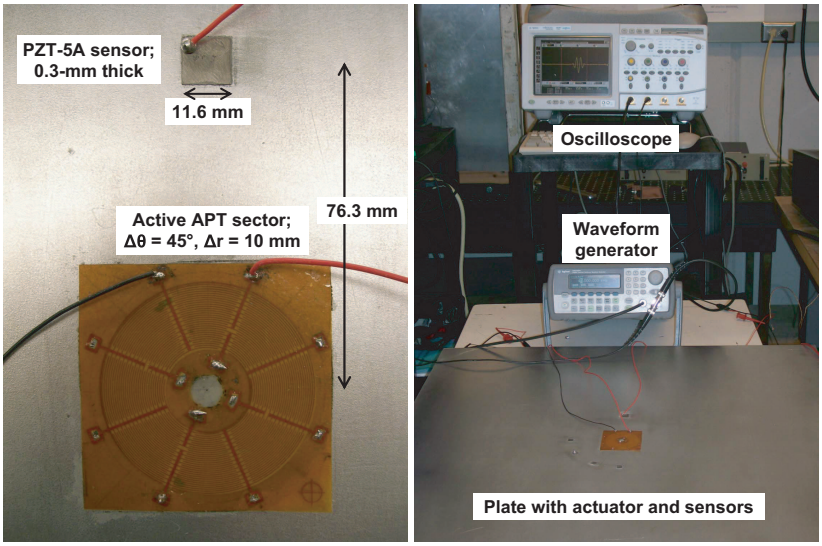

(a) (b)

Figure 3.7: Experimental Setup: (a) CLoVER transducer and sensor detail; (b) Overall arrangement.

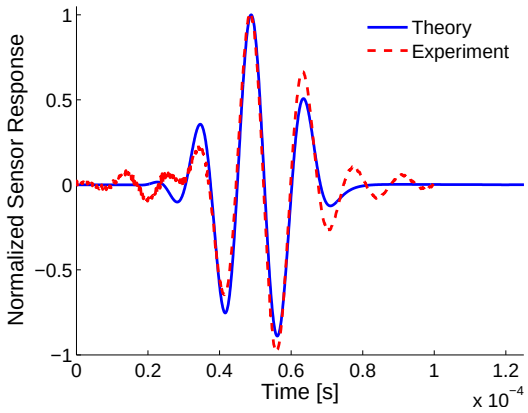

Figure 3.8: Time-history comparison for A_0 mode at 65 kHz excited by a CLoVER sector in an Al plate.

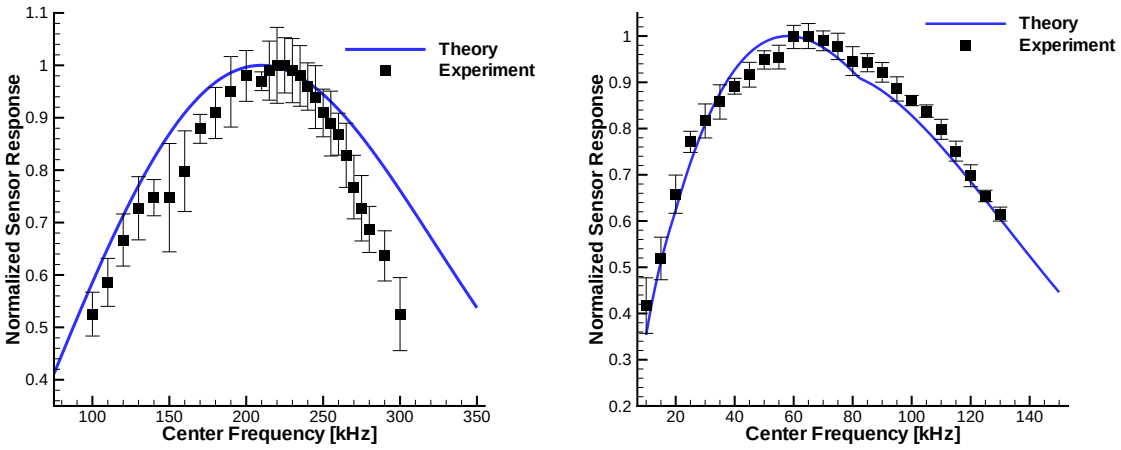

(a): S_0 mode **(b): A_0 mode**

Figure 3.9: Comparison between theoretical and experimental frequency response results for GW excitation by a CLoVER sector in an Al plate.

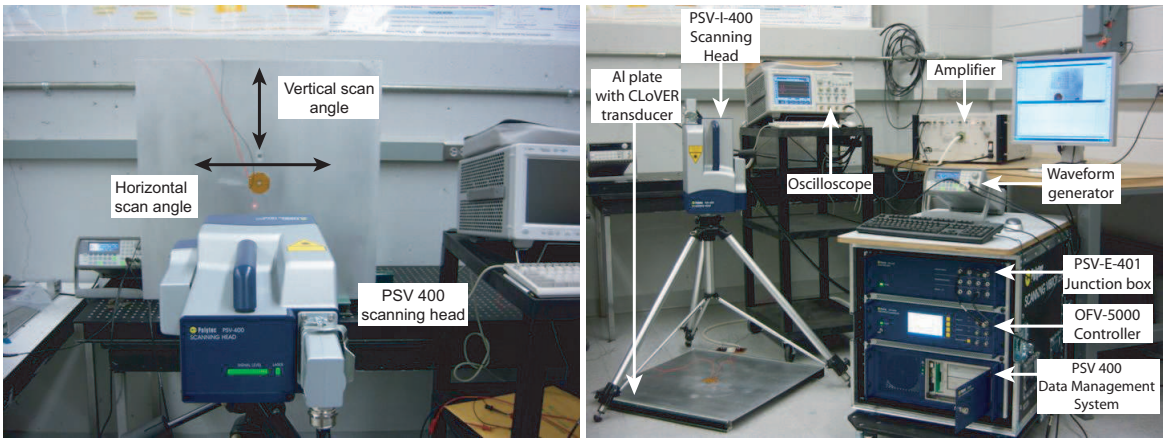

(a) **(b)**

Figure 3.10: **(a)** Definition of laser vibrometer horizontal and vertical scan angles; **(b)** Experimental setup used in laser vibrometer tests.

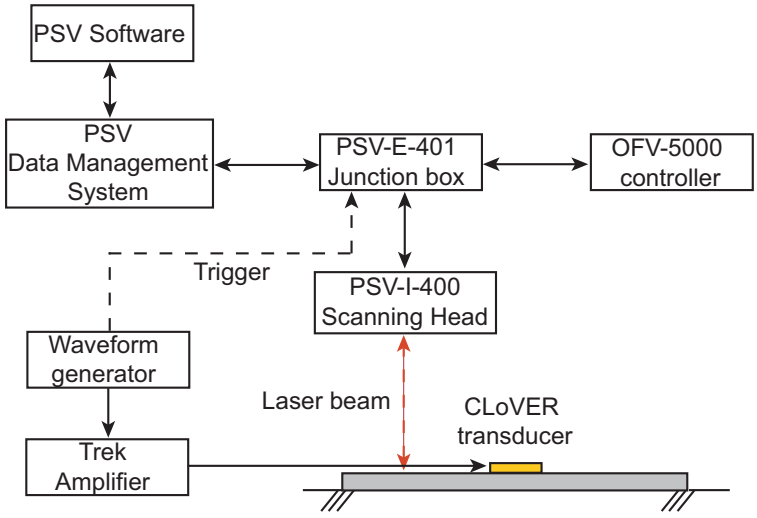

Figure 3.11: Block diagram illustrating the interaction among the different laser vibrometer setup components.

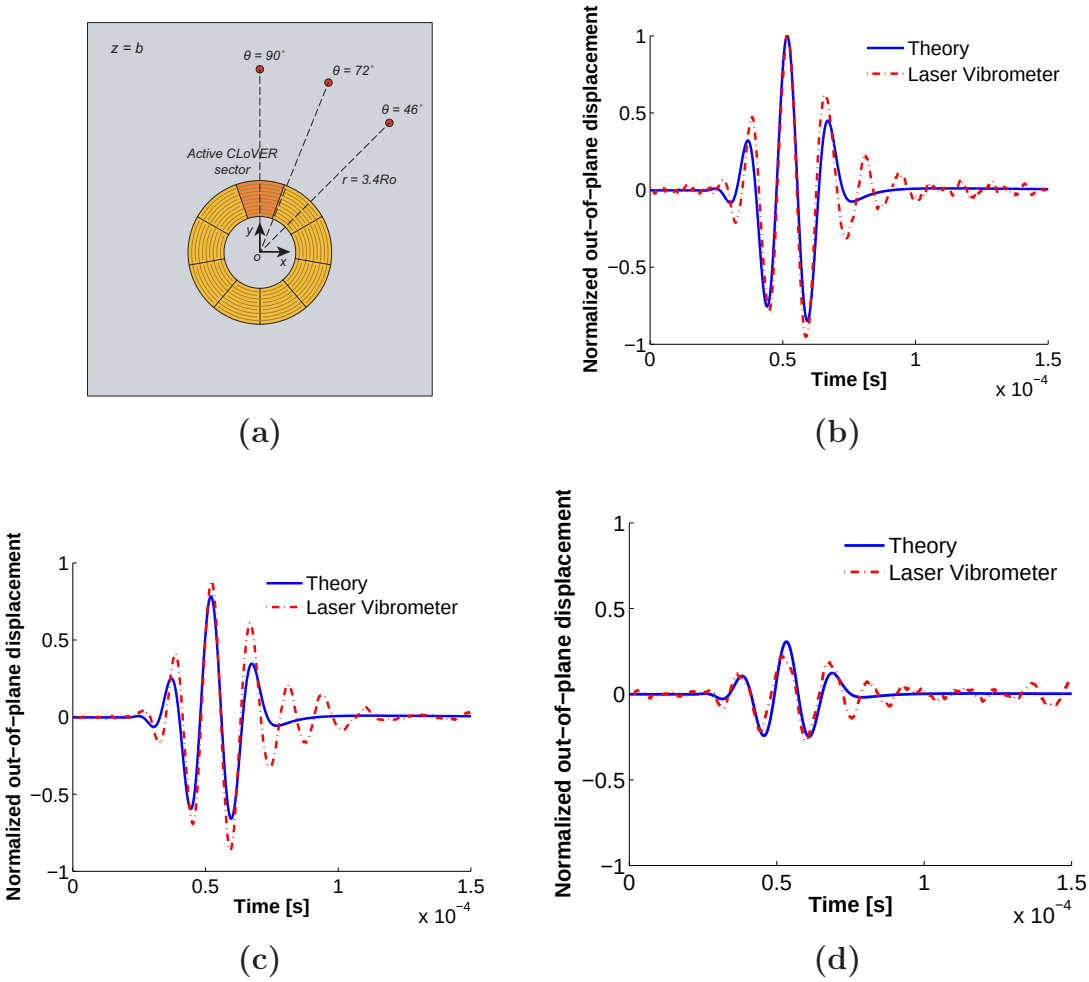

Figure 3.12: **(a)** Schematic illustrating distribution of laser measurement points; Time history comparison at $r = 3.2\ R_0$ and: **(b)** $\theta = 90°$; **(c)** $\theta = 72°$; **(d)** $\theta = 46°$.

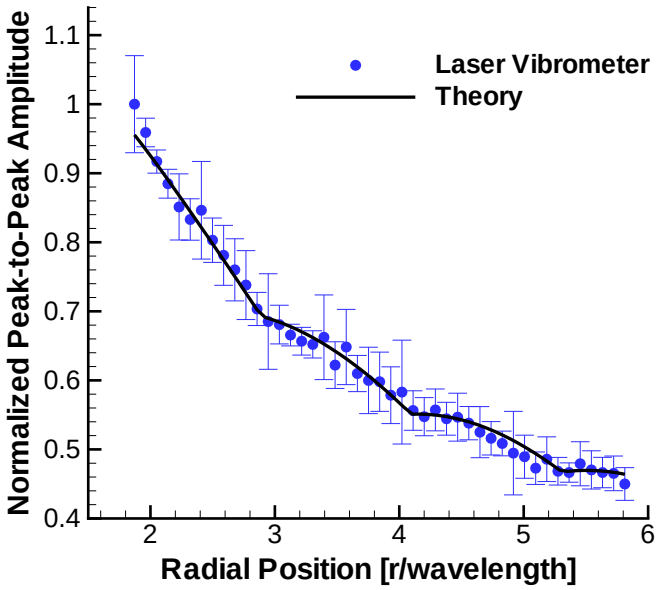

Figure 3.13: Comparison between theoretical and laser vibrometer results for peak-to-peak amplitude attenuation of GW excited by a CLoVER sector in an Al plate at 75 kHz.

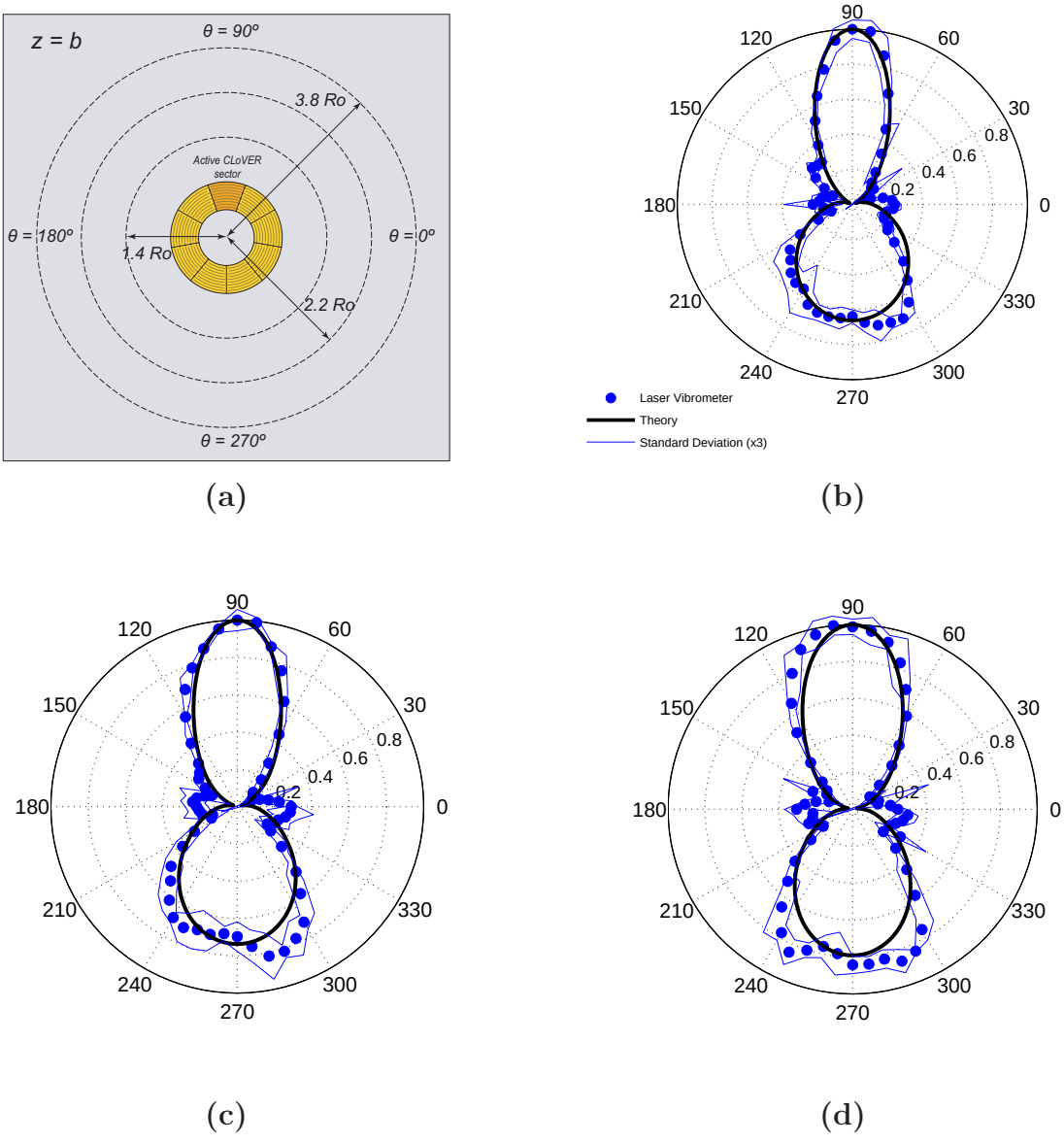

Figure 3.14: **(a)** Schematic showing location of the scan points used in azimuthal comparison tests; Comparison of peak-to-peak amplitudes at: **(b)** $r = 1.4R_O$; **(c)** $r = 2.2R_O$; **(d)** $r = 3.8R_O$.

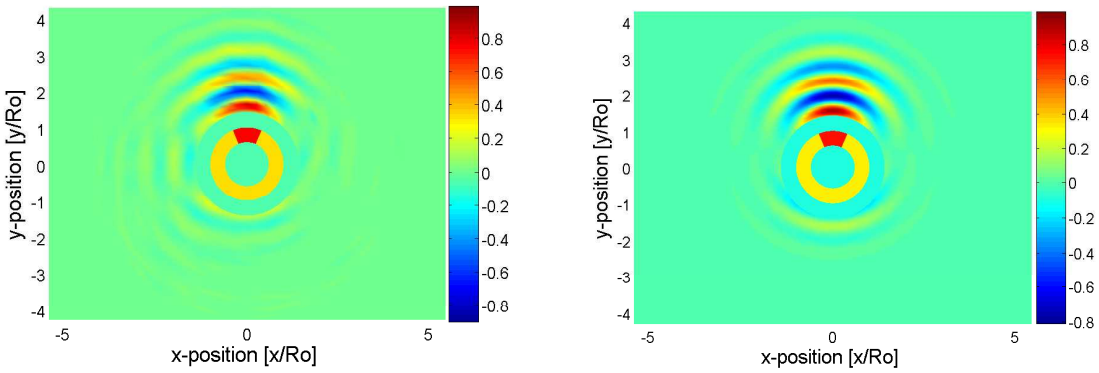

(a): Experiment **(b): Theory**

Figure 3.15: Full-field comparison between laser vibrometer and theoretical solution at time $t = 35$ μs.

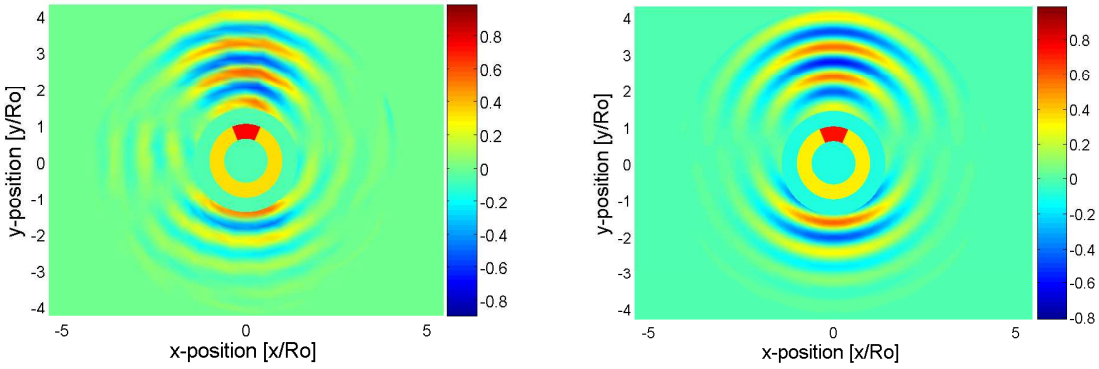

(a): Experiment **(b): Theory**

Figure 3.16: Full-field comparison between laser vibrometer and theoretical solution at time $t = 50$ μs.

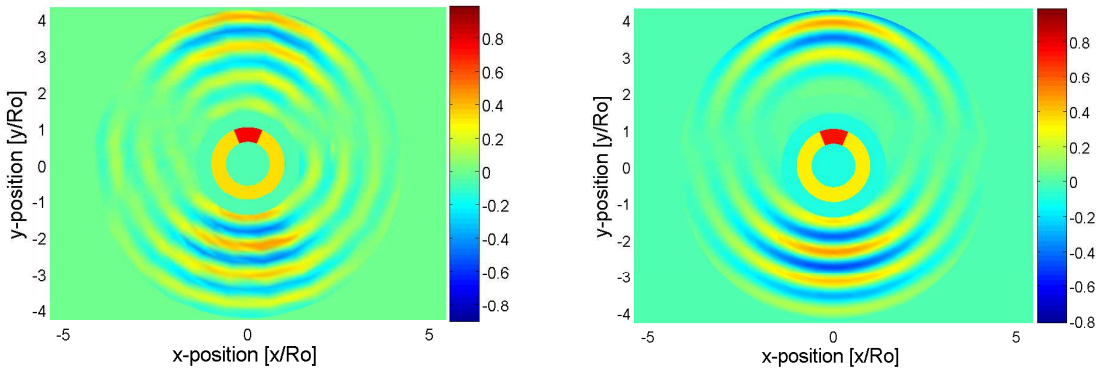

(a): Experiment **(b): Theory**

Figure 3.17: Full-field comparison between laser vibrometer and theoretical solution at time $t = 65$ μs.

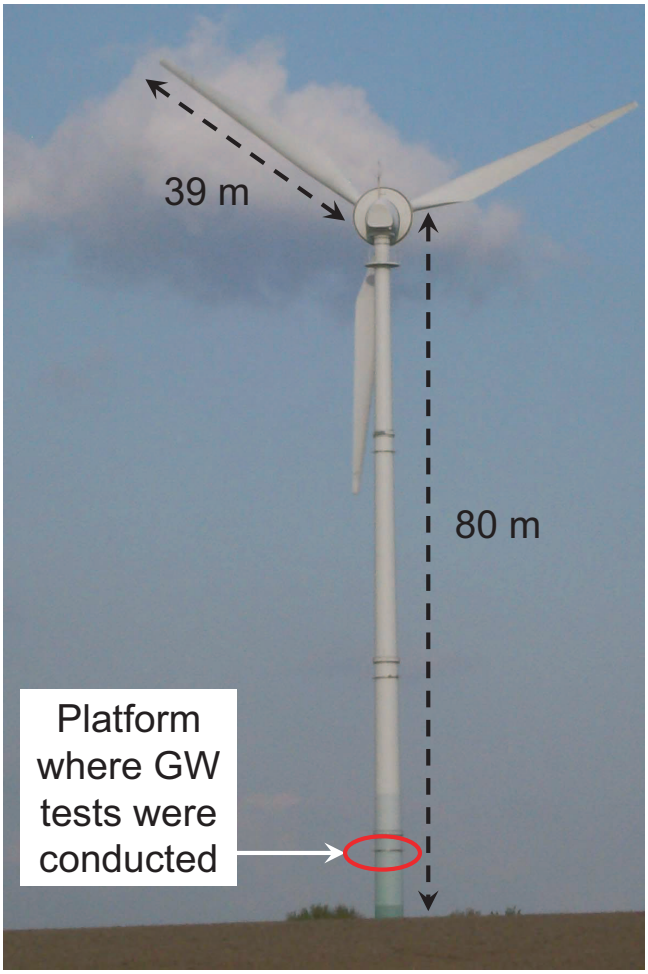

Figure 3.18: Photograph of a Vestas V80 wind turbine structure.

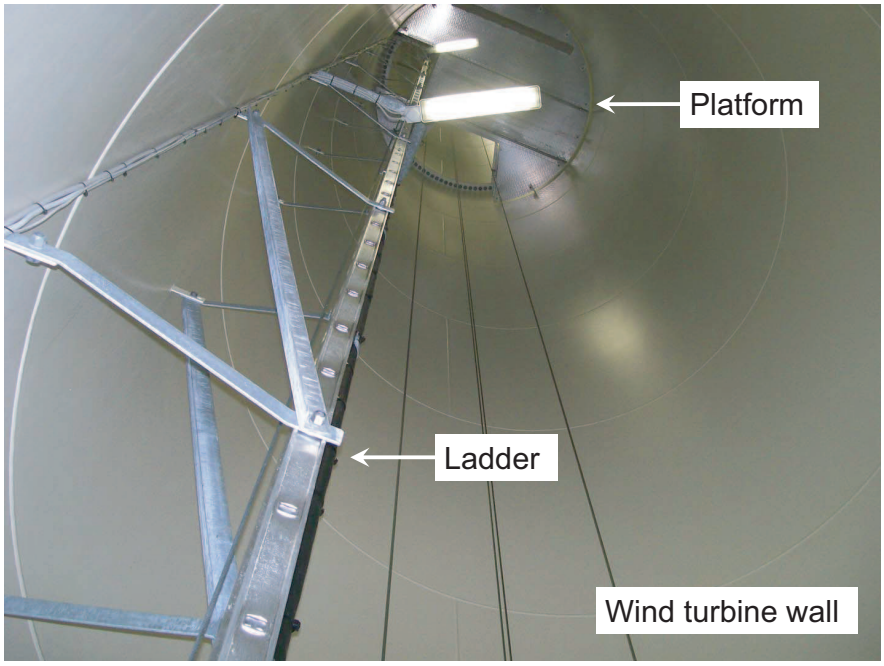

Figure 3.19: Detail of Vestas V80 structure's inner part.

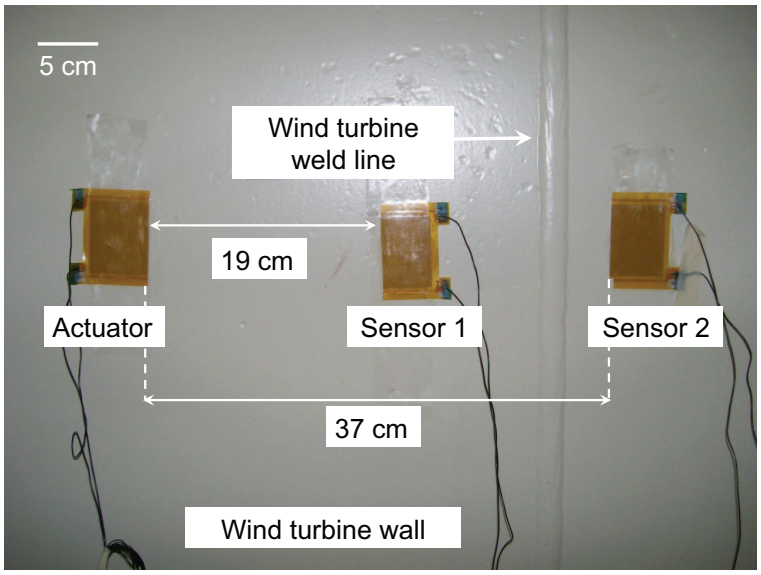

Figure 3.20: Transducer configuration used in Vestas V80 wind turbine wall testing.

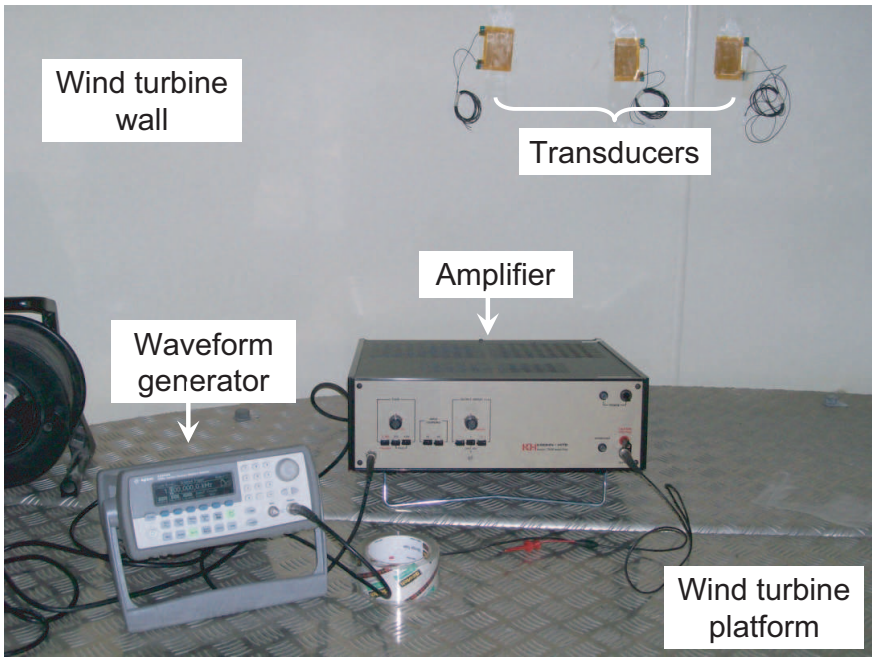

Figure 3.21: Overall experimental arrangement used in Vestas V80 wind turbine wall testing.

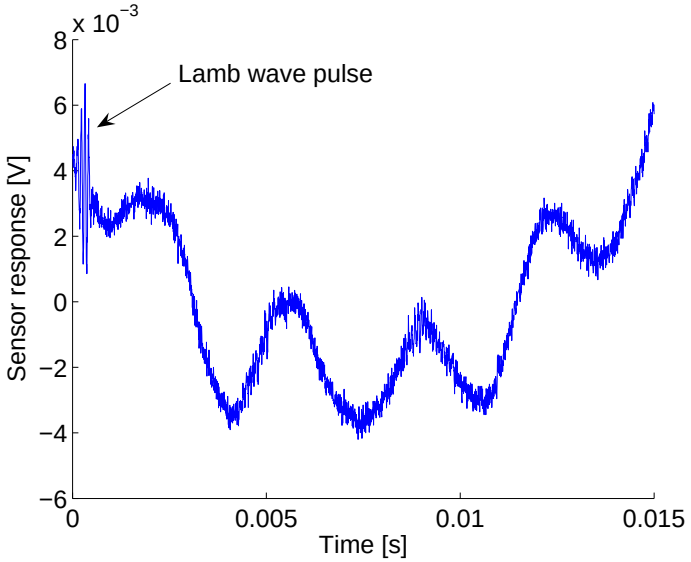

Figure 3.22: Sample time domain signals recorded in wind turbine wall with sensor 2 at 10 kHz for raw unfiltered signal with multiple frequency components.

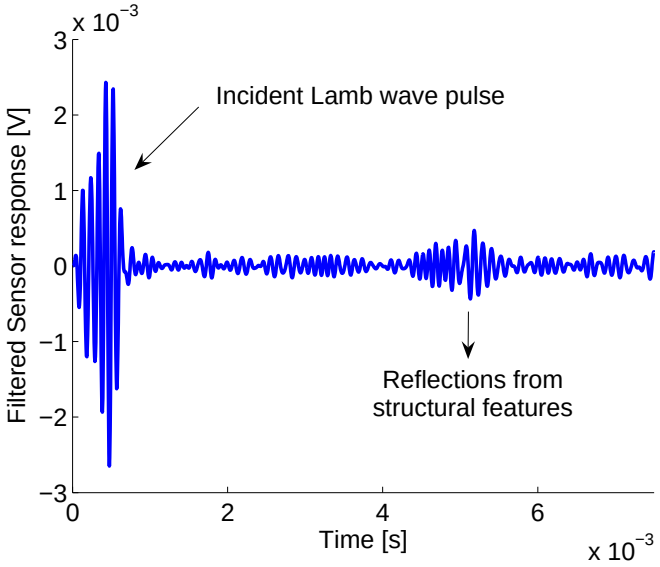

Figure 3.23: Sample time domain signals recorded in wind turbine wall with sensor 2 at 10 kHz passed through band-pass filter showing only GW pulses.

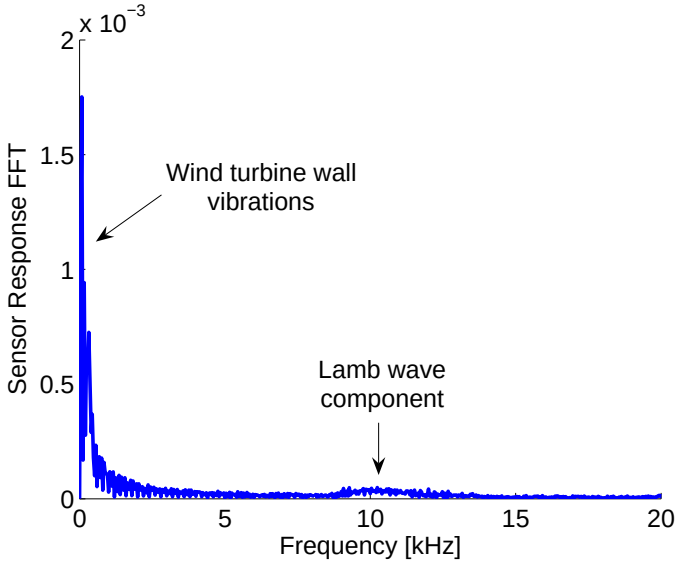

Figure 3.24: FFT of signal recorded with sensor 2 at 10 kHz.

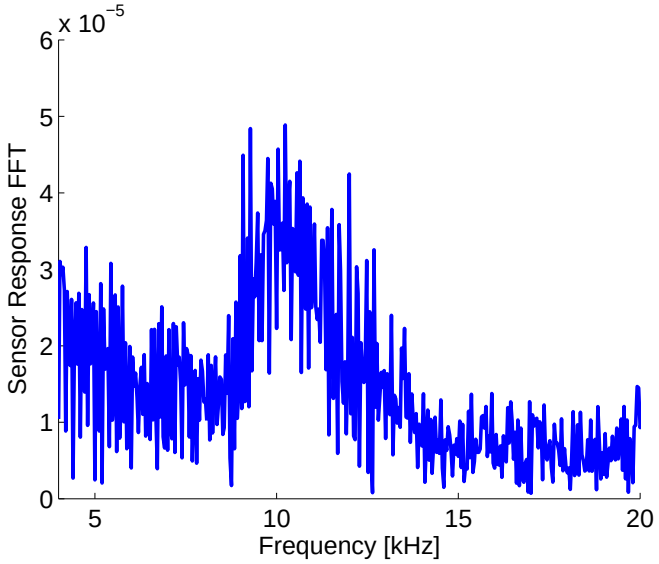

Figure 3.25: Zoomed FFT showing Lamb wave pulse frequency contribution.

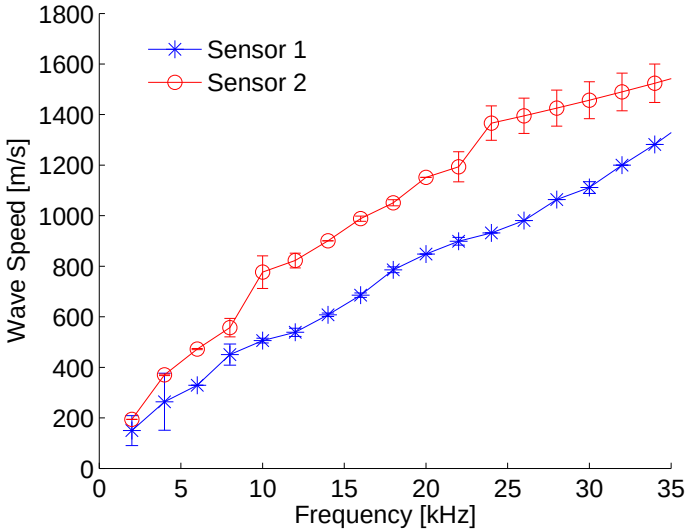

Figure 3.26: GW velocity curves in Vestas V80 wind turbine wall.

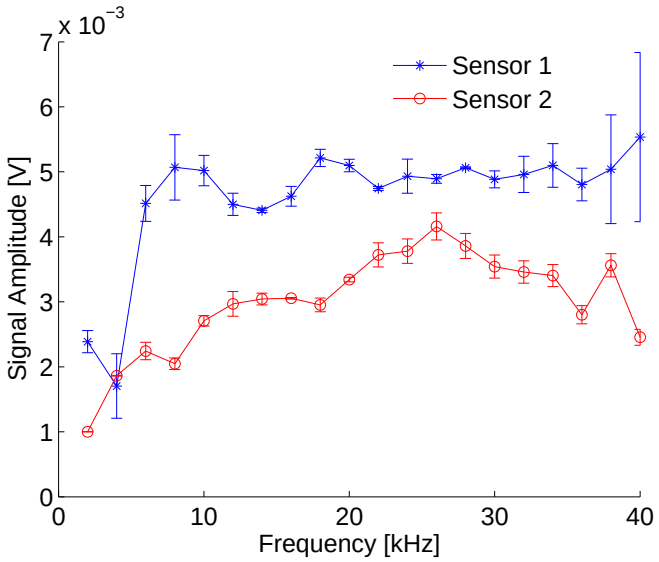

Figure 3.27: Modal amplitude in Vestas V80 wind turbine wall recorded with both piezocomposite sensors.

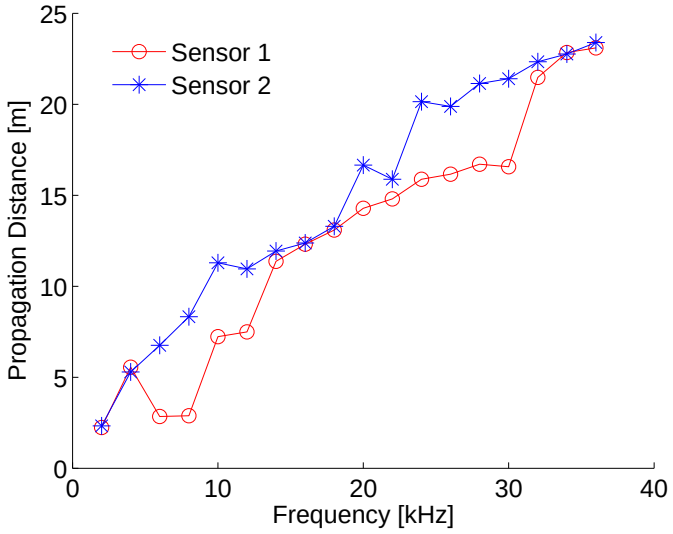

Figure 3.28: Physical propagation distance covered by GW pulses excited in Vestas V80 wind turbine walls using piezocomposite transducers.

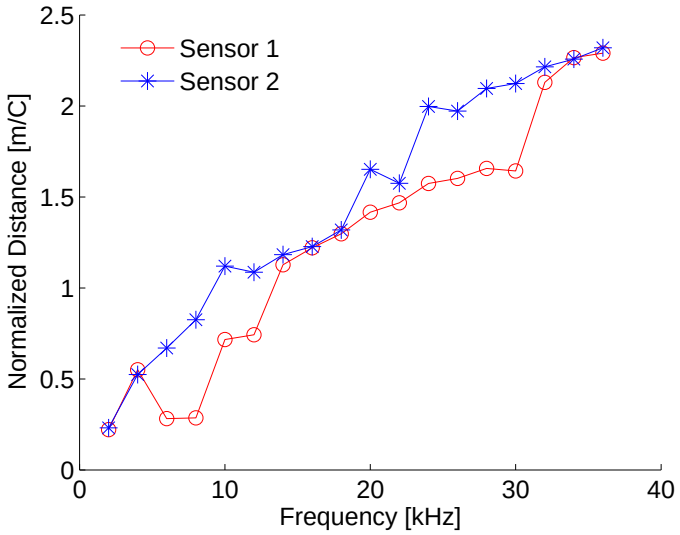

Figure 3.29: Normalized (by wind turbine tower circumference) propagation distance covered by GW pulses excited in Vestas V80 wind turbine walls using piezocomposite transducers.

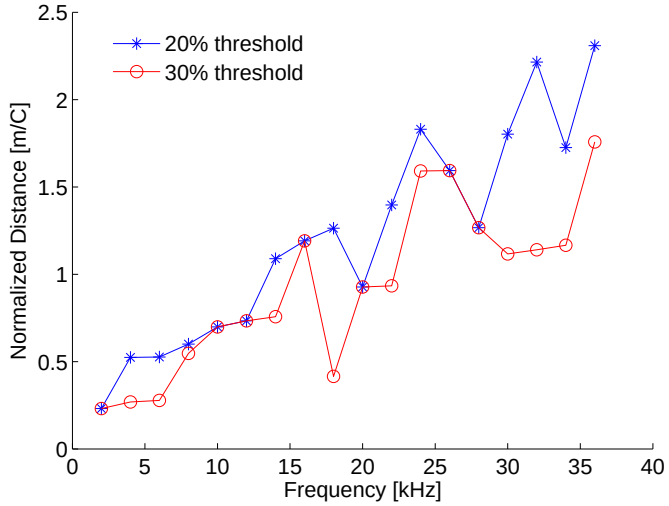

Figure 3.30: Normalized propagation distance covered by GW pulses excited in Vestas V80 wind turbine walls recorded with sensor 2 for different amplitude thresholds.

CHAPTER IV

Guided Wave Excitation by CLoVER Transducers in Composite Plates

This chapter presents a numerical and experimental investigation into the GW excitation characteristics of piezoelectric devices in composite materials. A systematic approach is employed where substrates with increasing level of anistropy are considered. The baseline case of piezoelectric wafers is considered first, followed by the GW excitation characteristics of CLoVER transducers in different composite laminates.

4.1 Introduction

Composite and multi-layered materials are being increasingly used in engineering applications due to their multiple advantages over traditional metallic materials. Their light weight, directional stiffness, and high specific strength, among other benefits, are being exploited for applications in the aerospace, mechanical, and civil engineering fields. The wider use of these materials has increased the need for effective methodologies to inspect their structural condition in a non-intrusive manner and in a real-time basis.

Guo and Cawley [6] were among the first to demonstrate the potential of GW methods for damage detection in composite materials. Their numerical and experimental investigations concentrated on the S_0 mode in cross-plies ($[0/90]_{nS}$), and determined its effectiveness in detecting interface delaminations. An important finding of their study was the large sensitivity of the reflections to the defect's location through the thickness of the specimens. This observation highlighted the potential of GW to selectively inspect specific interfaces in multi-layered materials by careful control of its through-thickness profile. Several subsequent studies have focused on verifying the viability of the GW approach to detect defects in different configurations

using piezoelectric transducers. For instance, Díaz-Valdés and Soutis [84] used piezoelectric elements to detect delaminations in thick composite plate-like structures. In their study they demonstrated the ability of the GW inspection pulses to propagate over two meters and to detect delaminations as small as 1 cm^2. Similarly, Kessler *et al.* [85] considered the use of Lamb waves for damage detection in quasi-isotropic composites. Their work identified how different inspection parameters such as frequency, pulse shape, and number of cycles affect GW-based damage detection in composites. More recently, Diamanti *et al.* [86] characterized the effect of defect size on the interaction of the incident GW field with damage in the form of delaminations. The inspection pulse used consisted of a nearly uniform A_0 mode wavefront generated by using a line of piezoceramic wafer transducers aligned along one direction of their specimens. Their results showed that the presence of the defects could be detected, but its extent along the width of their specimens could not be determined.

Several studies have also been directed towards assessing the performance of GW methods in damage detection of complex engineering structures in varying environments. For instance, Matt *et al.* [87] used MFC transducers for the inspection of bonded composite joints using coupled carrier modes and identified a consistent increase in the energy transmitted through the bond as its strength degraded. Similarly, Bottai *et al.* [88] successfully used piezoelectric active wafers for damage detection in various composite structures under ambient and cryogenic conditions. Yoo *et al.* [89] developed new damage metrics based on the Hilbert-Huang transform, and successfully applied it in damage detection of curved cylindrical composite panels. A more involved configuration was considered by Castaings and Hosten [90], who used GW methods to detect moisture content and micro-cracking of carbon-fiber composites wound around titanium liners in high-pressure tanks using air-coupled transducers. From the literature survey conducted it has been observed that most studies have employed simple piezoelectric wafers as the transduction mechanism for inspection. A different alternative was proposed by Gachagan *et al.* [91] where flexible piezocomposite transducers meant for interrogation of composite materials were developed. Their device consisted of individual piezoelectric wafers embedded in an epoxy matrix for improved flexibility. Their transducer was shown to produce strains comparable to those obtained from wedge-shaped transducers in quasi-isotropic composites, using embedded optical fibers as the sensing system.

While piezoelectric wafers are inexpensive and non-intrusive, their brittleness makes them highly susceptible to damage during operation and complicates their attachment to curved surfaces. Similarly, these transducers are only able to induce

omnidirectional GW fields. The majority of the studies reported in the literature have employed this type of wavefront, which may be sufficient in cases where one in-plane dimension of the structure is dominant, and only the distance between the defect and the GW source is required. However, for damage detection in two-dimensional structures, more sophisticated methodologies are needed. An alternative approach has been the use of phased arrays of transducers where virtual scanning beams are generated through post-processing algorithms. However, this approach is significantly more complicated in composite materials due to the energy steering induced by the substrate anisotropy. Yan and Rose [92] explored this issue for highly anisotropic composite plates. Their approach involved finding frequencies where a GW mode displayed nearly isotropic behavior. An improved phased-addition algorithm, accounting for the directional dependence of the wave speed, was employed in their experimental demonstrations. Similarly, Vishnuvardhan *et al.* [93] employed a single-transmitter-multiple-receiver transducer array in the inspection of quasi-isotropic plate-like composite structures. The array employed consisted of one emitter and thirty receivers all of which were circular piezoelectric wafers. Their approach utilized a phased addition algorithm, accounting for different dispersion characteristics along different material directions. Their method was successfully used in the detection of delaminations using the S_0 mode. While these methods are able to detect and localize defects, the large number of separate transducers needed could complicate their deployment in actual structures.

A second important observation from the literature survey is that most studies have employed a single representative composite lay-up in the numerical and experimental analyses. While this choice is typically sufficient to verify the feasibility of GW-based approaches, it is likely that the complexities of GW propagation in composites will play a critical role in the development of robust algorithms for damage detection and localization. Prominent among these complexities is the steering angle existing between the group and phase velocities for most composite configurations. This phenomenon results in a non-uniform distribution of energy along the propagation direction which, if unaccounted for, could result in an incorrect prediction of damage location. The first objective of this study is to conduct a systematic experimental investigation of the GW propagation characteristics in composite plate-like structures with different levels of material anisotropy. This is accomplished by employing axisymmetric sources in the form of circular piezoelectric wafers. In particular, the wave speed and wave amplitude distribution are measured as a function of in-plane azimuthal position to determine the directionality introduced in the GW

field as a result of the composite lay-up. The second objective is to characterize the GW excitation properties of the CLoVER transducer in composite plates.

The chapter begins with a brief review of the theory of GW in composite materials, to illustrate how the changing elastic properties introduce a directional dependence on the wave propagation parameters. The GW field excited by piezoelectric wafers is then analyzed through laser vibrometry and finite element simulations to provide a baseline for comparison with the CLoVER transducers. The GW excitation properties of these devices are subsequently analyzed.

4.2 Theoretical Background

This section provides a brief theoretical background of GW propagation in composite plates to illustrate how the varying material properties influence the GW propagation parameters. A key feature of GW is that they are dispersive as different frequency components can travel at different speeds. The most basic analysis of GW propagation, therefore, consists of finding the variation of wave speed with frequency for different modes. In the case of isotropic materials this is a relatively straightforward procedure as the well-known Rayleigh-Lamb dispersion equation can be solved numerically to find the wave speeds, as discussed in Chapter II. In that case, the dispersion equation is only a function of the material properties, frequency, and plate thickness. In the case of composites, this procedure is significantly more complicated as an explicit relationship cannot be found for all possible laminates. This section will illustrate this procedure for a unidirectional laminate. This part of the analysis is adapted from Auld [94] and Raghavan and Cesnik [45]. The analysis of GW propagation in composites begins using the equilibrium equations in displacement form for a transversely isotropic material:

$$\nabla \mathbf{c} \nabla^T \mathbf{u} = \rho \ddot{\mathbf{u}} \tag{4.1}$$

where $\mathbf{c}$ corresponds to the stiffness matrix for a transversely isotropic material, $\mathbf{u}$ corresponds to the displacement vector, ρ represents the material density, and the double dot over a variable indicates the second derivative with respect to time. In this case, the ∇ operator is defined as [45]:

$$\nabla = \begin{bmatrix} \frac{\partial}{\partial x_1} & 0 & 0 & 0 & \frac{\partial}{\partial x_3} & \frac{\partial}{\partial x_2} \\ 0 & \frac{\partial}{\partial x_2} & 0 & \frac{\partial}{\partial x_3} & 0 & \frac{\partial}{\partial x_1} \\ 0 & 0 & \frac{\partial}{\partial x_3} & \frac{\partial}{\partial x_2} & \frac{\partial}{\partial x_1} & 0 \end{bmatrix} \tag{4.2}$$

In this analysis, x_1 and x_2 represent the in-plane coordinates and x_3 corresponds to the out-of-plane coordinate. At this point a harmonic displacement wave field is assumed in the form:

$$\mathbf{u} = \mathbf{\Omega} e^{-i(\xi_1 x_1 + \xi_2 x_2 + \zeta x_3 - \omega t)} \tag{4.3}$$

where $\mathbf{\Omega}$ corresponds to a 3 x 1 vector of constants, ω represents the frequency, t corresponds to time, and ξ_1, ξ_2, and ζ correspond to the wavenumbers along the x_1-, x_2-, and x_3-directions respectively. The substitution of the assumed displacement field into the equilibrium equations yields an eigenvalue problem where the relationship between the through-thickness wavenumbers, ζ, and the in-plane wavenumbers and frequency is found. The eigenvalue problem is of the form:

$$(\mathbf{B} - \rho\omega^2 \mathbf{I})\mathbf{\Omega} = \mathbf{0} \tag{4.4}$$

where $\mathbf{I}$ represents a 3 x 3 identity matrix and the 3 x 3 matrix $\mathbf{B}$ is given as:

$$\mathbf{B} = \begin{bmatrix} c_{11}\xi_1^2 + c_{55}(\xi_2^2 + \zeta^2) & (c_{12} + c_{55})\xi_1^2\xi_2^2 & (c_{12} + c_{55})\xi_1\zeta \\ (c_{12} + c_{55})\xi_1\xi_2 & c_{55}\xi_1^2 + c_{22}\xi_2^2 + c_{44}\zeta^2 & (c_{23} + c_{44})\xi_2\zeta \\ (c_{12} + c_{55})\xi_1\zeta & (c_{23} + c_{44})\xi_2\zeta & c_{55}\xi_1^2 + c_{44}\xi_2^2 + c_{22}\zeta^2 \end{bmatrix} \tag{4.5}$$

and where c_{mn} corresponds to the elastic constants for a transversely isotropic material. The matrix given by Eq. (4.5) is generally referred to as the Christoffel matrix for anisotropic materials. By seeking non-trivial solutions to Eq. (4.4), three pairs of eigenvalues are found for ζ which correspond to quasi-longitudinal, quasi-shear, and pure shear waves. The expressions for these eigenvalues can be found in Raghavan and Cesnik [45]. These eigenvalues, along with the resulting eigenvectors, are used to expand the displacement field in the following manner:

$$\begin{aligned} \mathbf{u} = \big[& C_1^u \mathbf{e}_1^u e^{i\zeta_1 x_3} + C_2^u \mathbf{e}_2^u e^{i\zeta_2 x_3} + C_3^u \mathbf{e}_3^u e^{i\zeta_3 x_3} + \\ & + C_1^d \mathbf{e}_1^d e^{-i\zeta_1 x_3} + C_2^d \mathbf{e}_2^d e^{-i\zeta_2 x_3} + C_3^d \mathbf{e}_3^d e^{-i\zeta_3 x_3} \big] \, e^{-i(\xi_1 x_1 + \xi_2 x_2 - \omega t)} \end{aligned} \tag{4.6}$$

The terms C_k^u can be thought of as constants associated with upward traveling (through-the-thickness) waves while C_k^d are associated with downward traveling waves. The terms $\mathbf{e}_k$ for $k = 1$ to 3 correspond to the eigenvectors obtained from the solution of Eq. (4.5), and the superscripts u and d can also be associated with

upward and downward traveling waves, respectively. The specific definition of these values can be found in the work of Raghavan and Cesnik [45]. The displacement field given by Eq. (4.6) corresponds to a bulk transversely isotropic material of infinite dimensions. In order to seek Lamb-type modes in plate-like structures, the boundary conditions corresponding to free tractions on the upper and lower surface must be enforced. For brevity, only the case of a unidirectional laminate will be shown here. For this case, the origin of the coordinate system will be taken at the top surface of the plate. The displacement field can be written in the form:

$$\mathbf{u} = \begin{bmatrix} \mathbf{Q}_{11} & \mathbf{Q}_{12} \end{bmatrix} \begin{bmatrix} \mathbf{E_u} & \mathbf{0} \\ \mathbf{0} & \mathbf{E_d} \end{bmatrix} \begin{bmatrix} \mathbf{C_u} \\ \mathbf{C_d} \end{bmatrix} e^{-i(\xi_1 x_1 + \xi_2 x_2 - \omega t)} \tag{4.7}$$

where the following variables have been defined:

$$\mathbf{Q_{11}} = \begin{bmatrix} \mathbf{e}_1^u & \mathbf{e}_2^u & \mathbf{e}_3^u \end{bmatrix}; \quad \mathbf{Q_{12}} = \begin{bmatrix} \mathbf{e}_1^d & \mathbf{e}_2^d & \mathbf{e}_3^d \end{bmatrix} \tag{4.8}$$

$$\mathbf{E_u} = \begin{bmatrix} e^{i\zeta_1 x_3} & 0 & 0 \\ 0 & e^{i\zeta_2 x_3} & 0 \\ 0 & 0 & e^{i\zeta_3 x_3} \end{bmatrix}; \quad \mathbf{E_d} = \begin{bmatrix} e^{-i\zeta_1 x_3} & 0 & 0 \\ 0 & e^{-i\zeta_2 x_3} & 0 \\ 0 & 0 & e^{-i\zeta_3 x_3} \end{bmatrix} \tag{4.9}$$

The stresses in the material can be found from using a linear strain displacement relationship of the form:

$$\epsilon_{mn} = \frac{1}{2}\left(\frac{\partial u_m}{\partial x_n} + \frac{\partial u_n}{\partial x_m}\right) \tag{4.10}$$

so that the stresses with out-of-plane components can be expressed as:

$$\sigma_{\mathbf{m3}} = \mathbf{Q_{21}}\mathbf{E_u}\mathbf{C_u} + \mathbf{Q_{22}}\mathbf{E_d}\mathbf{C_d} \tag{4.11}$$

where $\mathbf{Q_{21}}$ and $\mathbf{Q_{22}}$ are matrices that depend on the wavenumbers, frequency, and material properties [45]. The traction free conditions on the upper and lower surfaces of the plate can then be enforced as:

$$\sigma_{\mathbf{m3}}(x_3 = 0) = \sigma_{\mathbf{m3}}(x_3 = h) = \mathbf{0} \tag{4.12}$$

to produce a system of equations of the following form:

$$\begin{bmatrix} \mathbf{Q_{21}} & \mathbf{Q_{22}} \\ \mathbf{Q_{21}E_u}(x_3 = h) & \mathbf{Q_{22}E_d}(x_3 = h) \end{bmatrix} \begin{bmatrix} \mathbf{C_u} \\ \mathbf{C_d} \end{bmatrix} = \mathbf{0} \tag{4.13}$$

In order to avoid obtaining exponential terms with positive real parts, the constant vector $\mathbf{C_d}$ is pre-multiplied by $\mathbf{E_u}(x_3 = h)$ and a restriction is placed on the wavenumbers ζ so that the imaginary part of each of them is always positive. This results in a system of the form:

$$\begin{bmatrix} \mathbf{Q_{21}} & \mathbf{Q_{22}E_u}(x_3 = h) \\ \mathbf{Q_{21}E_u}(x_3 = h) & \mathbf{Q_{22}} \end{bmatrix} \begin{bmatrix} \mathbf{C_u} \\ \mathbf{C_d^*} \end{bmatrix} = \mathbf{G} \begin{bmatrix} \mathbf{C_u} \\ \mathbf{C_d^*} \end{bmatrix} = \mathbf{0} \tag{4.14}$$

from which the in-plane wavenumbers ξ_1 and ξ_2 can be found by imposing the condition:

$$\det \mathbf{G} = 0 \tag{4.15}$$

This procedure is implemented by using a transformation between Cartesian and polar wavenumbers (ξ and ϕ) of the form $\xi_1 = \xi \cos\phi$ and $\xi_2 = \xi \sin\phi$. In contrast to the isotropic case, the solution of Eq. (4.15) will be a function of both the radial and azimuthal wavenumbers, which reflects the dependence of the wavenumber on azimuthal position in the plane of the plate. The procedure to determine the wavenumbers for different composite lay-ups is more complicated as interface continuity conditions must be enforced among the different layers. There are different methods to address this as, for example, the global matrix method introduced by Mal [95]. Sample slowness diagrams (inverse of phase velocity) for a unidirectional and cross-ply $[0/90]_{6S}$ laminates are shown in Fig. 4.1, where the directionality of the wave speeds can be appreciated. These results were generated using the global matrix approach implemented in the software *Disperse* originally developed at Imperial College, UK [96]. In GW propagation of composites, the slowness diagram, as opposed to the phase velocity diagram, is typically of interest as it indicates the direction in which a GW pulse will propagate. It is well known that in anisotropic materials the phase velocity vector does not generally coincide with the direction along which the energy propagates, which is determined by the group velocity vector. The direction of this vector is always normal to the phase slowness at any given angle. The experimental results presented in subsequent sections will clearly show how this phenomenon affects the propagation of inspection pulses in composite plates with

various orientations.

4.3 Experimental Procedures

This section describes the details of the experimental procedures followed in the course of this study. In particular, the material system used and the fabrication procedure employed are described. Subsequently, the laser vibrometer system used for the experimental measurements is explained and the surface preparation techniques considered to obtain consistent signal-to-noise ratio at all points on the surface of the specimens are discussed.

4.3.1 Composite Specimens

The material system used in this work consists of a unidirectional pre-impregnated composite tape with IM7 fibers and Cycom 977-3 resin from Cytec Engineered Materials [1] [97]. The tape thickness prior to cure is 0.125 mm and the fiber volume fraction is estimated to be 0.56. As one of the main drivers of the present study is the characterization of GW propagation phenomena as a function of substrate anisotropy, three different composite lay-ups are considered. The first corresponds to a 12-layer unidirectional plate which will be used as the case with the largest anisotropy. The second and third lay-ups correspond to a 12-layer cross-ply $[0/90]_{6S}$ and a 16-layer quasi-isotropic $[0/45/\text{-}45/90]_{4S}$ plate which are chosen as they are representative of configurations used in practice.

The composite plate specimens used were fabricated in-house following the fabrication procedure and cure cycle specified by the manufacturer [97]. In particular, individual layers were placed on a supporting metallic base plate and aligned according to the desired lay-up. Once this process was completed, a second metallic plate was placed on top of the composite layers to ensure a uniform pressure distribution on the surface of the material. Both plates were coated in advance with three to five layers of release agent to prevent the cured composite from permanently attaching to the metallic surface. The entire assembly was covered in a vacuum bag and cured in an autoclave at a pressure of 621 kPa (90 psi) and a temperature of 177° C (350° F) for six hours. In addition, a vacuum of -25 in Hg was maintained while heating and released once the final curing temperature had been reached. The resulting plates had a square in-plane geometry with a side length of 0.5 m. The unidirectional and cross-

[1] Cytec Industries - Engineered Materials, 5 Garret Mountain Plaza, Woodland Park, New Jersey 07424, Phone: 973-357-3100

ply plates had a post-cured thickness of 1.5 mm, while the quasi-isotropic specimens had a thickness of 2.0 mm. The material properties of the composite are necessary to generate phase and group velocity diagrams. The mechanical properties provided by the manufacturer were used as a starting point in the analysis, and the values for the modulus along and transverse to the fiber direction were refined with the results obtained through mechanical tests on unidirectional coupon specimens. In addition, it was found that the value of G_{12} indicated by the manufacturer resulted in over-predicted wave velocities (by as much as 30%). Consequently, its value was reduced to obtain better agreement with the finite element results. The material properties used in the present study are summarized in Table 4.1.

4.3.2 Laser Vibrometer

The key instrument used in these studies was a Polytec PSV-400 scanning laser vibrometer described in detail in Chapter III. In order to obtain consistent measurements using laser vibrometry, the surface under inspection must have an adequate finish so as to optimize the laser visibility. During initial tests it was found that it was, in general, possible to measure GW signals with high signal to noise ratios without any preparation on the surface of the composite. However, very small differences in the surface finish from point to point caused the amplitudes and signal to noise ratios to vary significantly, thereby introducing artificial variations in the measured results. Several surface preparation techniques were tested to resolve this problem including sanding and painting the surface using white spray paint, coloring the surface using metallic ink markers, applying retro-reflective glass beads on the surface, and using permanently bonded retro-reflective tape. The first two options did not provide a satisfactory solution to the problem as they were unable to remove minute (less than one mm) thickness variations on the surface of the specimens. The retro-reflective glass beads were obtained from the laser manufacturer and were found to significantly enhance the visibility of the laser at non-cooperative points. However, their uniform application on the surface proved problematic thereby preventing parts of the surface from being fixed. In addition, it was observed that non-uniformities in the thickness of the layer of glass beads applied influenced the amplitude of the signals measured. The retro-reflective tape was found to be the best option to resolve the non-cooperative points problem. This tape ($\sim$ 100 microns in thickness) is specifically designed with the appropriate surface reflectivity and roughness to optimize the visibility of the laser vibrometer. In order to verify that the presence of the tape did not introduce unwanted effects into the propagating GW field, the measured wave

velocities were compared before and after the application of the tape for one of the experimental specimens. This result summarized in Fig. 4.2 shows that the presence of the tape does not influence the GW field at cooperative points.

4.4 GW Excitation by Piezoelectric Wafers in Composite Plates

Piezoelectric wafers are the most commonly used transduction devices for GW SHM of both metallic and composite structures, and their GW excitation properties in various composite lay-ups are explored in this section. The main objective is to characterize the GW field induced by a single circular piezoelectric wafer in terms of the azimuthal distribution of the induced wave velocity and amplitude on the surface of the specimens through a combination of laser vibrometry and finite element analysis. These results are complemented with full field visualizations of the radiation patterns which provide important insight into the GW excitation of these devices. At the same time, the axisymmetric nature of the source will provide the necessary wave speed distribution that will be needed for future damage detection experiments. At this point it should be mentioned that previous researchers have argued the transducer bending modes prevent circular wafers from being true axisymmetric sources [37]. While the mechanical deformations of any transduction mechanisms are likely to influence the excited GW field, these effects should not be dominant if excited away from its natural frequencies. Moreover, within the realm of piezoelectric-based devices, circular wafers provide the largest attainable axisymmetry. Finally, previous theoretical and experimental studies have shown that for the range of frequencies and devices used in this study, piezoelectric wafers can be safely considered as axisymmetric sources [43].

4.4.1 Experimental Setup and Data Processing

The azimuthal distribution of wave speed and amplitude was obtained as a function of position for several specimens with the three layups under consideration. The scanning grids defined in the laser vibrometer system were composed of four circles located between four and seven centimeters from the origin of the coordinate system (taken to be at the center of the transducer) in intervals of one centimeter, in order to assess the evolution of the speed and amplitude distribution with propagation distance. A total of 120 azimuthal points were used in each grid to provide sufficient resolution of the waves. The values reported correspond to the average of 40 mea-

surements. A schematic of the transducer and laser scan point configuration used in these studies is shown in Fig. 4.3.

The transducer used in this part of the study was a circular piezoelectric wafer, with a diameter of 12.7 mm and a thickness (h) of 0.2 mm, bonded at the geometric center of the composite plates. In order to insulate the piezoceramic from the composite material, and to provide access to its top and bottom electrodes, two pieces of copper-clad kapton were bonded on its top and bottom surfaces using Loctite E-120HP adhesive system, which was also employed to bond the insulated transducer onto the surface of the composite plate. In order to ensure uniform bonding conditions among all specimens, the cure of the adhesive between the transducer and the plates was performed in an autoclave at a temperature of 80° C and a pressure of 345 kPa (50 psi) for 45 minutes. The excitation input used in all cases throughout this study was a 3.5 Hann-modulated toneburst signal with a center frequency of 75 kHz resulting predominantly in the excitation of the fundamental antisymmetric mode, but also exciting out-of-plane components of additional shear modes in some of the plates.

Due to the anisotropy of the composite substrate, it is possible that multiple modes will contribute to the out of plane velocities at frequencies where only one mode is observed in the isotropic case. As a result, in order to identify each propagating mode the Hilbert transform of the obtained time-domain signals was calculated. This transform takes a real time-domain signal and generates its complex conjugate, such that upon calculation of its absolute value, an envelope of the signal amplitude is obtained. A sample time-domain signal with the amplitude of its corresponding Hilbert transform is shown in Fig. 4.4. This method is successful in separating modes traveling at different speeds if a sufficient time difference exists among them. In order to identify the wave speeds, the Hilbert envelope of the signals was passed through a peak-finding algorithm which recorded the value of each peak as well as the times of arrival. The peaks in the Hilbert envelope correspond to the center of the propagating wave packets. The actual wave speed, c_g, was found through Eq. (4.16) by using the location of the measurement point, r, and assuming that the source of the waves occur at the edge of the transducer, R_p. Finally, the time of arrival must be adjusted to compensate for one half the period of the excitation pulse as the point being tracked in the signal corresponds to the center of the wave packet. The period of the signal can be found from the number of half-cycles, n, and the center frequency of excitation, f_0.

$$c_g = \frac{r - R_p}{t_{peak} - \frac{n}{2f_0}} \tag{4.16}$$

While the presence of the retro-reflective tape resulted in signals with high signal to noise ratios, the peak finding algorithm was still sensitive to small variations in the amplitudes of the time-domain signal thereby identifying artificial peaks, as shown in Fig. 4.4(b) . In order to resolve this, the Hilbert envelope signals were passed through a signal smoothing algorithm where these features were attenuated, while preserving the features associated with the propagating modes. This choice was selected instead of filtering as the latter results in the introduction of a time delay which affects the value of the measured wave velocity.

4.4.2 Finite Element Simulations

A set of finite element simulations was conducted to qualitatively verify several of the results obtained from laser vibrometry. The material properties in Table 4.1 were used in this analysis. Due to the geometry of the transducer employed, a combination of wedge-shaped three-dimensional brick (C3D8) and tetrahedron elements (C3D6) were used in the commercial solver ABAQUS 6.8 [63]. The combination of in-plane dimensions of the elements and time step were selected so as to resolve the fastest traveling wave speed in the material, which typically corresponds to the dilatational wave speed along the fiber direction. In particular, the radial dimension of the elements was selected at 0.25 mm while the azimuthal dimension used was one degree. This radial dimension provided approximately 15 nodes along the smallest wavelength, which was obtained normal to the fiber direction. Similarly, the time step was selected as 10^{-7} s which also provided sufficient resolution of the excitation input.

In the case of the unidirectional plate, only one eighth of the plate was modeled due to in-plane and through-the-thickness symmetry conditions. In particular, antisymmetric conditions were enforced through the thickness to capture only antisymmetric modes. A similar analysis was followed for the cross-ply plate. Initial convergence studies indicated that using six elements through the thickness of the unidirectional plate provided converged results for the wave speed normal to the fiber direction. Similarly, the rate of change of the speed normal to the fiber direction with increasing elements was nearly constant indicating that convergence had almost being reached. Consequently, this number of elements was selected for the unidirectional plate. In the case of the cross-ply plate, two elements were used per layer in the

laminate resulting in 12 elements through the thickness of the model. Note that no effective properties were used in the analysis as the engineering constant properties were defined for each material along with the corresponding orientations. Furthermore, no damping was considered in the numerical simulations. This is a simplifying assumption as it is well known that the cured matrix exhibits viscoelastic material behavior. The effect of the transducer on the substrate was represented as shear tractions of equal magnitude applied on the surface of the substrate in the radial direction. An implicit dynamic analysis was conducted in ABAQUS [63] to ensure the stability of the solution with the parameters indicated above.

4.4.3 Results and Discussion

The results for the wave speed distribution in the unidirectional plate are shown in Fig. 4.5(a) in the form of polar plots, where the wave speed is represented by the radial distance from the origin to each point. A comparison between the experimental and numerical results is also provided in the figure. The fiber direction coincides with the 0-degree direction in the figure. Clearly, the largest wave velocity is observed along the fiber direction for the antisymmetric mode which reduces to approximately half of its value along the direction normal to the fibers. Note also that a second mode is present in the result, which corresponds to the out-of-plane component of a horizontally polarized quasi-shear wave. Note that this coupled mode is not observed along the fiber direction, which corresponds to a principal material direction. The agreement between the numerical simulations and the experimental results is satisfactory along certain azimuthal directions. In particular, the speed of both modes is adequately captured for an azimuthal span of approximately 60 degrees center along 90-degree direction.

A similar result for the distribution of peak-to-peak amplitude is presented in Fig. 4.5(b), where it can be observed that the largest amplitudes occur along the fiber direction. The waves propagating along the normal direction are significantly weaker in comparison (smaller by a factor of approximately eight). The results are normalized by the maximum in each field for easier comparison. The agreement of the amplitude distribution between the experimental and numerical results is acceptable, and the simulations confirm that the largest amplitudes are in fact observed along the fiber direction. Note that this has important implications for GW-based inspection as any damage features present along the 90-degree direction, which in this type of laminate is the one most susceptible to damage, will likely be overshadowed by the large amplitude of the waves along the fiber direction. The results also show that the

directionality observed for the wave speed is maintained as the waves propagate away from the source.

The agreement between the finite element and experimental results for the peak-to-peak amplitude distribution provides important insight into the nature of the wave steering phenomenon observed in composites. Previous researchers have shown that the traction exerted by the transducer on the substrate depends on the stiffness-thickness product ratio between the transducer and the substrate. Due to the anisotropy of the composite, this ratio varies along the in-plane azimuthal direction changing the strain transfer effectiveness of the transducer. Therefore, the directionality of the induced wave field could be partly attributed to the changing stiffness ratio. The finite element simulations remove this stiffness ratio variation by applying shear tractions of equal magnitude along the circumference of the transducer. In other words, the modeling approach is such that the piezoelectric element effectively acts on an isotropic substrate. The directionality observed, therefore, indicates that the varying stiffness ratio has a minor effect on the GW field excited. Instead, the steering phenomenon is the dominant factor as waves generated normal to the fiber direction concentrate their energy along the stiffer fiber direction [98, 99]. A two-dimensional view of these phenomena is shown in Fig. 4.5(c)-(d) which shows the radiation pattern of the induced GW field on the surface of the unidirectional plate at different time instants. The piezoelectric wafer used as the source is represented as the light blue circle placed at the origin. Note that, as expected, the wavelength along the zero degree direction is larger than that along the 90-degree direction as a result of the larger wave speed.

A similar result for the wave velocity distribution is shown in Fig. 4.6(a) for the cross-ply $[0/90]_{6S}$ plates. Note that in this case only one mode is identified using the laser vibrometer, and that the directionality of the wave speed is significantly smaller than for the unidirectional plate. Close examination of the distribution shows that the largest speeds along and normal to the fiber direction (a small difference in the order of 1% was observed between both directions with the larger value along the fiber direction of the top layer), while the lowest speed is observed along the 45-degree direction (the difference is approximately 10%). These observations are consistent with the distribution of moduli in the plane of the specimen which has a minimum along the 45-degree direction. Note that there is good qualitative agreement between the laser and numerical results, but the simulations over-predict at certain azimuthal locations. The maximum error, however, is in the order of 10%.

The peak-to-peak amplitude distribution is shown in Fig. 4.6(b) where, as in the previous case, both results have been normalized by their maximum value. The

result shows that the largest amplitude occurs along the fiber direction of the top layer, being 20% larger than that observed normal to the fiber direction of the top layer. This indicates that the orientation of the surface on which the transducer is bonded is not likely to bias the group velocity distribution, but will have a small effect on the distribution of peak-to-peak amplitude which would in turn be related to the maximum inspection distance attainable. Note that in the case of the cross-ply, the zero- and ninety-degree directions are effectively similar in terms of the steering expected when the entire laminate is considered (as determined by the slowness curve). However, the strong directionality of the top layer towards its fiber direction appears to influence the wave amplitude in a similar manner as the unidirectional plate. This therefore results in a small (20%) increase in amplitude along the fiber direction. The directionality of the radiation pattern for this composite layup can be observed in Fig. 4.6(c)-(d) for different time instants. Once again, note that the pattern is not as directional as that observed for the unidirectional plate [98, 99].

The results for the quasi-isotropic $[0/+45/\text{-}45/90]_{4S}$ plate are shown in Fig. 4.7(a). In this case, no finite element simulations were conducted due to the large computational cost. As in the case of the cross-ply plate, only one mode is observed. Note that the wave velocity distribution shows some degree of directionality, and that no in-plane symmetries are observed. This observation is a result of the configuration of the substrate which provides no in-plane symmetries. Note that the largest speeds are observed near the fiber direction, as expected. The peak-to-peak amplitude is shown in Fig. 4.7(b). Note that the pattern does not display strong directionality, and that the amplitudes along the 0- and 90-degree directions are nearly equal. The radiation pattern is shown in Fig. 4.7(c)-(d) which again shows a very mild degree of directionality and highlights the lack of symmetry along the 0- and 90-degree directions. Note that this propagation pattern is the closest to that observed in isotropic plates when excited by axisymmetric sources.

4.5 GW Excitation by CLoVER Transducers in Composite Plates

4.5.1 The CLoVER Transducer

The CLoVER transducers used in this study were fabricated in-house following the manufacturing procedure presented earlier by the authors [28, 65] and reported in Chapter III. Two different electrode designs, referred to as CLoVER 1 and CLoVER

2, were employed and are illustrated in Fig. 4.8. The electrode design in CLoVER 1 yielded devices with an azimuthal span of 45 degrees, an inner radius of 10 mm, and outer radius of 25 mm. Each sector in this array had a segment with an active radius of 5 mm and a second one with an active radius of 10 mm, as shown in Fig. 4.8(a). In the experiments that use this device, the active segment with a radial dimension of 10 mm was employed. The electrode design in CLoVER 2 yielded devices with an azimuthal span of 22.5 degrees, an inner radius of 17.5 mm and an outer radius of 25 mm. In this case, the active sectors were also divided into two radial segments with active radii of 2.5 mm and 5 mm, respectively. Similar to the case of CLoVER 1, only the active segment with a radial dimension of 5 mm was used in this study. In both cases, the electrode fingers had a width of 0.1 mm and an interdigital finger spacing of 0.5 mm. The electrode patterns were transferred onto a copper-clad kapton film (Pyralux LF7062R) by using a transparency mask and following a standard photolithography process at the Lurie Nanofabrication Facility at the University of Michigan. The final electrodes were obtained by wet etching of the copper in the resulting films. The piezoceramic material employed was PZT-5A which was obtained in rings with inner and outer radii consistent with the electrode designs described previously. These rings were diced into radial fibers with a cut angle of two degrees for CLoVER 1 and one degree for CLoVER 2. These angles were chosen so that the width of the fibers at the inner radius position is similar to that used in the prismatic rectangular fibers used in conventional piezoceramic devices [11, 65]. The cure of the device was conducted following a procedure similar to the one described previously by the authors [28, 65]. The poling of the finalized transducers was conducted at a temperature of 50° C and an electric field of 2.92 kV/mm for 30 minutes.

4.5.2 Experimental results

Through the baseline measurements using piezoelectric wafers, the wave velocities corresponding to the fundamental antisymmetric mode were calculated for each composite layup under consideration. Therefore, the characterization of the GW field induced by the CLoVER sectors was conducted based on full field visualizations of the GW radiation pattern induced by each device. The results presented in this section clearly show the steering phenomenon characteristic of GW propagation in anisotropic materials.

The unidirectional plate used in this study was instrumented with a CLoVER transducer fabricated with the electrode design defined as CLoVER 1. Therefore, three sectors with an azimuthal span of 45 degrees each were used to cover only one

quarter of the plate due to material in-plane symmetries. The measurement grid used in the laser vibrometer system consisted of 32 circles, each with 80 azimuthal points, centered at the origin of the CLoVER array. The spacing between consecutive circles was selected at two millimeters which was expected to sufficiently resolve the minimum wavelength of the antisymmetric mode at 75 kHz ($\sim$ 9 mm) in the unidirectional plate, which occurs normal to the fiber direction. Note that this also corresponds to the smallest wavelength in all the specimens tested as the normal to the fiber direction in the unidirectional plate has the lowest phase velocity. A total of four averages were taken at each measurement point. In addition, as no wave velocity information was necessary, the resulting time-domain data were passed through a third order band-pass Butterworth filter. Its limits were selected as 0.7 and 1.3 times the center frequency.

Figure 4.9 shows the GW field excited by a sector aligned with the fiber direction. Note that the CLoVER transducer has been included in the figure, where the active sector has been highlighted. Note that in this case there is no steering present. This is consistent with the phase slowness diagram which is nearly constant with azimuthal position along the fiber direction, and the phase of the waves is aligned with the fiber direction (the phase of the waves connects the origin with the centerline of the active CLoVER sector), as shown in Fig. 4.9(a). Therefore, all waves launched in this region will tend to propagate strictly along the fiber direction.

A similar result for the sector aligned with the 45-degree direction is shown in Fig. 4.10. Note that in this case the steering phenomenon is clearly visible, and can be explained by considering the phase slowness diagram shown in Fig. 4.10(a). Along the 45-degree direction, the normal vector to the slowness surface points nearly along the horizontal direction indicating that this is the direction in which the wave packet will propagate. However, the phase of the waves is now parallel to the 45-degree direction so that relative to the phase of the wave its propagation direction is steered.

Finally, the radiation pattern obtained when the sector aligned with the 90-degree direction is used is shown in Fig. 4.11. Note that along this direction, the phase slowness diagram is also nearly constant with azimuthal position. However, its radius of curvature is significantly larger indicating that as the waves propagate away from the source, there will be a tendency to steer towards the fiber direction. This behavior is observed in the experimental results as the directionality of the propagating pulse is not as strong as it is along the 90-degree direction. The directionality of the GW field obtained with the CLoVER transducer along this direction is an improvement over that obtained using conventional wafers, as seen in Fig. 4.5(c)-(d), as it allows

for damage interrogation specifically along this direction. The larger attenuation observed transverse to the fiber direction in Fig. 4.5(c)-(d) also occurs in this case. Moreover, the directionality of the inspection pulse is likely to increase the coherent signal to noise ratio of the reflections from any damage identified along this direction.

The cross-ply plate was instrumented with a CLoVER transducer fabricated with the electrode pattern previously defined as CLoVER 2. In this case, due to in-plane symmetries only five of the 16 sectors available were employed for the characterization studies. A similar scanning grid as in the case of the unidirectional plate was used in this case with similar radial and azimuthal steps. The results are shown in Figs. 4.12 through 4.16. Figure 4.12 shows the GW propagation pattern observed when sector 1, aligned with the horizontal direction, is used. As expected from the phase slowness diagram shown in Fig. 4.12(a), there is no steering in this case as the phase and the group velocity vectors are parallel. The induced GW field therefore is highly directional and propagating along the fiber direction. Figure 4.13 shows similar results when CLoVER sector 2 is activated. From the phase slowness diagram shown in Fig. 4.13 it can be seen that the group velocity will be steered towards the fiber direction relative to the phase velocity vector. This behavior is evident in Figs. 4.13(b)-(d) where the pulse propagates primarily towards the horizontal direction. Figure 4.14 shows the propagation pattern when sector 3 is activated. In this case, the normal to the phase slowness and the phase velocity vector are nearly parallel and therefore very little steering is observed. Nevertheless, it can be appreciated that a small steering angle towards the horizontal direction is also present in this case. The behavior observed when CLoVER sector 4 is used is markedly different as shown in Fig. 4.15(b)-(d). In this case, the normal to the phase slowness is nearly aligned with the vertical direction and therefore a very strong steering towards that direction is observed. Finally, when sector 5 is activated the normal to the phase slowness and the phase velocity are once again aligned and therefore the wave packet propagates directionally along the direction in which it was launched as can be seen in Fig. 4.16.

Sample results are shown for the quasi-isotropic plate in Fig. 4.17. In this case, the steering phenomenon is also present, but the results presented highlight the fact that for this composite configuration there are local regions where the waves propagate as if the substrate were an isotropic material. Note for instance that when CLoVER sector 4 (Fig. 4.17(c))is activated the propagating pattern is quite directional and stays within the bounds of the active CLoVER sector. This can be explained by the accompanying phase slowness diagram which shows that in that region, the curve is nearly circular and therefore no steering will occur.

4.6 Concluding Remarks

This chapter explored the GW excitation characteristics of various piezoelectric transducers in composite plates. The central factor in these studies is the GW energy steering produced by the stiffness directionality of the substrate. A brief theoretical background was provided to highlight the origin of the steering effect in anisotropic media using a unidirectional composite as an example. The GW excitation properties of piezoelectric wafers were subsequently analyzed in a systematic manner, using unidirectional, cross-ply $[0/90]_{6S}$, and quasi-isotropic $[0/45/\text{-}45/90]_{4S}$ laminates. The GW fields induced showed various levels of directionality under axisymmetric sources due to the anisotropy of the composite material. The directionality was shown to result from the energy steering, and the varying stiffness ratio between the transducer and substrate was observed to have a negligible effect. The GW excitation properties of CLoVER transducers were subsequently analyzed for all three composite systems. The GW pulses emitted were observed to steer as they propagated through the structure, and their direction could be predicted through the laminate slowness diagram. The effect was most evident in the unidirectional composite, and not as dominant in the more common cross-ply and quasi-isotropic configurations. In spite of the material directionality, the GW interrogation proposed with CLoVER transducers was shown to provide adequate structural coverage. In particular, directions not attainable with piezoelectric wafers (such as normal to the fiber direction in a unidirectional laminate) can be interrogated due to the directionality of the sectors.

Property	Value
E_1 [GPa]	146.9
E_2 [GPa]	9.8
G_{12} [GPa]	3.25
G_{23} [GPa]	2.8
ν_{12} [GPa]	0.27
ρ [kg/m^3]	1558

Table 4.1: Material properties for IM7/Cycom 977-3 composite.

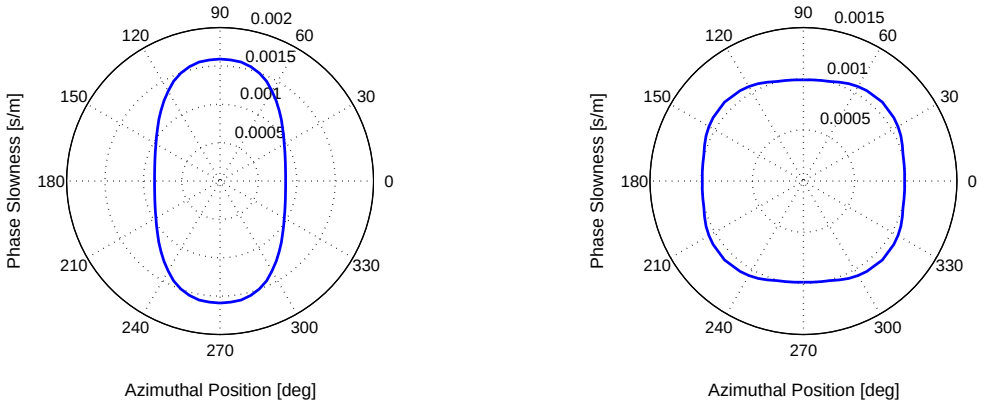

(a) **(b)**

Figure 4.1: Phase slowness diagrams for A_0 mode for **(a)** 12-layer unidirectional plate and **(b)** 12-layer cross-ply $[0/90]_{6S}$ plate at 75 kHz.

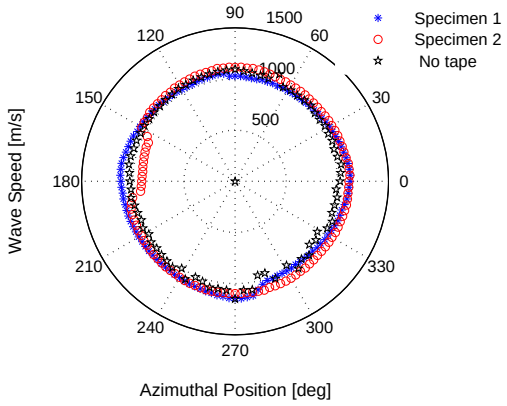

Figure 4.2: Comparison of GW speed measured with and without retro-reflective tape on the surface of a cross-ply $[0/90]_{6S}$ laminate.

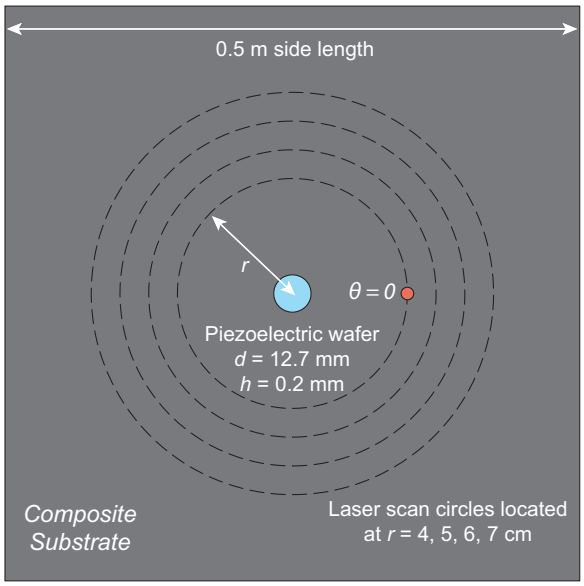

Figure 4.3: Schematic illustrating the scanning grid used with the laser vibrometer to determine the azimuthal variation of wave speed and peak-to-peak amplitude.

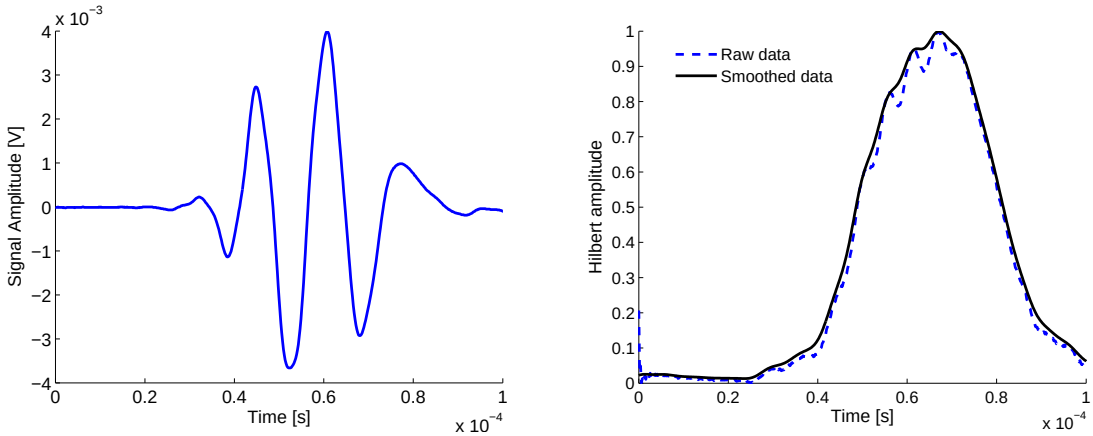

(a) **(b)**

Figure 4.4: **(a)** Typical time-domain signal collected through laser vibrometer; **(b)** Hilbert amplitude of the time domain signal both before and after smoothing is applied.

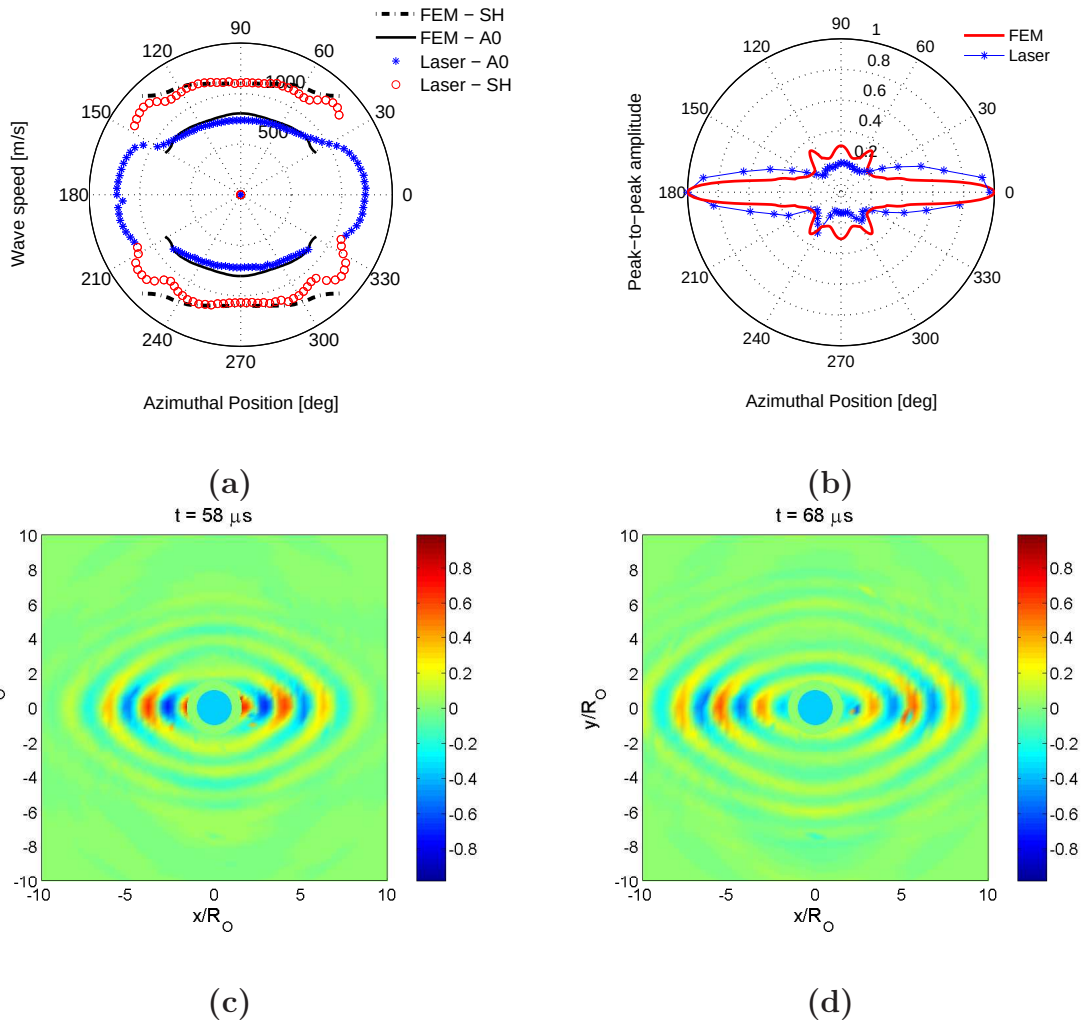

Figure 4.5: **(a)** Azimuthal distribution of wave velocity for a 12-layer unidirectional plate at 75 kHz; **(b)** Azimuthal distribution of peak-to-peak amplitude in a 12-layer unidirectional plate at 75 kHz; Full field visualization of GW excited by a circular piezoelectric wafer in a unidirectional plate at **(c)** 58 μs **(d)** 68 μs as measured using laser vibrometry.

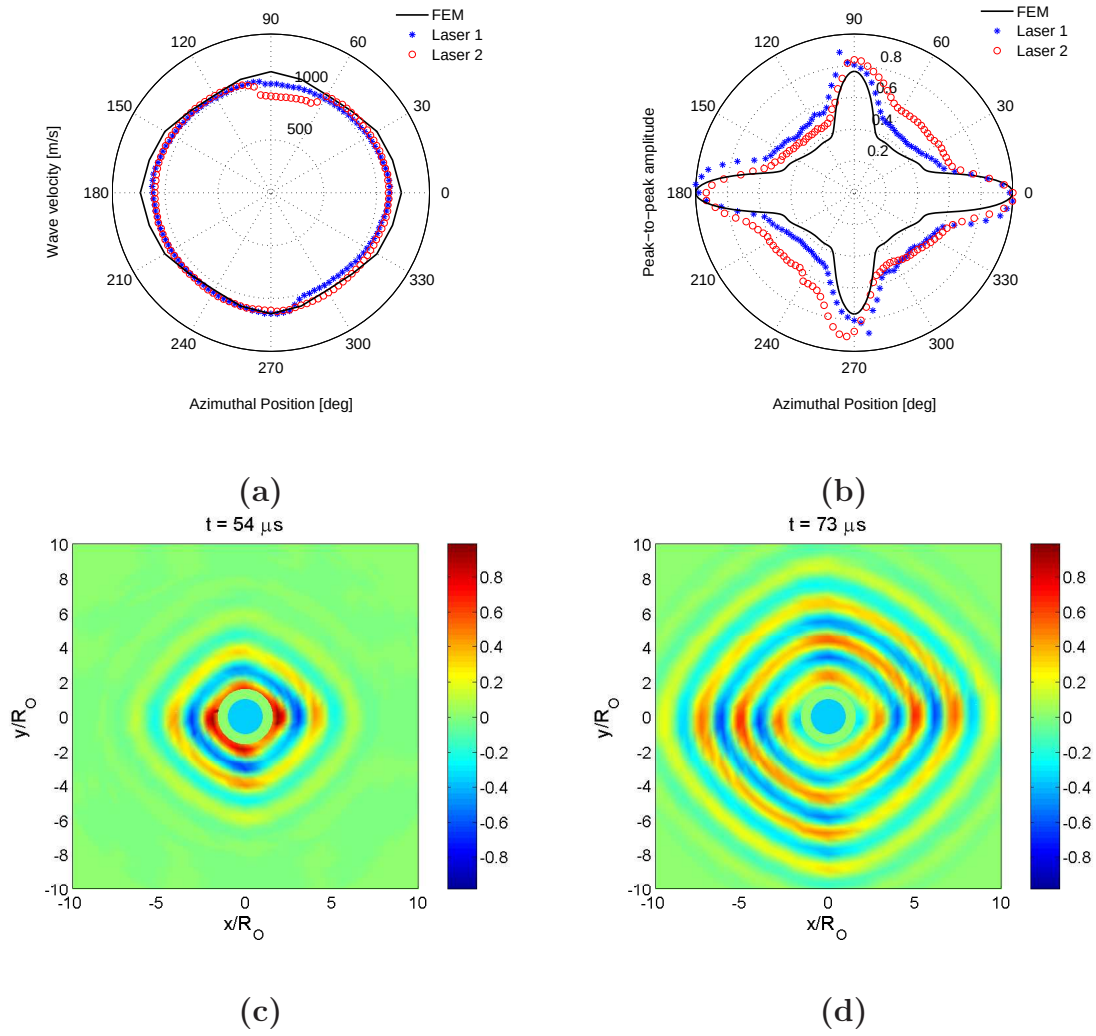

Figure 4.6: **(a)** Azimuthal distribution of wave velocity for a cross-ply $[0/90]_{6S}$ plate at 75 kHz; **(b)** Azimuthal distribution of peak-to-peak amplitude in cross-ply $[0/90]_{6S}$ plate at 75 kHz; Full field visualization of GW excited by a circular piezoelectric wafer in a cross-ply $[0/90]_{6S}$ plate at **(c)** 54 μs **(d)** 73 μs as measured through laser vibrometry.

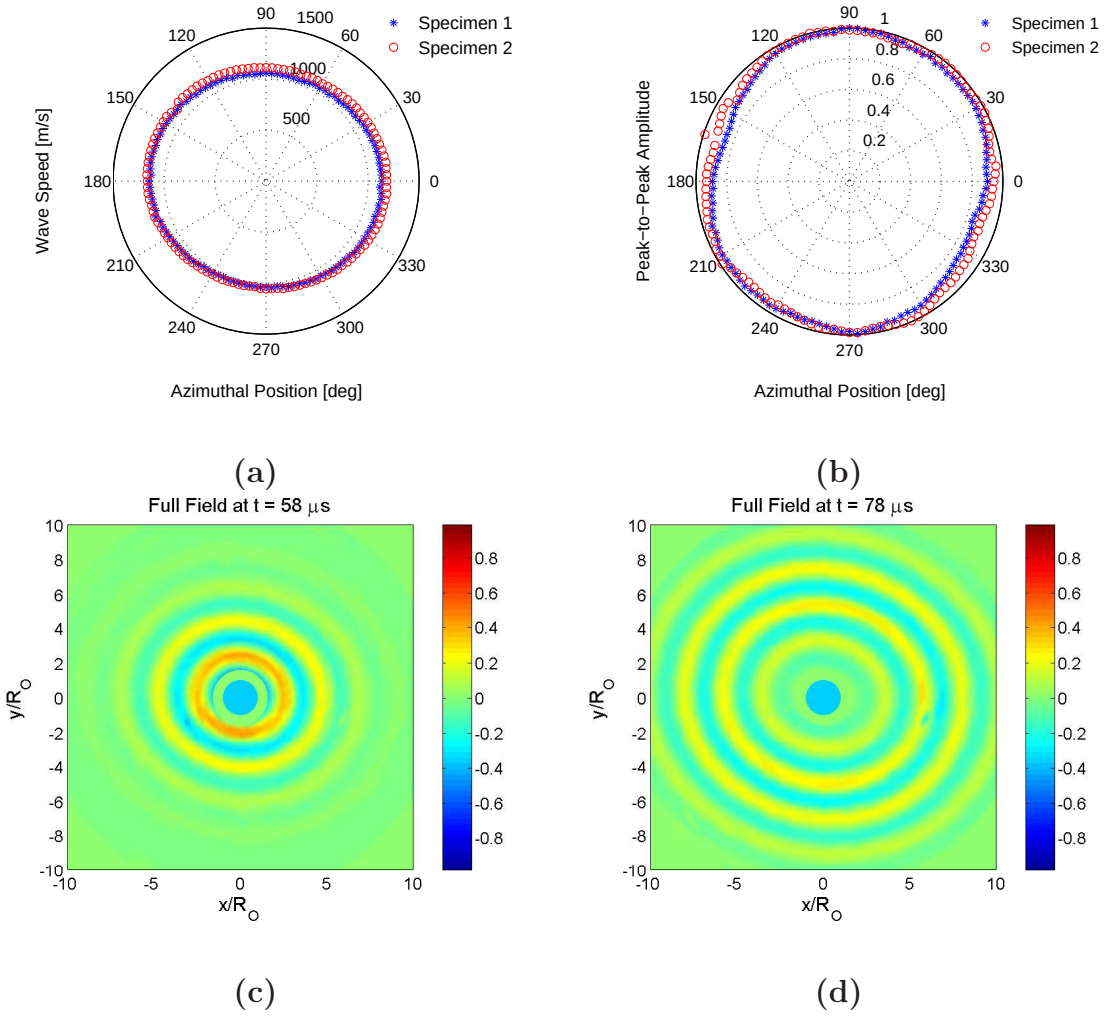

Figure 4.7: Azimuthal distribution of **(a)** wave velocity and **(b)** peak-to-peak amplitude in quasi-isotropic $[0/45/\text{-}45/90]_{4S}$ plates; Full field visualization of GW excited by a circular piezoelectric wafer in a quasi-isotropic $[0/45/\text{-}45/90]_{4S}$ plate at **(c)** 58 μs **(d)** 78 μs as measured using laser vibrometry.

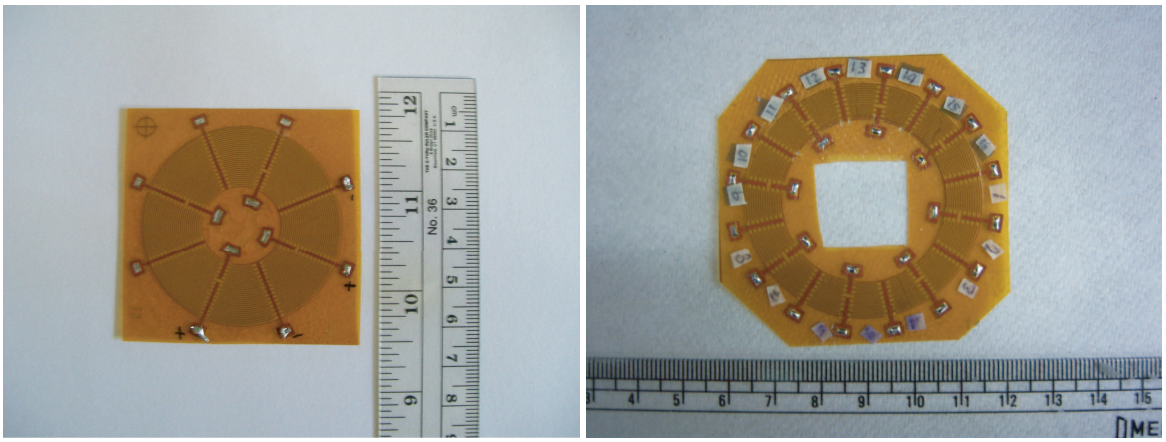

(a) **(b)**

Figure 4.8: CLoVER transducer designs used in the present study **(a)** CLoVER 1 and **(b)** CLoVER 2.

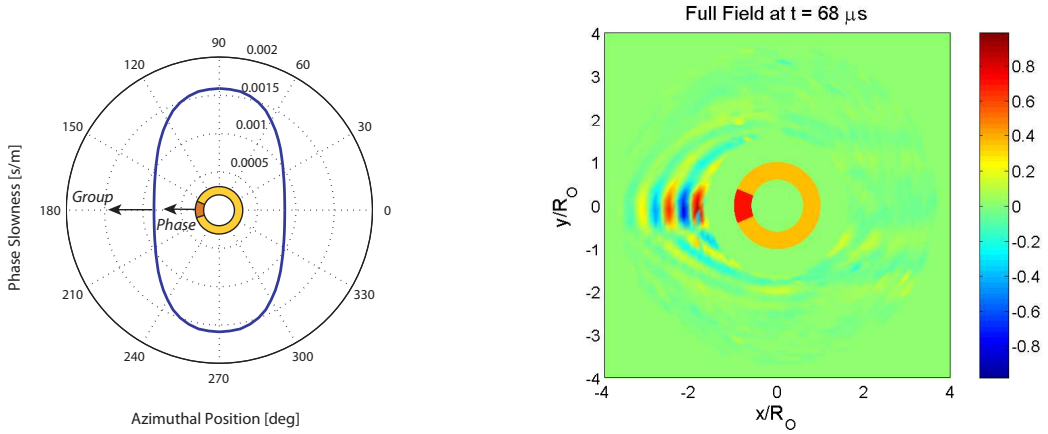

(a) **(b)**

Figure 4.9: **(a)** Steering expected when using a CLoVER sector aligned with the fiber direction in a unidirectional plate based on its phase slowness diagram; **(b)** Surface radiation at 68 μs.

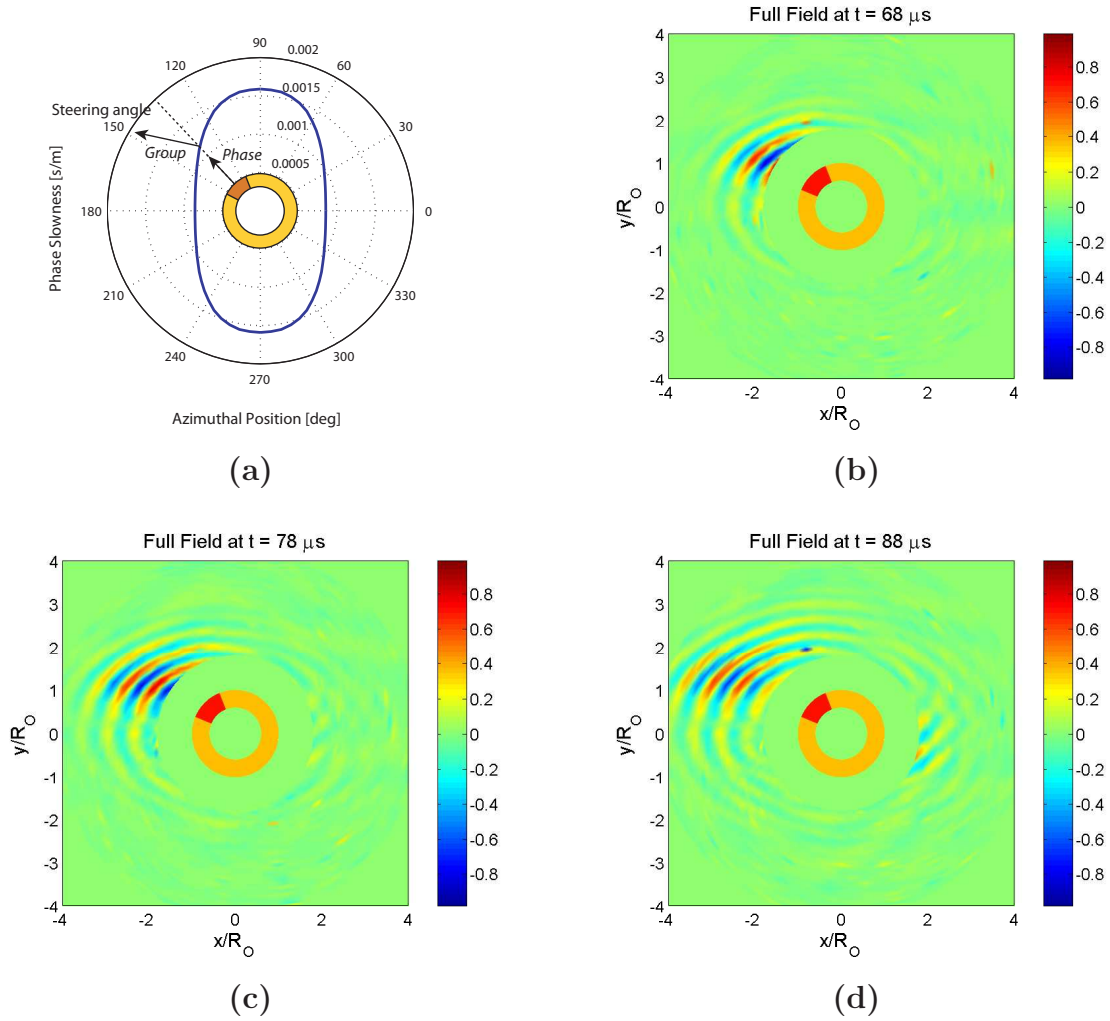

Figure 4.10: **(a)** Steering expected when using a CLoVER sector aligned 45 degrees from the fiber direction in a unidirectional plate based on its phase slowness diagram; Surface radiation at **(b)** 68 μs; **(c)** 78 μs; **(d)** 88 μs.

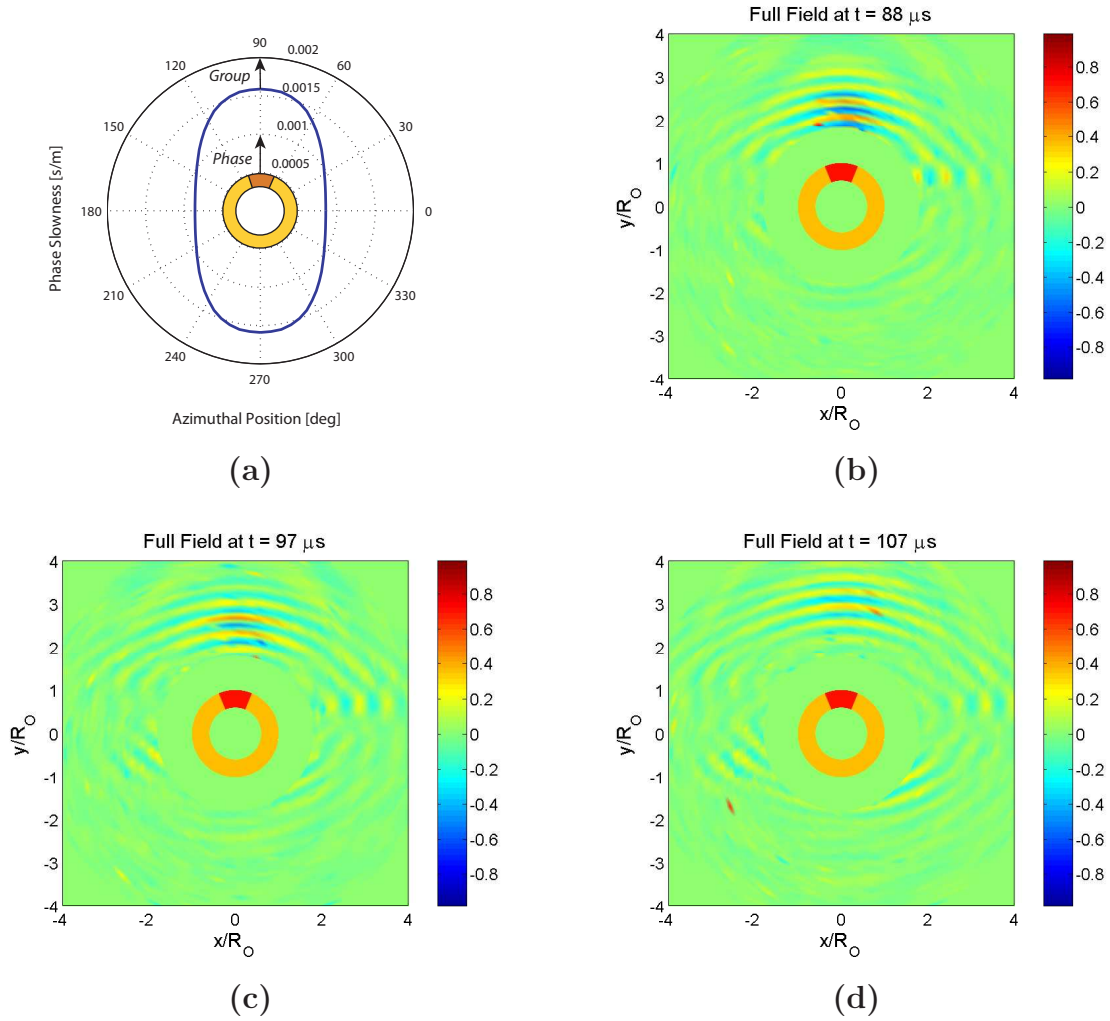

Figure 4.11: **(a)** Steering expected when using a CLoVER sector aligned 90 degrees from the fiber direction in a unidirectional plate based on its phase slowness diagram; Surface radiation at **(b)** 88 μs; **(c)** 97 μs; **(d)** 107 μs.

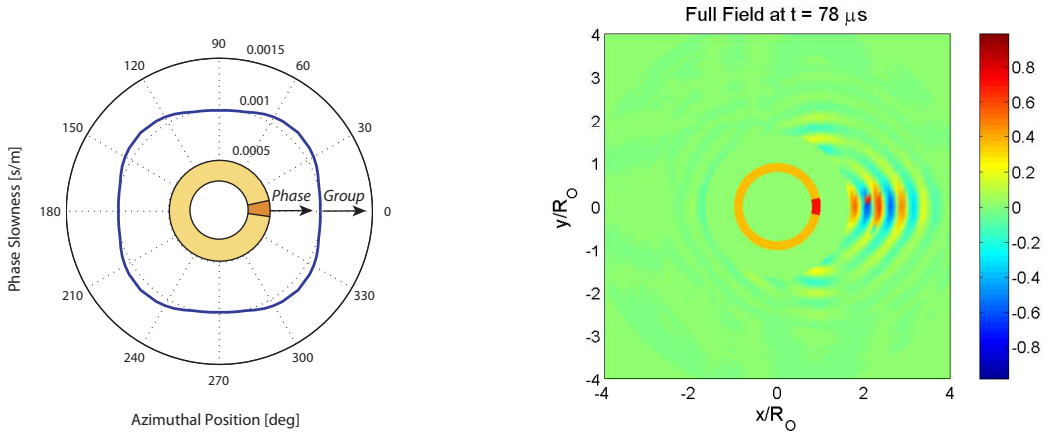

(a) **(b)**

Figure 4.12: **(a)** Steering expected when using a CLoVER sector along the fiber direction in a cross-ply plate based on its phase slowness diagram; **(b)** Surface radiation at 78 μs.

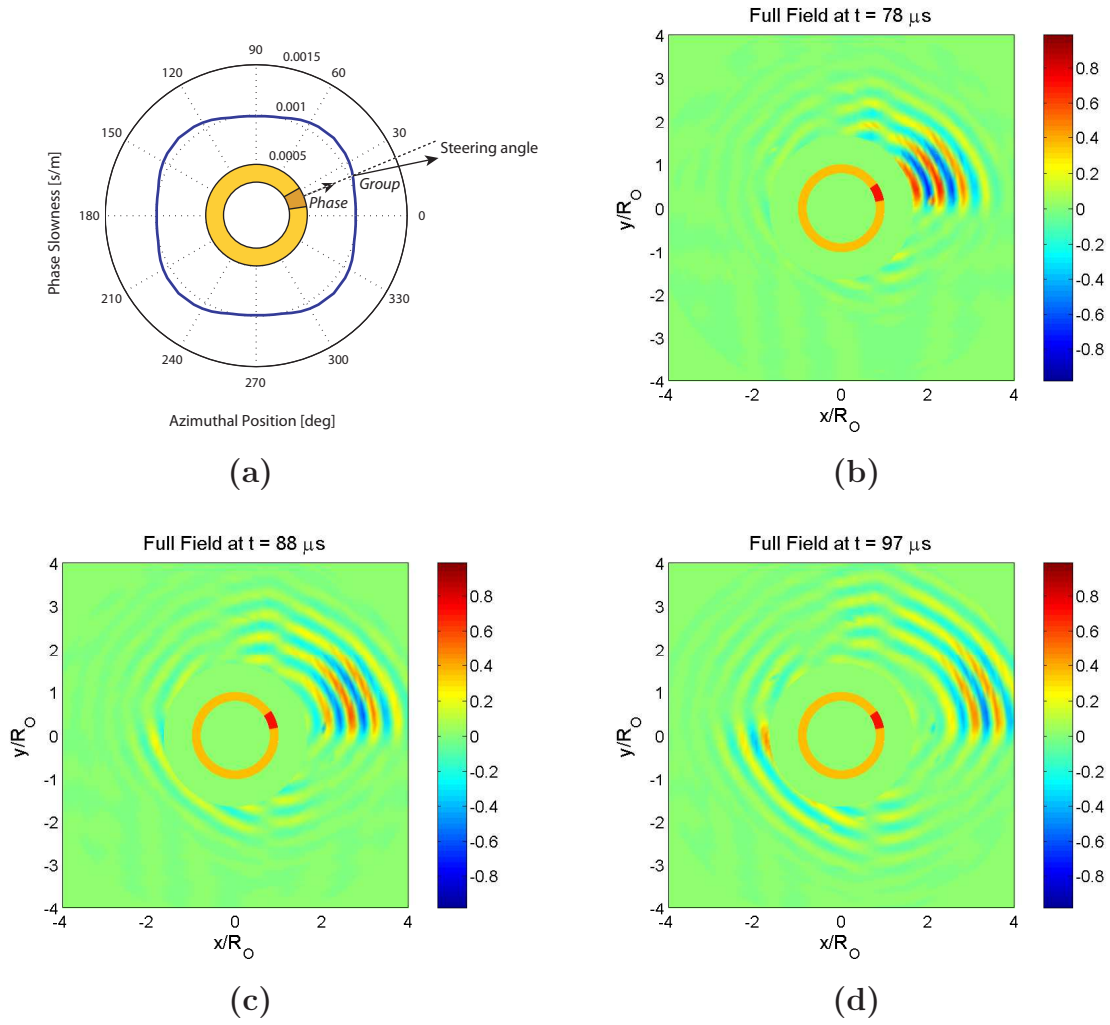

Figure 4.13: **(a)** Steering expected when using a CLoVER sector aligned 22.5 degrees (counterclockwise) from the fiber direction in a cross-ply plate based on its phase slowness diagram; Surface radiation at **(b)** 78 μs; **(c)** 88 μs; **(d)** 97 μs.

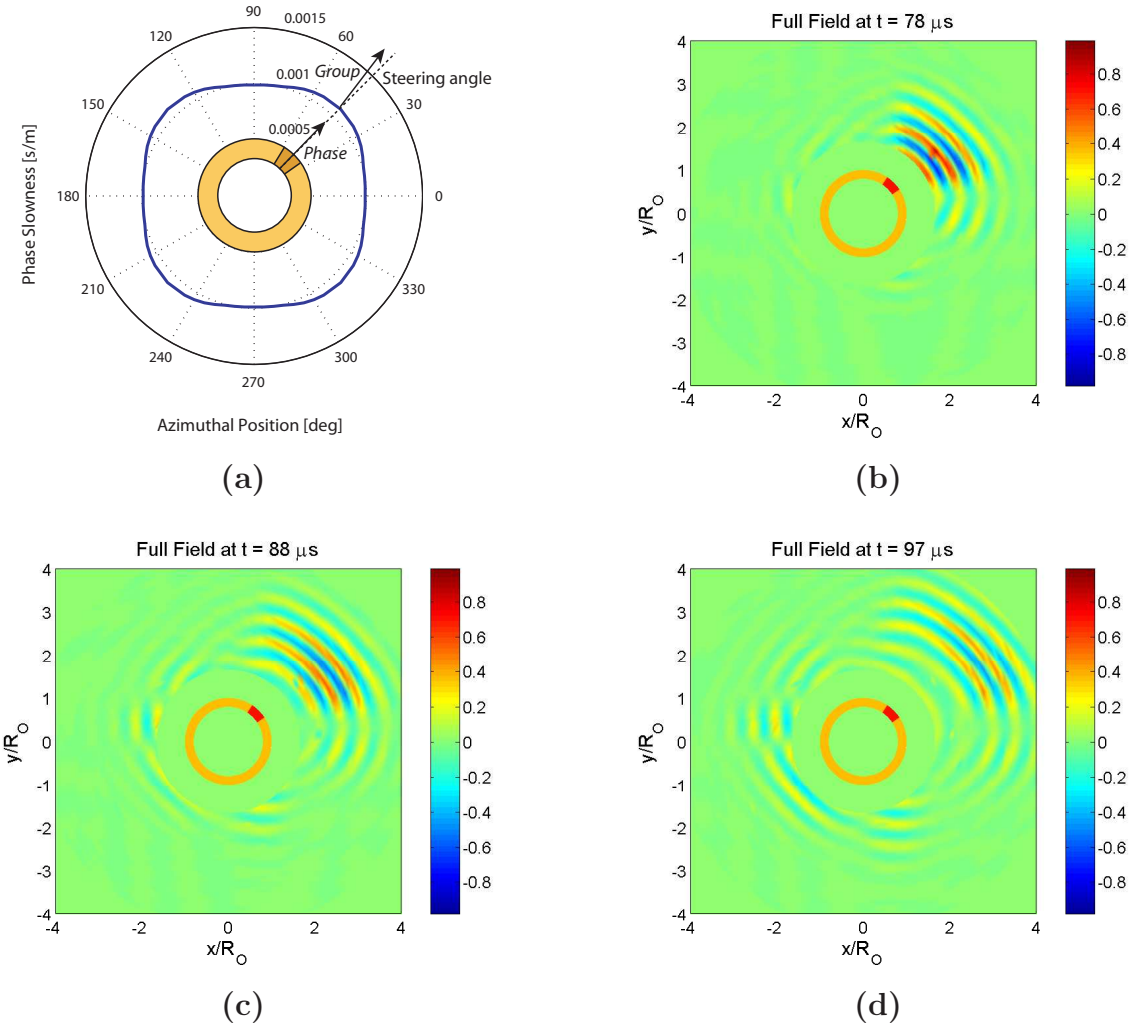

Figure 4.14: **(a)** Steering expected when using a CLoVER sector aligned 45 degrees (counterclockwise) from the fiber direction in a cross-ply plate based on its phase slowness diagram; Surface radiation at **(b)** 78 μs; **(c)** 88 μs; **(d)** 97 μs.

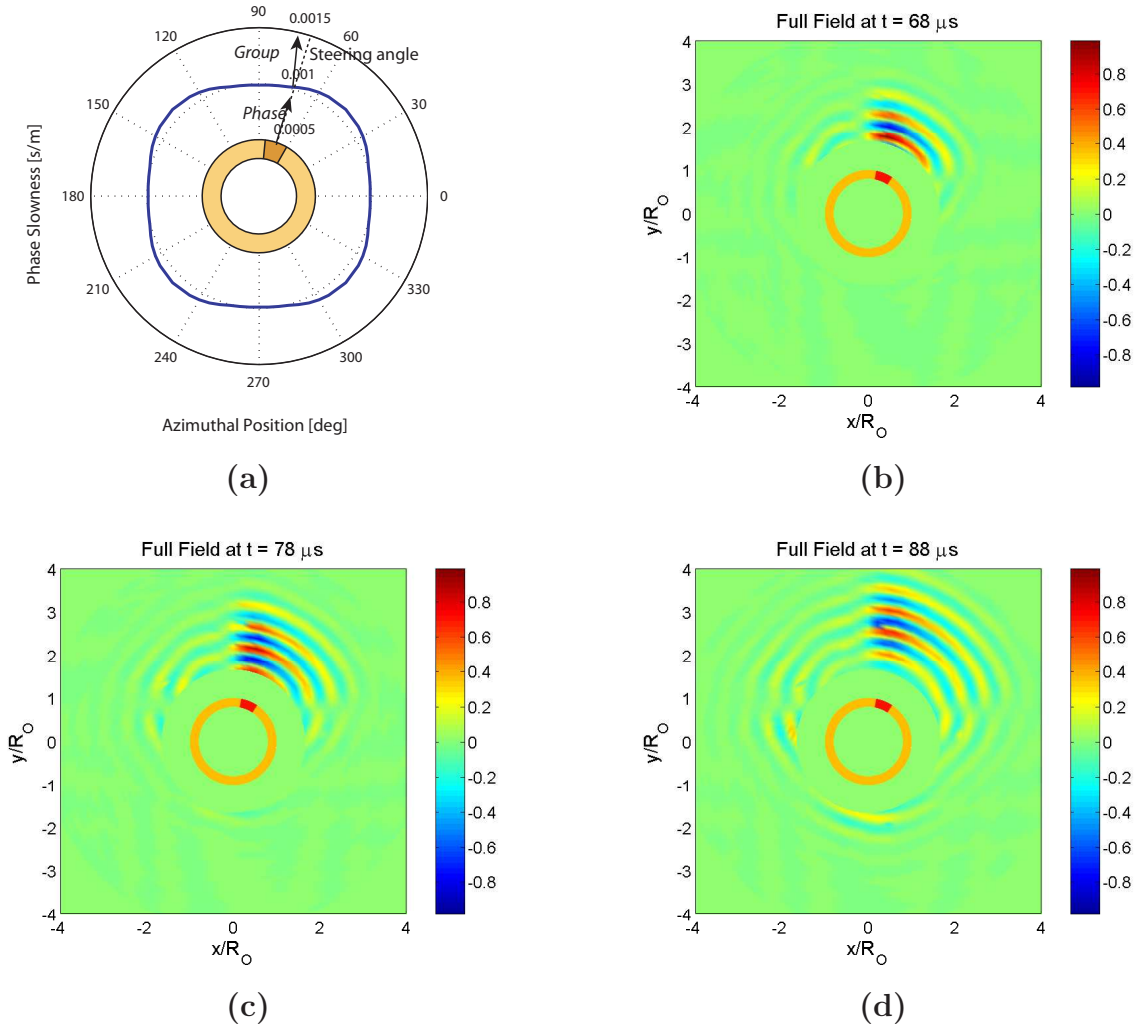

Figure 4.15: **(a)** Steering expected when using a CLoVER sector aligned 67.5 degrees (counterclockwise) from the fiber direction in a cross-ply plate based on its phase slowness diagram; Surface radiation at **(b)** 68 μs; **(c)** 78 μs; **(d)** 88 μs.

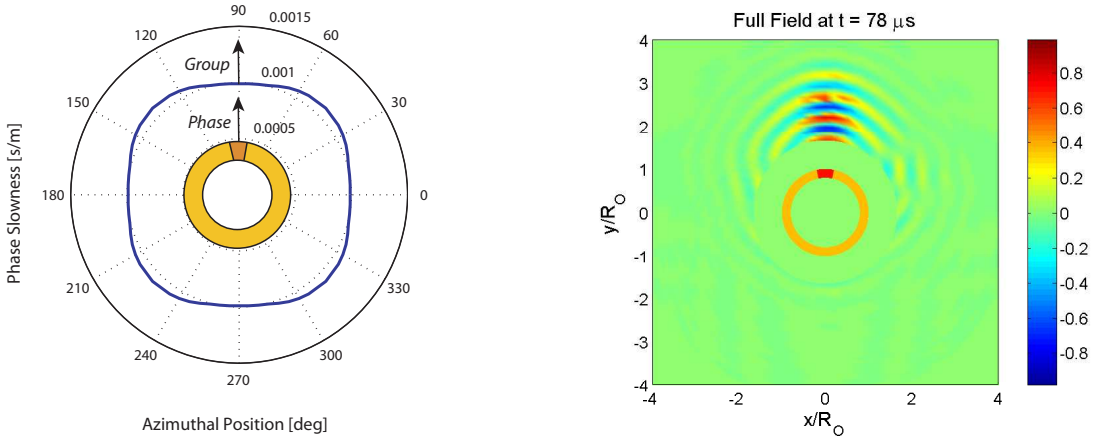

(a) **(b)**

Figure 4.16: **(a)** Steering expected when using a CLoVER sector normal to the fiber direction in a cross-ply plate based on its phase slowness diagram; **(b)** Surface radiation at 78 μs.

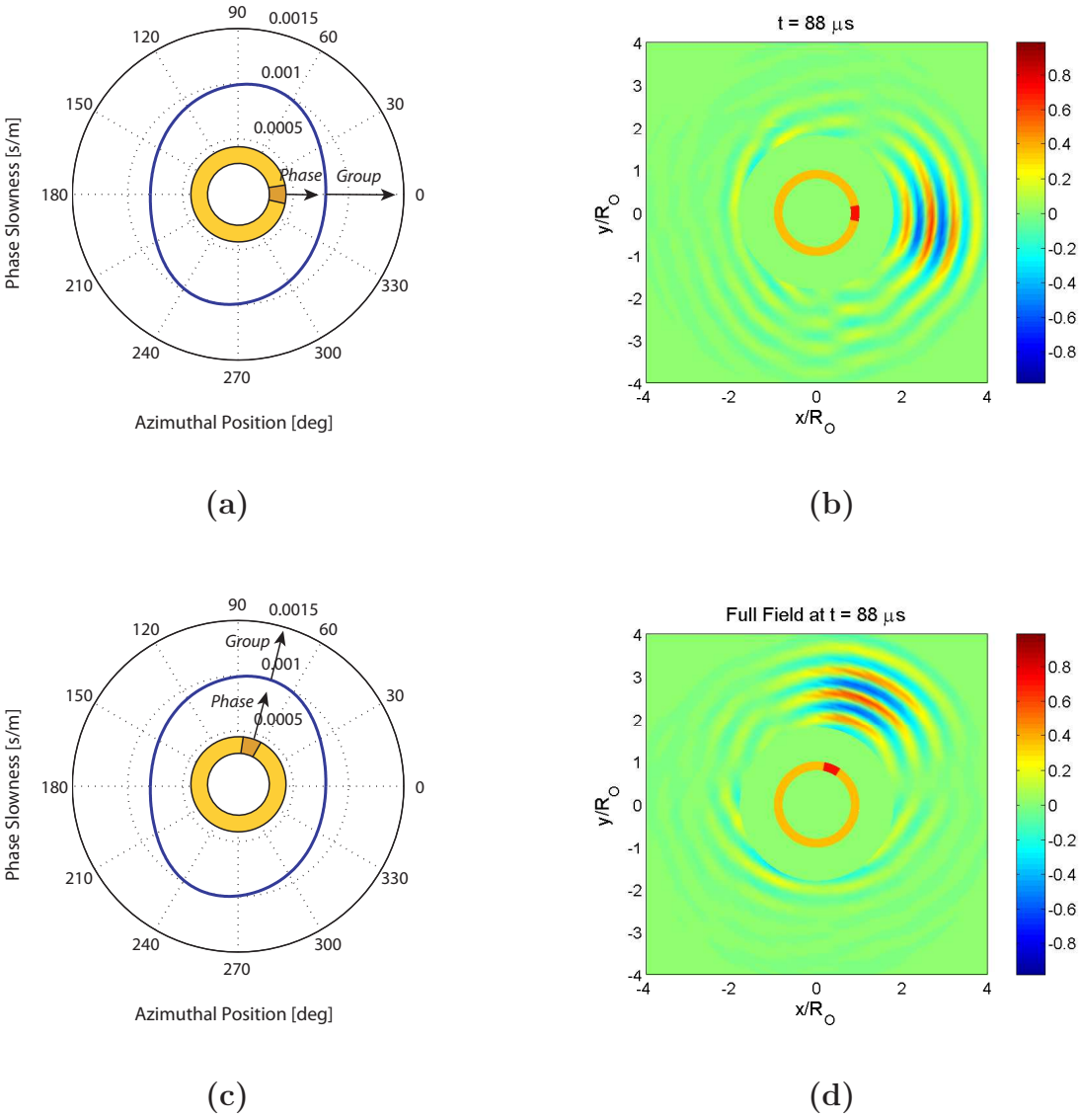

Figure 4.17: **(a)** Steering expected when using a CLoVER sector along the fiber direction in a quasi-isotropic $[0/45/\text{-}45/90]_{4S}$ plate based on its phase slowness diagram; **(b)** Surface radiation at 88 μs; **(c)** Steering expected when using a CLoVER sector aligned 67.5 degrees (counterclockwise) from the fiber direction in a quasi-isotropic $[0/45/\text{-}45/90]_{4S}$ plate based on its phase slowness diagram; **(d)** Surface radiation at 78 μs.

CHAPTER V

Damage Detection Using Prototype CLoVER Transducers

This chapter presents the experimental characterization of the damage detection and localization capabilities of the CLoVER transducer in isotropic and composite structures. The interrogation approach proposed is demonstrated using simulated structural defects in the form of concentrated masses and through-thickness holes. The results illustrate the ability of this new transducer to correctly localize simulated damage using a smaller number of devices than conventional interrogation approaches such as phased arrays.

5.1 Damage Interrogation in Metallic Structures

The objectives of the experimental tests presented in this section are to demonstrate the damage interrogation approach proposed with CLoVER transducers in metallic plates, and to evaluate the interaction of the GW field induced by a transducer sector with simulated defects. The next section explores the damage interrogation capability of the devices in composite materials. Two different simulated damage types were considered, namely, a concentrated mass and a through-thickness hole. This section describes the overall experimental setup while the specific details and results for each damage type are presented in the subsequent sections. A square aluminum 5005 plate with a side length of 0.7 m and a thickness of 3.2 mm was used in the experimental tests. The plate was supported by unistrut bars on two sides and was free on the remaining two sides. A CLoVER transducer was bonded on the surface of the plate at its geometric center by applying a thin layer of Epotek 301 bonding agent and allowing it to cure for 24 hours. The active CLoVER sector used had a radial dimension of 10 mm (inner radius, R_I, of 15 mm and outer radius, R_O, of

25 mm) and an azimuthal span of 45 degrees. A piezoceramic sensor with a diameter of 5 mm and a thickness of 0.2 mm was bonded at the center of the CLoVER array to record the induced strains. The sensor was bonded by applying a thin layer of Epotek 730 bonding agent. The transducer was excited using a 3.5 Hann-modulated toneburst signal at 65 kHz and various peak-to-peak amplitudes. The excitation signal was created using an Agilent 33220A arbitrary waveform generator and amplified using a Krohn-Hite Model 7500 wide band amplifier, while the sensor data were recorded using a digital oscilloscope (Agilent Infinuum 54831DSO).

5.1.1 Simulated Damage I: Concentrated Mass

The first damage type considered was a concentrated mass located at different radial and azimuthal positions on the surface of the plate. The mass was provided by a metallic bar as shown in Fig. 5.1. This bar had a square cross section with a side length of 2 cm, a height of 25.4 cm, and a mass of 1.1 kg. In this case, the excitation peak-to-peak amplitude was 175 V.

The A_0 mode is dominant at the excitation frequency used in these studies. This is advantageous for several reasons. First, the S_0 mode is very weak at low frequencies, which improves the purity of the propagating pulse. Furthermore, the reflections from the simulated damage will also be composed primarily of A_0 components facilitating its identification in the difference signal. Secondly, the dominant out-of-plane component characteristic of the A_0 mode is expected to be more sensitive to the simulated damage being used. Typically, in pulse-echo mode, a baseline sensor response signal corresponding to the pristine condition of the structure is measured using a sensor collocated with the actuator. Subsequently, damage is introduced and the reflections from it exposed by subtracting the baseline result from the signal corresponding to the damaged condition. In this part of the study, the main goal is to evaluate how the reflection amplitude varies with position, and consequently the damage location is assumed to be known *a priori*. Therefore, the group velocity for the A_0 mode, c_g (2324 m/s for the specimen used), can be used to estimate the time at which the damage reflection should arrive at the sensor. Since the metallic bar that simulates damage has a significant cross-sectional size, two bounds were calculated for the arrival time. The lower bound assumes that the waves will start reflecting back immediately upon hitting the front of the bar while the upper bound assumes that the reflections will begin once the incoming pulse reaches the back of the bar. The expressions for these times are given by:

$$t_L = \frac{2d_b + d_s}{c_g} + \frac{\overline{T}_p}{2}; \quad t_U = \frac{2(d_b + L_b) + d_s}{c_g} + \frac{\overline{T}_p}{2} \tag{5.1}$$

where d_b represents the distance between the damage location (front of the bar) and the outer radial edge of the transducer, d_s represents the distance from the radial edge of the transducer to the sensor, L_b represents the size of the damage, T_p represents the excitation pulse period (used to track the center of the pulse), and the L and U subscripts refer to the lower and upper bound for the arrival time, respectively.

The first set of tests consists of evaluating the decay in reflection amplitude with radial distance to gain insight into the attainable inspection distance. In addition, these results are used to select suitable radial positions for the subsequent azimuthal tests that simulate the proposed interrogation approach. The simulated damage was placed at 21 different radial positions, starting at $1.6R_O$ from the outer radial edge of the transducer in increments of $0.4R_O$. A schematic of this setup is shown in Fig. 5.2(a). Four different data sets were collected at each point, and each of these consisted of 64 averages. Fig. 5.2(b) shows a comparison between the sensor response signal for the pristine and damaged conditions. The excitation pulse and boundary reflections are clearly visible, which allows the time range where damage reflections are expected to be identified. Sample time histories for the difference signal can be seen in Fig. 5.3. From these, it is evident that the damage reflection is easily discerned. Furthermore, the time of arrival calculated using the group velocity is in good agreement with the experimental result.

Figure 5.4 shows how the peak-to-peak amplitude of the damage reflection changes with radial distance. In this case, the error bars correspond to the standard deviation, and the noise level has been indicated by the dashed horizontal line (this corresponds to a response of 2 mV peak to peak). Note that for the combination of parameters considered (substrate material and frequency-thickness product), an inspection range in the order of at least ten times the transducer outer radius can be attained without advanced processing of the inspection signals. This in turn corresponds to approximately ten wavelengths for the A_0 mode at the frequency-thickness product tested. It is likely that this distance can be increased for more realistic damage types where the S_0 mode is used, and by using advanced signal processing algorithms on the inspection signals (see for example Ref. [100]). As previously discussed, the A_0 mode has a dominant out-of-plane displacement component which makes it more susceptible to attenuation from structural features or environmental conditions (as for instance fluid loading). In the case considered here, it is likely that part of the

energy in the incoming pulse leaks into the bar that provides the simulated damage, thereby reducing the inspection distance that can be attained. It is interesting to note that the reflection amplitude does not decrease monotonically with distance, as would be expected. A similar phenomenon was observed by Diligent *et al.* [101] for the case of reflections from part-depth circular defects in plates using the S_0 mode. In that work, it was argued that these oscillations were due to interference between the main reflection from the damage and what they termed secondary reflections, such as circumferential creeping waves and SH_0 waves [101, 102]. From this result, two radial positions were selected for the azimuthal tests which are described next.

The second set of tests simulated the damage interrogation approach presented earlier using CLoVER transducers. In this case, however, the damage was manually placed at different azimuthal positions, so as to eliminate any effect associated with possible variations in piezoelectric properties or bond line conditions among the sectors. This process is equivalent to maintaining the damage location fixed and sequentially using each CLoVER sector to interrogate the structure. This approach is illustrated in the next section. The only parameter not simulated is the time delay between the activation of each sector. This, however, will likely be a fixed parameter primarily dependent on the time needed for all reflections (both from damage and other structural features) to be completely attenuated.

In this case, the distance between the simulated damage and the outer radial edge of the transducer was fixed at two different distances D, $2R_O$ and $4R_O$, while the azimuthal position was varied from -90^0 to 90^0 in increments of approximately 25^0. As in the previous case, the group velocity for the A_0 mode was used to estimate the time when reflections are expected. These results are shown in Fig. 5.5 where, as in the previous case, the error bars represent the standard deviation, while the noise level is represented by the black dashed line (note that this level was again selected as 2 mV peak-to-peak). In this case, the CLoVER sector's centerline coincides with the 0^0 direction. From the figure it is clear that the input energy to the CLoVER sector is primarily used to detect damage within its azimuthal projection. This illustrates the usefulness of the proposed interrogation approach, as the actuation can be directed primarily along the intended scan direction. This trend is further supported by the similarity in the response values observed for azimuthal positions with an amplitude larger than 50^0, as shown in Fig. 5.5(b). This indicates that for azimuthal positions that are away from the interrogation direction, the presence of the damage is not sensed as the GW energy along such directions is very small due to the directionality of the transducer.

5.1.2 Simulated Damage II: Through-thickness Hole

Four sectors (labeled CLoVER sector 1 through CLoVER sector 4) were used in additional simulations of the damage interrogation approach proposed with the CLoVER transducer, as shown in Fig. 5.6. Each of these was excited using a 3.5 Hann-modulated toneburst with a center frequency of 65 kHz, where the A_0 mode is dominant. The signal was amplified using a Trek PZD2000 amplifier and the peak-to-peak amplitude was slightly different for each sector to ensure that the peak-to-peak amplitude of the main pulse received by the sensor was similar for all of them (the variations in the input voltage were within 50 V among all the sectors). As in the previous case, the only parameter not simulated in this study is the time delay that exists between alternating sectors, as they were activated manually.

A through-thickness hole with a diameter of 4.8 mm was drilled at a radial distance of $4R_O$ away from the outer radial edge of one CLoVER sector to simulate structural damage, as also shown in Fig. 5.6. The same isotropic plate structure and CLoVER transducer used in the previous cases was employed here. The diameter of the hole to wavelength ratio was approximately 0.3. This dimension was selected so that the reflections from the front and back of the hole would interfere constructively as shown by Diligent for the case of part-depth holes [101]. However, it is expected that the reflection amplitude from a through-hole should increase monotonically with dimension as also discussed by Diligent *et al.* [103]. The damage location was again detected using the pulse-echo mode, and the same piezoelectric sensor used in the previous section was employed. By again assuming the location of the damage to be known, the following expression for the time-of-arrival of the damage reflection is obtained:

$$t_r = \frac{2d_h + d_s}{c_g} + \frac{\overline{T}_p}{2} \tag{5.2}$$

In preliminary studies it was found that the times of arrival obtained assuming the reflections originated at the front of the hole were very similar to those obtained assuming they originated at its back. Consequently, only the value corresponding to the front of the hole was used to track the damage reflections. It should be noted that it has been previously reported that the S_0 mode is more sensitive to through-the-thickness damage due to its dominant in-plane components [20, 31]. However, in order to excite a pure symmetric mode at lower frequencies two transducers are typically needed (one on each surface of the substrate). When these are excited in phase, the S_0 mode propagates in the plate, while if the A_0 mode is desired, they are excited

out of phase. Some of the CLoVER sectors on one of the transducers employed were unavailable for testing as they had sustained damage during earlier electric poling tests, therefore making the excitation of symmetric modes for all sectors impossible. Consequently, the present study uses the A_0 mode to provide a concept demonstration of the proposed damage interrogation approach.

Figure 5.7(a)-(d) shows sample difference signals collected with the piezoelectric sensor where the expected time of arrival for the A_0 mode defect reflections is highlighted. Two measurements were taken with each sector and 128 averages were collected in each of these. The peak-to-peak amplitude of these signals in the region where the reflection is expected was measured, and the result is summarized in Fig. 5.8. The results presented correspond to average values, while the error bars represent three times the standard deviation. Each of these signals was post-processed by removing linear and constant trends and passed through a bandpass filter. The maximum amplitude is recorded when CLoVER sector 2 is activated, which is the expected result as the damage is located along this sector's centerline. Furthermore, the reflection amplitude for the remaining sectors decreases with increasing index (for sectors 3 and 4), as the centerline of these transducers moves farther away from the damage location. Note in particular that the signal recorded when CLoVER sector 4 was used does not appear to have a significant contribution at the expected arrival time. This observation is expected as the wave field induced by this sector is very small near the damage location. This result illustrates the improvement offered by the interrogation approach attainable with the CLoVER transducer, as with prior knowledge of the device's configuration (namely the azimuthal direction of each sector), information about the presence of damage can be inferred. Note that in this particular experimental test, only four transducers were required to interrogate a structural area spanning 180^0 degrees. Furthermore, due to the directionality of the transducer and the geometry of the device, the azimuthal location of the defect relative to the CLoVER transducer can be easily identified without phased-addition or other post-processing algorithms.

5.1.3 Laser Vibrometer Tests

The interaction between the GW field excited by the CLoVER transducer and the through-thickness hole was examined in more detail using laser vibrometry. This non-contact technique is able to provide information near the location of the defect. The objective is to show that the GW interaction with the simulated damage stays predominantly within the azimuthal projection of the CLoVER sector whose centerline

is best aligned with the damage site. The key instrument used was a Polytec PSV-400 scanning laser vibrometer, which is composed of the PSV-I-400 scanning head, the OFV-5000 controller, the PSV-E-401 junction box, and a data management system. The light source used in the PSV-400 is a helium neon laser that provides a linear polarized beam [73]. The vibrometer system is able to measure the out-of-plane velocities by measuring the difference in path lengths between a reference beam and an object beam that is backscattered from the surface under inspection. The scanning head was supported using a tripod and maintained at a distance of 915 mm from the scanning surface for most of the experimental tests conducted. This distance was selected to operate at a laser visibility maximum [73]. The details of this experimental setup are similar to those described in Chapter III.

In the case of laser vibrometry, pulse-echo type of approaches where a signal corresponding to the pristine condition is compared to one after damage has been introduced are difficult to implement. This would require positioning the laser at exactly the same location on the surface of the inspected structure before and after the damage has been introduced. Since the laser beam diameter is very small ($\sim$ 130 μm for the middle range lens at the separation distance between the laser and specimen used [73]), this is nearly impossible to achieve as small positioning errors inevitably result during the introduction of damage. Consequently, the first set of tests consisted of evaluating the decay in peak-to-peak amplitude of the propagating pulse along the centerline of different CLoVER sectors. This test provides insight into how the presence of the hole influences the propagating pulse. Two different CLoVER sectors were considered, as shown in Fig. 5.9(a), with the first of them aligned with the damage and the second one located adjacent to the first one. The result is shown in Fig. 5.9(b), where the effect of the hole on the incoming pulse is clearly visible. In this case only a relative comparison is sufficient, and the results have been normalized by the maximum value in each data set. The data points represent average values while the error bars represent three times the standard deviation, which was calculated based on two separate measurements with 64 averages each. The result shows that the hole produces an increase in amplitude only very close to its edge when the transducer aligned with it is used. The result observed for the case of CLoVER sector 2 is consistent with the results reported by Staszewski [104] for the interaction of axisymmetric GW fields with rectangular notches and circular defects in aluminum plates using laser vibrometry.

The second set of tests consisted of measuring the peak-to-peak amplitude for points located on a circle whose radius coincides with the position of the hole, as

shown in Fig. 5.10(a). The same CLoVER sectors as in the previous case were used, and the results are shown in Fig. 5.10(b). In this case, the raw data are presented as the maximum value in the data set collected is expected to occur where the damage is located, and therefore a baseline value is not available. Note that the effect of the hole is predominant within the azimuthal projection of CLoVER sector 2, whose centerline is aligned with the damage site. The hole appears to have a weak effect on the GW field induced by sector 3, but this occurs in a region of small wave amplitudes where the uncertainty in the measurements is larger. A two-dimensional presentation of these results is given in Fig. 5.11 where the peak-to-peak amplitude of the out-of-plane velocities in the region surrounding the hole is shown. The main conclusion from the previous tests is that the presence of the defect is most clearly visible when the sector whose centerline is best aligned with its position is employed. This characteristic demonstrates that the input energy to a CLoVER sector is efficiently used, and will play a key role in the design of damage detection algorithms using these transducers.

5.2 Damage Interrogation in Composite Materials

A set of results that illustrate the ability of the CLoVER transducer to detect damage in composite structures are presented in this section. A particular goal in this context is to determine whether the directionality of GW propagation observed in Chapter IV influences the ability of the device to localize the azimuthal position of the defect sites.

The cross-ply $[0/90]_{6S}$ and quasi-isotropic $[0/45/\text{-}45/90]_{4S}$ layups described in Chapter IV were selected for these studies as they are representative of actual configurations used in practice. In this case, the CLoVER transducers were used as directional sensors, while the GW excitation pulse was generated by a circular piezoelectric disc bonded at the center of the CLoVER array. The piezoceramic disc has a diameter of 12.7 mm and a thickness of 0.2 mm. Similar to the setup described in Chapter IV, a piece of copper-clad kapton was placed between the composite surface and the lower surface of the piezoelectric disc. Due to its piezocomposite construction, a CLoVER sector is significantly more sensitive to strains along the piezo-fiber direction than along its transverse direction. Thus, the benefit in defect detection obtained through its directionality and geometry when used as an actuator (as seen in the previous section) is also expected to occur when used as a sensor.

The simulated defect used in this part of the study was a concentrated mass

provided by a metallic bar with a mass of 0.65 kg and a square cross section with a side length of 2.2 cm. The bar is similar to the one used in the previous section, except for its mass being reduced by half. This simulated defect was selected, in part, to avoid introducing permanent damage to the specimens (such as delaminations due to impact damage) during the early stages of testing. A more important reason, however, is that the mobility of the defect allows the azimuthal characterization of CLoVER sectors not aligned with it. In other words, it is of interest to find if the response displayed by the sectors adjacent to the one aligned with the simulated damage will vary depending on the azimuthal location being tested. As was seen in Chapter IV, the steering phenomenon tends to concentrate part of the GW energy along specific portions of the wavefront, which are not necessarily aligned with the direction of travel. Therefore, if steering effects were present it might be expected that, depending on the azimuthal location of the defect, the adjacent sectors would display a larger response than the one directly aligned with it. Such spatial characterization would not be possible with a fixed damage site, and introducing multiple defects would unnecessarily complicate the analysis of the data at this stage. Furthermore, the study is concerned with the directionality of the CLoVER sectors and their ability to detect and localize defects. The ability to detect delaminations, for instance, is characteristic of the GW approach and has been demonstrated by other researchers (see for instance the work of Diamanti and Soutis [86]).

The concentrated mass was placed at a radial position of 10 cm from the outer edge of the CLoVER sensors which corresponded to approximately 19 times the outer radius of the emitting piezoelectric transducer. The excitation input to the piezoelectric wafer was a 3.5 Hann-modulated toneburst at a frequency of 75 kHz as used in the testing of the pristine plates, but with a peak-to-peak amplitude of 15 V. The GW signals were recorded using a digital oscilloscope (Infinuum 54831B) with a sampling frequency of 1 MHz. In an effort to prevent the damage detection results from being influenced by different sensitivities of individual CLoVER sectors, the pristine and damaged signals for each sensor were normalized by the amplitude of the incoming GW pulse, so that the maximum in each data set was equal to one. A standard pulse-echo method was employed in these experiments whereby a signal corresponding to the pristine condition of the structure is compared to one obtained after the introduction of damage. The difference from these two measurements is then used to expose the reflections from any existing damage sites. In particular, the peak-to-peak amplitude of the difference signal is taken as the damage metric. To assess the effectiveness of the CLoVER interrogation approach in sensing, the simulated defect

was aligned with the centerlines of different sectors, one at a time, and the response was recorded using all active CLoVER sectors.

The first set of experiments were conducted on the cross-ply $[0/90]_{6S}$ plate, where two different damage configurations were considered. First, the bar was aligned so that its flat edge faced a specific CLoVER sector, while the second configuration consisted of placing the bar so that its corner was aligned with the centerline of any given sensor in the array. These configurations, shown in Fig. 5.12, will be referred to as flat and sharp, respectively, from this point onwards. As the emphasis of the present investigation is in verifying the effectiveness of the transducer in azimuthally localizing defects, its distance from the array was assumed to be known *a priori* and the wavespeeds measured in the previous chapter using laser vibrometry were used to identify the region where damage reflections were expected. A total of nine CLoVER sectors spanning a continuous range of 180 degrees were used in this case. These sectors are illustrated in Fig. 5.13. Due to the symmetry of the source and the material, this spatial range suffices for the defect detection studies. Figure 5.14(a)-(b) shows sample difference signals between the pristine and damaged conditions of the plate when the damage is aligned with different sectors. Figure 5.14(a) shows the difference signal when sector 5 is used as a sensor and the simulated damage is aligned with sectors 2 through 7. Similarly, Fig. 5.14(b) shows the difference signals when sector 1 is used as a sensor and the defect is aligned with sectors 1 through 6. Note that in both cases, the reflection from the defect is easily discerned and its time of arrival is consistent with the expected time based on the wave velocity and distance. Furthermore, note that for the sensors not aligned with the defect, the difference signal is significantly smaller.

One objective of the damage interrogation tests is to determine whether the steering phenomenon observed in the previous sections has a significant influence on the transducer's ability to determine the azimuthal location of the defect site. Due to the material symmetry of the substrate, the response of sectors 1 through 4 should be qualitatively similar to that of sectors 6 through 9 as they are placed in separate quadrants of the plate. Therefore, any effect associated with steering should become apparent in both measurements. The results from these experiments are illustrated in Figs. 5.15 through 5.17 where the response for both damage configurations (flat and sharp edge respectively) have been superimposed. Note that the results reported in the figures correspond to average values collected from three independent measurements with each measurement consisting of over 100 averages. Similarly, the error bars correspond to the standard deviation calculated from the three independent data

sets. Furthermore, the results obtained for sensors whose responses are expected to be symmetric have been placed side by side in the figure for easier comparison. The first clear observation from these results is that the transducers are effective in identifying the azimuthal location of the defect site. In particular, the amplitude of the response for the sectors that are aligned with the damage is consistently larger than those around it. Note that, in general, large responses are observed for the CLoVER sector aligned with the damage as well as an adjacent one. The fact that this pattern is observed for both damage configurations (flat and sharp edge) indicates that this is likely associated with the cross-sectional size of the simulated defect and not with the details of its shape at the point where it first interacts with the incident GW pulse.

A comparison of the response from symmetric sensors is therefore used to determine whether this effect is the result of any steering arising from the anisotropy of the substrate. If the simulated defect is idealized as an omnidirectional source of GW, then any steering or azimuthal variation of amplitude would affect symmetric sectors in a similar manner. For instance, consider the result observed when the simulated defect is aligned with sector 4. In this case the maximum amplitude is observed for sensor number 4, but a reflection of similar amplitude is also recorded by sector number 5. If this observation were due to steering of the reflected pulse or variations in its amplitude, it would indicate that the propagating pulse is steering or has a larger amplitude contribution towards the horizontal direction. Therefore, the reflected pulse recorded when the damage is aligned with sector 6 should also be steering towards the horizontal direction so that both sectors 5 and 6 would record large reflection amplitudes. However, this is not the observed result as when the damage is aligned with sector 6, a large amplitude is recorded by both sector 6 and sector 7. This observation is confirmed by the measurement recorded with sensor 5. Based on the slowness diagram illustrated in Fig. 4.1(b) and the peak-to-peak amplitude distribution reported in the previous chapter, no steering due to material anisotropy is expected along this direction. However, it is observed that a large reflection amplitude is recorded by both sectors 4 and 5. Therefore, it can be concluded that the large amplitudes observed by adjacent sectors is not due to steering effects or material anisotropy, but could rather be attributed to the size of the defect, imperfect alignment relative to the CLoVER sectors, or to the spread in energy of the reflected GW pulse as it propagates in the plane of the plate. Nevertheless, the results indicate the effectiveness of the CLoVER transducer in correctly identifying the azimuthal location of the defect site. Note also that this is accomplished using a smaller number of transducers than alternative concepts such as phased arrays.

Similar experiments were conducted on the quasi-isotropic $[0/45/\text{-}45/90]_{4S}$ plate to verify the performance of the transducer in different composite configurations. In this case, sixteen CLoVER sectors spanning a continuous range of 360 degrees were used. In this case, however, only the sharp damage configuration was considered as it was found in the experiments with the cross-ply plate that the specific alignment of the defect did not have a significant role in the reflection amplitude of the sectors aligned with it. The transducer arrangement used is shown in Fig. 5.18 where the active sensors are highlighted. As previously indicated, these sectors correspond to the electrode design defined as CLoVER 2 in Chapter IV. As in the previous case, the simulated defect was aligned with different sectors, one at a time, and the response recorded with all eight sectors. The results for this case are shown in Figs. 5.19 through 5.26 where the damage was aligned with sectors 3, 4, 5 and 7. Note that as in the case of the cross-ply plate the directionality of the CLoVER sectors allows the device to correctly identify the azimuthal location of the simulated defects. While in this case there are no in-plane material symmetries as in the cross-ply case, steering effects are also not apparent as the reflection amplitude is always largest for the sectors directly aligned with the defect. Note that as in the previous case, this is often accompanied by an adjacent sector having a large reflection amplitude as well. As previously indicated, however, this is likely due to the in-plane energy spread of the reflected GW pulse as it reaches the CLoVER transducer.

5.3 Concluding Remarks

The damage detection and localization capabilities of the CLoVER transducers were experimentally demonstrated in this chapter. The simulated defect types considered were a concentrated mass and a through-thickness hole. It was shown that the directionality of the GW field induced and sensed by each sector, combined with the arrangement of the array, is critical in correctly localizing simulated defects. Furthermore, experiments based on the pulse-echo method and laser vibrometry for isotropic structures showed that when the damage is not aligned with the active CLoVER sector the response obtained does not contain any significant damage-related features. The damage interrogation experiments in composite structures, using cross-ply $[0/90]_{6S}$ and quasi-isotropic laminates $[0/45/\text{-}45/90]_{4S}$, demonstrated that the simulated defects can be correctly detected and localized. This result indicates that steering effects induced by the material anisotropy do not significantly influence the damage localization ability of the CLoVER transducer.

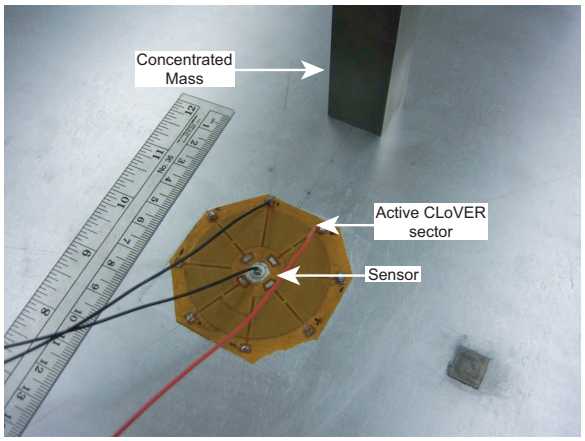

Figure 5.1: Experimental setup used in preliminary damage detection experiments.

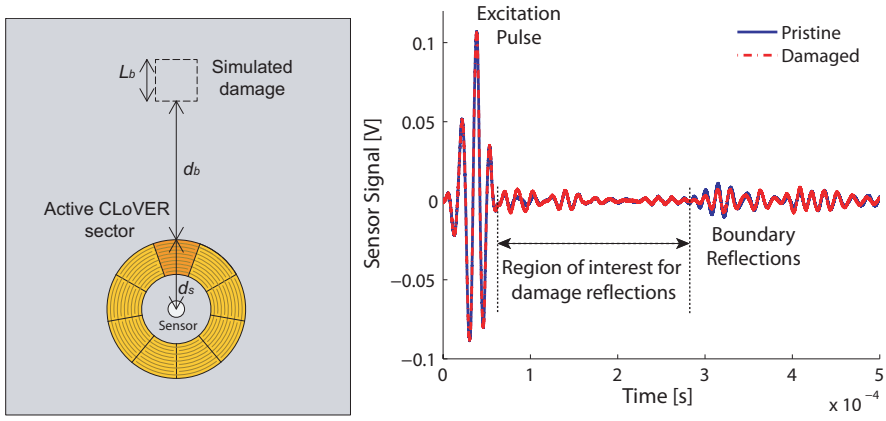

(a) **(b)**

Figure 5.2: (a) Schematic of damage location for reflection amplitude decay study; (b) Comparison between pristine and damaged sensor signals for damage located at d_b of $2R_O$.

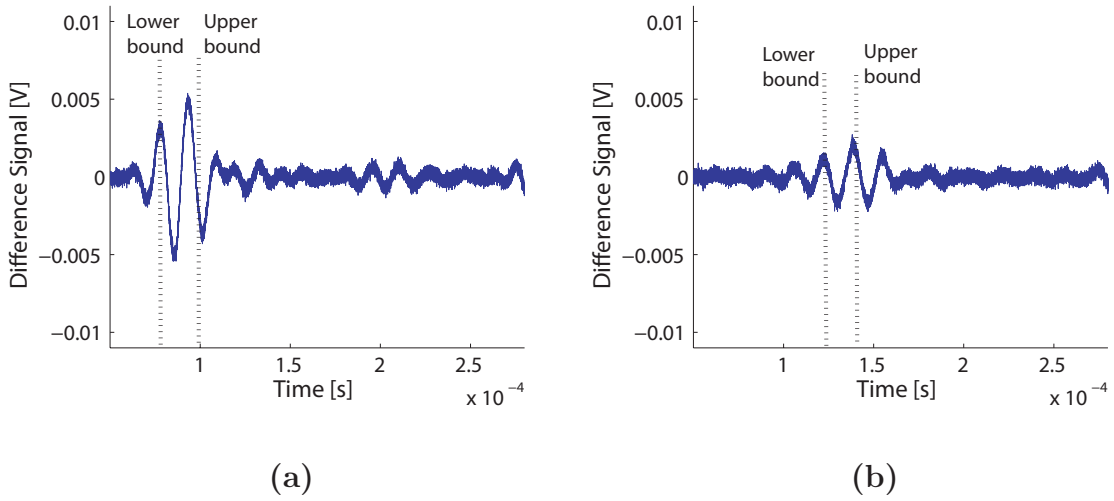

Figure 5.3: Difference between pristine and damaged sensor response signals for damage located at (a) $2R_O$, and (b) $4R_O$ from the outer radial edge of the transducer.

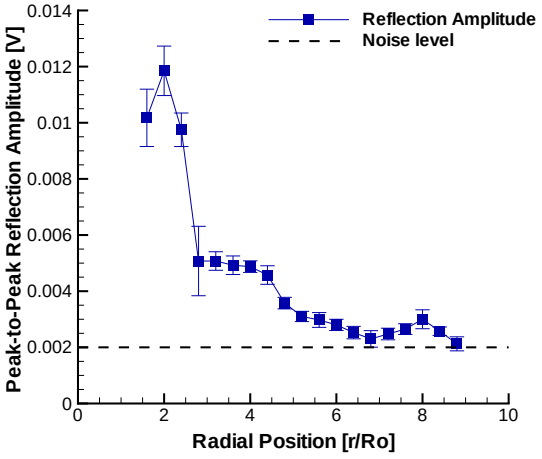

Figure 5.4: Variation of damage reflection amplitude with radial position along the transducer centerline.

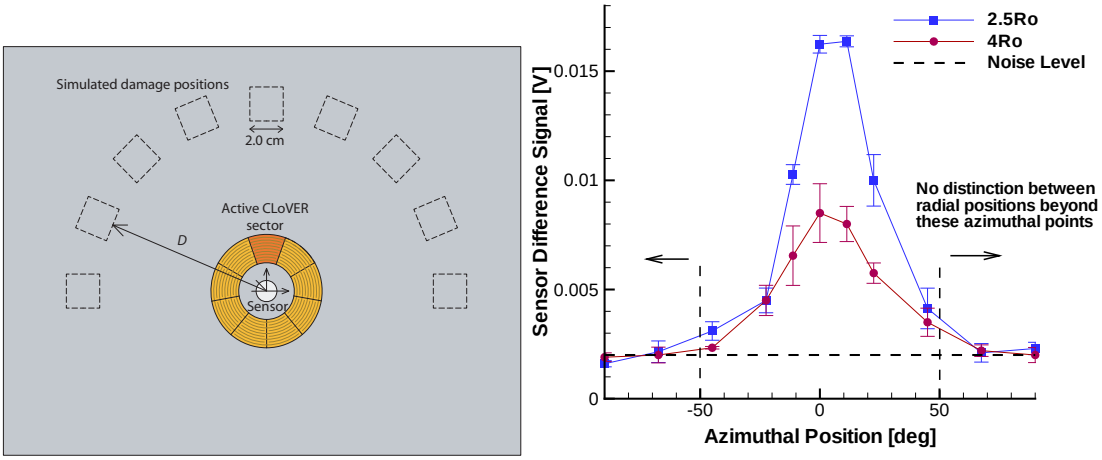

(a) (b)

Figure 5.5: (a) Schematic showing simulated damage locations for azimuthal tests; (b) Variation of damage reflection amplitude with azimuthal position for various radial locations.

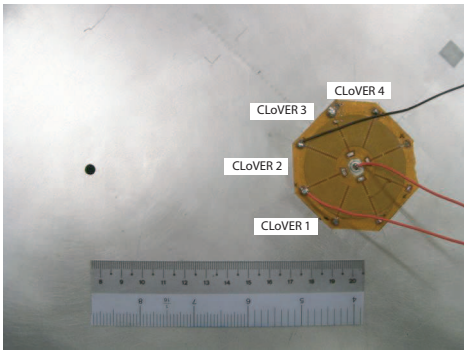

Figure 5.6: Detail of the through-thickness introduced for damage interrogation approach demonstration.

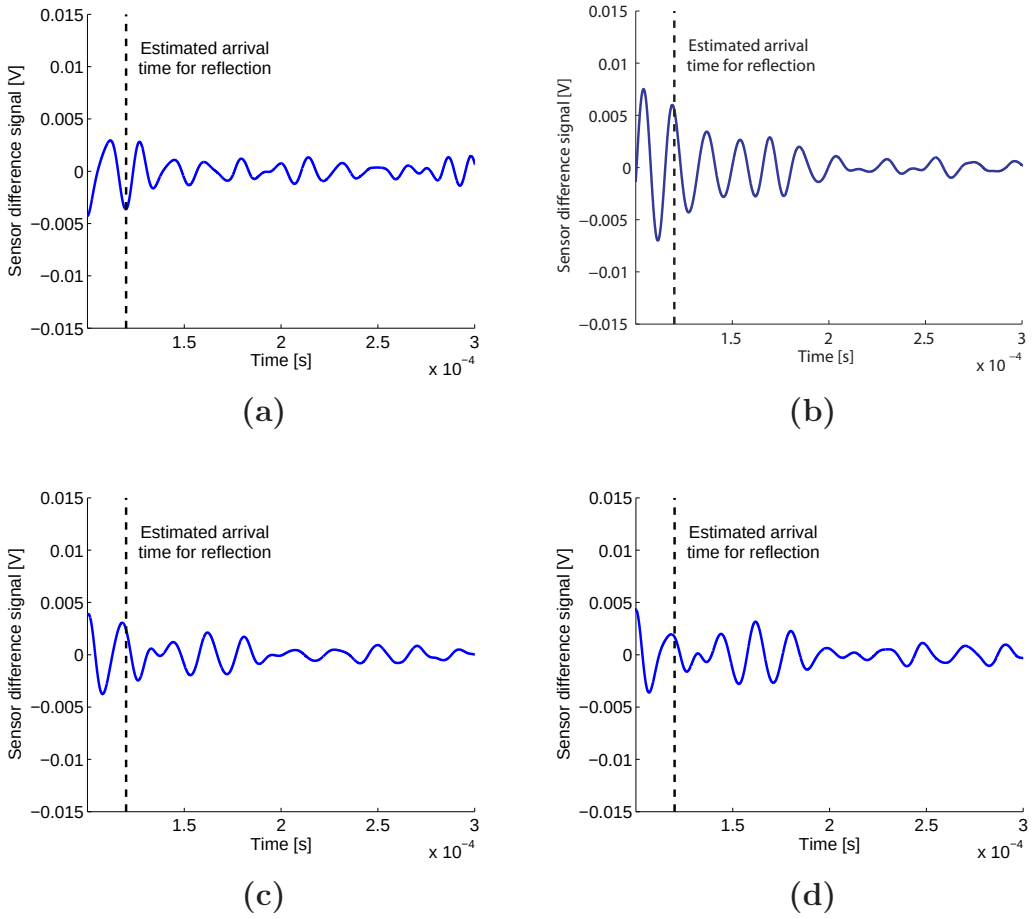

Figure 5.7: Difference signal between pristine and damaged conditions recorded with: (a) CLoVER sector 1 (b) CLoVER sector 2 (c) CLoVER sector 3 (d) CLoVER sector 4

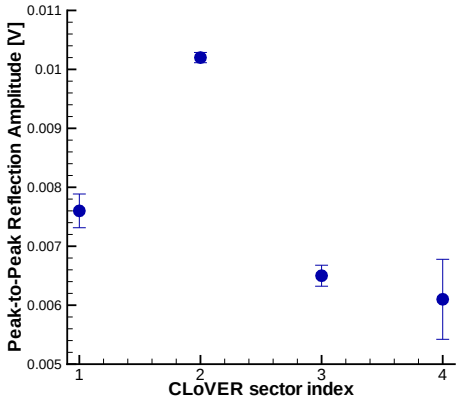

Figure 5.8: Comparison of reflection amplitudes among different CLoVER sectors.

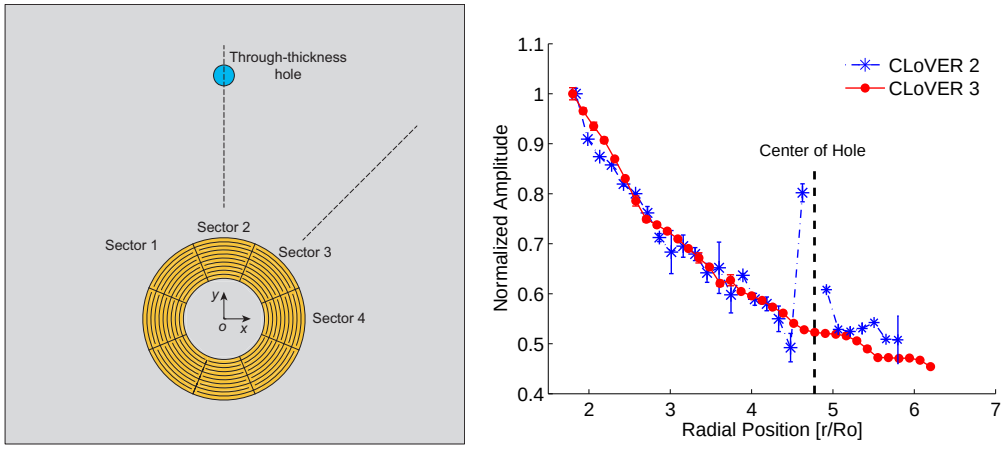

(a) **(b)**

Figure 5.9: (a) Schematic illustrating the location of the leaser measurement points in amplitude attenuation studies; (b) Effect of through-thickness hole on incident GW field for CLoVERs 2 and 3.

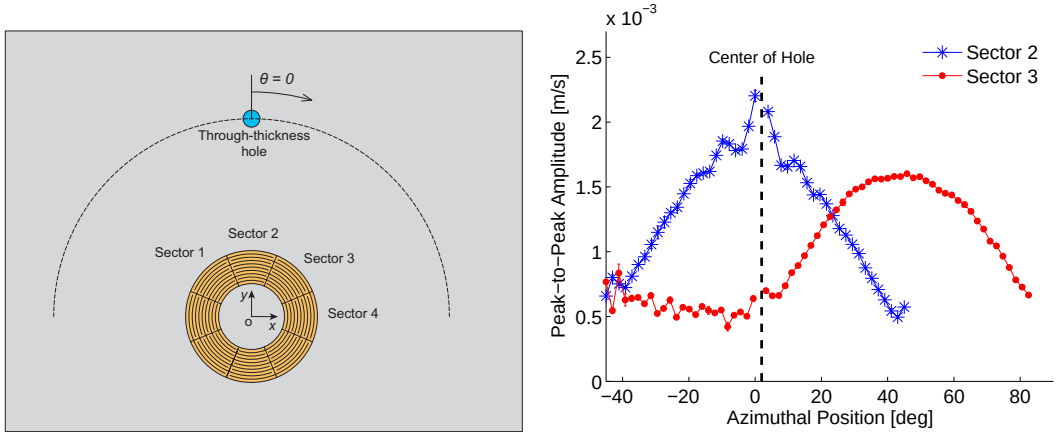

(a) **(b)**

Figure 5.10: (a) Schematic illustrating the location of the leaser measurement points in azimuthal tests; (b) Effect of through-thickness hole on azimuthal distribution of incident GW field from CLoVERs 2 and 3.

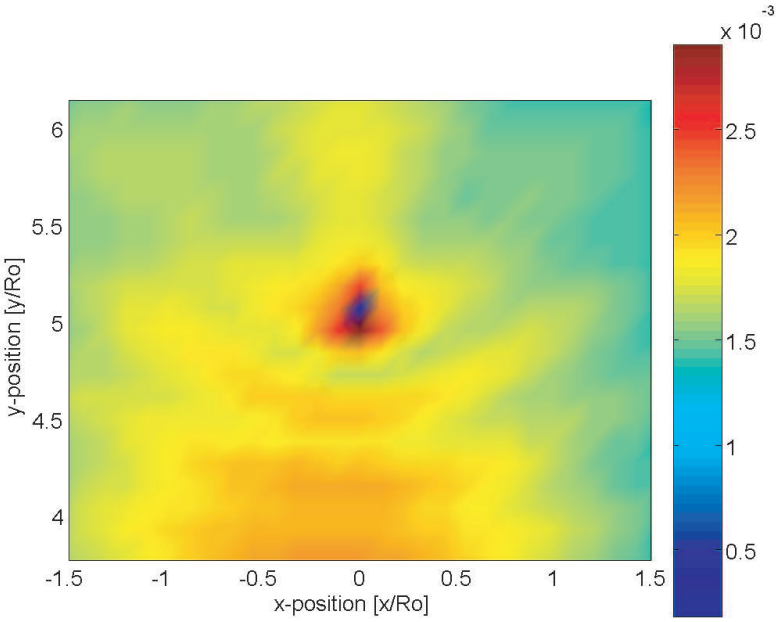

Figure 5.11: Interaction of incident GW field with structural defect: peak-to-peak amplitude of out-of-plane velocity component near the through-thickness hole.

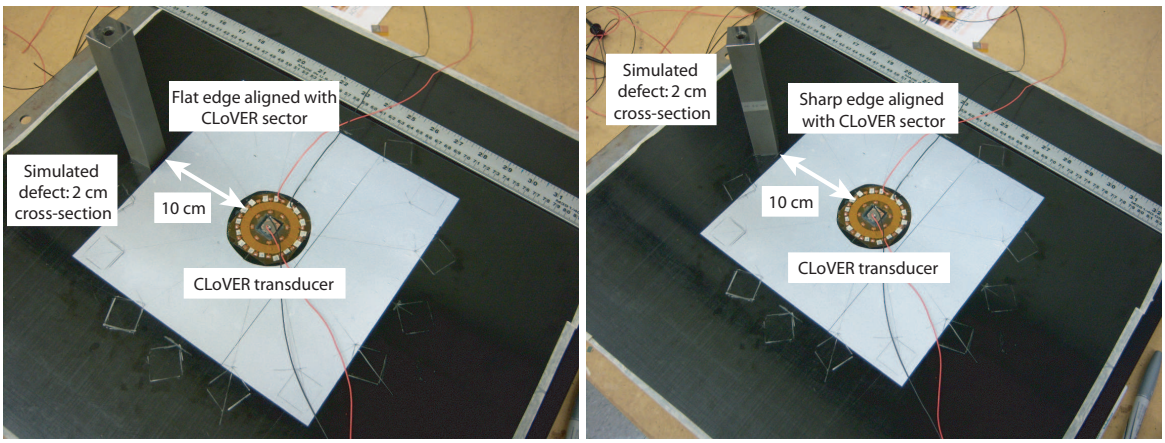

(a) **(b)**

Figure 5.12: Detail of CLoVER transducer and simulated defect used in damage detection experiments: **(a)** Flat side aligned with CLoVER sector; **(b)** Sharp side aligned with CLoVER sector.

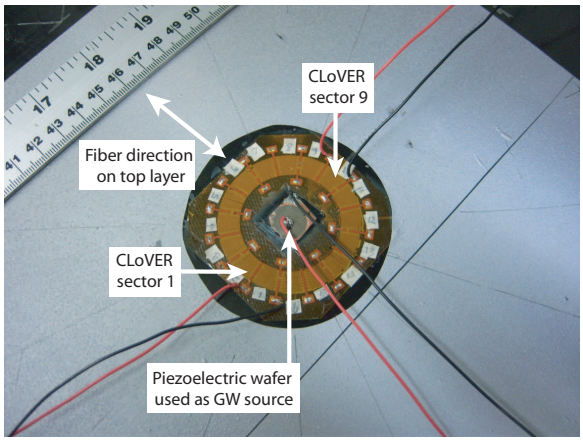

Figure 5.13: Detail of the CLoVER and piezoelectric wafer transducers used in the damage detection experiments in cross-ply plate.

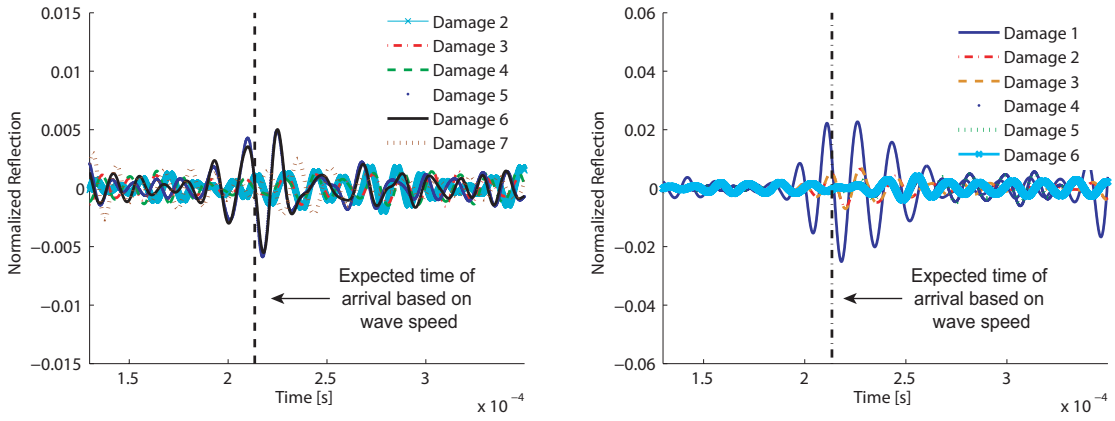

(a) **(b)**

Figure 5.14: Difference signals between pristine and damaged condition of the 12-layer cross-ply $[0/90]_{6S}$ plate when **(a)** Sector 5 is used as a sensor and the defect is aligned with sectors 2 through 7 and **(b)** Sector 1 is used as a sensor and the defect is aligned with sectors 1 through 6.

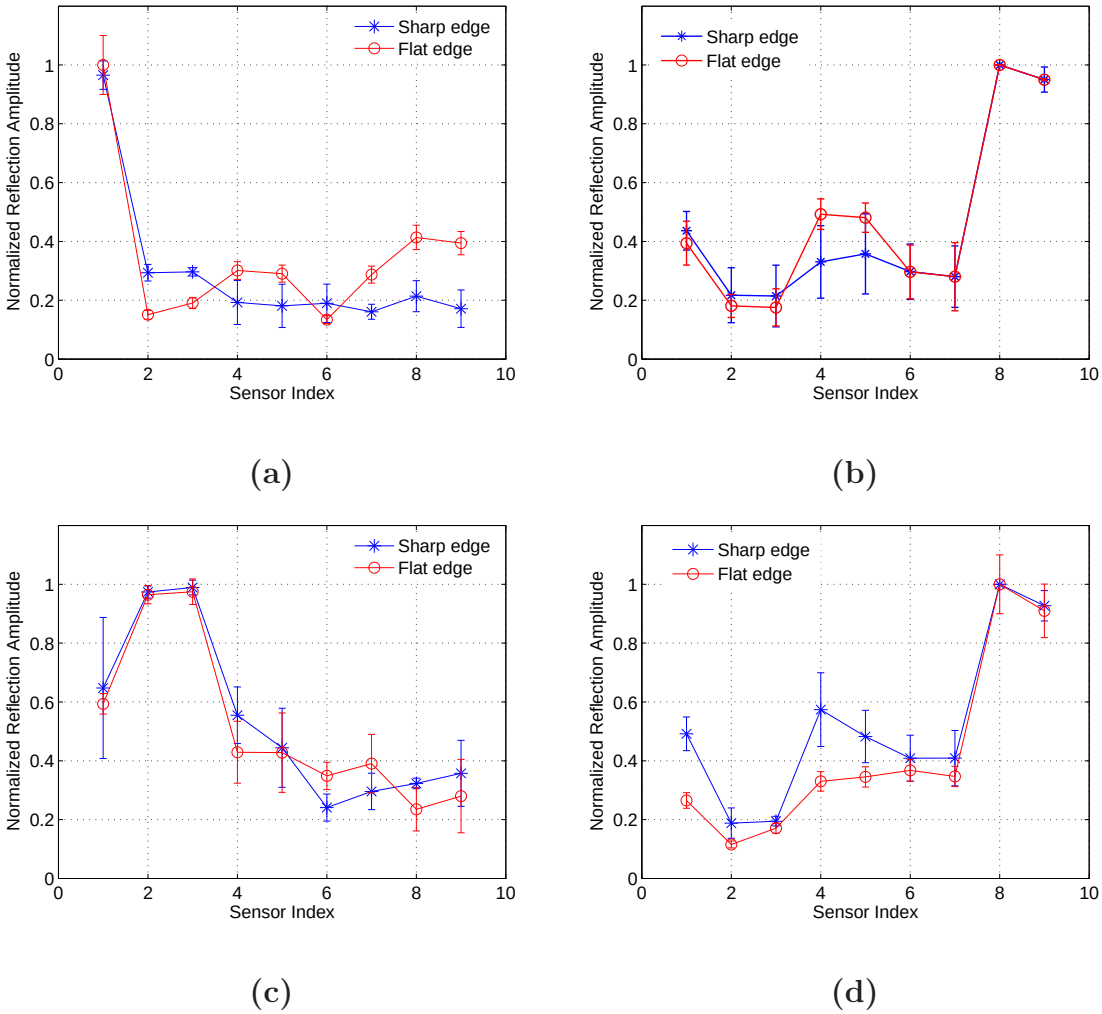

Figure 5.15: Normalized peak-to-peak reflection amplitude recorded with the CLoVER transducer in the 12-layer cross-ply $[0/90]_{6S}$ plate when the damage is aligned with **(a)** sector 1 **(b)** sector 9 **(a)** sector 2 **(a)** sector 8.

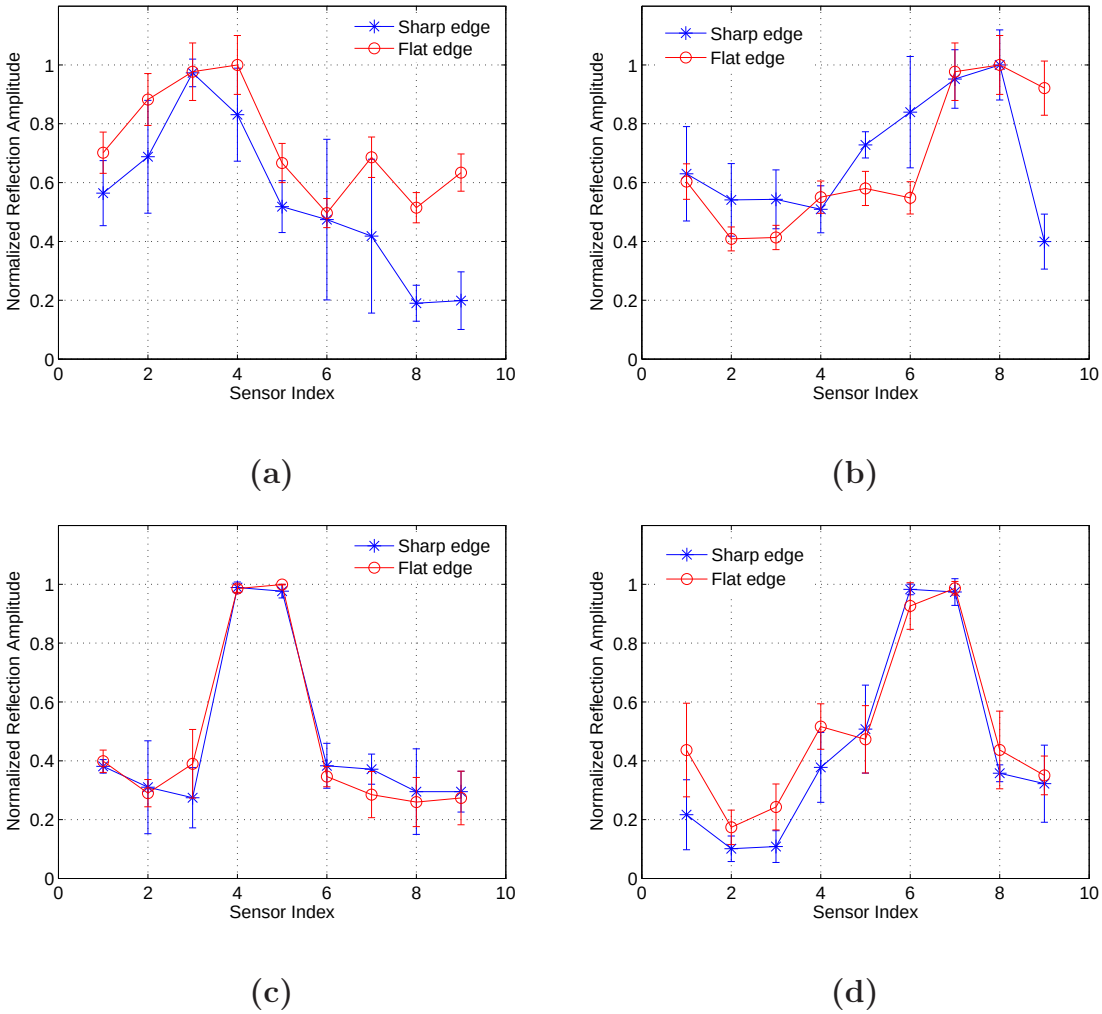

Figure 5.16: Normalized peak-to-peak reflection amplitude recorded with the CLoVER transducer in the 12-layer cross-ply $[0/90]_{6S}$ plate when the damage is aligned with **(a)** sector 3 **(b)** sector 7 **(a)** sector 4 **(a)** sector 6.

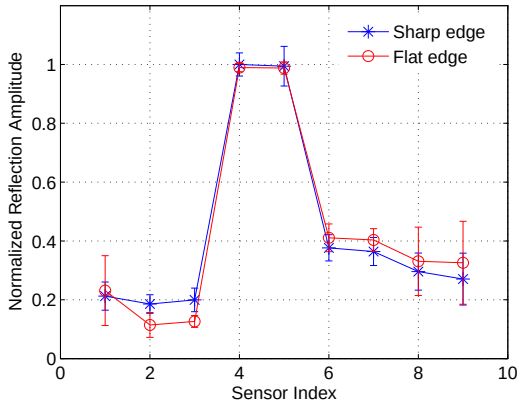

Figure 5.17: Normalized peak-to-peak reflection amplitude recorded with the CLoVER transducer in the 12-layer cross-ply $[0/90]_{6S}$ plate when the damage is aligned with sector 5.

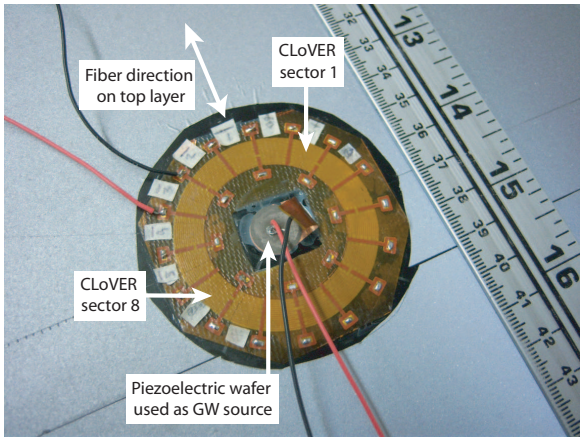

Figure 5.18: Detail of the CLoVER and piezoelectric wafer transducers used in the damage detection experiments in quasi-isotropic plate.

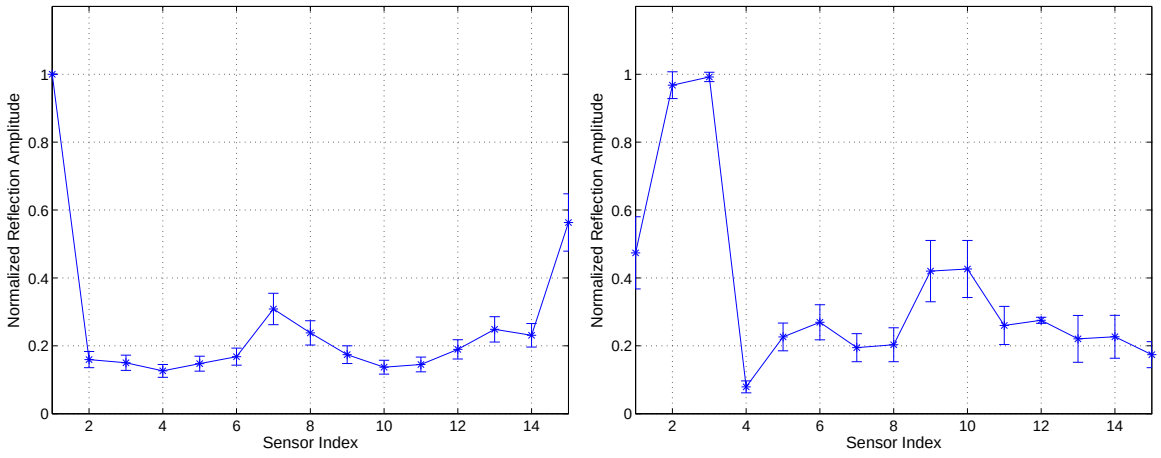

(a) **(b)**

Figure 5.19: Normalized peak-to-peak reflection amplitude recorded with the CLoVER transducer in the 16-layer quasi-isotropic $[0/45/\text{-}45/90]_{4S}$ plate when the damage is aligned with **(a)** sector 1 **(b)** sector 2 .

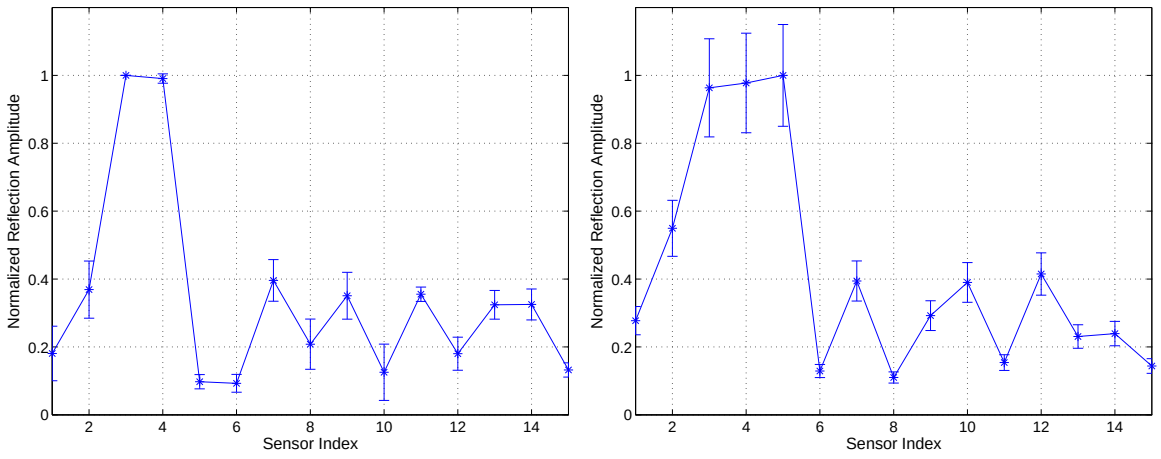

(a) **(b)**

Figure 5.20: Normalized peak-to-peak reflection amplitude recorded with the CLoVER transducer in the 16-layer quasi-isotropic $[0/45/\text{-}45/90]_{4S}$ plate when the damage is aligned with **(a)** sector 3 **(b)** sector 4 .

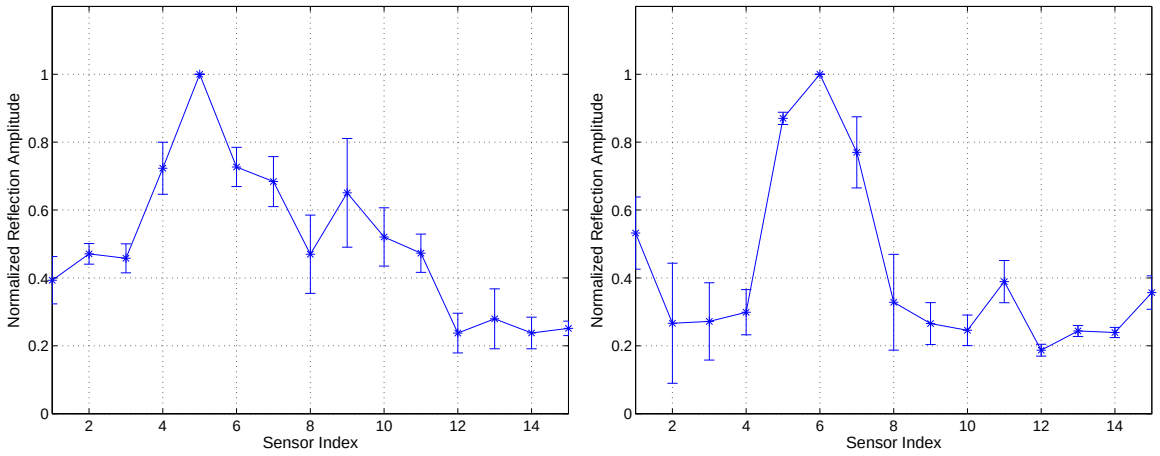

(a) **(b)**

Figure 5.21: Normalized peak-to-peak reflection amplitude recorded with the CLoVER transducer in the 16-layer quasi-isotropic $[0/45/\text{-}45/90]_{4S}$ plate when the damage is aligned with **(a)** sector 5 **(b)** sector 6 .

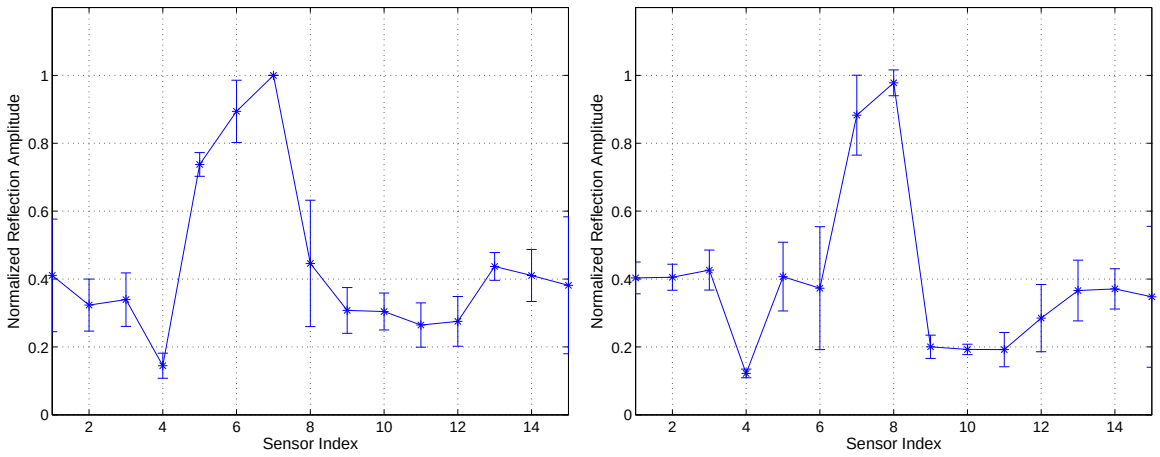

(a) **(b)**

Figure 5.22: Normalized peak-to-peak reflection amplitude recorded with the CLoVER transducer in the 16-layer quasi-isotropic $[0/45/\text{-}45/90]_{4S}$ plate when the damage is aligned with **(a)** sector 7 **(b)** sector 8 .

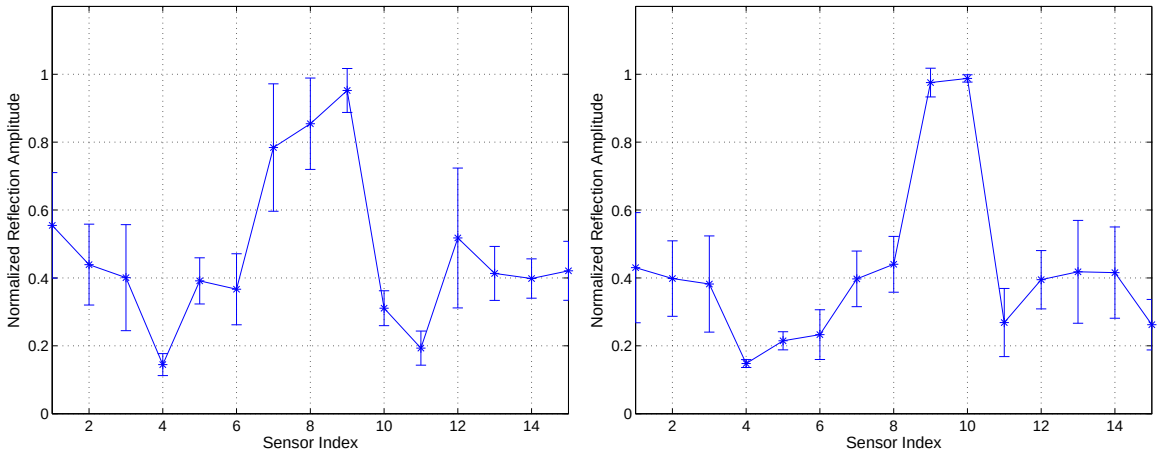

(a) **(b)**

Figure 5.23: Normalized peak-to-peak reflection amplitude recorded with the CLoVER transducer in the 16-layer quasi-isotropic $[0/45/\text{-}45/90]_{4S}$ plate when the damage is aligned with **(a)** sector 9 **(b)** sector 10 .

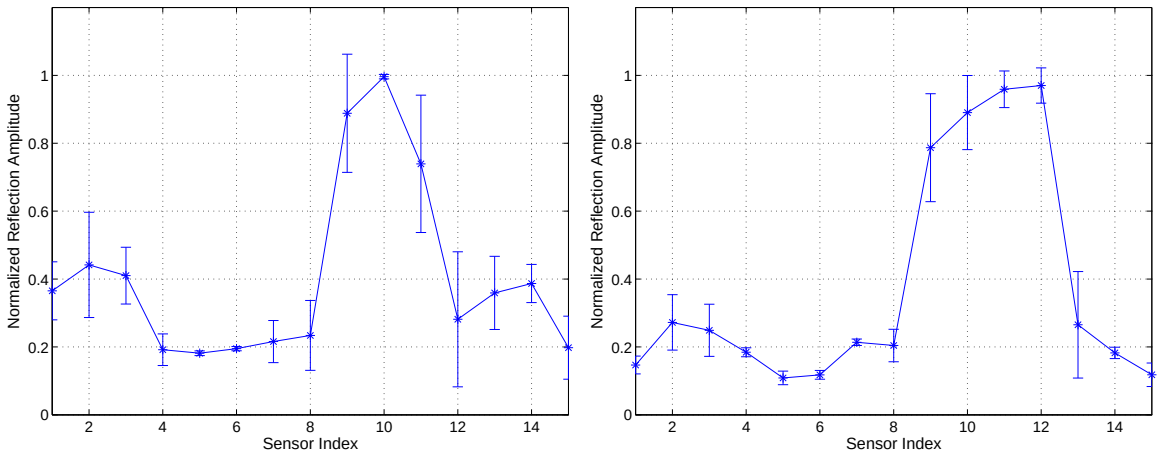

(a) **(b)**

Figure 5.24: Normalized peak-to-peak reflection amplitude recorded with the CLoVER transducer in the 16-layer quasi-isotropic $[0/45/\text{-}45/90]_{4S}$ plate when the damage is aligned with **(a)** sector 11 **(b)** sector 12 .

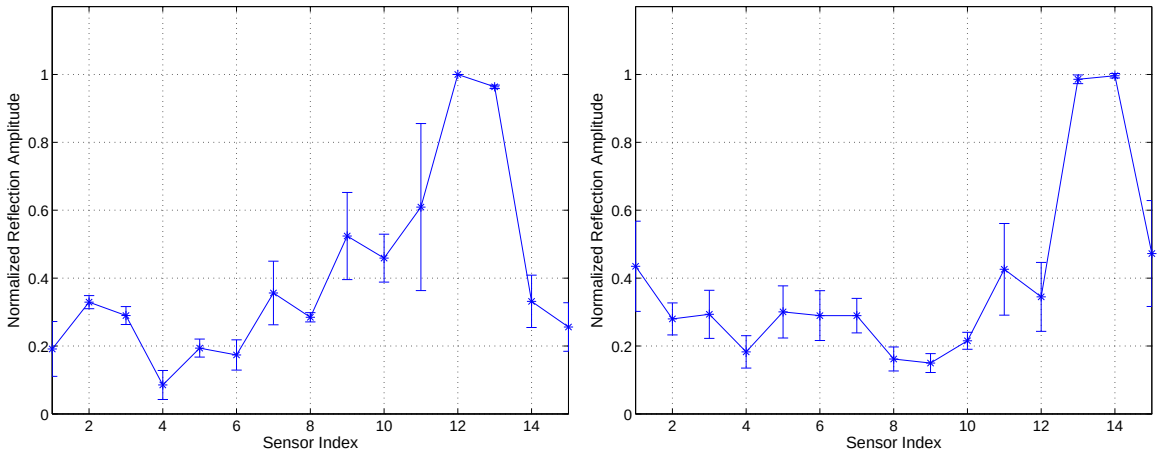

(a) **(b)**

Figure 5.25: Normalized peak-to-peak reflection amplitude recorded with the CLoVER transducer in the 16-layer quasi-isotropic $[0/45/\text{-}45/90]_{4S}$ plate when the damage is aligned with **(a)** sector 13 **(b)** sector 14 .

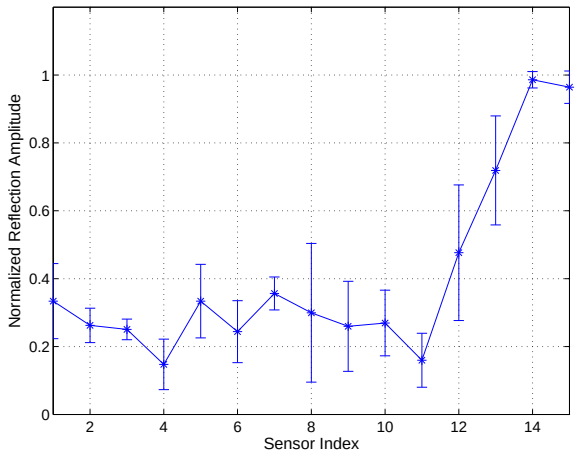

Figure 5.26: Normalized peak-to-peak reflection amplitude recorded with the CLoVER transducer in the 16-layer quasi-isotropic $[0/45/\text{-}45/90]_{4S}$ plate when the damage is aligned with sector 15.

CHAPTER VI

Design and Characterization of a Variable-length Piezocomposite Transducer

The design and characterization of a variable-length piezocomposite transducer is described in this chapter. The motivation for the variable-length capability is outlined first, and the transducer dimensions that optimize the transmission of specific modes are later derived. The design of the interdigitated electrode pattern is subsequently discussed, along with a brief summary of the transducer fabrication procedure. The resulting devices are used in a series of experimental tests in isotropic structures where their ability to selectively excite and sense specific GW modes is demonstrated. Finally, the ability of the variable-length transducer to provide active compensation in damage interrogation and detection is explored through numerical simulations with different types of damage.

6.1 Background

As discussed in Chapter I, there are many advantages associated with using GW for SHM. Prominent among them is the ability to tune the testing conditions so that the interrogation pulse is sensitive to specific damage types. This feature can be controlled based on the excitation frequency and transducer geometry. In the excitation of GWs using finite dimensional transducers, there are two main contributions to the induced displacements or strains. The first of these, which is typically referred to as the excitability function, is primarily dependent on the substrate under inspection. That is, for a given set of material properties and geometry, there will be frequencies at which displacements from specific GW modes will be maximized. This fact, along with dispersion considerations, is typically used to determine the excitation frequency to be used. The second component is related to the transducer geometry and size.

These parameters can be selected so that they are most effective at exciting specific GW modes (this is done according to the wavelength of the desired mode as discussed later).

There are multiple potential benefits in using variable-length devices for GW transduction. The first, and likely most important, benefit is the potential ability to selectively excite and sense individual modes. This would be advantageous as the propagating pulse could be specifically designed to be sensitive to different damage types. Conversely, using a sensor able to predominantly receive contributions from specific modes, while minimizing those from undesired ones, would greatly facilitate the processing of inspection signals. Similarly, a variable-length transducer can potentially operate at points of low dispersion in the frequency-thickness domain, to ensure that the different frequency components do not separate as the pulse propagates through the structure. This is advantageous as it maintains the signal-to-noise ratio and facilitates the processing of reflections from closely spaced features, as discussed by Monkhouse *et al.* [13] and Alleyne and Cawley [31].

Another important potential benefit is the ability for compensation of environmental effects on GW transduction. The transducer dimensions necessary to obtain a specific mode ratio are likely to be selected for a specific set of operating conditions, that is, specific temperature, loading, and material conditions, all of which may change while the structure is in operation. Consider for instance the effect of temperature. This parameter is of crucial importance for GW propagation and damage detection, and its effects have addressed by several researchers in the past (e.g. Konstantinidis, Drinkwater, and Wilcox [105]; Raghavan and Cesnik [106]; Clark and Cawley [107]). While the primary complications arise due to the influence of temperature on baseline signals typically used for damage detection and localization, GW transduction is also affected due to the changing transducer material properties. Furthermore, the mechanical loads acting on the substrate can also influence its wave propagation properties. For instance, the work of Chen and Wilcox [108] showed that for the A_0 mode in an aluminum plate, the phase velocity increased by a factor of as much as four under strain levels of 0.1% for frequency-thickness products of up to 10 kHz-mm. This effect would directly influence the transducer dimension as it typically depends on the mode wavelength, itself a function of the phase velocity. Finally, in the case of anisotropic structures the transducer dimensions will be dependent on the inspection direction. This effect can be observed in Fig. 6.1, which shows the directional dependence of the S_0 mode wavelength in a 4-layer IM7-based cross-ply $[0/90]_S$ laminate at 200 kHz. These results were generated using the software *Dis-*

perse v2.0.16d developed at Imperial College, UK [96]. As the transducer dimensions are based on the wavelength, it is clear that its value should change with angular position so as to maintain a constant mode transmission and sensing ratio.

The theoretical background for GW excitation that will be used to determine the optimal transducer dimensions is briefly discussed next, and an expression for the transducer dimension that maximizes the transmission of a specific mode is presented. The criteria for the design of the transducer are subsequently described, along with a brief overview of its fabrication procedure. A set of experimental studies are later presented to illustrate the ability of the device to attain specific mode transmission and sensing ratios.

6.2 Theoretical Considerations

The transducer dimensions in each variable-length device are selected so as to maximize the transmission and excitation purity of the S_0 or A_0 modes at different frequencies. These dimensions are obtained from the theory developed by Raghavan and Cesnik [44] for GW excitation by a rectangular, finite-dimensional piezocomposite transducer in isotropic plates. Note that, as shown in Chapter II, a CLoVER transducer sector with a sufficiently large (≥ 0.9) ratio of inner to outer radius will behave similar to a rectangular device. Their theoretical model is based on the 3-D equations of elasticity and is based on assuming uncoupled dynamics and perfect bond between the transducer and substrate. These assumptions result in the interaction between the substrate and the actuator being represented through shear tractions along the edges of the transducer in the piezoceramic fiber direction, as shown in Fig. 6.2. In the figure, the transducer is assumed to be bonded on the upper surface, and the origin of the coordinate system is placed at the half-point through the thickness of the plate. It was shown by Crawley and de Luis [54] that if these conditions are not satisfied, a shear-lag solution accounting for the thickness of the bond-line is necessary for accurate results. Nevertheless, the fitness of these assumptions in the theoretical modeling of GW excitation by these transducers has been numerically and experimentally verified in previous studies [43, 44] and in a previous chapter of this thesis. Under the above assumptions, the equilibrium equations expressed in displacement form are solved using Fourier transforms and complex calculus under the set of boundary conditions given by Eq. (6.1), from which the dependence of the induced GW field on the transducer dimensions can be derived.

$$\begin{gathered}\sigma_{zx}=0\\ \sigma_{zy}=\tau_0\left[u\left(x-\tfrac{L_1}{2}\right)-u\left(x+\tfrac{L_1}{2}\right)\right]\left[\delta\left(y-\tfrac{L_2}{2}\right)-\delta\left(y+\tfrac{L_2}{2}\right)\right]\\ \sigma_{zz}=0\end{gathered} \tag{6.1}$$

In Eq. (6.1) σ_{ij} corresponds to the stress components, b represents the substrate half-thickness ($t=2b$), τ_0 represents the traction amplitude, $u(.)$ corresponds to the unit step function, and $\delta(.)$ represents the Dirac delta function. Similarly, L_1 and L_2 represent the transducer dimensions along the $x-$ and y-directions, respectively. The results from this theory have been extensively verified numerically and experimentally, and good correlation has been obtained in the time, frequency, and space domains as shown in Chapter III and Ref. [43]. Upon application of the spatial Fourier transform (as defined in Chapter II) on Eq. (6.1), the following expression is obtained for the transform of the only non-zero shear stress:

$$\overline{\sigma}_{zy}=\frac{-i\tau_0\sin(\xi_x\frac{L_1}{2})\sin(\xi_y\frac{L_2}{2})}{\xi_x} \tag{6.2}$$

where ξ_x and ξ_y correspond to the wavenumbers along the $x-$ and y-directions, respectively. By replacing the Cartesian wavenumbers with their polar counterpart, ξ and ϕ, Eq. (6.2) can be expressed as:

$$\overline{\sigma}_{zy}=\frac{-i\tau_0\sin(\xi\cos\phi\frac{L_1}{2})\sin(\xi\sin\phi\frac{L_2}{2})}{\xi\cos\phi} \tag{6.3}$$

In a rectangular APT transducer the displacements are to be maximized along the direction aligned with the piezoelectric fibers. If this direction is assumed to be parallel to the y-axis, as depicted in Fig. 6.2, the value of the azimuthal wavenumber, ϕ, is equal to $\pi/2$. The evaluation of this wavenumber results in a singularity in the definition of the exerted stress. Nevertheless, by recognizing that the dependence of the transformed stress on the product $\xi\cos\phi$ can be expressed by a function of the form $\sin\hat{x}/\hat{x}$, which approaches unity as $\hat{x}$ approaches zero, the transformed stress can be expressed in the following form:

$$\overline{\sigma}_{zy}\left(\phi=\frac{\pi}{2}\right)=-i\tau_0\frac{L_1}{2}\sin\left(\xi\frac{L_2}{2}\right) \tag{6.4}$$

From Eq. (6.4) it follows that the transducer dimension along the fiber direction that maximizes the displacements at a given frequency, a^*, should be selected as [44]:

$$a^*=\left(n+\frac{1}{2}\right)\frac{2\pi}{\xi} \tag{6.5}$$

where n represents an integer (n = 0,1,2,...). The necessary wavenumber in Eq. (6.5) is obtained from the dispersion relation for either the S_0 or A_0 mode which, for the antisymmetric case, is given by:

$$D_A = (\xi^2 - \beta^2)^2 \sin \alpha b \cos \beta b + 4\xi^2 \alpha\beta \cos \alpha b \sin \beta b \tag{6.6}$$

where the terms α and β represent through-the-thickness wavenumbers , as defined in Chapter II. Eq. (6.5) can be expressed in terms of the mode wavelength, λ, by using the equality $\lambda = 2\pi/\xi$, so that the desired transducer dimension is expressed as:

$$a^* = (2n+1)\frac{\lambda}{2} \tag{6.7}$$

The result given in Eq. (6.7) is useful as it readily indicates that the transducer dimension that maximizes a given mode is equal to integer multiples of one half its wavelength. The result given by Eq. (6.5) can be generalized for a substrate of any thickness by using the definition of the phase velocity, c_p, which is known to be a function of the frequency-thickness product, ft [56]:

$$c_p = \frac{\omega}{\xi} = \frac{2\pi f}{\xi} = function(ft) \tag{6.8}$$

By substituting the definition in Eq. (6.8) into the result obtained in Eq. (6.5) one finds:

$$a^* = (2n+1)\frac{c_p(ft)}{2f} \tag{6.9}$$

where the parentheses in the c_p term indicate that this variable is a function of the frequency-thickness product, ft. Finally, dividing both sides by the substrate thickness, t, and defining $\chi = ft$ results in:

$$\frac{a^*}{t} = (2n+1)\frac{c_p(ft)}{2ft} = (2n+1)\frac{c_p(\chi)}{2\chi} \tag{6.10}$$

Sample results from Eq. (6.10) are shown in Fig. 6.3, which shows the transducer dimension that maximizes the transmission of the A_0 mode in an aluminum plate (E = 70 GPa, ν = 0.33, ρ = 2700 kg/m^3). Note that the dimensions that result in no transmission of a specific mode can be found analogously by setting the right hand side of Eq. (6.2) equal to zero. Denoting this transducer dimension by o^*, it can be expressed as:

$$\frac{o^*}{t} = n\frac{c_p(\chi)}{\chi} \tag{6.11}$$

where, as in the previous case, n represents an integer number. In the following section, the results in Eq. (6.10) and Eq. (6.11) are used to select the transducer dimensions so that the transmission of a specific mode is maximized, while that of the opposite mode is minimized.

6.3 Transducer Design and Fabrication

Several important parameters must be considered during the selection of the dimension of each segment in the variable-length transducer. First, the mode transmission ratio (defined as the ratio of the peak-to-peak amplitude of the propagating S_0 to A_0 modes, S_0/A_0) must be considered so that each dimension is able to selectively excite either the symmetric or antisymmetric mode. Ideally, the transducer would be sized at a point where one mode has a peak while the opposite mode has a minimum. As Fig. 6.4 and Fig. 6.5 show, there are a small number of points in the frequency-thickness domain where this can be exactly achieved. Note that the results shown correspond to an aluminum 5005 alloy ($E = 68.9$ GPa, $\nu = 0.33$, $\rho = 2700$ kg/m^3), but similar results are expected for other isotropic material systems. It should be noted that, as seen in Figs. 6.4 and 6.5, for low frequency-thickness products (less than 100 kHz-mm for the material parameters considered here), this requires a large transducer dimension (in the order of 30 times the substrate thickness for the symmetric mode and larger than 40 times the substrate thickness for the antisymmetric mode for the material parameters considered) which is not desirable based on power-consumption and implementation considerations.

The second important parameter is the wavelength range desired in order to be sensitive to different defect types and sizes. Previous studies have shown that the reflection amplitude from defects can be correlated to the ratio of the wavelength to a defect characteristic dimension. For instance, in Lowe *et al.* [109], the interaction of the fundamental Lamb modes with part-depth notches was studied through finite element analysis and experimental measurements. Their results indicated that for relatively shallow notches (less than 15% of the substrate thickness), the reflection amplitude was maximized if the S_0 mode wavelength was equal to four times the defect diameter, or if the A_0 mode wavelength was equal to two times the defect diameter. Similar correlations have been found for different defect types and depths (Diligent and Lowe [110]; Fromme *et al.* [111]). The mode wavelength is a function

of the material properties and thickness of the substrate under consideration as well as the testing frequency, and therefore the desired range needs to be selected on a case-by-case basis.

The transducer dimensions selected in this study, along with the expected mode transmission ratios expected at two frequency-thickness products of interest, are summarized in Table 6.1 and illustrated in Figs. 6.4 and 6.5 [112, 113]. Note that the dimensions selected are expected to produce large transmission ratios for each mode at two different points, and that the mode ratios indicated are based only on Eq. (6.10) and Eq. (6.11) and therefore do not account for the different substrate excitability at different frequency-thickness ranges. The actual frequencies based on a 3.2-mm aluminum plate were selected as they produced a range of wavelengths that will be useful in damage detection experiments. These wavelengths are summarized in Table 6.2.

In the case of the symmetric mode at 240 kHz-mm, the dimension was chosen so as to minimize the A_0 transmission without maximizing the S_0 mode as this would require a larger transducer, as seen in Fig. 6.6. Similarly, in the case of the antisymmetric mode at the same frequency-thickness the dimension selected maximizes the A_0 transmission without minimizing the S_0 amplitude as this would result in an even larger device. Similarly, Fig. 6.7 shows that, due to the smaller wavelengths, the dimensions selected at 720 kHz-mm maximize one mode transmission while minimizing that of the other mode. Finally, it is important to mention that the transducer dimensions selected are expected to provide similar transmission ratios for neighboring frequencies as well.

Based on the dimensions discussed above, the interdigitated electrode pattern shown in Fig. 6.8 was designed to attain the variable-length effect. It can be seen that each subdivision is connected to a separate electrode bus for independent actuation. Also note that the tabs for wire lead connections have been placed on the sides of the device, which decreases the transducer disturbance to the GW field. The specific parameters in the electrode pattern were selected based on those of the NASA-standard MFC devices [11]. In particular, the finger width was selected at 0.1 mm, while the finger spacing was chosen as 0.5 mm. The electrode pattern was transferred to a copper-clad kapton film (Pyralux LF7062R) using a photolithography process at the Lurie Nanofabrication Facility at the University of Michigan. There was no specific criterion followed to select the width of the device, other than to maintain a value within acceptable bounds. This dimension is only expected to scale the amplitude of the strains induced or sensed by the transducer, and to have no effect

in the trends observed for the transducer as the piezoelectric properties of the device are very weak along this direction. As previously indicated, the length along the piezoelectric fibers is the critical dimension to control in these transducers.

6.4 Experimental Procedures and Results

The variable-length APT was bonded on a 3.2-mm thick aluminum 5005 plate at its geometric center using a thin layer of Epotek 730 bonding agent. The in-plane dimensions of the square plate were 0.7 m on each side. It is important that the bond-line between the transducer and the substrate be as thin as possible to ensure that shear-lag effects can be neglected [54]. If the bonding line is excessively thick the strains from the actuator will be transferred to the substrate over a finite distance along its length instead of at its edges. This would in turn result in the effective dimension of the transducer being smaller than its nominal dimension. In order to ensure that a thin and uniform bond line was obtained, the transducer and plate were placed in an autoclave and cured for two hours at a temperature of 80° C (according to the manufacturer instructions) and pressure of 345 kPa (50 psi). This procedure was observed to yield the thinnest possible bond line without the risk of causing damage to the device due to excessive pressure, and has been previously shown to produce bonding layers that satisfy the perfect-bonding assumption. A combination of laser vibrometer and sensor-based measurements were collected to characterize the transduction properties of the variable-length device. The experimental details and results for each of these are presented in the following subsections.

6.4.1 Laser Vibrometer Experiments

The objective of these tests was to obtain a detailed characterization of the anti-symmetric mode in near-harmonic excitation conditions, which is expected to result in a closer correlation with the expected results from the selection of the transducer dimensions (calculated using a single frequency component). As a result, a Polytec PSV-400 scanning laser vibrometer, sensitive to the out-of-plane velocities of the specimen under inspection, was used. This device operates under the Doppler shifting phenomenon and uses a Helium-Neon laser beam approximately 60 μm in diameter at the used standoff distance (915 mm between the laser scanning head and the plate) [73]. As the symmetric out-of-plane displacement and velocity components are very weak, the laser is mostly sensitive to the antisymmetric mode.

In an effort to excite the transducer with a single frequency component, a 10-cycle

sinusoidal function was used as the excitation signal. An Agilent 33220A arbitrary waveform generator was used in conjunction with a Trek PZD2000 high power amplifier for this purpose. The acquisition frequency used with the laser vibrometer was 5.12 MHz. An overview of the experimental setup is shown in Fig. 6.9. The peak-to-peak input voltage to each APT segment was in the order of 500 V (somewhat larger voltages were used at higher frequencies to compensate for the decreasing amplifier gain). The wavelength for each of the frequencies tested was different, being larger for the lower frequencies. It is well known that the amplitude attenuation of GWs is a function of the propagation distance relative to the mode wavelength. Therefore, multiple measurement points were selected so as to always collect signals at a normalized distance of three wavelengths away from the edge of the transducer. A summary of these positions is presented in Fig. 6.10, where they range from 103 mm for 25 kHz to 28 mm for 250 kHz. The peak-to-peak amplitude of the recorded pulses was used as the metric in this case.

Sample results from these experiments are shown in Fig. 6.11 and Fig. 6.12. Figure 6.11 shows a sample time domain signal recorded with the laser vibrometer. All the measurements presented subsequently were made between the fourth and seventh propagating pulses. Each measurement was averaged a total of 64 times and three separate measurements were collected at each testing frequency. The peak-to-peak amplitude for each segment in the variable-length device is shown in Fig. 6.12, where the error bars represent three times the standard deviation.

Several important observations can be made from these results. First, note that for the 10-mm and 25-mm segments the peaks occur at 100 kHz in contrast to the 20-mm segment where the peak occurs at 125 kHz. This fact is directly related to the ratio of the transducer dimension to the mode wavelength. At 100 kHz, the A_0 mode has a wavelength of approximately 16 mm so that the 10-mm and 25-mm devices correspond to approximately one half and three times the half wavelength, respectively. Note that if shear lag effects are accounted for in the transducer, so that its effective dimension is slightly smaller than its nominal dimension (in the order of 15%), then the ratios would be in better agreement as observed in the experiment. Similarly, at 125 kHz the A_0 mode wavelength is approximately 14 mm making the ratio of mode wavelength to transducer dimension close to 0.5. Furthermore, note that the wavelength at 150 kHz is equal to approximately 12.5 mm so that the 25-mm segment is expected to minimize the induced displacements as it is equal to twice the wavelength. While this is not exactly observed, note that there is a local minimum at this frequency.

These results provide a preliminary demonstration that the variable-length transducer can preferentially excite specific modes when sized according to the desired wavelength [112, 113]. The following subsection provides a detailed study on the effectiveness of the variable-length device in attaining different mode transmission and sensing ratios.

6.4.2 Sensor-based Experiments

The objective of this section is to evaluate the performance of the variable-length device in selectively exciting symmetric and antisymmetric modes at different frequencies. In this case, the GW field was recorded using a circular 5-mm diameter piezoelectric wafer bonded 12 cm away from the edge of the transducer along its centerline, as shown in Fig. 6.13. This distance was selected as a good compromise among several factors. First, there must be sufficient distance between the actuator and sensor to allow the modes to separate due to their different group velocities. Similarly, the sensor must not be placed too far from the transducer as this would result in the amplitudes being unnecessarily attenuated and in boundary reflections interfering with the GW pulses. A 3.5-cycle Hann-modulated toneburst was used as the excitation signal in this case. The apparatus used to generate the pulse as well as the input voltages were similar to those in the previous set of experiments. The sensor data were recorded using a digital oscilloscope (Agilent Infinuum 54831DSO) with a sampling frequency of 5 MHz. The sensor signals were post-processed by removing constant and linear trends and passed through a 4th order Butterworth band-pass filter. The frequency band-pass was selected based on the number of cycles in the modulation window. While 128 averages were collected at each tested frequency, the standard deviation provided by the oscilloscope corresponded to the peak-to-peak amplitude of the entire signal. Therefore, this value was not used in the results as there were contributions from electromagnetic interference (EMI) as well as the propagating GW modes. Instead, over the large number of averages, it was observed that the standard deviation corresponded to at most 5% of the peak-to-peak amplitude. Consequently, the following convention was adopted for reporting the experimental error: When the specific mode under consideration had a dominant contribution in the signal, its error was assigned to be 5% of its peak-to-peak value. Conversely, when the contribution had to be manually tracked based on wave speeds, the error was raised to 15% of the peak-to-peak value. Considering the large number of averages taken, the error convention is expected to provide conservative estimates. For the transmission ratio, the error was computed using suitable error propagation

equations.

Figure 6.14 and 6.15 show sample time domain signals recorded with the sensor at frequencies where the A_0 and S_0 modes are dominant, respectively. Similar measurements were recorded over a large range of frequencies and the peak-to-peak amplitude of each mode was recorded for each segment of the variable-length transducer. Sample results for the frequency response of these segments are shown in Fig. 6.16. Note that, as expected, the A_0 mode is dominant at low frequencies, while the S_0 mode contribution increases at higher frequencies. In this case, however, the metric of interest is the ratio of S_0 to A_0 transmission attainable with each device. This ratio is used as a measure of the selectivity the transducer in GW generation. Figure 6.17 shows the comparison of this transmission ratio as a function of frequency for all the segments in the variable-length device, including the individual 5-mm segment needed to obtain the 25-mm dimension, in dB scale. From the figure it is clear that the smallest actuator has a lower transmission ratio (S_0/A_0) over a wider frequency range due to the shorter wavelength of the antisymmetric mode, whose value decreases from approximately 18 mm at 75 kHz to 12 mm at 150 kHz. Similarly, the S_0 mode wavelength is very large in this frequency region (from 70 mm at 75 kHz to 35 mm at 150 kHz) so that the transducer is small enough to excite it in a weaker manner. This segment could enable surface damage inspection (e.g., surface cracks) using the A_0 mode in a nearly pure manner over a relatively large range of wavelengths.

As previously discussed, the 10-mm segment was selected to obtain a small S_0/A_0 transmission ratio at lower frequencies and a maximum transmission ratio in the neighborhood of 225 kHz (720 kHz-mm). The results show that, until 100 kHz, this transducer dimension produces the lowest transmission ratio (along with the 25-mm segment) except for the 5-mm segment for the reasons discussed previously. Similarly, this segment produces the largest S_0/A_0 transmission ratio attainable with the entire transducer at higher frequencies as a result of its wavelength being close to half the wavelength of the S_0 mode. Note that in this case, unlike other segments, the transmission ratio is expected to continue to increase with higher frequencies. While the wavelengths corresponding to the S_0 mode in this region are still relatively large, the results illustrate that by using a variable-length device the peak transmission ratios can be tailored to occur at specific frequencies according to the wavelength desired. Finally, the 25-mm transducer was designed so as to maximize the transmission of the A_0 mode at 225 kHz. The results illustrate that for this transducer dimension, the S_0/A_0 ratio is the lowest in all overall device, except for the 5-mm segment. It is important to emphasize once more the advantage offered by the variable-length

capability of the transducer. Note that for the particular combination of parameters selected in this experimental demonstration, the largest improvement in mode purity occurs for the A_0 mode at 150 kHz. At this frequency, using the 5-mm segment yields a gain of approximately 4.6 dB relative to the 10-mm segment [112, 113]. This indicates that due to the ability of the device to electrically vary its length, the wavelength of the A_0 mode can be exploited for damage detection at this frequency without compromising, for instance, on the purity of the S_0 mode at 225 kHz. This illustrates the usefulness of the transducer, as different wavelengths can be selectively excited using a single, compact device.

During the selection of the transducer dimensions, the points chosen predicted a very low mode ratio at different frequencies, in fact lower than what is actually observed in the experiment. This observation is due to the inherent property of the substrate to have better excitability for each mode in different frequency-thickness ranges. Therefore, attempting to maximize the transmission of the S_0 mode at lower frequencies by selecting a dimension where the predicted A_0 excitation is minimal (or even zero) will only result in a higher S_0/A_0 ratio than otherwise possible. However, the A_0 mode will still be dominant. A second important observation is that in real applications, the specimens under inspection are excited with signals that contain a finite frequency bandwidth (typically a modulated toneburst), and therefore the center frequency, used in the transducer sizing, will not represent the only contribution. A possible future direction for development is the linkage between the excitation signal and the transducer dimension to generate a design that will result in a desired ratio once accounting for all frequency contributions. This can be especially important in the inspection of composite materials as the elastic coupling of different modes may not provide such simple mode separation over a wide frequency range [98, 99].

The selectivity attainable when the variable-length device was used as a sensor was also evaluated. In this case, a circular piezoelectric wafer with a diameter of 16-mm was bonded on the surface of the plate, at 12 cm from the edge of the transducer as in the previous case, to act as a GW emitter. Due to the presence of additional sensors, the actuator was bonded on the opposite surface of the plate, as shown in Fig. 6.18. In this set of experiments, the use of the amplifier was not necessary and the peak-to-peak voltage input was maintained at 18 V. A total of 64 averages were taken at each frequency, and due to similar considerations, the same error convention as in the actuator tests was adopted. The results, shown in Fig. 6.19, indicate that, when used as a sensor, the transducer preferentially senses the symmetric mode. This is likely due to its operation under the 3-3 piezoelectric effect which makes the transducer

mostly sensitive to in-plane strains. This may be responsible for the larger S_0/A_0 sensing ratios observed in this case in contrast to the lower ratios observed for the transmission ratio. Note, however, that the peaks where the transmission ratios occur are not a function of the sensor dimension, but instead of the emitting transducer. The trends observed when the device is used as an actuator are also present in this case. For instance, the 20-mm segment was designed to maximize the S_0 mode at 75 kHz, and it is observed that this device also has the largest S_0/A_0 sensing ratio at lower frequencies. Furthermore, the 10-mm device was selected to maximize the S_0 transmission at 225 kHz and minimize the A_0 transmission at 75 kHz. It can be observed that these trends are supported in the sensing results as well. Finally, the 25-mm device was sized so as to maximize the A_0 transmission at 225 kHz, and it can be seen that among all the combinations, except for the 5-mm device, this segment has the lowest S_0/A_0 sensing ratio.

These observations are equally important, as they indicate that independently of the source used, the sensor can be designed such that specific wavelengths are sensed more effectively. Note that in this case, the maximum performance improvement occurs at 75 kHz. At this frequency, using the 5-mm segment yields a gain of approximately 6.2 dB relative to the 20-mm segment. Once again, this indicates that the wavelength at 75 kHz can be exploited without sacrificing the device sensitivity to the S_0 mode at 150 kHz, for instance. Having a sensor tuned for different wavelengths is particularly important in damage detection, where the reflection signals are typically small compared to the excitation pulses.

6.5 Active compensation using variable-length transducers

This section numerically demonstrates an application of the compensation capability offered by a variable-length device in damage detection. The baseline scenario consists of an isotropic structure with a simulated defect in the form of a part-depth notch. It is assumed that the defect originally has a small dimension and that, through continuous operation, its width and thickness can increase. Furthermore, it is assumed that the transducer length selected is intended for optimal interrogation of a specific defect type and size. The analysis involves exciting an interrogating pulse in the structure and assessing the amplitude of the reflected signal from the defect as its dimension changes. As previous researchers have shown, this reflection will vary depending on the defect depth and the ratio of the defect length to the interrogating pulse wavelength. The following subsections provide a brief description

of the numerical simulations and a discussion of the results obtained.

6.5.1 Finite element simulations

A set of plane strain finite element simulations was conducted to analyze the reflection characteristics from a simulated defect in an aluminum plate (E = 68.9 GPa, $\nu = 0.33$, $\rho = 2700$ kg/m^3). A part-depth notch was introduced by removing elements from the model at desired locations in order to maintain specific notch-width to mode wavelength ratios. The notch width, w_N, and depth, h_N, were varied in the analysis to characterize different levels of damage. A 1-mm thick plate with a length of 0.55 m was considered in ABAQUS 6.8 using CPS4 plane strain elements. The element size used was 0.25 mm in the axial direction and 0.1 mm in the thickness direction. As reported in previous chapters, the effect of the transducer was represented through shear tractions on the top and bottom surfaces of the model. These were used in phase to excite symmetric modes and out of phase for antisymmetric excitation. The front of the notch was located at a distance of 0.265 m from the origin, while the monitoring point was placed at an axial location of 0.115 m. These parameters provided sufficient separation between the incoming pulse, the notch reflections, and the boundary reflections. For the symmetric mode a frequency of 350 kHz with a corresponding wavelength of 16 mm was used. Similarly for antisymmetric excitation, a frequency of 100 kHz was used with a corresponding wavelength of 15 mm. Figure 6.20 shows a schematic of the model used.

A sample time-domain signal collected at the monitoring point is shown in Fig. 6.21. The Hilbert amplitude of the signal has also been superimposed. As discussed in Chapter IV, the amplitude of the Hilbert transform provides an envelope for the signal that is useful in identifying different contributions. Note that the interrogating pulse, the notch reflection, and the boundary reflection are all clearly discernible. The metric of interest in this case is the reflection coefficient, defined as the amplitude of the Hilbert envelope of the notch reflection normalized by the maximum Hilbert amplitude of the incoming pulse. The following section discusses the variation of the reflection coefficient for different notch parameters and its implications on the selection of the transducer dimensions.

6.5.2 Results and discussion

The results for the symmetric mode are shown in Fig. 6.22. As can be seen, varying the length of the defect results in a change in the necessary inspection wavelength

for all notch depths. In particular, consider the deepest notch modeled, where a maximum reflection coefficient is obtained if the notch length to wavelength ratio is in the order of 0.2 and 0.8 (for the following discussion it will be assumed that the transducer was sized so that the notch-width to wavelength ratio is 0.2). If through continued structural operation the length of the notch increases so that its ratio to the original wavelength is in the order of 0.5, the reflection coefficient will be at a minimum. Furthermore, if the signal processing and damage localization algorithms are calibrated to specific tolerances, this change may compromise the performance of the inspection system. To compensate for this change, the wavelength of the interrogating mode should be increased to maintain a constant ratio of 0.2. This would require a proportional increase in the transducer dimension to maintain or improve the purity of the interrogating mode. The variable-length device would enable this possibility thereby maintaining the performance of the health monitoring system. For the parameters considered in the present simulations and assuming a transducer dimension equal to one half the wavelength, this would result in the transducer increasing from 8 mm to 20 mm in length. As experimentally demonstrated in this chapter, this is a feasible possibility. The underlying physics for the oscillations in the reflection coefficient is related to the interference between reflections from the front and back of the notch as discussed by Lowe [109]. If these are constructive, then the amplitude of the reflected signal will be maximized. In contrast, if they are destructive a minimal reflection amplitude will result. Note that in this case, the effect of the notch depth is not very significant. This can be understood by considering the low dispersiveness of the symmetric mode in the frequency-thickness region studied. As the wave velocity does not vary significantly with frequency or thickness, the wave travels at the same speed in the main plate and in the thinner region under the notch. Thus, the interference between the front and back reflections is always similar regardless of the thickness reduction introduced by the notch.

Similarly, consider the result shown in Fig. 6.23 for the antisymmetric mode. In this case there is a significant difference among the different notch depths. This can be physically explained by the dispersive nature of the A_0 mode in the frequency-thickness region used. The thinner notch region results in a significantly lower wave speed relative to that in the main plate, so that the phase difference from the front and back reflections is more evident. For the thinnest notch considered, it can be seen that the wavelength should be in the order of 0.65 to maximize the reflection coefficient. As the notch depth increases, however, the mode wavelength needed to maintain the reflection coefficient needs to change even though the notch length remains constant.

In particular, note that for a 50% thickness reduction, the ratio should be in the order of 0.5 while for a 75% thickness reduction it should be in the order of 0.4. The length of the transducer would need to vary along with the wavelength of the interrogation pulse to once again maintain the mode purity. For the parameters considered in this study, this would result in a maximum transducer length increase from 7.5 mm to 11.5 mm which is a realistic alternative as demonstrated in this chapter. The variable-length capability is particularly important as the new wavelengths required to obtain a high reflection coefficient could be incorrectly matched to the original transducer dimension, thereby resulting in a device that minimizes the reflection of the specific mode. This risk is removed by allowing the length of the emitting actuator or sensor to vary according to the testing conditions.

6.6 Concluding Remarks

In this chapter, the design, manufacture, and testing of a variable-length anisotropic piezocomposite transducer were presented targeting SHM applications. The theoretical background necessary to determine the transducer dimensions, and their dependence on the mode wavelength were outlined. In particular, it was shown that the transducer dimension should be equal to integer multiples of the half-wavelength of the mode whose transmission is to be maximized and equal to integer multiples of the wavelength of the mode to be minimized. Using these results, the segments in the variable-length device were sized so as to maximize the transmission of individual modes at multiple frequencies. The variable-length effect was obtained through the design of an interdigitated electrode pattern with subdivisions for independent actuation and sensing. A combination of laser vibrometer and sensor-based experiments was used to characterize the transmission of the fundamental antisymmetric and symmetric Lamb modes in isotropic plates. It was shown that by using segments with different dimensions, the transmission and sensing ratios (S_0 to A_0 modes) could be tailored to peak at different frequencies. Furthermore, it was demonstrated that for the material system used a maximum mode purity gain of approximately 5 dB in transmission and 6 dB in sensing, relative to other elements in the variable-length device, could be obtained. This was done by appropriately selecting the transducer dimension based on the testing frequency. In addition, a numerical demonstration of the compensation capability of the variable-length device was presented, where it was shown that the optimal transducer dimensions to ensure large reflections from different defect sizes can be realistically combined into a single device. This is advantageous

as it allows a single, compact device to interrogate a structure using a nearly pure mode at different wavelengths, which is expected to improve the damage sensitivity of the transducer. Directions for future work include sizing the individual segments according to the damage size to be detected, evaluating the variable-length effect in composite structures, and the design of variable-length transducers that account for the multiple frequencies contained in a typical excitation signal.

Transducer Dimension [mm]	S_0/A_0 at 240 kHz-mm	S_0/A_0 at 720 kHz-mm
10	0.4	5
20	4	—
25	—	~ 0

Table 6.1: Summary of transducer dimensions and mode transmission ratio available in variable-length APT.

Frequency [kHz]	S_0 wavelength [mm]	A_0 wavelength [mm]
75	71.3	18.7
225	23.6	9.4

Table 6.2: Mode wavelengths at design frequencies for variable-length APT.

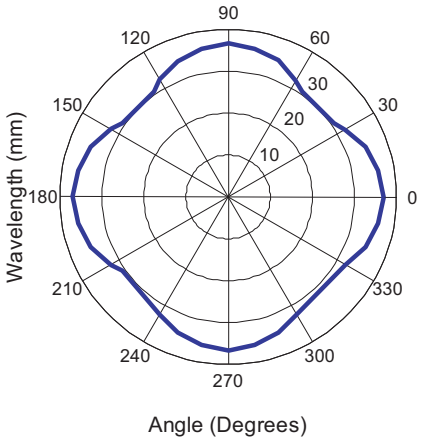

Figure 6.1: Directional dependence of S_0 mode wavelength at 200 kHz on 4-layer $[0/90]_S$ cross-ply laminated composite plate.

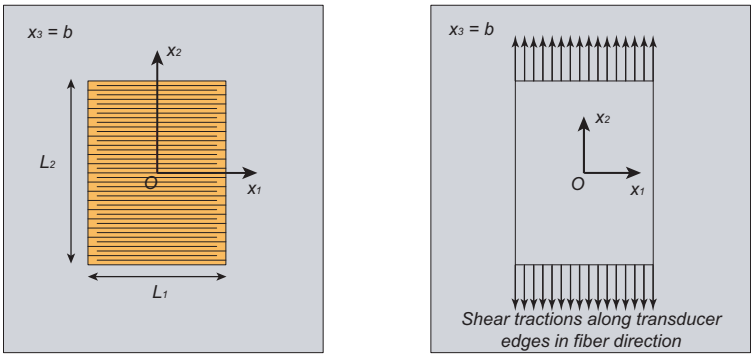

Figure 6.2: (a) Piezocomposite transducer bonded on the surface of the specimen (note that the horizontal lines represent the electrode pattern and that the fibers are aligned with the x_2-direction); (b) The transducer is modeled as shear tractions along its edges on the surface of the substrate.

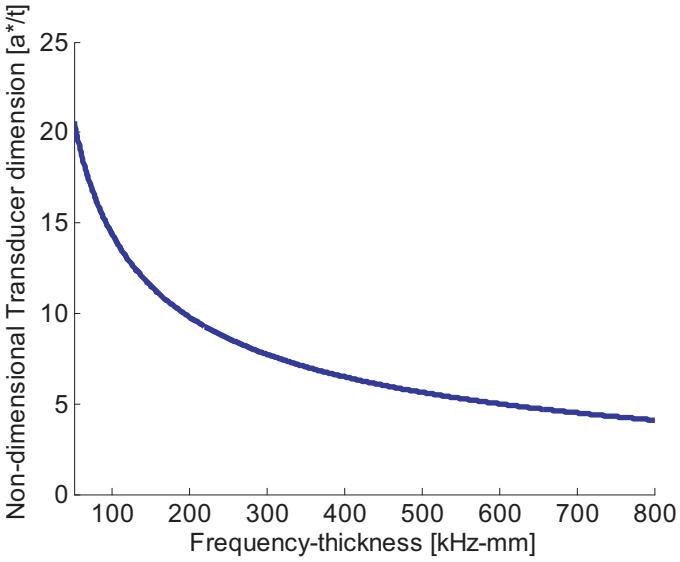

Figure 6.3: Transducer dimensions normalized by substrate thickness needed to maximize A_0 mode transmission in aluminum 5005 plate.

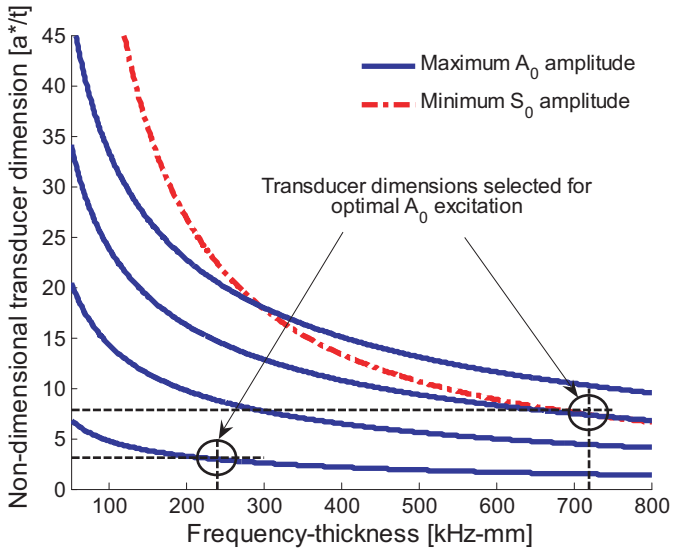

Figure 6.4: Transducer dimensions selected to maximize A_0 mode transmission at 240 kHz-mm and 720 kHz-mm.

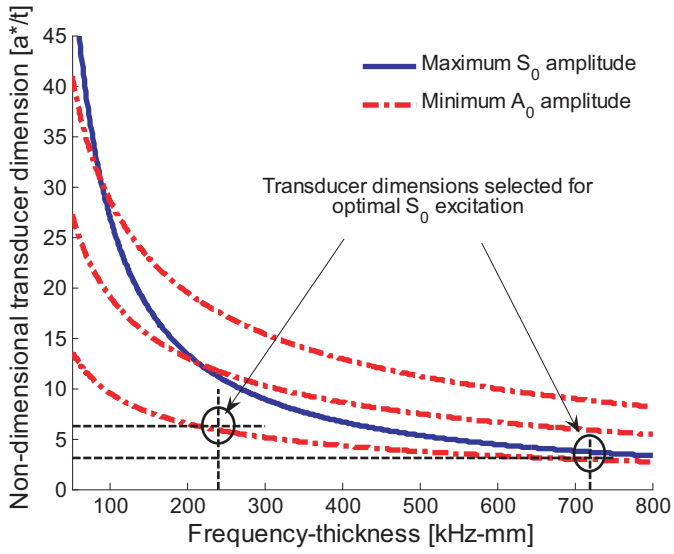

Figure 6.5: Transducer dimensions selected to maximize S_0 mode transmission at 240 kHz-mm and 720 kHz-mm.

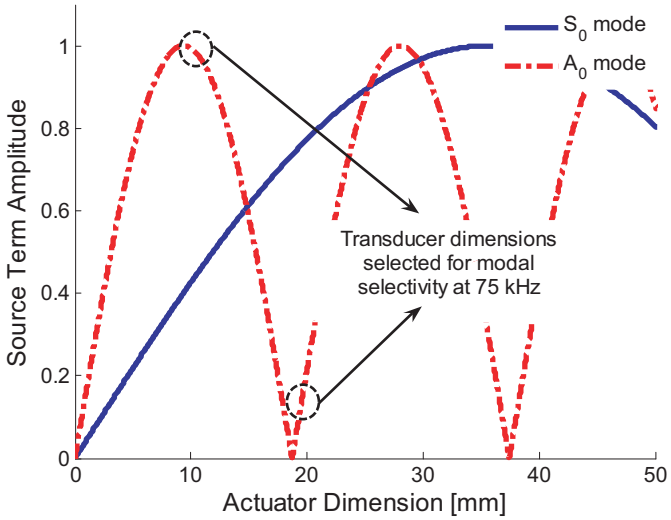

Figure 6.6: Ratio of S_0 to A_0 transmission for the different transducer dimensions selected at 75 kHz.

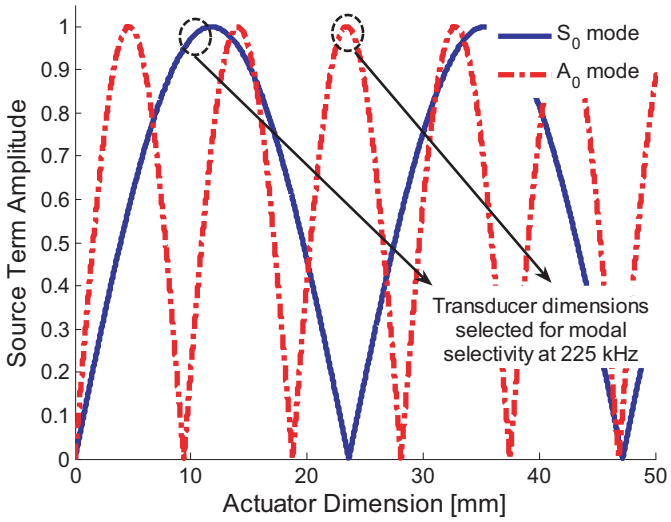

Figure 6.7: Ratio of S_0 to A_0 transmission for the different transducer dimensions selected at 225 kHz.

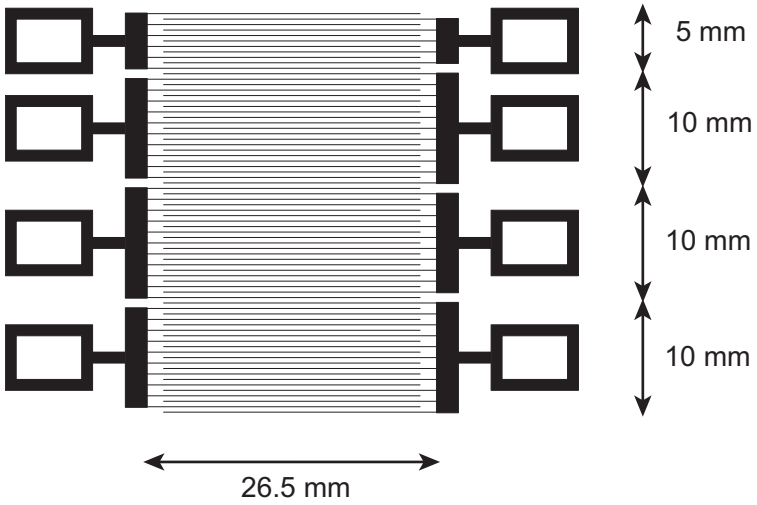

Figure 6.8: Interdigitated electrode pattern used in variable-length APT.

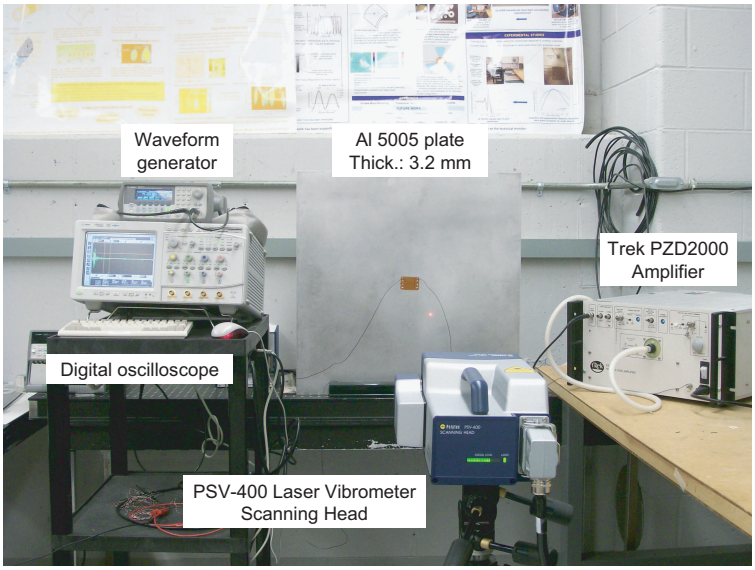

Figure 6.9: Overview of experimental setup used in laser vibrometer experiments.

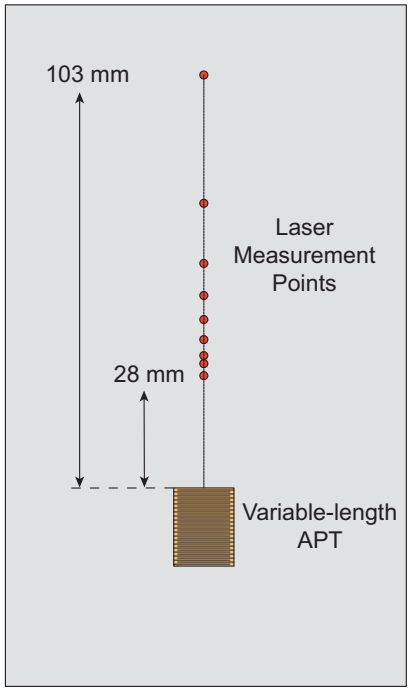

Figure 6.10: Schematic of laser vibrometer monitoring points.

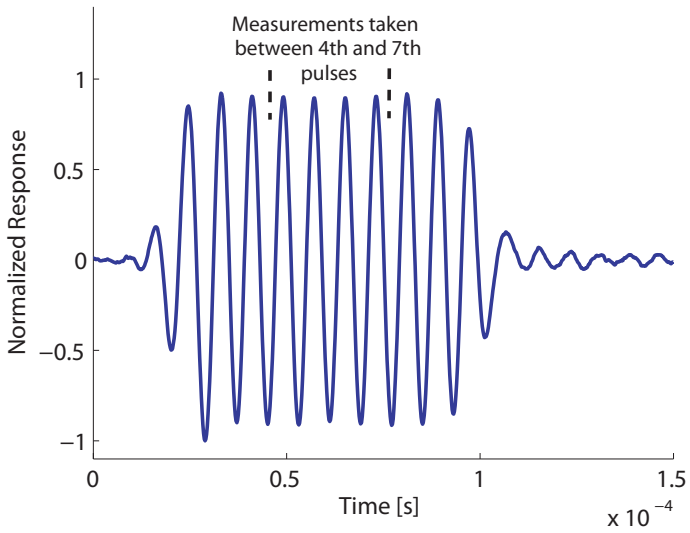

Figure 6.11: Sample response measured with laser vibrometer for 10-cycle sinusoidal excitation at 125 kHz for 10-mm segment.

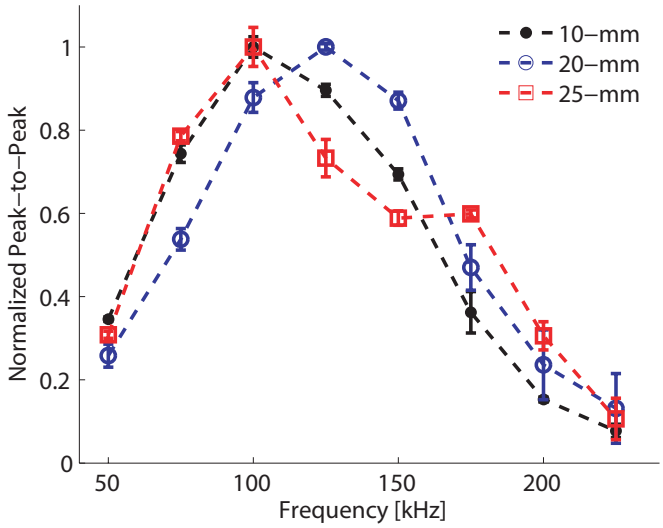

Figure 6.12: Comparison of peak-to-peak amplitudes measured with laser vibrometer under near harmonic excitation conditions for various segments.

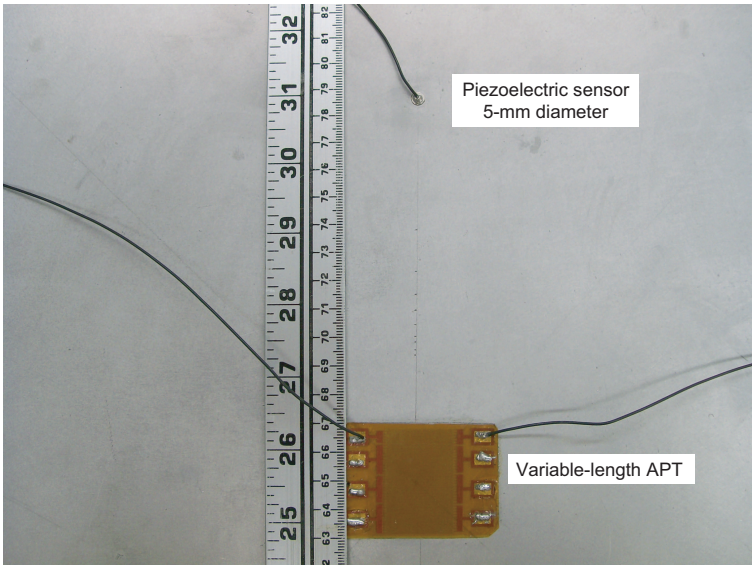

Figure 6.13: Placement of the piezoceramic sensor relative to the variable-length APT on the substrate's surface.

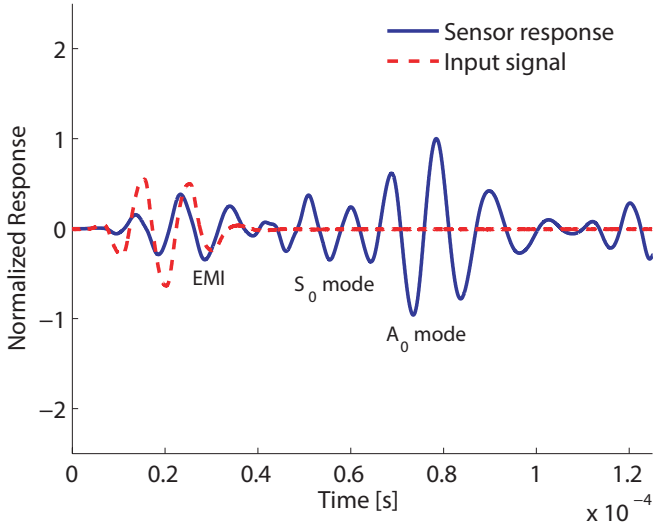

Figure 6.14: Sample signal recorded with piezo sensor when A_0 mode is dominant using the 10-mm segment at 100 kHz.

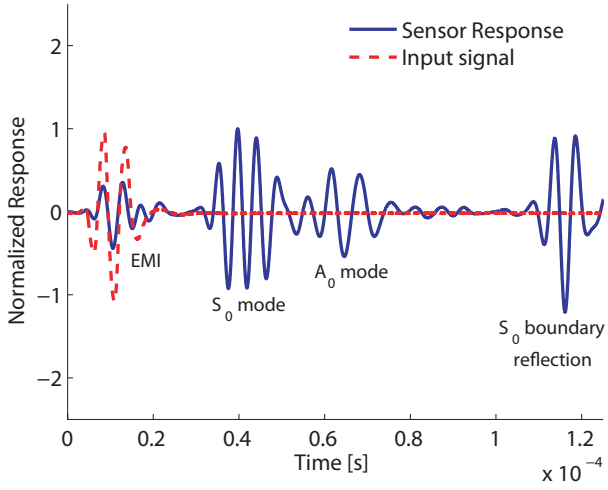

Figure 6.15: Sample signal recorded with piezo sensor when S_0 mode is dominant using the 10-mm segment at 200 kHz.

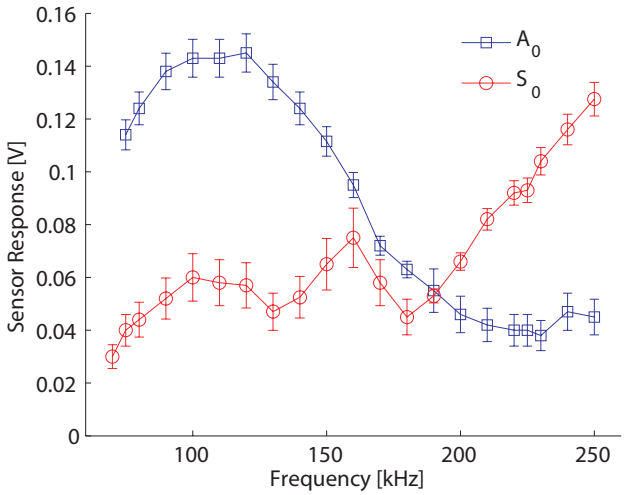

Figure 6.16: Sample frequency response recorded for 20-mm segment using the piezoelectric sensor.

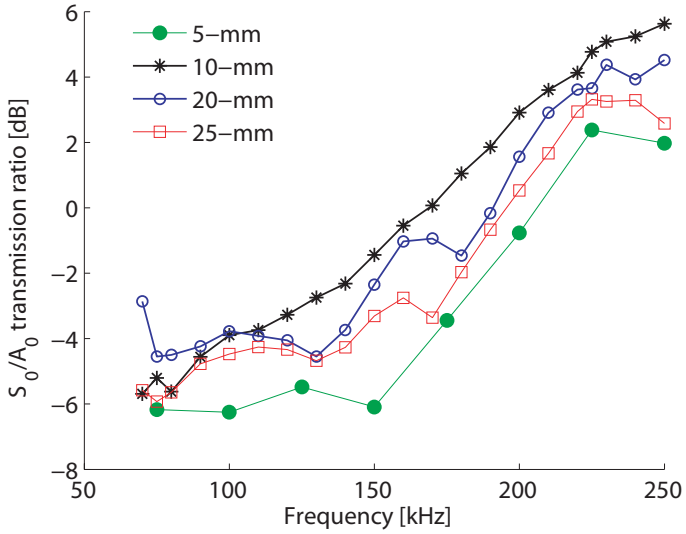

Figure 6.17: Summary of S_0/A_0 transmission ratio as a function of frequency and transducer dimension.

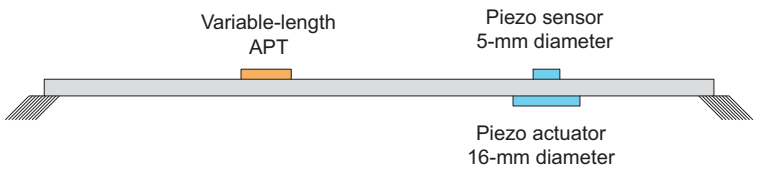

Figure 6.18: Schematic illustrating the location of the piezoelectric wafer used as actuator for the sensing characterization of the variable-length transducer.

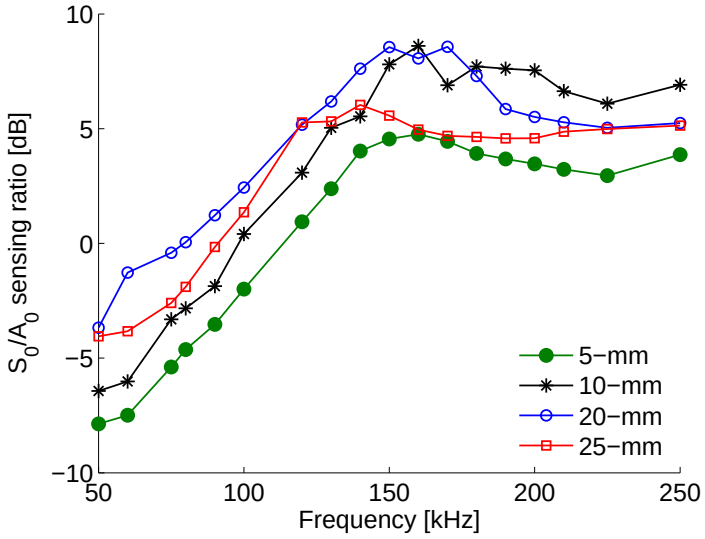

Figure 6.19: Summary of S_0/A_0 sensing ratio as a function of frequency and transducer dimension.

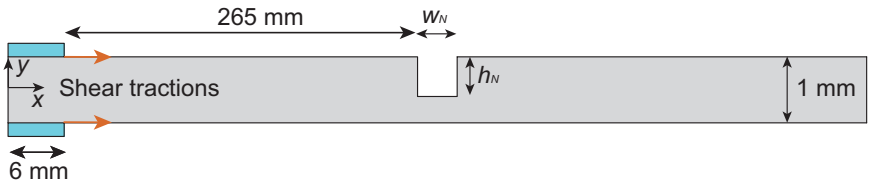

Figure 6.20: Schematic of plane strain finite element model with part-depth notch.

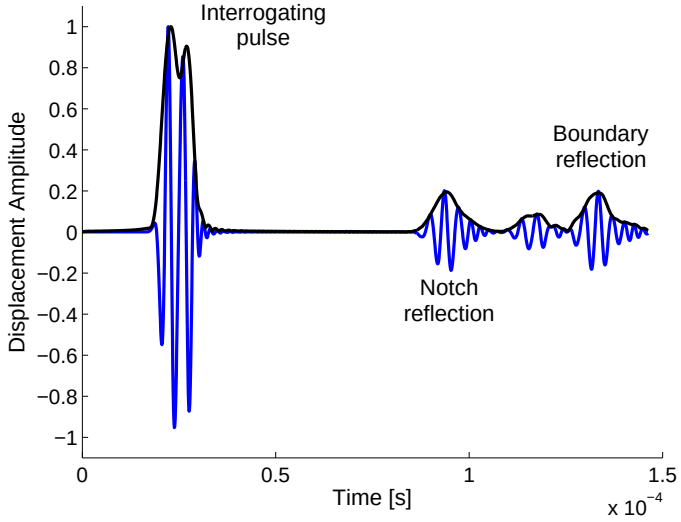

Figure 6.21: Sample signal illustrating interrogating pulse, defect reflection, and boundary reflection for symmetric mode at 350 kHz.

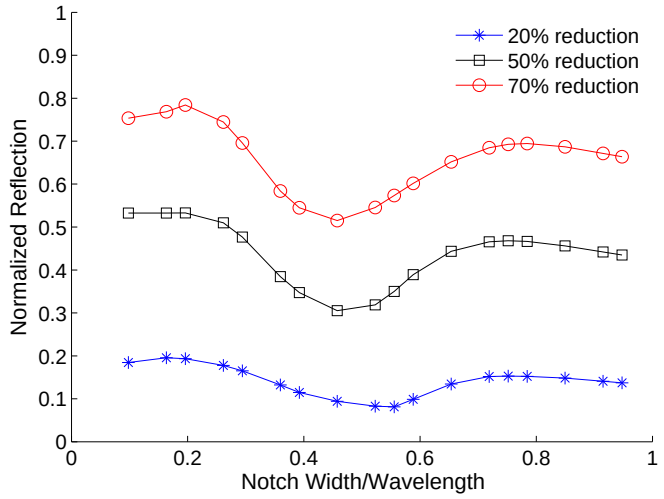

Figure 6.22: Effect of notch depth and width on reflection coefficient for symmetric mode at 350 kHz in a 1-mm thick Al plate.

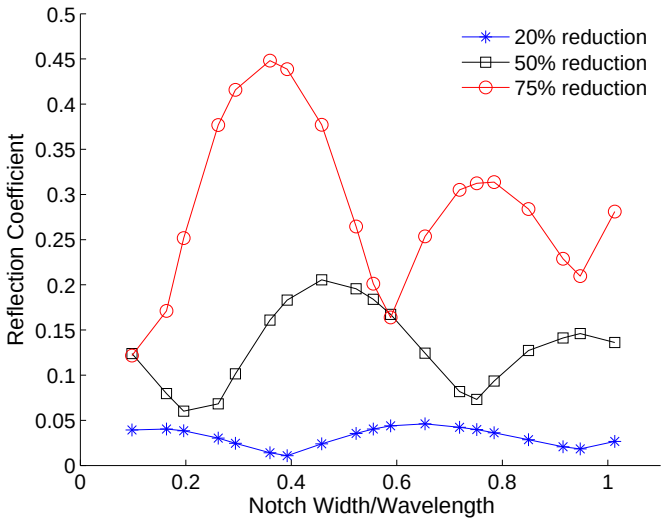

Figure 6.23: Effect of notch depth and width on reflection coefficient for antisymmetric mode at 100 kHz in a 1-mm thick Al plate.

CHAPTER VII

Summary, Key Contributions, and Recommendations for Future Research

This dissertation reported the development of new transducer technologies for guided wave (GW) structural health monitoring (SHM) of engineering structures. The literature survey conducted revealed a void in the transduction alternatives for active structural inspection based on ultrasonic waves. In particular, a majority of the studies employed simple piezoelectric wafers either independently or collectively in phased arrays. The brittleness and omnidirectionality of these wafers prevents them from efficiently interrogating structures from a central location when used independently, while phased arrays result in increased system complexity and power requirements. As a result, the Composite Long-range Variable-length Emitting Radar (CLoVER) transducer was designed, fabricated, and tested in various structural configurations. This device leverages the directionality obtained using active fiber transducers and a unique geometric arrangement to efficiently interrogate a complete structural surface from a central location.

The first step in the conception of the device involved developing a robust and numerically efficient methodology to characterize its GW excitation properties. This development was reported in Chapter II where a theoretical model for GW excitation in isotropic materials, based on three-dimensional elasticity, was derived and numerically verified. The directionality and electrical efficiency of the transducer were also theoretically demonstrated. The theoretical model provides important insight to determine optimal transducer dimensions, and can be exploited for element placement studies in structural transducer networks. The fabrication and characterization of the devices was reported in Chapter III. It was experimentally shown that the in-house developed transducers had similar performance to those available commercially. Furthermore, an extensive set of tests in pristine isotropic structures, using piezoelectric

sensors and laser vibrometry, was used to verify the theoretical model and validate the transducer concept.

The increasing use of composite materials in aerospace and mechanical applications has emphasized the need for inspection strategies to determine their structural condition in an online manner. This need was addressed in Chapter IV where the GW excitation characteristics of piezoelectric wafers and CLoVER transducers in composite materials were examined. In particular, the steering phenomenon was experimentally characterized for both transduction mechanisms for substrates with different levels of anisotropy. It was shown that for structural configurations of practical interest this effect was not as significant as for highly anisotropic, i.e. unidirectional, composites. The characterization of the GW excitation properties of the CLoVER transducer was followed by an experimental investigation into its damage detection capabilities. The results of this investigation were reported in Chapter V. It was shown that its directionality and geometric arrangement allow it to correctly determine the location of simulated defects in isotropic and composite materials. Furthermore, the observations of Chapter IV were confirmed as the damage detection ability of the device was not significantly affected by the steering phenomenon in composite laminates of practical interest.

There are several areas where the transducer design is critical in GW-based health monitoring. Among the most important ones is ensuring that highly pure modes are excited in the most effective manner. Similarly, a transducer design that allows to compensate for changing environmental conditions and different defect types would be highly desired. These areas were addressed in Chapter VI where the development of a variable-length piezocomposite transducer was reported. A prototype device was fabricated and it was shown that the envelope of optimal operation of the device could be greatly expanded by adjusting the dimension of the transducer in an online manner.

The key contributions from this dissertation and directions for future work are presented in the following sections.

7.1 Key Contributions

The main contributions to the field of GW SHM resulting from the research in this thesis are listed below:

- Design, fabrication, and characterization of a novel piezocomposite transducer (CLoVER) for efficient long-range structural interrogation of isotropic and com-

posite structures from a central location. The device combines the directionality and structural flexibility enabled by the piezo-fiber construction with unique electrode pattern designs to provide a superior transduction alternative for GW SHM systems. An extensive experimental characterization of its GW excitation and damage detection properties was conducted.

- Design, fabrication and testing of a novel variable-length anisotropic piezocomposite transducer. The developed transducer enables modal selectivity and environmental compensation in GW-based structural health monitoring systems. The ability to preferentially excite and sense different modes using a single transducer was experimentally demonstrated for the first time. Furthermore, the capability of the transducer to maintain the performance of the health monitoring system through online changes in its dimension was shown through numerical experiments.

- Development and validation of a three-dimensional elasticity model for GW excitation by a finite dimensional wedge-shaped piezocomposite transducer (CLoVER transducer sector) in isotropic structures. The theoretical solution is based on Fourier series, enabling the formulation to be used for any transducer whose geometry can be parametrized through this analysis. The model was extended to characterize the response of piezoelectric-based sensors to the GW field excited by CLoVER transducers.

- Demonstration of a transducer symmetry requirement (relative to an axis normal to the fiber direction) to nullify the transmission of specific GW modes through actuator sizing. The nullification of a particular mode is required to excite or sense highly pure pulses as GWs are multimodal and, therefore, at least two modes propagate in a structure at any frequency-thickness product.

- Numerical and experimental characterization of the GW excitation characteristics of piezoelectric devices in composite materials for various transduction mechanisms. The effects of material anisotropy in GW excitation were systematically analyzed. It was shown that the GW directionality observed in anisotropic substrates is dominated by the steering phenomenon. Specifically, it was demonstrated that large transducer to substrate stiffness ratios (up to and beyond 10) cannot compensate for the weak displacement amplitudes observed along directions unfavorable for energy propagation (as determined by the slowness diagram).

- Experimental characterization of the GW excitation properties of CLoVER transducers in various composite laminates. It was shown that the induced directional pulses are affected by the steering effect, and it was verified that the steered propagation direction can be found from the corresponding phase slowness diagrams. The effect was shown to be dominant in highly anisotropic materials (e.g., unidirectional laminates), and only moderate in configurations typically used in practice (e.g., cross-plies and quasi-isotropic laminates). The experimental results demonstrated that complete structural coverage can be attained, in spite of steering effects, using CLoVER sectors with azimuthal spans in the order of 20°.

- Experimental demonstration of the piezocomposite transducer ability to excite ultrasonic waves in thick structures under realistic environmental conditions through experiments in operational wind turbine structures. The feasibility of the GW inspection approach was supported by propagation distances in excess of 10 m. Furthermore, the potential of the devices to be used in hybrid health monitoring systems, due to its wideband frequency sensitivity, was highlighted.

7.2 Recommendations for Future Research

While significant progress has been made in GW SHM over the past few years, the field is still far from mature and many research avenues exist. Suggested directions for future research are listed below:

- **GW Modeling**: many aspects of GW propagation need better understanding, particularly for complex structural configurations typically encountered in engineering applications. In particular, the propagation of GW in stiffened composites and sandwich structures needs thorough analysis as these are widely used in aerospace and mechanical systems. Due to the geometric complexities of these constructions, theoretical approaches should be complemented with numerical tools. Prominent among these are the spectral finite element method and the local interaction simulation approach. The development of these tools will critically aid the selection of testing parameters and transducer designs, and can provide a complete simulation environment for performance analysis of different transducer networks.

- **GW Interaction with Defects**: there is presently little understanding of the interaction of GW modes with structural defects. Understanding the under-

lying mechanisms responsible for the features observed in reflected modes will better guide system designers in selecting appropriate transducers and testing parameters. Theoretical approaches have been previously developed for metallic structures, and similar studies should be extended for composite laminated materials.

- **GW Transduction Technology**: while this dissertation introduced several advances in the transducer technology used for GW SHM, further development is needed. Within the realm of piezoelectric-based devices, several areas can be pursued. For instance, the variable-length technology should be further developed for optimal interrogation of composite materials and stiffened engineering structures. Further developments on the construction of the devices should also be pursued. For example, an important area where piezocomposite devices can be improved is their low stiffness. The strain transfer can be increased, and the power requirements decreased, by increasing the stiffness of the transducers. This must be carefully done so as to maintain the conformability of the device. Hybrid transducers combining piezoelectric materials and nanocomposites may offer an alternative in this regard.

- **GW Signal Processing**: while not directly addressed in this dissertation, signal processing plays a crucial role in GW SHM. As was shown in several chapters, the signals reflected from defects are often near the noise levels in the system, and robust tools for their identification and classification are needed. In particular, algorithms that exploit physics-based models of GW interaction with defects should be pursued as these can potentially be employed for combined defect localization and classification.

- **GW SHM Transduction Network Design**: the deployment of SHM technologies in aerospace structures will eventually require careful characterization of the mass and power requirements of the system, as well as its operational and maintenance cost. As the actual requirements are likely to be application specific, these aspects should be addressed and incorporated in GW SHM system design tools where trade-off and sensor placement studies can be conducted.

- **Field Tests for GW SHM**: the vast majority of GW SHM developments have been based on testing in laboratory settings where environmental and loading conditions are controlled. Further testing of these systems in operational structures can potentially reveal new opportunities or areas in need of development.

APPENDICES

APPENDIX A

Definition of Variables used in the Theoretical Solution

The column vector of coefficients, $\mathbf{\Delta}$, first introduced in Eq. (2.45), is defined through:

$$\mathbf{\Delta} = \left\{ \begin{array}{c} \varrho_{-2-k}^{(1)} - \varrho_{-k}^{(2)} - \varrho_{2-k}^{(3)} \\ \varsigma_{-2-k}^{(1)} - \varsigma_{-k}^{(2)} - \varsigma_{2-k}^{(3)} \\ \overline{\delta}_{1-k}^{(1)} + \overline{\delta}_{-1-k}^{(2)} \end{array} \right\} \tag{A.1}$$

where the individual components have the following definitions:

$$\varrho_k^{(1)} = \left[c_k^{(2)} \gamma_5^{(1)} - c_k^{(1)} \gamma_4^{(1)} \right] (-i)^k \chi_k \tag{A.2}$$

$$\varrho_k^{(2)} = c_k^{(1)} \gamma_3^{(1)} (-i)^k \chi_k \tag{A.3}$$

$$\varrho_k^{(3)} = \left[c_k^{(1)} \gamma_4^{(1)} + c_k^{(2)} \gamma_5^{(1)} \right] (-i)^k \chi_k \tag{A.4}$$

$$\varsigma_k^{(1)} = \left[c_k^{(1)} \gamma_1^{(2)} - c_k^{(2)} \gamma_5^{(2)} \right] (-i)^k \chi_k \tag{A.5}$$

$$\varsigma_k^{(2)} = c_k^{(2)} \gamma_4^{(2)} (-i)^k \chi_k \tag{A.6}$$

$$\varsigma_k^{(3)} = \left[c_k^{(1)} \gamma_1^{(2)} + c_k^{(2)} \gamma_5^{(2)} \right] (-i)^k \chi_k \tag{A.7}$$

$$\overline{\delta}_k^{(1)} = \frac{1}{2}\left(c_k^{(1)} + ic_k^{(2)}\right)(-i)^k \chi_k \tag{A.8}$$

$$\overline{\delta}_k^{(2)} = \frac{1}{2}\left(c_k^{(1)} - ic_k^{(2)}\right)(-i)^k \chi_k \tag{A.9}$$

Similarly, the column vector $\mathbf{\Lambda}$ is defined as:

$$\mathbf{\Lambda} = \left\{ \begin{array}{c} \eta_{-2-k}^{(1)} - \eta_{-k}^{(2)} - \eta_{2-k}^{(3)} \\ \kappa_{-2-k}^{(1)} - \kappa_{-k}^{(2)} - \kappa_{2-k}^{(3)} \\ \overline{\nu}_{1-k}^{(1)} + \overline{\nu}_{-1-k}^{(2)} \end{array} \right\} \tag{A.10}$$

where the individual components have the following definitions:

$$\eta_k^{(1)} = \left[c_k^{(2)}\gamma_5^{(1)} - c_k^{(1)}\gamma_4^{(1)}\right]\left[R_O H_k^{(2)}(\xi_A r) - R_I H_k^{(2)}(\xi_A r)\right](-i)^k \tag{A.11}$$

$$\eta_k^{(2)} = c_k^{(1)}\gamma_3^{(1)}\left[R_O H_k^{(2)}(\xi_A r) - R_I H_k^{(2)}(\xi_A r)\right](-i)^k \tag{A.12}$$

$$\eta_k^{(3)} = \left[c_k^{(1)}\gamma_4^{(1)} + c_k^{(2)}\gamma_5^{(1)}\right]\left[R_O H_k^{(2)}(\xi_A r) - R_I H_k^{(2)}(\xi_A r)\right](-i)^k \tag{A.13}$$

$$\kappa_k^{(1)} = \left[c_k^{(1)}\gamma_1^{(2)} - c_k^{(2)}\gamma_5^{(2)}\right]\left[R_O H_k^{(2)}(\xi_A r) - R_I H_k^{(2)}(\xi_A r)\right](-i)^k \tag{A.14}$$

$$\kappa_k^{(2)} = c_k^{(2)}\gamma_4^{(2)}\left[R_O H_k^{(2)}(\xi_A r) - R_I H_k^{(2)}(\xi_A r)\right](-i)^k \tag{A.15}$$

$$\kappa_k^{(3)} = \left[c_k^{(1)}\gamma_1^{(2)} + c_k^{(2)}\gamma_5^{(2)}\right]\left[R_O H_k^{(2)}(\xi_A r) - R_I H_k^{(2)}(\xi_A r)\right](-i)^k \tag{A.16}$$

$$\overline{\nu}_k^{(1)} = \frac{1}{2}\left(c_k^{(1)} + ic_k^{(2)}\right)\left[R_O H_k^{(2)}(\xi_A r) - R_I H_k^{(2)}(\xi_A r)\right](-i)^k \tag{A.17}$$

$$\overline{\nu}_k^{(2)} = \frac{1}{2}\left(c_k^{(1)} - ic_k^{(2)}\right)\left[R_O H_k^{(2)}(\xi_A r) - R_I H_k^{(2)}(\xi_A r)\right](-i)^k \tag{A.18}$$

The column vector $\widetilde{\mathbf{\Upsilon}}$ is defined as:

$$\tilde{\mathbf{\Upsilon}} = \left\{ \begin{array}{c} \tilde{\rho}_{-2-k}^{(1)} - \tilde{\rho}_{-k}^{(2)} - \tilde{\rho}_{2-k}^{(3)} \\ \tilde{\psi}_{-2-k}^{(1)} - \tilde{\psi}_{-k}^{(2)} - \tilde{\psi}_{2-k}^{(3)} \\ \tilde{\upsilon}_{1-k}^{(1)} + \tilde{\upsilon}_{-1-k}^{(2)} \end{array} \right\} \tag{A.19}$$

where the individual components are given by:

$$\tilde{\rho}_k^{(1)} = \left[c_k^{(2)}\gamma_5^{(1)} - c_k^{(1)}\gamma_4^{(1)}\right](-i)^k R_O H_k^{(2)}(\xi_A R_O) \tag{A.20}$$

$$\tilde{\rho}_k^{(2)} = c_k^{(1)}\gamma_3^{(1)}(-i)^k R_O H_k^{(2)}(\xi_A R_O) \tag{A.21}$$

$$\tilde{\rho}_k^{(2)} = \left[c_k^{(1)}\gamma_4^{(1)} + c_k^{(2)}\gamma_5^{(1)}\right](-i)^k R_O H_k^{(2)}(\xi_A R_O) \tag{A.22}$$

$$\tilde{\psi}_k^{(1)} = \left[c_k^{(1)}\gamma_1^{(2)} - c_k^{(2)}\gamma_5^{(2)}\right](-i)^k R_O H_k^{(2)}(\xi_A R_O) \tag{A.23}$$

$$\tilde{\psi}_k^{(2)} = c_k^{(2)}\gamma_4^{(2)}(-i)^k R_O H_k^{(2)}(\xi_A R_O) \tag{A.24}$$

$$\tilde{\psi}_k^{(3)} = \left[c_k^{(1)}\gamma_1^{(2)} + c_k^{(2)}\gamma_5^{(2)}\right](-i)^k R_O H_k^{(2)}(\xi_A R_O) \tag{A.25}$$

$$\tilde{\upsilon}_k^{(1)} = \frac{1}{2}\left(c_k^{(1)} + ic_k^{(2)}\right)(-i)^k R_O H_k^{(2)}(\xi_A R_O) \tag{A.26}$$

$$\tilde{\upsilon}_k^{(2)} = \frac{1}{2}\left(c_k^{(1)} - ic_k^{(2)}\right)(-i)^k R_O H_k^{(2)}(\xi_A R_O) \tag{A.27}$$

Finally, the column vector $\boldsymbol{\Upsilon}$ is defined as:

$$\boldsymbol{\Upsilon} = \left\{ \begin{array}{c} \overline{\rho}_{-2-k}^{(1)} - \overline{\rho}_{-k}^{(2)} - \overline{\rho}_{2-k}^{(3)} \\ \hat{\psi}_{-2-k}^{(1)} - \hat{\psi}_{-k}^{(2)} - \hat{\psi}_{2-k}^{(3)} \\ \upsilon_{1-k}^{(1)} + \upsilon_{-1-k}^{(2)} \end{array} \right\} \tag{A.28}$$

where the individual components are given by:

$$\overline{\rho}_k^{(1)} = \left[c_k^{(2)}\gamma_5^{(1)} - c_k^{(1)}\gamma_4^{(1)}\right](-i)^k R_I J_k(\xi_A R_I) \tag{A.29}$$

$$\overline{\rho}_k^{(2)} = c_k^{(1)}\gamma_3^{(1)}(-i)^k R_I J_k(\xi_A R_I) \tag{A.30}$$

$$\overline{\rho}_k^{(2)} = \left[c_k^{(1)}\gamma_4^{(1)} + c_k^{(2)}\gamma_5^{(1)}\right](-i)^k R_I J_k(\xi_A R_I) \tag{A.31}$$

$$\hat{\psi}_k^{(1)} = \left[c_k^{(1)}\gamma_1^{(2)} - c_k^{(2)}\gamma_5^{(2)}\right](-i)^k R_I J_k(\xi_A R_I) \tag{A.32}$$

$$\hat{\psi}_k^{(2)} = c_k^{(2)}\gamma_4^{(2)}(-i)^k R_I J_k(\xi_A R_I) \tag{A.33}$$

$$\hat{\psi}_k^{(3)} = \left[c_k^{(1)}\gamma_1^{(2)} + c_k^{(2)}\gamma_5^{(2)}\right](-i)^k R_I J_k(\xi_A R_I) \tag{A.34}$$

$$\upsilon_k^{(1)} = \frac{1}{2}\left(c_k^{(1)} + ic_k^{(2)}\right)(-i)^k R_I J_k(\xi_A R_I) \tag{A.35}$$

$$\upsilon_k^{(2)} = \frac{1}{2}\left(c_k^{(1)} - ic_k^{(2)}\right)(-i)^k R_I J_k(\xi_A R_I) \tag{A.36}$$

The distinction between symmetric and antisymmetric modes occurs in the definition of the coefficients $\gamma_j^{(i)}$. The following equations provide their definition for the antisymmetric case. The coefficients for the symmetric mode are found analogously by interchanging sine and cosine terms whose arguments depend on the substrate half-thickness b, and by replacing the antisymmetric wavenumber, ξ_A, by its symmetric counterpart, ξ_S.

$$\gamma_1^{(1)} = \sin\alpha b \cos\beta b \tag{A.37}$$

$$\gamma_2^{(1)} = 4\alpha\beta\cos\alpha b \sin\beta b \tag{A.38}$$

$$\gamma_3^{(1)} = \gamma_1^{(1)}\left(\frac{\xi_A^4}{2} + \beta^4 - \beta^2\frac{\xi_A^2}{2}\right) + \gamma_2^{(1)}\frac{\xi_A^2}{2} \tag{A.39}$$

$$\gamma_4^{(1)} = \gamma_1^{(1)}\left(\frac{3}{4}\xi_A^2\beta^2 - \frac{\xi_A^4}{4}\right) - \frac{\gamma_2^{(1)}}{2}\xi_A^2 \tag{A.40}$$

$$\gamma_5^{(1)} = -i\frac{\xi_A^2}{4}\left[\left(\xi_A^2 - 3\beta^2\right)\sin\alpha b\cos\beta b + 4\alpha\beta\cos\alpha b\sin\beta b\right] \tag{A.41}$$

$$\gamma_1^{(2)} = -i\frac{\xi_A^2}{4}\left[\left(\xi_A^2 - 3\beta^2\right)\sin\alpha b\cos\beta b + 4\alpha\beta\cos\alpha b\sin\beta b\right] \tag{A.42}$$

$$\gamma_2^{(2)} = \sin\alpha b\cos\beta b \tag{A.43}$$

$$\gamma_3^{(2)} = 4\alpha\beta\cos\alpha b\sin\beta b \tag{A.44}$$

$$\gamma_4^{(2)} = \gamma_2^{(2)} \left(\frac{\xi_A^4}{2} + \beta^4 - \beta^2 \frac{\xi_A^2}{2} \right) + \gamma_3^{(2)} \frac{\xi_A^2}{2} \tag{A.45}$$

$$\gamma_5^{(2)} = \gamma_2^{(2)} \left(\frac{\xi_A^4}{4} - \frac{3}{4} \xi_A^2 \beta^2 \right) + \frac{\gamma_3^{(2)}}{4} \xi_A^2 \tag{A.46}$$

APPENDIX B

Notes on the development of a piezocomposite transducer for shear wave excitation

B.1 Motivation

The most attractive advantage of the fundamental shear-horizontal (SH) mode for interrogating structural areas is the fact that it is non-dispersive, indicating that all its frequency components travel at the same speed. In practice, this results in the inspection pulse not spreading in time with propagation distance. The dispersion phenomenon is one of the most important challenges in GW SHM systems as it tends to complicate the processing of inspection signals, as mentioned earlier in this dissertation. One of the disadvantages of dispersion is that, at frequencies where it is high, the inspection range that can be covered is typically reduced. This occurs because the energy of both the inspection and any potential reflection pulses is spread over different frequency components traveling at different speeds. While upon interacting with a defect a non-dispersive inspection pulse would tend to inevitably generate dispersive Lamb waves, the distance over which they spread can be significantly reduced (by half if the excitation and sensing devices are collocated). Another important characteristic of the SH mode is that its energy profile is uniformly distributed through the thickness of the structure in which it travels. This feature can be useful during initial structural interrogations where an indication of damage is sought. After an anomaly has been identified, different Lamb wave modes could be used for a more precise characterization.

The excitation of pure shear modes in a structure would require a circumferential traction distribution on its surface which, in order to avoid the excitation of Lamb

modes, would need to be rotationally symmetric. A potential complication arising from this requirement is that the inspection pulse would therefore be mostly generated in an omnidirectional manner. This would only allow the distance to the defect, without information regarding its azimuthal location, to be determined with a single device. This could be resolved by employing a set of similar actuators distributed on the structure for triangulation, or by using the device in conjunction with other transducer arrays able to identify the direction such as the CLoVER transducers.

B.2 Background and Initial Design

The design of the transducer prototype is based on the device developed and tested by Glazounov [114, 115, 116] for rotorcraft applications. This configuration takes advantage of the shear piezoelectric coefficient, which is typically the largest coupling coefficient in piezoelectric materials. In order to excite the shear coupling, the direction of the applied electric field must be perpendicular to the polarization direction. Glazounov proposed an assembly where a series of piezoelectric arches combined to form a tubular structure. Each arch segment was poled along its length, and the perpendicularly-oriented electric field needed for excitation was provided by electrodes placed along the interface between adjacent arches. An important feature of the design is that the polarization direction of a given arch must be along the opposite direction to that of its two adjacent arches in order to ensure a continuous shear deformation. Glazounov [116] showed that this assembly was able to provide a constant shear strain which closely matched the expected deformation based on the piezoelectric coupling coefficient and the applied electric field.

The assembly developed by Glazounov is taken as a starting point in the present study. The initial design of the proposed transducer is composed of individual piezoelectric wedges arranged in a ring configuration. These wedges are bonded using a structural epoxy and the overall assembly is embedded between two layers of copper-clad kapton film where the electrodes needed for actuation are placed. The piezoelectric material selected for this study was PZT-5H. This ceramic has the largest shear coupling coefficient (d_{15} = 730e-12 m/V) of commercially available lead zirconium titanates (as reference, PZT-5A has a shear coupling coefficient of 584e-12 m/V). The piezoceramics were procured in ring-geometries and were poled through the thickness following the manufacturers standard procedure. After polarization, the nickel electrodes were etched from the surface of the rings so as to provide the actuation only through the copper electrodes present in the surrounding kapton film. The piezoce-

ramic rings were diced into 45-degree wedges with the polarization direction clearly labeled in each segment.

The electrode pattern designed and the piezoceramic materials used for the shear transducer are shown in Figs. B.1 and B.2. The electrode pattern is composed of independent lines that provide an electric field perpendicular to the piezoceramic polarization direction. The electrodes were fabricated from a copper-clad kapton film with support from the Lurie Nanofabrication Facility at the University of Michigan. An important consideration in the design of the electrode pattern is that the width of each line be sufficient to cover the piezoceramic wedges for at least 0.5 mm beyond their interface. The electrodes used in the present study had a width of 2 mm, which was found adequate to ensure sufficient coverage while also yielding a degree of flexibility in the arrangement of the wedges. The piezoceramic wedges were manually placed on one layer of the electrode film ensuring that adjacent segments had opposite polarization directions (this ensures a continuous shear deformation). This process must be conducted carefully to allow the electrode lines to cover a sufficient area for the electric field application. During testing, it was found that a partial cure similar to the one used in the CLoVER fabrication was advantageous as it prevented the wedges from displacing from their position once the remaining electrode layer was applied. Prior to the partial cure, each piezoceramic wedge was mechanically attached to the electrode film using a small piece of flash tape to prevent them from moving during the application of vacuum. Once the segments were securely attached to one electrode layer, the remaining electrode pattern was bonded on the opposite side and the device was subjected to a complete cure. The curing pressure and vacuum were similar to those used for the CLoVER transducers. The temperature profile used during final cure was modified, however, to accommodate for the lower Curie temperature of PZT-5H. During fabrication of typical piezocomposite transducers, the piezoelectric material is used in an unpoled configuration during assembly and cure, and therefore the exposure to high temperatures is not a significant concern. In the present case, however, the polarization of the piezoceramic (poled prior to fabrication) must be maintained for the device to function properly. The original cure cycles utilized a steady-state temperature of 121° C for two hours. The Curie temperature for PZT-5H is close to 190° C and it was determined that in order to prevent any degradation in piezoelectric properties, the device would be cured at a temperature of 80° C for two hours. This curing temperature and time have been previously reported by Williams [72] to yield a high cure level in the same epoxy system used in this case. Figure B.3 shows a photograph of the finalized device.

It is important to note that the electric field varies along the radial direction in the transducer, being inversely proportional to the product of the azimuthal span of each wedge and the radial position. This can potentially result in the excitation of Lamb waves as there is a radial strain induced by the transducer. The SH transducer prototype was instrumented with strain gages to monitor the induced strains. The finalized device was bonded on a metallic plate along with three piezoceramic sensors as shown in Fig. B.4. The sensors were placed at intervals of 45 degrees and at a radial position of 5 cm from the outer radial edge of the actuator. The circular sensors had a diameter of 5 mm and were bonded on the plate with an insulating layer between the plate and the lower electrodes as shown in the figure. To cure the adhesive in the actuator and sensors, the instrumented plate was placed in the autoclave and subjected to 50 psi pressure and 75 degrees C for 45 minutes. The sensors were labeled sensor 1 through 3 with sensor 1 being the left-most sensor in Fig. B.4.

The initial testing of the transducer was conducted by collecting time-domain signals at 75, 100, 125, and 150 kHz using a maximum peak-to-peal voltage of 400 V. However, as shown in Fig. B.5 (100 kHz), the sensors only recorded the electromagnetic interference produced by the large voltages and high frequencies. To determine whether any shear strains were induced in the ceramic, a small strain gage that was bonded on the surface of the transducer, as shown in Fig. B.6. The strain gage was installed tangentially to one of the wedges as shown in the figure. It was expected that in this way it would be sensitive to any azimuthal strain induced. For the characterization tests with the strain gage a sinusoidal excitation signal with a frequency of 0.1 Hz was used at various amplitudes. Due to the location of the gage, the distance between electrodes (to calculate the electric field) was taken to be the outer radius of the transducer multiplied by the wedgess azimuthal span (11.3 mm and 45 degrees respectively). Sample time-domain signals showing both the actuation input along with the strain gage response are shown in Fig. B.7. The signal on the left corresponds to a peak-to-peak voltage amplitude of 0.9 kV while the one on the right corresponds to 1.3 kV. Note that while the strains produced are small, a response is in fact observed.

Figure B.8(a) shows the variation of the azimuthal strain with electric field (calculated using the transducer outer radius) while Fig. B.8(b) shows the same result plotted versus voltage input. Note that the strains produced are very small. The star-shaped values correspond to the average of 12 measurements while the red circles correspond to the peak-to-peak value of the last reading which was more representa-

tive of the steady-state response (once initial peaks in the signal had died down due to averaging). As reference, the strain values recorded with the CLoVER transducers at electric fields of up to 500 V (and therefore electric fields of 1 kV/mm) are in the order of 200-300 $\mu\epsilon$. In this case, even though the inputs are going as high as nearly 1.5 kV the electric field is only 0.14 kV/mm therefore being the most likely source of the small strains induced. Also note that an additional reason for the relatively small values may be that in the case of the CLoVERs the free-strain response was measured while these transducers are already bonded to the metallic plate. The last parameter calculated was the piezoelectric coupling coefficient, which was obtained by dividing the measured strain by the applied electric field. This result in shown in Fig. B.9 along with the value reported by the manufacturer for the pristine PZT-5H ceramic. While the shear actuator seems to have a lower constant, the value is still within the expected ballpark. The results from the transducer tests indicate that the large electric voltages needed to obtain a significant electric field result in a severe amount of electromagnetic interference that prevented the signal from being recorded with the sensors. Consequently, the following design iteration consisted of devising a method to obtain very narrow piezoelectric wedges with alternating polarization directions.

B.3 Improved Design

The main goal of the improved design is to obtain narrow piezoceramic segments with alternating polarity. The small segment width would result in large electric fields using low voltage inputs. However, this is nearly impossible to achieve using conventional dicing and flipping methods because of the large number of fibers and the high accuracy required in their placement. Therefore, an innovative poling technique was employed to obtain the desired arrangement. The method is based on selectively poling independent segments of the piezoceramic material. The process begins by depositing a thin layer of a metallic material on a pristine, unpoled PZT-5H piezoceramic disk (a thickness of 0.2 mm and a radius of 25.4 mm was employed). In the present study a 3000-Angstrom thick layer of copper was deposited on both surfaces using physical vapor deposition [1]. Copper was selected as it attached well to the PZT and its etching solution did not attack the ceramic material. A transparency mask is subsequently used to transfer the desired poling pattern onto the copper-coated

[1]The process was conducted using a Cooke evaporator at the Lurie Nanofabrication Facility at the University of Michigan

piezoceramic using a photolithography process. The pattern is first transferred onto one side and the ceramic is then placed in a sodium persulfate etching solution to remove the copper from undesired locations. A microscope-equipped mask aligner is subsequently used to ensure that the pattern to be transferred on the opposite side is exactly aligned with the one on the original surface. The side containing the poling pattern transferred earlier must be coated with photoresist to prevent the copper from dissolving when placed in the etching solution.

A unit cell of the poling pattern used in this study is shown in Fig. B.10, while the entire pattern is shown in Fig. B.11. As the figure indicates, the active ceramic has a radial dimension of 7.5 mm, with wedges that span four degrees. In addition, a 0.125 mm gap exists between adjacent wedges to electrically isolate them. These dimensions were chosen so as to obtain the desired strain levels using reasonable electric voltages as discussed subsequently. The first segment in the unit cell (leftmost for instance) is connected to a positive electrode while the adjacent segment is connected to a ground electrode. On the opposite side of the ceramic, this arrangement is reversed so that the first segment is connected to a ground terminal and the second one to a positive electrode. This approach results in a through thickness polarization oriented from top to bottom in the first segment and from bottom to top in the second segment, therefore resulting in the desired alternating pattern. The poling pattern also contains alignment marks (crosses on the sides) so that the electrode pattern that provides the necessary electric field in the device can be aligned with the poled segments. A photograph of the piezoceramic ring with the deposited poling pattern is shown in Fig. B.12. Once the pattern was transferred to the ceramic, the device was poled under an electric field of 1.5 kV/mm for thirty minutes. This electric field is expected to be more than twice the coercive field for PZT-5H. The capacitance recorded after poling indicated that an adequate degree of polarization was achieved as an increase of approximately 35% was observed. This compares well with the maximum capacitance changes of 44% observed by Bent [10] in piezocomposite transducers.

The electrode pattern used for this device is similar to that used in the CLoVER transducers, and is shown in Fig. B.13. The main difference occurs in the electrode finger width which was increased from 0.1 mm in the case of the CLoVER to 0.35 mm in the case of the SH actuator. This was done to ensure that a sufficient contact area existed between the electrode fingers and the ceramic. This dimension also compensates for the small decrease in finger width expected from the isotropic etching of the copper-clad kapton film. The electrode pattern has a radial dimension of 7.5 mm (consistent with the poling pattern) with an inner radius of 10.5 mm and an outer

radius of 17.5 mm. As the electrode fingers are prismatic, the separation distance increases with radial position, albeit at a much smaller rate than in the previous design. The active electric field distance increases from 0.38 mm at the inner radius location to 0.96 mm at the outer radius location. By assuming the piezocomposite device will display a similar shear coupling coefficient to the pristine ceramic, a strain of 430 $\mu\epsilon$ is expected at the inner radius position. The device was assembled and cured following a similar procedure to the one described above for the first design iteration. The finalized device was subsequently instrumented with strain gages along the axial and tangential directions, and subsequently bonded on an aluminum plate for testing. A photograph of the finalized device is shown in Fig. B.14.

Figures B.15 and B.16 show the results obtained for the tangential and axial strains when the transducer was supplied with different electric field inputs. The excitation was provided by a sinusoidal signal with a frequency of 1 Hz. As the results show, the strain recorded is significantly smaller than originally expected. Figure B.15(a) shows a peak-to-peak tangential strain of 7.1 $\mu\epsilon$ when an electric field of 1.37 kV/mm is supplied, while Fig. B.15(b) shows a peak-to-peak tangential strain of 8.45 $\mu\epsilon$ when an electric field of 1.72 kV/mm is supplied. Using these values, an effective shear coupling coefficient of approximately 5.1e-9 mm/V is found which is two orders of magnitude smaller than the expected result. Following a similar analysis on the results shown in Fig. B.16 results in an effective axial coupling coefficient of 7.45e-9 mm/V which is also negligible. The final set of experiments consisted of measuring the wave field induced using a shear wave-sensitive transducer (Panametrics V151). This was done to eliminate the possibility that the unidirectionality of the strain gages and the poling direction of the piezoceramic sensors used in the first iteration prevented the shear waves from being recorded. These results are not included in this appendix, but the readings indicated that no waves were induced by any of the transducers tested.

The original conception of the device was based on the assumption that the through-thickness shear strains on the transducer would induce tractions on the substrate. In particular, as the substrate would prevent the lower surface of the transducer from deforming, a set of tractions was expected to result. However, the piezoceramic material is able to deform freely in shear so that its top surface rotates by a small amount. This free deformation prevents any forces from being exerted on the substrate. A better approach to exert the desired tractions on the substrate would be to conceive a device with shear deformations along its radial dimension. In other words, if a ring-shaped device is considered, the points at the inner radius

location should rotate in the counter-clockwise direction with the points at the outer radius position rotating in the clockwise direction, for example. A combination of poling and electric field application directions that result in such deformations should be pursued.

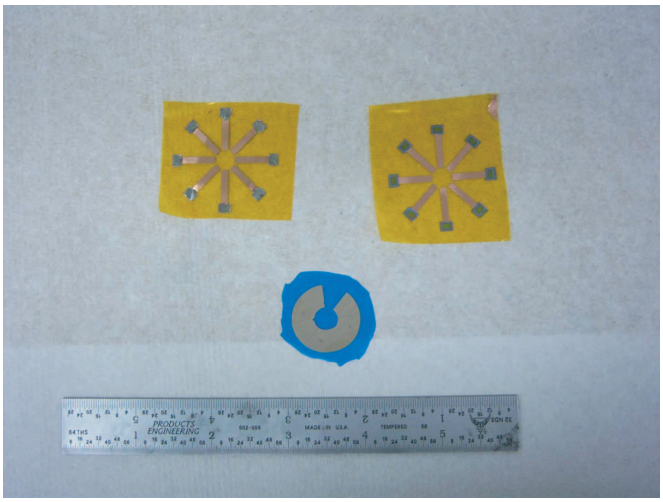

Figure B.1: Independent components used in the fabrication of the first design iteration of the SH transducer: piezoceramic wedges and electrode patterns.

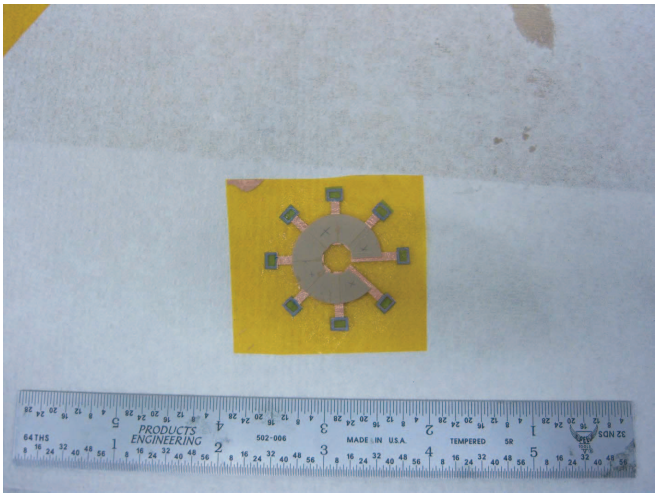

Figure B.2: Piezoceramic wedges aligned on electrode pattern in partially assembled SH transducer.

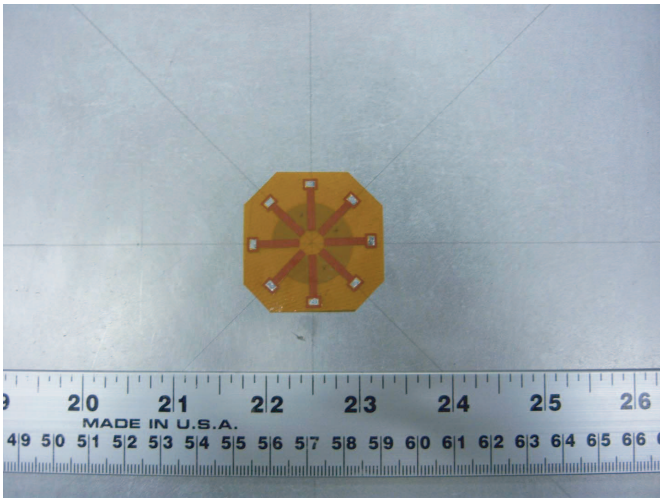

Figure B.3: Finalized SH transducer bonded on an aluminum plate.

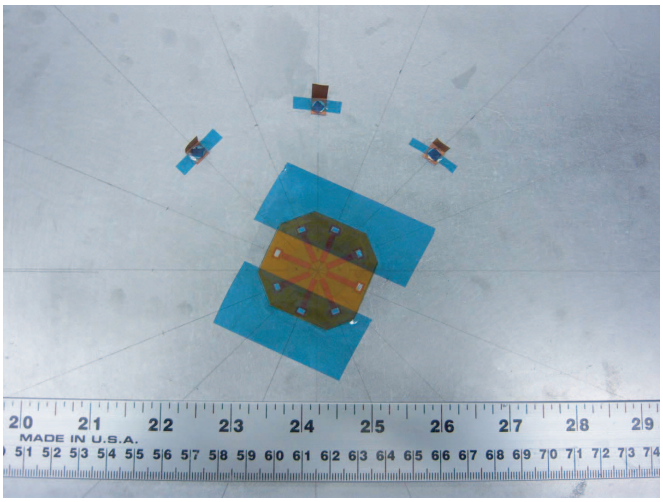

Figure B.4: Finalized SH transducer bonded on an aluminum plate with piezoelectric sensors.

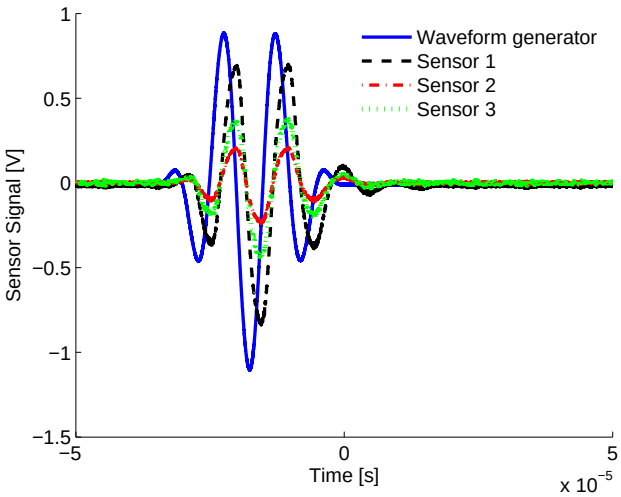

Figure B.5: Time signals recorded with piezoelectric sensors under GW field excited by SH actuator.

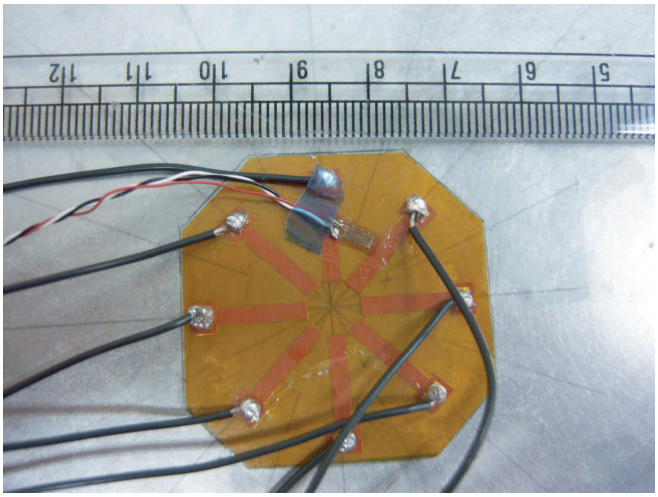

Figure B.6: SH transducer segment instrumented with a strain gage aligned to record tangential motion.

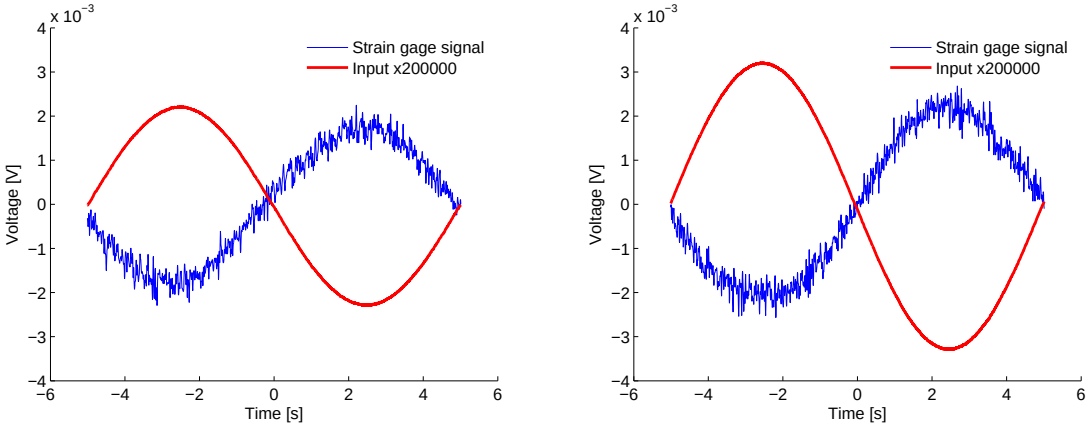

(a) **(b)**

Figure B.7: Response recorded using tangentially-oriented strain gages in SH transducer with electric field inputs of (a) 0.9 kV/mm and (b) 1.3 kV/mm.

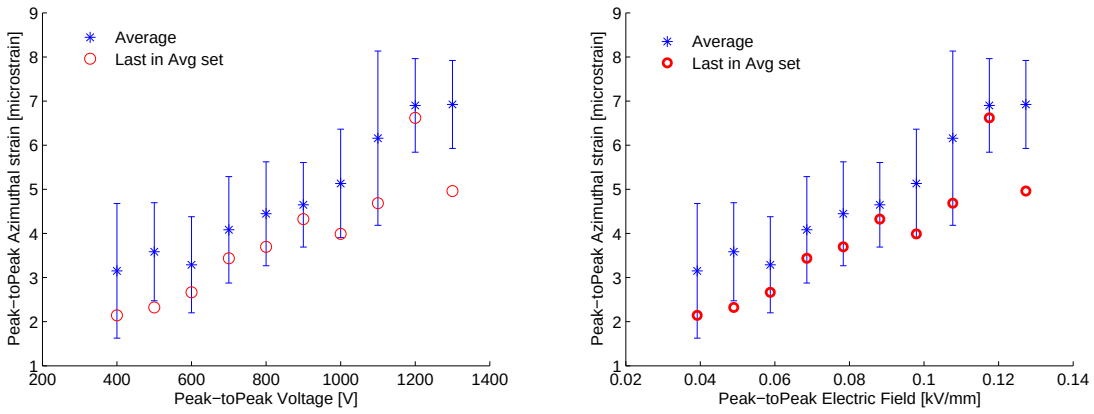

(a) (b)

Figure B.8: Response recorded using tangentially-oriented strain gages in SH transducer with electric field inputs of (a) 0.9 kV/mm and (b) 1.3 kV/mm.

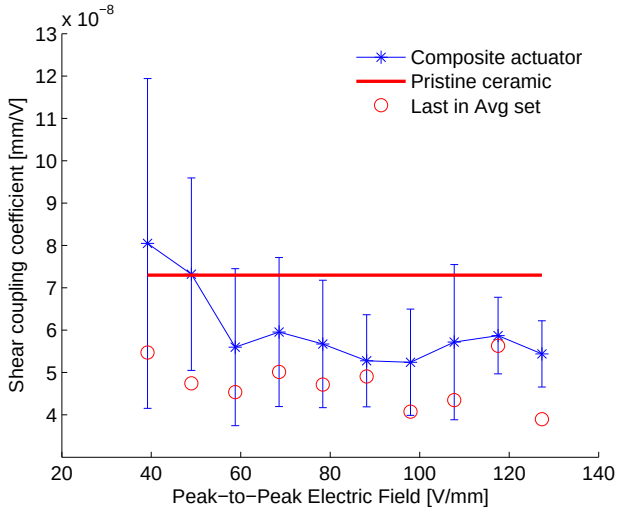

Figure B.9: Shear coupling coefficient measured with tangential strain gage bonded on surface of SH actuator.

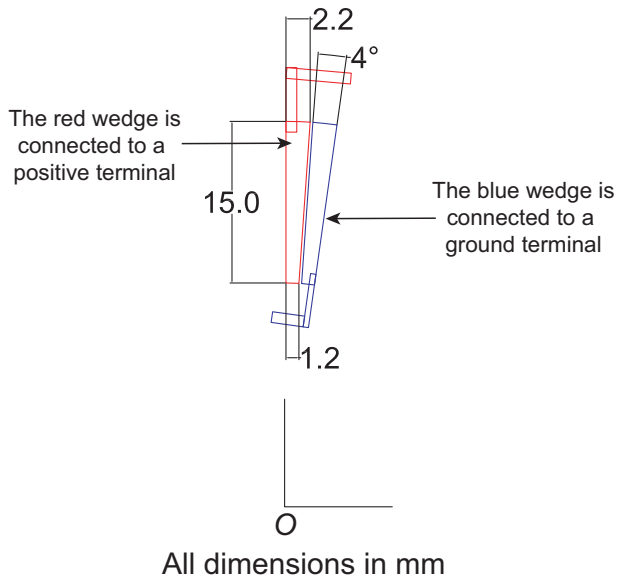

Figure B.10: Shear coupling coefficient measured with tangential strain gage bonded on surface of SH actuator.

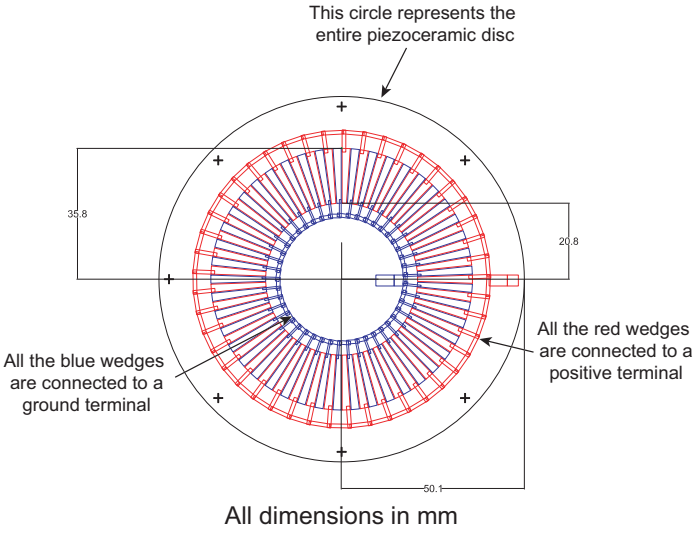

Figure B.11: Shear coupling coefficient measured with tangential strain gage bonded on surface of SH actuator.

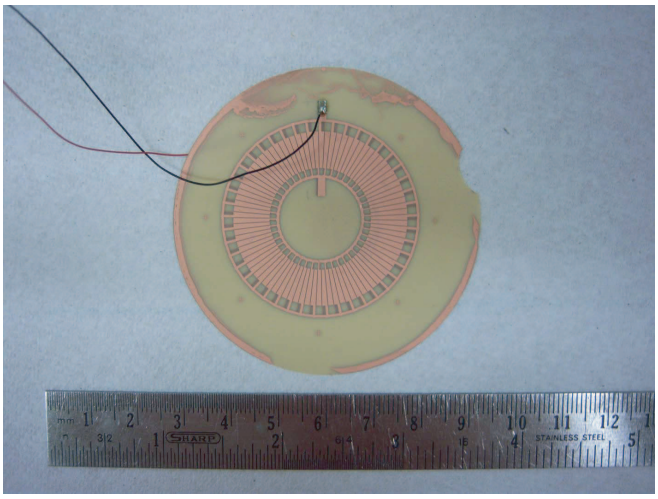

Figure B.12: Copper selective poling pattern deposited on surface of piezoceramic disk for second design iteration of SH actuator.

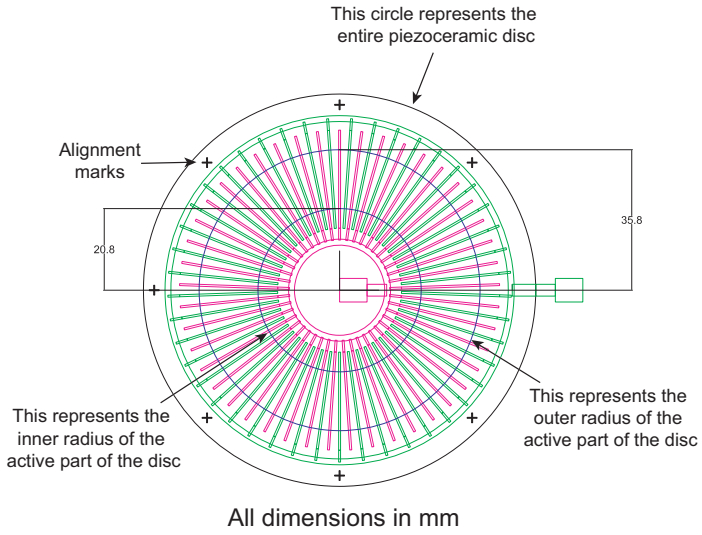

Figure B.13: Electrode pattern used in second design iteration of SH transducer.

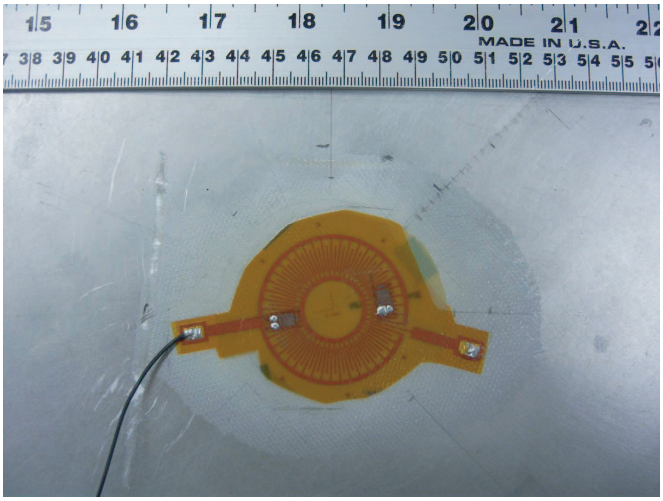

Figure B.14: Second design iteration of SH transducer instrumented with strain gages bonded on an aluminum plate.

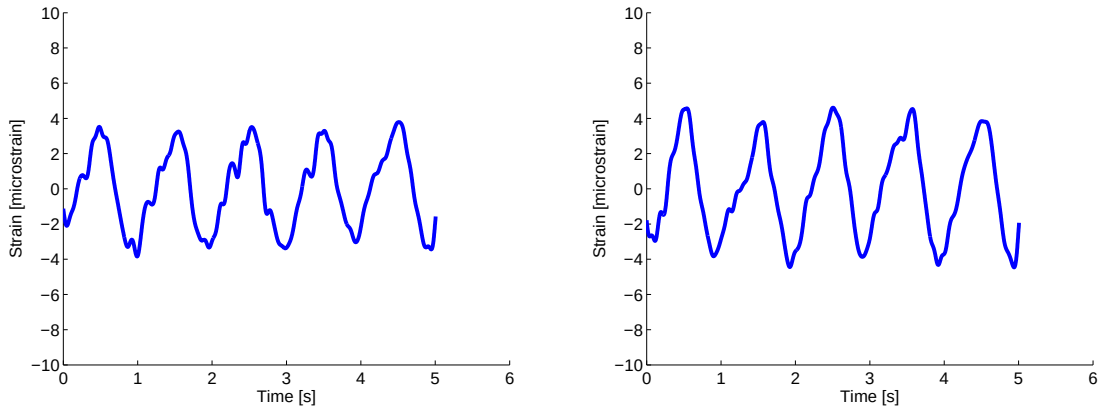

(a) **(b)**

Figure B.15: Response recorded using tangentially-oriented strain gages in second design iteration of SH transducer with electric field inputs of (a) 1.37 kV/mm and (b) 1.72 kV/mm.

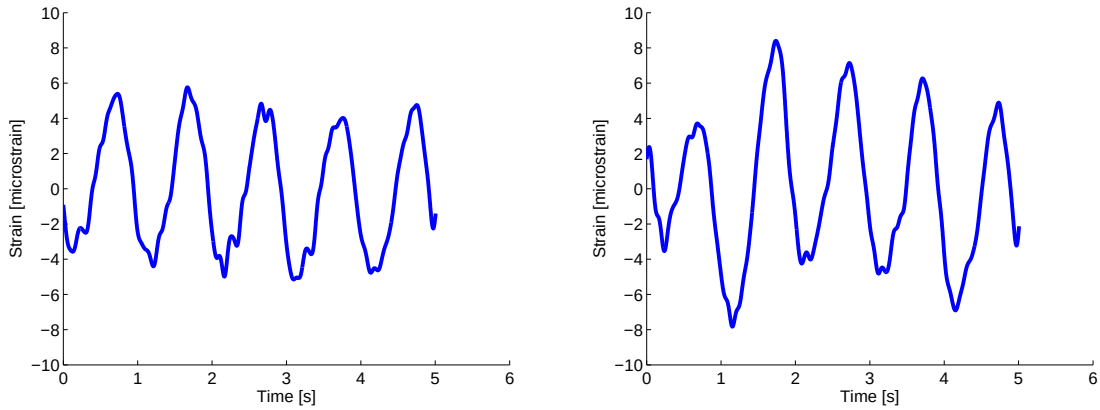

(a) **(b)**

Figure B.16: Response recorded using axially-oriented strain gages in second design iteration of SH transducer with electric field inputs of (a) 1.37 kV/mm and (b) 1.72 kV/mm.

BIBLIOGRAPHY

BIBLIOGRAPHY

[1] W. K. Wilkie, J. W. High, and J. Bockman. Reliability Testing of NASA piezocomposite actuators. *Proceedings of the 8th International Conference on New Actuators, Bremen, Germany*, 2002.

[2] P. Wilcox, M. Lowe, and P. Cawley. An EMAT array for the rapid inspection of large structures using guided waves. *Review of Quantitative Nondestructive Evaluation, American Institute of Physics*, 22:814–821, 2003.

[3] Olympus. Panametrics NDT ultrasonic transducers catalogue. 2009.

[4] L. Yu and V. Giurgiutiu. Design, implementation and comparison of guided wave phased arrays using embedded piezoelectric wafer active sensors for structural health monitoring. *Proceedings of the SPIE*, 6173, 2006.

[5] C.R. Farrar and K. Worden. An introduction to structural health monitoring. *Philosophical Transactions of the Royal Society A*, 365(1851):303–315, 2007.

[6] K. Worden and C.R. Farrar. The fundamental axioms of structural health monitoring. *Philosophical Transactions of the Royal Society A*, 463(2082):1639–1664, 2007.

[7] W.K. Chiu D. Rees and R. Jones. A numerical study of crack monitoring in patched structures using a piezo sensor. *Smart Materials and Structures*, 1(2):202–205, 1992.

[8] C.B. Van Way C. Marantidis and J.N. Kudva. Acoustic-emission sensing in an on-board smart structural health monitoring system for military aircraft. *Proceedings of the SPIE Conference on Smart Structures and Integrated Systems*, 2191:258–264, 1994.

[9] P. Cawley and D. Alleyne. The use of Lamb waves for the long range inspection of large structures. *Ultrasonics*, 34(1):287–290, 1996.

[10] N. Guo and P. Cawley. The interation of Lamb waves with delaminations in composite materials. *Journal of the Acoustical Society of America*, 94(4):2240–2246, 1993.

[11] P. Cawley R. P. Dalton and M. J. S. Lowe. The potential of guided waves for monitoring large areas of metallic aircraft fuselage structure. *Journal of Nondestructive Evaluation*, 20(1):29–46, 2001.

[12] A. Raghavan and C. E. S. Cesnik. Review of guided-wave based Structural Health Monitoring. *The Shock and Vibration Digest*, 39(2):91–114, 2007.

[13] A. A. Bent and N. W. Hagood. Anisotropic Actuation with Piezoelectric Fiber Composites. *Journal of Intelligent Materials, Systems and Structures*, 6(3):338–349, 1995.

[14] Aaron A. Bent. Active Fiber Composites for Structural Actuation. Ph.D thesis, Massachusetts Institute of Technology, 1997.

[15] W. K. Wilkie and J. W. High. Method of Fabricating NASA-Standard Macro-Fiber Composite Piezoelectric Actuators. NASA/TM-2003-212427, NASA, 2003.

[16] R.S.C. Monkhouse, P. D. Wilcox, and P. Cawley. Flexible interdigital PVDF transducers for the generation of Lamb waves in structures. *Ultrasonics*, 35(7):489–498, 1997.

[17] R. S. C. Monkhouse, P. D. Wilcox, M. J. S. Lowe, R. P. Dalton, and P. Cawley. The rapid monitoring of structures using interdigital Lamb wave transducers. *Smart Materials and Structures*, 9(3):304–309, 2000.

[18] P.D. Wilcox, P. Cawley, and M.J.S. Lowe. Acoustic fields from PVDF interdigital transducers. *IEEE Proceedings on Science Measurement Technology*, 145(5):250–259, 1998.

[19] P. Wilcox, M. Lowe, and P. Cawley. Omni-directional guided wave transducer arrays for the rapid inspection of large areas of plate structures. *IEEE Transactions on Ultrasonics, Ferroelectrics, and Frequency Control*, 50(6):699–709, 2003.

[20] P. Wilcox, M. Lowe, and P. Cawley. Omnidirectional Guided Wave Inspection of Large Metallic Plate Structures Using an EMAT Array. *IEEE Transactions on Ultrasonics, Ferroelectrics, and Frequency Control*, 52(4):653–665, 2005.

[21] Y. Y. Kim J. S. Lee and S. H. Cho. Beam-focused shear-horizontal wave generation in a plate by a circular magnetostrictive patch transducer employing a planar solenoid array. *Smart Materials and Structures*, 18(1), 2009.

[22] S. H. Cho et al. Y. Y. Kim, J. S. Lee. Damage detection in a plate by using beam-focused shear-horizontal wave magnetostrictive patch transducers. *Proceedings of the 17th AIAA/ASME/AHS Adaptive Structures Conference, Palm Springs, CA*, 2009.

[23] P. Wilcox, M. Lowe, and P. Cawley. Lamb and SH wave transducer arrays for the inspection of large areas of thick plates. *AIP Conference Proceedings Review of Progress in Quantitative Nondestructive Evaluation*, (509A):1049–1056, 2000.

[24] P. Fromme, P. D. Wilcox, M. J. S. Lowe, and P. Cawley. On the development and testing of a guided ultrasonic wave array for structural health monitoring. *IEEE Transactions on Ultrasonics, Ferroelectrics, and Frequency Control*, 53(4):777–785, 2006.

[25] L. Yu, V. Giurgiutiu, and J. R. Kendall. Omnidirectional Guided Wave PWAS Phased Array for Thin-wall Structure Damage Detection. *Proceedings of the SPIE*, 6529, 2007.

[26] D. Kim and M. Philen. On the beamsteering characteristics of MFC phased arrays for structural health monitoring. *Proceedings of the 49th AIAA/ASME/ASCE/AHS/ASC Structures, Structural Dynamics, and Materials Conference, Schaumburg IL*, 2008.

[27] A. I. Zemmour. The Hilbert-Huang Transform for Damage Detection in Plate Structures. M.S. Thesis, University of Maryland, 2006.

[28] H. M. Matt and F. Lanza di Scalea. Macro-fiber-composite piezoelectric rosettes for acoustic source location in complex structures. *Smart Materials and Structures*, 16(4):1489–1499, 2007.

[29] C. E. S. Cesnik. Integrated Vehicle Health Management System. Proceedings of the NASA Reusable Launch Vehicle URETI, Cleveland, Ohio, NASA Task 5c Annual Report, 2003.

[30] K. I. Salas and C. E. S. Cesnik. Design and characterization of the CLoVER transducer for structural health monitoring. *Proceedings of the SPIE*, 2008.

[31] K. I. Salas and C. E. S. Cesnik. Guided-wave experimentation using CLoVER transducers for structural health monitoring. *Proceedings of the 49th AIAA/ASME/ASCE/AHS/ASC Structures, Structural Dynamics, and Materials Conference, Schaumburg IL*, 2008.

[32] K. I. Salas and C. E. S. Cesnik. Design, characterization, and modeling of the CLoVER transducer for structural health monitoring. *Proceedings of the 4th International Workshop on Structural Health Monitoring, Krakow, Poland*, 2008.

[33] D. Alleyne and P. Cawley. The interation of Lamb waves with defects. *IEEE Transactions on Ultrasonics, Ferroelectrics, and Frequency Control*, 39(3):381–397, 1992.

[34] H. Lamb. On the waves in an elastic plate. *Proceedings of the Royal Society A*, 93:293–312, 1917.

[35] D.C. Gazis. Exact analysis of the plane-strain vibrations of thick-walled hollow cylinders. *Journal of the Acoustical Society of America*, 30:786–794, 1958.

[36] J.D. Achenbach and Y. Xu. Wave motion in an isotropic elastic layer generated by a time-harmonic point force of arbitrary direction. *Journal of the Acoustical Society of America*, 106(1):83–90, 1999.

[37] T. Pamphile H. Huang and M. Derriso. Effect of bending dynamics of piezoelectric patch actuator on Lamb wave displacement field. *Smart Materials and Structures*, 17(5), 2008.

[38] X. Lin and F.G. Yuan. Diagnostic Lamb waves in an integrated piezoelectric sensor/actuator plate: analytical and experimental results. *Smart Materials and Structures*, 10(5):907–913, 2001.

[39] L.R.F. Rose and C.H. Wang. Mindlin plate theory for damage detection: source solutions. *Journal of the Acoustical Society of America*, 116(1):154–171, 2003.

[40] S. Yang and F.G. Yuan. Transient wave propagation of isotropic plates using higher-order plate theory. *International Journal of Solids and Structures*, 42(14):4115–4153, 2005.

[41] V. Giurgiutiu. Lamb wave generation with piezoelectric wafer active sensors for structural health monitoring. *Proceedings of the SPIE*, 5056:111–122, 2003.

[42] A. Cuc and V. Giurgiutiu. Embedded non-destructive evaluation for structural health monitoring, damage detection, and failure prevention. *The Shock and Vibration Digest*, 37(2):83–105, 2005.

[43] A. Raghavan and C. E. S. Cesnik. Finite-dimensional piezoelectric transducer modeling for guided wave based structural health monitoring. *Smart Materials and Structures*, 14(6):1448–1461, 2005.

[44] A. Raghavan and C.E.S. Cesnik. 3-D elasticity-based modeling of anisotropic piezocomposite transducers for guided wave structural health monitoring. *Journal of Vibration and Acoustics*, 129(6):739–751, 2007.

[45] A. Raghavan and C. E. S. Cesnik. Modeling of guided-wave excitation by finite-dimensional piezoelectric transducers in composite plates. *Proceedings of the 48th AIAA/ASME/ASCE/AHS/ASC Structures, Structural Dynamics, and Materials Conference, Honolulu HI*, 2007.

[46] Ajay Raghavan. Guided wave structural health monitoring. Ph.D. Thesis, The University of Michigan, 2007.

[47] B.C. Lee and W.J. Staszewski. Modelling of Lamb waves for damage detection in metallic structures: Part I. Wave Propagation. *Smart Materials and Structures*, 12(5):804–814, 2003.

[48] P. P. Delsanto. Connection machine simulation of ultrasonic wave propagation in materials. I: the one-dimensional case. *Wave Motion*, 16(1):65–80, 1992.

[49] H. H. Chaskelis et al. P. P. Delsanto, R. S. Schechter. Connection machine simulation of ultrasonic wave propagation in materials. II: the two-dimensional case. *Wave Motion*, 20(4):295–314, 1994.

[50] R. S. Schechter P. P. Delsanto and R. B. Mignogna. Connection machine simulation of ultrasonic wave propagation in materials III: The three-dimensional case. *Wave Motion*, 26(4):329–339, 1997.

[51] B.C. Lee and W.J. Staszewski. Modelling of Lamb waves for damage detection in metallic structures: Part II. Wave interactions with damage. *Smart Materials and Structures*, 12(5):815–824, 2003.

[52] S. Hanagud N. Apetre, M. Ruzzene and S. Gopalakrishnan. Spectral and perturbation analysis of first-order beams with notch damage. *Journal of Applied Mechanics*, 75(3):1–10, 2008.

[53] A. Chakraborty S. Gopalakrishnan and D. R. Mahapatra. *Spectral Finite Element Method*. Springer, 2007.

[54] E.F. Crawley and J. de Luis. Use of piezoelectric actuators as elements of intelligent structures. *AIAA Journal*, 25:1373–85, 1987.

[55] A. Raghavan and C. E. S. Cesnik. Modeling of piezoelectric-based lamb wave generation and sensing for structural health monitoring. *Proceedings of the SPIE Symposium on Smart Structures and Materials / NDE 2004*, 2004.

[56] K. Graff. *Wave Motion in Elastic Solids*. Dover Publications, 1991.

[57] K. I. Salas, C. E. S. Cesnik, and A. Raghavan. Modeling of Wedge-shaped Anisotropic Piezocomposite Transducer for Guided wave-based Structural Health Monitoring. *Proceedings of the* 15^{th} *AIAA/ASME/AHS Adaptive Structures Conference, Honolulu, HI*, 2007.

[58] K. I. Salas and C. E. S. Cesnik. Guided-wave excitation by a CLoVER transducer: theory and experiments. *Smart Materials and Structures*, 18(7), 2009.

[59] http://www.efunda.com/materials/piezo. *Engineering Fundamentals Material Database*, 2007.

[60] J. Lim. *Two-Dimensional Signal and Image Processing*. Prentice Hall Signal Processing Series, 1989.

[61] R.V. Churchill, J.W. Brown, and R.F. Verhey. *Complex Variables and Applications, 3rd Edition*. McGraw-Hill Book Company, 1974.

[62] P.D. Wilcox, M.J.S. Lowe, and P. Cawley. Mode and transducer selection for long range Lamb wave inspection. *Journal of Intelligent Materials Systems and Structures*, 12:553–565, 2001.

[63] *2008 ABAQUS/Standard User's Manual Version 6.8*. Hibbitt, Karlsson, and Sorensen Inc., Providence, RI, 2008.

[64] A. Werwer, M.A Polak, and J.C. Santamarina. Rayleigh wave propagation for the detection of near surface discontinuities: Finite element modeling. *Journal of Nondestructive Evaluation*, 22(2):39–52, 2003.

[65] K. I. Salas and C. E. S. Cesnik. CLoVER: an alternative concept for damage interrogation in structural health monitoring systems. *Aeronautical Journal of the Royal Aeronautical Society*, 113(1144):339–356, 2009.

[66] P. Chaudry and C. A. Rogers. The pin-force model revisited. *Journal of Intelligent Materials Systems and Structures*, 6(3):347–354, 1994.

[67] C. H Nguyen and X. Kornmann. A comparison of dynamic piezoactuation of fiber-based actuators and conventional PZT patches. *Journal of Intelligent Materials Systems and Structures*, 17(1):45–55, 2006.

[68] Justin Michael Lloyd. Electrical properties of macro-fiber composite actuators and sensors. M.s. thesis, Virginia Polytechnic Institute and State University, 2004.

[69] http://www.loctite.com. *Loctite Research, Development and Engineering; Technical Data Sheet for Hysol 9491*, 2003.

[70] W. K. Wilkie, D. J. Inman, J. M. Lloyd, and J. W. High. Anisotropic Laminar Piezocomposite Actuator incorporating machined PMN-PT Single-crystal fibers. *Journal of Intelligent Materials Systems and Structures*, 17(1):15–28, 2006.

[71] R. B. Williams, B. W. Grimsley, D. J. Inman, and W. K. Wilkie. Manufacturing and Cure Kinetics Modeling for Macro Fiber Composite Actuators. *Journal of Reinforced Plastics and Composites*, 23(16):1741–1754, 2004.

[72] Robert Brett Williams. Nonlinear Mechanical and Actuation Characterization of Piezoceramic Fiber Composites. PhD. thesis, Virginia Polytechnic Institute and State University, 2004.

[73] Polytec. *Polytec Scanning Laser Vibrometer PSV 400 Hardware Manual*. Polytec GmbH, 2007.

[74] W. H. Leong, W. Staszewski, B. C. Lee, and F. Scarpa. Structural health monitoring using scanning laser vibrometry: III. Lamb waves for fatigue crack detection. *Smart Materials and Structures*, 14:1387–1395, 2005.

[75] C. C. Ciang, J.R. Lee, and H.J. Bang. Structural health monitoring for a wind turbine system: a review of damage detection methods. *Measurement Science and Technology*, 19(2):1–20, 2008.

[76] A. Goshal, M.J. Sundaresan, M. Schulz, and P.F. Pai. Structural health monitoring techniques for wind turbine blades. *Journal of Wind Energy and Industrial Aerodynamics*, 85(3):309–324, 2000.

[77] M.A. Rumsey and J.A. Paquette. Structural health monitoring of wind turbine blades. *Proceedings of the SPIE*, 6933, 2008.

[78] C. Pitchford, B.L. Grisso, and D.J. Inman. Impedance-based structural health monitoring of wind turbine blades. *Proceedings of the SPIE*, 6532, 2007.

[79] Vestas. Vestas v80 brochure http://www.vestas.com/en/media/brochures.aspx. 2009.

[80] S. Zerbst. Personal communication. *Institute for Structural Analysis - University of Hanover*, 2008.

[81] K. I. Salas, C. E. S. Cesnik, and J.P. Lynch. Guided-wave excitation in wind turbine structures using anisotropic piezo-fiber transducers. *Proceedings of the 7th International Workshop on Structural Health Monitoring, Stanford, CA*, pages 1563–1570, 2009.

[82] R. A Swartz A. Zimmermann, M. Shiraishi and J. P. Lynch. Automated modal parameter estimation by parallel processing within wireless monitoring systems. *ASCE Journal of Infrastructure Systems*, 14(1):102–113, 2008.

[83] Y. S. Yang K.-C. Lu, C.-H. Loh and J. P. Lynch et al. Real-time structural damage detection using wireless sensing and monitoring system. *Smart Structures and Systems*, 4(6):759–778, 2008.

[84] S.H. Dias-Valdez and C. Soutis. Real-time nondestructive evaluation of fiber composite laminates using low-frequency Lamb waves. *Journal of the Acoustical Society of America*, 111(5):2026–2033, 2002.

[85] S.S. Kessler, S.M. Spearing, and C. Soutis. Damage detection in composite materials using Lamb wave methods. *Smart Materials and Structures*, 11(2):269–278, 2002.

[86] K. Diamanti, C. Soutis, and J.M. Hodgkinson. Piezoelectric transducer arrangement for the inspection of large composite structures. *Composites Part A*, 38(4):1121–1130, 2007.

[87] H. Matt, I. Bartoli, S. Coccia, F. Lanza, J. Oliver, J. Kosmatka, G. Park, and C. Farrar. Ultrasonic guided wave monitoring of composite bonded joints using macro fiber composite transducers. *Proceedings of the SPIE*, 6174, 2006.

[88] G.S. Bottai, P.J. Pollock, T.A. Behling, V. Giurgiutiu, S.M. Bland, and S.P. Joshi. Damage detection in cryogenic composites for space applications using piezoelectric wafer active sensors. *Proceedings of the 49th AIAA/ASME/ASCE/AHS/ASC Structures, Structural Dynamics, and Materials Conference, Schaumburg IL*, 2008.

[89] B. Yoo, D. Pines, and A.S. Purekar. Guided Lamb wave interrogation of a curved composite plate [0/90] using the Hilbert-Huang transform approach. *Proceedings of the 1st ASME Smart Materials, Adaptive Structures, and Intelligent Systems, Ellicot City MD*, Paper SMASIS2008-591, 2008.

[90] M. Castaings and B. Hosten. Ultrasonic guided waves for health monitoring of high-pressure composite tanks. *NDT and E International*, 41(8):648–655, 2008.

[91] A. McNab A. Gachagan, G. Hayward and P. Reynolds et al. Generation and reception of ultrasonic guided waves in composite plates using conformable piezoelectric transmitters and optical-fiber detectors. *IEEE Transactions on Ultrasonics, Ferroelectrics, and Frequency Control*, 46(1):72–81, 1999.

[92] F. Yan and J. L. Rose. Guided wave phased array beam steering in composite plates. *Proceedings of the 14th SPIE Smart Structures and Materials Symposium*, 6532, 2007.

[93] J. Vishnuvardhan, A. Muralidharan, C.V. Krishnamurthy, and K. Balasubramaniam. Structural health monitoring of anisotropic plates using ultrasonic guided waves stmr array patches. *NDT and E International*, 42(3):193–198, 2009.

[94] B.A. Auld. *Acoustic field and waves in solids Volumes I and II.* R.E. Kreiger Publishing Florida, 1990.

[95] S.-S. Lih and A.K. Mal. On the accuracy of approximate plate theories for wave field calculations in composite laminates. *Wave Motion*, 21(1):17–34, 1995.

[96] B. Pavlakovic and M.J.S. Lowe. Disperse software manual version 2.0.1 6B. *Imperial College London, UK*, 2003.

[97] Cytec Engineered Materials. Im7/cycom 977-3 toughed epoxy resin material data sheet. Technical report, 2009.

[98] K. I. Salas and C. E. S. Cesnik. Guided-wave structural health monitoring using CLoVER transducers in composite plates. *Proceedings of the 50th AIAA/ASME/ASCE/AHS/ASC Structures, Structural Dynamics, and Materials Conference, Palm Springs CA*, 2009.

[99] K. I. Salas and C. E. S. Cesnik. Guided wave structural health monitoring in composite materials using CLoVER transducers. *Journal of Intelligent Materials Systems and Structures*, In review, 2009.

[100] A. Raghavan and C. E. S. Cesnik. Guided-wave signal processing using chirplet matching pursuits and mode correlation for structural health monitoring. *Smart Materials and Structures*, 16:355–366, 2007.

[101] O. Diligent and M. J. S. Lowe. Reflection of the S_0 Lamb mode from a flat bottom circular hole. *Journal of Acoustical Society of America*, 118(5):2869–2879, 2005.

[102] Olivier Diligent. Interaction between Fundamental Lamb modes and Defects in Plates. Ph.D thesis, Imperial College of Science, Technology, and Medicine, 2003.

[103] O. Diligent, T. Grahn, A. Bostrom, P. Cawley, and M. J. S. Lowe. The low-frequency reflection and scattering of the S_0 Lamb mode from a circular through-thickness hole in a plate: Finite Element analytical and experimental studies. *Journal of the Acoustical Society of America*, 112(6):2589–2601, 2002.

[104] A. Mallet, B. C. Lee, W. Staszewski, and F. Scarpa. Structural health monitoring using scanning laser vibrometry: II. Lamb waves for damage detection. *Smart Materials and Structures*, 13:261–269, 2004.

[105] G. Konstantinidis, B.W. Drinkwater, and P.D. Wilcox. The temperature stability of guided wave structural health monitoring systems. *Smart Materials and Structures*, 15(4):967–976, 2006.

[106] A. Raghavan and C. E. S. Cesnik. Studies on effects of elevated temperature for guided-wave structural health monitoring. *Proceedings of the SPIE Symposium on Smart Structures and Materials / NDE 2007*, 6529, 2007.

[107] T. Clarke and P. Cawley. Monitoring of complex structures using guided waves. *Proceedings of the 4^{th} European workshop on structural health monitoring, Krakow, Poland*, pages 672–680, 2008.

[108] F. Chen and P.D. Wilcox. The effect of load on guided wave propagation. *Ultrasonics*, 47(4):111–122, 2008.

[109] M.J.S. Lowe, P. Cawley, J.Y. Kao, and O. Diligent. The low frequency reflection characteristics of the fundamental antisymmetric Lamb wave mode A_0 from a rectangular notch in a plate. *Journal of the Acoustical Society of America*, 112(6):2612–2622, 2002.

[110] O. Diligent and M.J.S. Lowe. Reflection of the S_0 Lamb mode from a flat bottom circular hole. *Journal of Acoustical Society of America*, 118(5):2869–2879, 2005.

[111] P. Fromme, P. Wilcox, M.J.S. Lowe, and P. Cawley. On the scattering and mode conversion of the a_0 Lamb wave mode at circular defects in plates. *Review of Progress in QNDE*, 22A:142–149, 2004.

[112] K. I. Salas and C. E. S. Cesnik. Design of a variable-length anisotropic piezocomposite transducer for structural health monitoring. *Proceedings of the 1st ASME Smart Materials, Adaptive Structures, and Intelligent Systems Conference, Ellicott City, MD*, 2008.

[113] K. I. Salas and C. E. S. Cesnik. Design and characterization of a variable-length piezocomposite transducer for structural health monitoring. *Journal of Intelligent Materials Systems and Structures*, To appear, 2009.

[114] Q. M. Zhang A.E. Glazounov and C. Kim. Piezoelectric actuator generating torsional displacement from piezoelectric d_{15} shear response. *Applied Physics Letters*, 72(20):2526–2528, 1998.

[115] A.E. Glazounov C. Kim and F.D. Flippen et al. Piezoelectric ceramic assembly tubes for torsional actuators. *Proceedings of the SPIE*, 3675:53–63, 1999.

[116] Q.M. Zhang A.E. Glazounov and C. Kim. Torsional actuator and stepper motor based on piezoelectric d_{15} shear response. *Journal of Intelligent Materials Systems and Structures*, 11(6):456–468, 2000.